THE UNIVERSITY *of* EDINBURGH

The Electrodeposition and Characterisation of Thin Films for the Fabrication of Microinductors

Jeremy Murray

Doctor of Philosophy

School of Chemistry

The University of Edinburgh

2014

There is a sort of mythology that grows up about what happened, which is different from what really did happen. It's about understanding... understanding the world!

Peter Higgs

Abstract

Stress in electrochemically deposited (ECD) magnetic films is an important parameter that can have a critical effect on the performance of MEMS devices such as microinductors. This is especially the case when thick layers of materials are required and where it is important to monitor and hence control stress to prevent cracking and delamination. The reliability of devices, therefore, deeply depends on process parameters and conditions used in depositing these materials on silicon wafers.

A MEMS technique for measuring stress spatially around such a wafer has been developed and used to characterise the materials involved in the fabrication of a microinductor. This thesis discusses the design and fabrication of test structures, along with a custom built automatic measurement technique to wafer map the spatial variation of strain, on any sized wafers. The effect of agitation on the grain structure of NiFe has been observed to affect strain which were spatially mapped and correlated with the film composition and thickness. Film uniformity were also shown to improve in the absence of agitation in the bath.

To further understand the fundamentals of ECD small scale beaker level galvanostatic experiments have been employed to use the same test structures fabricated on small Si chips. The effects of hydrogen evolution on film stress and efficiency with the inclusion of boric acid and saccharin, have been discussed. It was concluded that the tensile stress developed in Ni and NiFe films have an inversely proportional relationship with the plating efficiency.

The characterisation of electrodeposited copper films is also of importance as copper films are integrated with magnetic materials in the form of windings for microinductors. The variations in recrystallization and evolution of grains of ECD copper, is for the first time demonstrated spatially using the test structures. The

effect of additives in bath on film uniformity was investigated and it was observed that with carrier and additive together the three phases of self annealing were more pronounced.

Finally the use of these strain test structures have been demonstrated on thick polymer SU-8 films, which is employed as a structural material in microinductors. The effect of UV exposure dose on the cross linking properties of SU-8 has also been studied. It was observed that non-uniformity in the coated film thickness over the wafer can cause variations in the UV exposure during photolithography that effects the cross linking of the polymer hence, inducing different levels of tensile stress in the material.

This unique methodology has therefore opened up many possibilities and can be used for characterising newer materials employed in MEMS, fine-tuning the manufacturing processes to achieve set goals in terms of material properties as well as uniformity and gaining a better understanding of the influence of processing conditions on the produced films.

Acknowledgements

Without the endless help and precious support of my supervisors Prof. Anthony Walton and Prof. Andy Mount this work wouldn't have been possible. Thanks to the awarding bodies of the University of Edinburgh (ORS) and the Scottish Funding Council (SPIRIT) alongside National Semiconductors (now Texas Instruments) for the funding support.

Many thanks to Stewart Smith for his help on the fabrication and electrical measurements on the semiautomatic prober and Nathan Brockie for getting me started on ECD. Jon Terry and Andy Bunting who were always there for the cleanroom fabrication queries and laboratory assistance and Byron Shulver for off-site measurements at Texas Instruments (Greenock). Thanks to my fellow magnetic group members especially Giuseppe Schiavone and Richard Perry for the humour and cheer alongside the hard work conducted for this project.

Material characterisation wouldn't have been possible without the technical and motherly support of Camelia Dunare, speaking of which Valerie McDermott cannot be forgotten for her family like charm and support. Thanks to Richard Blair, Ewan Macdonald and Stewart Ramsay for their technical support with cleanroom equipment.

The release of test structures were crucial for this work and I would like to acknowledge MEMSSTAR engineers Tony O'Hara and Daniel Drysdale for the endless work on HF vapour and XeF_2 etch tools.

Outside of the University environment I would like to thank my friends and family for their support throughout the duration of my PhD. I especially thank my parents (John and Cecilia) and my sister (Juliet) for continually backing me up and also helping me financially during my undergraduate studies. A special thankyou to Agne for her love and support till the very end.

Declaration

The candidate confirms that the work submitted is his own, except where work which has formed part of jointly-authored publications has been included. The contribution of the candidate and the other authors to this work has been explicitly indicated below. The candidate confirms that appropriate credit has been given within the thesis where reference has been made to the work of others.
The nano-indentation measurements described in Chapter 5 (section 5.3.2) was performed by Giuseppe Schiavone at the University of Edinburgh and the stress maps therein have been jointly published (DOIs: 10.1109/ICMTS.2012.6190629).
The candidate hereby declares that the work has not been submitted for any other degree or professional qualification.

_____

Jeremy Murray

Contents

Figures and Tables

Figures

Tables

Acronyms and abbreviations

AFM	Atomic Force Microscope
Al	Aluminium
BEOL	Back end of line
CE	Counter electrode
CD	Critical dimension
CMOS	Complementary Metal Oxide Semiconductor
CMP	Chemical Mechanical Polishing
Cu	Copper
CVD	Chemical Vapour Deposition
DI	De-ionised water
DC	Direct Current
E	Young's modulus
ECD	Electrochemical deposition
EQCM	Electrochemical quartz crystal microbalance
FEA	Finite element analysis
FSM	Frontier Semiconductor Measurement (wafer curvature tool)
FIB	Focused Ion Beam
GPIB	General purpose interface bus
GUI	Graphical user interface
HCl	Hydrochloric acid
HF	Hydrofluoric Acid
IC	Integrated Circuit
ICP	nductively Coupled Plasma
IMAQ	Image Acquisition for Labview
LPCVD	Low Pressure Chemical Vapour Deposition

M	Molar concentration
MEMS	MicroElectroMechanical Systems
MPa	Mega Pascal
Ni	Nickel
NiFe	Nickel-Iron alloy
NIST	The National Institute of Standards and Technology
OCD	Optical Critical Dimension
OCP	Open circuit potential
PC	Personal computer
PEB	Post exposure bake
PECVD	Plasma Enhanced Chemical Vapour Deposition
PEG	Polyethylene glycol
PGMEA	Propylene glycol monomethyl ether acetate
pH	power of hydrogen
PVD	Physical Vapour Deposition
RE	Reference electrode
RGB	Red-green-blue
RIE	Reactive Ion Etching
SCE	Saturated Calomel Electrode
SEM	Scanning Electron Microscopy
SOI	Silicon On Insulator
SNR	Signal-to-noise ratio
SPM	Scanning Probe Microscopy
TEM	Transmission Electron Microscopy
TSV	Through-silicon-vias
UV-Vis	Ultraviolet-visible spectroscopy
VI	Virtual Instrument (Labview program)
WE	Working electrode
XRD	X-Ray Diffraction
XRF	X-Ray fluorescence

List of Publications

The following accepted journal or conference papers were prepared in the development of this thesis:

1. R. Zhang, Y. Li, J. Murray, C.C. Dunare, A.S. Bunting, S. Smith, J.T.M. Stevenson, A.J. Walton; "Test Structures for Electrical Evaluation of High Aspect Ratio TSV Arrays Fabricated Using Planarised Sacrificial Photoresist", Proceedings of IEEE International Conference on Microelectronic Test Structures, pp. 37-42, 25-28th Mar 2013.

2. G. Schiavone, J. Murray, J.G. Terry, S. Smith, M.P.Y. Desmulliez, A.J. Walton; "Micromechanical Test Structures for the Characterization of the Magnetic Response of Electroplated NiFe Cantilevers and their Viability for use in MEMS Switching Devices", Proceedings of IEEE International Conference on Microelectronic Test Structures, pp. 13-18, 25-28th Mar 2013.

3. G. Schiavone, M.P.Y. Desmulliez, S. Smith, J. Murray, E. Sirotkin, J.G. Terry, A.R. Mount, A.J. Walton; "Quantitative mapping of residual stress in micromachined materials by coupling independent strain and Young's modulus measurements", IEEE International Conference on Microelectronics Test Structures, pp. 105-110, April 2012.

4. J. Murray, G. Schiavone, S. Smith, N.L. Brockie, J.G. Terry, A.R. Mount, A.J. Walton; "Correlation of Optical and Electrical Test Structures for Characterisation of Copper Self- Annealing", IEEE International Confer-

ence on Microelectronics Test Structures, pp. 152-157, April 2012.

5. S Smith, N.L. Brockie, J. Murray, C.J. Wilson, A.B. Horsfall, J.G. Terry, J T M Stevenson, A.R. Mount, A J Walton, "Fabrication and Measurement of Test Structures to Monitor Stress in SU-8 Films", Semiconductor Manufacturing, IEEE Transactions on , vol.25, no.3, pp.346,354, Aug. 2012

6. J. Murray, G. Schiavone, S. Smith, J. Terry, AR. Mount, A.J.Walton, ' Characterisation of Electroplated NiFe Films using Test Structures and Wafer Mapped Measurements", 24th International Conference on Microelectronic Test Structures, Amsterdam, 4th - 7th April 2011.

7. S. Smith, J. Murray, N.L. Brockie, C.J. Wilson, A.B. Horsfall, J.G. Terry, J.T.M. Stevenson, A.R. Mount, A.J. Walton; "Analysis of the Performance of a Micromechanical Test Structure to Measure Stress in Thick Electroplated Metal Films", IEEE International Conference on Microelectronics Test Structures, pp. 80-85, March 2010.

8. S. Smith, J. Murray, N.L. Brockie, C.J. Wilson, A.B. Horsfall, J.G. Terry, J.T.M. Stevenson, A.R. Mount, A.J. Walton; "Fabrication of Test Structures to Monitor Stress in SU-8 Films used for MEMS Application", IEEE International Conference on Microelectronics Test Structures, pp. 8-13, March 2010.

9. J.Murray, R.Perry, A.R.Mount, A.J.Walton; "Self-Annealing Studies of Electrodeposited Copper Films using MEMS Test Structures", 2014 .. in preparation

10. J.Murray, R.Perry, A.R.Mount, A.J.Walton; "Characterisation of Stress in Electrodeposited NiFe using MEMS Test Structures", 2014 ..in preparation

Chapter 1

Introduction

Integrated circuits (ICs) have penetrated virtually every electronics sector in the past half century. These consist of discrete circuits all fabricated on one small substrate, usually silicon and can be composed of millions of transistors each acting as a switch to manipulate electronic signals. These transistors, when arranged in a specific sequence, can be used to perform basic calculations and this has become the basis of what is called a microprocessor (commonly referred to as a chip). The more transistors in a chip, the more complex calculations it can perform per second. In a paper published by Moore in 1965, on the state of the semiconductor industry, he predicted that the number of transistors in an integrated circuit would double each year [13]. This prediction known as Moore's Law was revised in 1975 stating that the number of transistors per chip would double every 18 months [14]. Being less of a prediction it has now become a goal for the electronics industry to compact the chip and fit as many transistors as possible. Since 1971, the number of transistors in a microprocessor has increased from 2300 (Intel 4001 [15]) to 5 billion in 2012 (Intel Xeon Phi [16]). At the heart of this tremendous progress in miniaturisation, lies the properties of semiconductor materials such as silicon [17] and advance fabrication techniques of materials that are either grown or deposited to form the transistors.

Currently for many applications, ICs are dependent upon sensors to provide input from the surrounding environment. Attention in this area was first focused on microsensor development with the invention of silicon pressure sensors in 1954 [18]. Now, micro-sized machines such as accelerometers and gyroscopes are

being fabricated by selectively etching the silicon substrate in order to leave behind the desired mechanical element of the device [19] [20]. Being able to use the same technology as IC fabrication, these microsensors and structures have found increased commercial use and are now commonly known as "micro-electro-mechanical systems" or MEMS [21]. The term 'micro' is used because their dimensions typically vary in the micron scale (from 1 micron to a few hundred microns).

Conventionally, MEMS sensors have often been built separately and packaged alongside the IC on a substrate (e.g. ceramic) a schematic of which is shown in Figure 1.1(a). In this case, the electrical interconnection between the two chips is carried out through wire bonds. This configuration is called the hybrid approach. A few disadvantages of this setup is the increased size of the package, higher costs for the assembly and performance limiting parasitics arising from the bond pads and long bonding wires [22]. However, an alternative approach is to integrate MEMS with the IC chip by fabricating both on the same silicon substrate (Figure 1.1(b)). This integration technique has gained a lot of interest

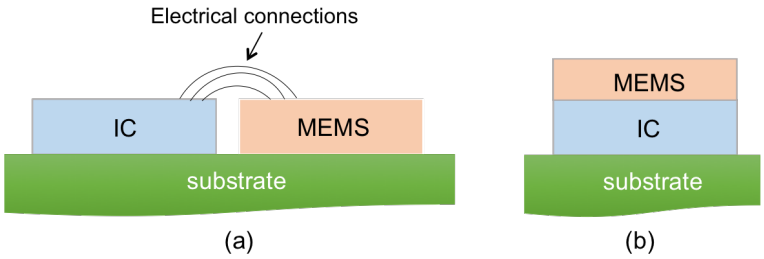

Figure 1.1: Schematic of the MEMS/IC integration (a) Hybrid (b) integrated approach.

in the semiconductor industry as it has shown to improve the performance of micromechanical devices as well as the cost of manufacturing by combining the micromechanical devices with an electronic sub-system in the same manufacturing and packaging process [23].

The demand for 'on chip' magnetic actuators, sensors and passive devices such as inductors has increased drastically in recent years with the mass production of smartphones and the emergence of wireless power technologies. For such applica-

tions, the devices need to be small, low powered and low cost. Therefore the integration of planarised versions of discrete passive devices such as microinductors has been of great interest [24, 25, 26, 27, 28]. A typical 'microinductor' requires a copper coil and magnetic core which have vertical thicknesses ranging from a few microns to tens of microns, and this can pose a series of integration challenges in IC technologies. Residual stress is one of the important yield and reliability issue for MEMS. This typically results from bonding dissimilar materials with different thermal expansion coefficients (thermal stress)[29], lattice mismatch in heteroepitaxial growth (epitaxial stress) [29][30] and the nucleation and growth process (intrinsic stress) [30][31][32]. Even though, defects due to stress in deposited films might not be evident at first, they can lead to stacking faults, cracking, warping and delamination [32]. An example of a delaminated MEMS structure made out of nickel which underwent a thermal annealing step is presented in Figure 1.2. Numerous journal articles have been published showcasing this topic, however,

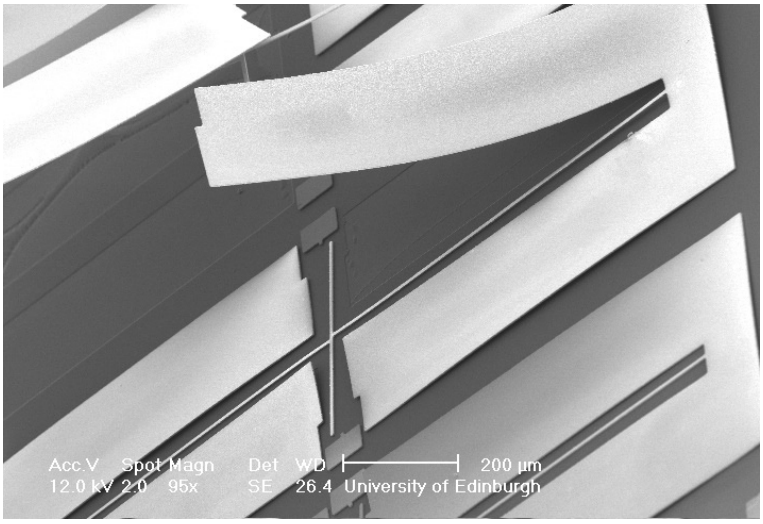

Figure 1.2: SEM image of a MEMS structure showing the delamination of the thin film due to the development of high residual stress

the characterisation of these stresses has been problematic. To improve manufacturing yields and device reliability, a more comprehensive approach towards the characterisation of stress in the deposited films of a microinductor is required, which has been the motivation of this work.

1.1 Electrochemical Deposition

A schematic representation of a typical planar microinductor is shown in Figure 1.3(a) which showcases the preferred material layers required for its fabrication. To achieve a high inductance and Q-factor in a microinductor, the use of a thick

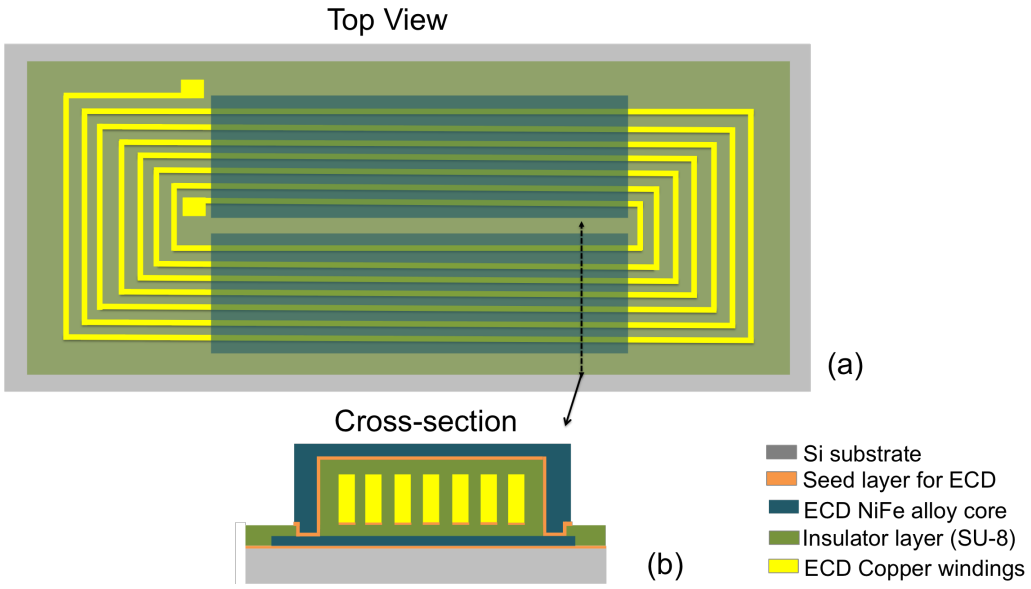

Figure 1.3: (a) Schematic representation of a typical planar microinductor with its cross-section (b)

magnetic core surrounded by a highly conducting metal winding is essential. Alloys of nickel and iron, particularly Permalloy ($Ni_{80}Fe_{20}$) are the main candidates for the magnetic core due to their high saturation magnetisation and low coercivity [33]. Copper on the other hand is well established in the silicon industry for its use as metal interconnects, mainly due to its low resistivity compared to aluminium [34]. Using a lower resistivity material like copper decreases the interconnect RC delay, which, in turn, increases the IC speed. For microinductor applications, permalloy core and copper windings are required to be thick (tens of microns), therefore electrochemical deposition (ECD) is an obvious candidate as conventional 'sputtering' techniques are better suited to much thinner layers. Firstly, it guarantees a much faster deposition rate and secondly, it can be patterned to any desired shape by plating bottom up through a photoresist mould.

This immediately eliminates any lift-off or chemical/dry etching process that would have been employed for patterning a sputtered film. ECD copper is also being employed for through-silicon-vias (TSV) in the back end of line (BEOL) process in the IC industry [35]. With these advantages, ECD proves to be an ideal low cost process for the deposition of copper windings and the NiFe magnetic core, required for the fabrication of a microinductor.

Besides the above advantages, ECD thick films can result in reliability issues for MEMS device due to the development of residual stress during deposition. The presence of high stress levels can lead to defects such as cracking, degraded magnetic properties, stacking faults, wrapping and film delamination [32]. It has been reported that stress levels in electroplated NiFe can be controlled by introducing chemical additives, such as boric acid and saccharin in the bath. However, the exact purpose of using e.g. boric acid has been controversial since the very beginning. In a acidic nickel(II) bath, boric acid is widely known for buffering the pH near the cathodic surface, resulting in an improved cathode quality [36], but its role as a surface catalyst, complexing agent and hydrogen inhibitor has also been reported [37, 38, 39, 40]. Conversely, with the presence of iron(II) in the nickel(II) bath, none of these phenomena of boric acid are observed. Plated films in this case yield much higher internal stresses [41]. This is known to occur due to the anomalous codepositon of NiFe, as the less noble metal Fe deposits preferentially to the more noble metal Ni [42]. A noble metal, when comparing two metals in an electrochemical system, is the one with a higher reduction potential (E^{ϕ}) compared to the other. In this case E^{ϕ} for ($Ni^{2+}(aq) + 2e^{-} \rightarrow Ni(s)$) = -0.26 V and ($Fe^{2+}(aq) + 2e^{-} \rightarrow Fe(s)$) = -0.44 V versus the standard hydrogen electrode (SHE) [43], so nickel is more noble than iron. The hypothesis on the exact role of boric acid because of this anomaly is still contradicting and needs further clarification. Understanding the mechanism of stress development within ECD films, induced by plating variations, is of great interest. Therefore, the need of developing a system, able to fully characterise the spatial variations of stress in ECD films is required.

Historically residual stress in thin films, deposited on silicon wafers, has been measured using the wafer bow method before and after the process. The change in curvature is directly related to the stress caused by that process, usually through Stoney's equation [44]. This formula was derived based on a number of restrictive assumptions. Two of these are the assumptions of a spatially uniform film thickness and a spatially uniform misfit strain; taken together, these assumptions imply constant curvature and film stress over the entire wafer. In practice, these conditions are rarely met, and yet the Stoney's equation is still the film stress measurement standard. Clearly, improved stress characterisation methods are required.

1.2 MEMS Test Structures

In the microelectronics industry, electrical tests structures are typically included in IC designs to enable in-situ measurements of the process yield during the device fabrication cycle. If the results do not meet specifications, then the wafer is discarded and not processed any further, thus, avoiding unnecessary expenses. The data obtained can be used to identify the root cause of the failure and also to optimise future processes.

To characterise the structural properties of a film, such as residual stress, a mechanical (MEMS) approach can be considered. A film exhibiting high stress would be expected to induce strain (deformation) in the structure. Moreover, this deformation may subsequently move any released parts of the structure, causing a displacement (strain), which coupled with the elastic modulus can be used to quantify stress levels in that film. A deeper insight on the existing and ongoing research on the development of such test structures is given in Chapter 2.

This approach has shown great interest because of two major advantages over the curvature method. Firstly, the compact size of the MEMS test structure allows for localised measurements, to ensure process uniformity on wafer level. Secondly, the design and process can be integrated seamlessly with the microinductor

manufacturing line. This would allow real time information of stress development during the different process phases.

The essence of this unique MEMS approach has led to the development of a novel system capable of characterising the spatial variations of strain in thin films. The results obtained have also provided a striking insight on some processes and material behaviours which can be used as a foundation stone for further characterisation and ultimately manufacturing microinductors on industrial scale.

1.3 Thesis Plan

This section briefly outlines the contents of the chapters which follow. As this thesis is a compilation of peer reviewed conference and journal papers published over the period of 3 years, these have been transformed into individual chapters. Below is a summary of the contents of each chapter, for ease of reference.

Chapter 2: State of the Art

Literature review of the recent advancement in the ECD of Ni, NiFe and Cu have been discussed in this chapter, with the main focus on the influence of plating conditions and additives on the plating efficiency. The MEMS approach used to quantifying stain in these films has been reviewed which lays the main foundation of this work.

Chapter 3: MEMS Test Structures and Measurement Techniques

This chapter details the design and use of MEMS pointer arm test structure to quantify local strain in electrodeposited films. The complete fabrication procedure, along with a unique etching technique for selectively etching the copper seed layer has also been reported. An automated measurement system, designed to extract spatial strain around a 200 mm wafer, was built in-house, and its complete working is discussed. This system was then employed to map strain on a test Ni plated wafer and results have been reported.

Chapter 4: Chip Level Metal ECD Studies of NiFe

The effect of plating conditions such as bath composition, plating currents and

additives on plating efficiency and strain have been examined on chip level (small scale) which led to the optimum bath design for full wafer fabrication.

Chapter 5: Wafer-level Strain Measurements and Correlations with other Properties of NiFe Films

Variations in process parameters like annealing on the spatial variation of strain have been reported. These results were also correlated with alloy film composition, thickness, sheet resistance and structural properties of the grains to acquire more understanding on the development of stress in NiFe.

Chapter 6: Recrystallization Studies of Electrodeposited Copper Films

Correlation of optical and electrical test structures for the characterisation of copper recrystallisation at room temperature were investigated. Plating parameters such as current density, thickness and bath additive/carrier concentrations, were reported to influence the self-annealing of copper and these have been analysed and presented in this chapter.

Chapter 7: Fabrication and Measurement of Test Structures to Monitor Stress in SU-8 Films

SU-8 material is a negative tone epoxy-based photoresist that has previously been used in the fabrication of microinductors usually as a structural material. This chapter investigates the wafer level changes in stress arising from the variations in the process parameters such as hard bake step and exposure dose.

Chapter 8: Conclusions and Future Work

This chapter summarises the results reported in the previous chapters and discusses the obtained achievements and the impact of the presented research, as well as directions for future work.

Appendix:

Comprehensive summaries of the experimental theory, fabrication run-sheets, LabView VIs, copper bath analysis procedures and re-prints of published journal and conference papers can be found in the appendices.

Chapter 2

State of the Art

2.1 Introduction

The key focus of this work is the characterisation of materials towards the development of a MEMS microinductor. The three materials, potentially required for the fabrication of a microinductor on silicon are copper (conducting coils), permalloy (NiFe magnetic core) and SU-8 (insulating mold between coil and magnetic core). All these materials are known to induce high residual stress when deposited on a different substrate (silicon). The wafer-level spatial characterisation of stress is of great importance as it can be a factor dictating the non-uniformity in device performance, yield losses and poor reliability. However, stress levels can be lowered by precisely controlling the deposition parameters and conditions related to each of these materials. ECD technology of copper and permalloy is well established, but little work has been published towards characterising local stress on wafer level for these materials.

Therefore, this chapter has been designed to provide a literature review of recent advances in the ECD of copper and NiFe, and the issues involved, some of which could be responsible towards the development of stress in films. This is followed by a review of stress measurement techniques formerly employed for characterising stress. Finally, the MEMS approach, has been evaluated, which led to the design and development of a novel spatial strain measurement system which was later used in this work.

2.2 Electrodeposition of Copper

2.2.1 Advantages

Copper is the most common metal electrodeposited in the microelectronics industry for the past two decades [45]. The main advantage of copper is its high electrical and thermal conductivity as a metal which can be electrodeposited with a high rate resulting in an excellent coverage over most metal surfaces [45][46][47]. Copper can be patterned easily by electroplating it 'bottom-up' through photoresist moulds, which has proved to be a very cost effective and fast process. This technique can therefore, be used to pattern minute features essential for microelectronic applications. In the semiconductor industry the use of ECD copper in the interconnect technology was hailed as a major breakthrough by IBM in 1997 when the process termed *damascene copper electroplating* was first introduced [48]. This process met the challenges of filling trenches and vias with copper without creating a void or seam. Under proper conditions, ECD inside trenches (vias) occurs preferentially in the bottom, leading to void-free deposits, a phenomenon known as *superfilling*. Since then, copper has successfully replaced aluminium, previously employed for (BEOL) back end of line via filling using a sputtering technique which is much slower, complex and costly than ECD [49]. Another major advantage of copper is that it has 100 times more resistance to electromigration failures than aluminium. Electromigration is a phenomenon which causes transport of the conductor material as a result of high current densities, which can ultimately lead to voids in the conductor [50]. As TSV filling using copper ECD is well established and integrated in IC technology, it has been chosen to be suitable for microinductor coils.

There are numerous bath chemistries being used which are dependent upon applications, therefore, a review of some common baths have been presented in the following section.

2.2.2 Copper plating from acidic copper(II)sulfate

In the semiconductor industry, acid chloride, sulfate and fluoroborate solutions are most commonly used. The acidic medium is employed because of low chemical costs and low power required for electrodeposition [51]. Copper(II)sulfate ($CuSO_4.5H_2O$) and sulphuric acid (H_2SO_4) are the main constituents of the sulfate solutions. The copper salt dissolves in aqueous solution as:

$$CuSO_4(s) \longrightarrow Cu^{2+}(aq) + SO_4^{2-}(aq) \tag{2.1}$$

At the cathode surface either H_2O or Cu(II) could undergo reduction depending on the reduction potential (E^{ϕ}/V vs. SHE):

$$Cu^{2+}(aq) + 2\,e^- \longrightarrow Cu(s) \quad +0.32 \text{ V [52]}$$
$$2\,H_3O^+(ag) + 2\,e^- \longrightarrow 2\,H_2O(l) + H_2(g) \quad 0.00 \text{ V [52]}$$

Since the standard reduction potential of copper is more positive it will readily undergo reduction at cathode. Similarly, either H_2O or SO_4^{2-} could undergo oxidation at anode. The final redox reaction can therefore be written as:

$$2\,Cu^{2+}(aq) + 4\,e^- \longrightarrow 2\,Cu(s) \quad \text{Cathode (ECD)}$$
$$2\,H_2O \longrightarrow O_2 + 4\,H^+ + 4\,e^- \quad \text{Anode}$$

The cathode and anode reactions balance each other in order to maintain electrical neutrality in the solution. To avoid an overall depletion of copper in the plating solution the use a solid copper anode is made, in which case the cell reactions will be as follows:

$$Cu^{2+}(aq) + 2\,e^- \longrightarrow Cu(s) \quad \text{Cathode (ECD)}$$
$$Cu(s) \longrightarrow Cu^{2+}(aq) + 2\,e^- \quad \text{Anode}$$

Taft *et al.* investigated the film properties from a pure copper(II)sulfate bath and observed a spongy or coarse deposition of copper at low plating current densities which is undesirable due to its poor adhesion with the substrate [53][54]. However, in the presence of free acid (H_2SO_4) the conductivity of solution improved which lead to greater film uniformity, smooth deposits (finer grains) and higher plating

rates [55][56]. Higher concentrations of copper(II)sulfate also increased the conductivity of the bath [57]. Cathode polarisation was observed to improve slightly at copper(II)sulfate concentrations above 1 M (250 g/l) [58]. However, increasing the sulphuric acid concentration (>220 g/l) while decreasing the copper(II)sulfate to (50 g/l) drastically increased the throwing power of the solution [59].
The crystalline morphology of copper has been reported to be modified by changing the sulphuric acid concentration. The grain size did not show any change with copper(II)sulfate, but finer grains were deposited with increasing sulphuric acid to 72 g/l [60]. This was caused by the increase in surface overpotential which introduced three dimensional nucleation, upon which copper grew. X-ray diffraction patterns confirmed this effect which is represented by Fukunaka *et al.* [61].

2.2.3 Effect of chloride in copper baths

In modern ECD sulfate baths the inclusion of chloride ion (Cl^-) produces bright, high throw [62] and clear deposits in high current density areas of the film [63]. The main source of Cl^- is hydrochloric acid, as its inclusion in the already highly acidic bath would have no disadvantage. In an extensive study by Kao *et al.* in 2005, it was reported that when Cl^- was below 30 parts per million (ppm) the deposits were dull, striped and non-uniform. Above 120 ppm, deposits were found to be coarse grained and dull again and the anode polarised causing the plating to stop [64][65]. However, chloride ions concentrations between 40-150 mg/l have shown to produce films with near zero stress, increase the micro-hardness and also increase on the throwing power of the bath [66][67][62]. Therefore, a small amount of chloride is known to improve film quality by promoting the binding of surfactants (discussed in the next section) such as polyethylene glycol (PEG) to the cathode surface [68], which results in a more uniformly plated film. However, excess chloride ions should be avoided as it reduces to insoluble copper chloride at the anode surface, causing passivation and slowing down the plating process

[69]. A summary of the different acid copper(II)sulfate bath formulations with conventional and high throw characteristics are presented in Table 2.1.

Table 2.1: Formulations of Acid Copper Solutions

Bath contents	**Conventional Solutions**	**High-Throw Solutions**
$CuSO_4.5H_2O$ (aq), g/L	200-250	60-100
H_2SO_4 (aq), g/L	45-90	180-270
Chloride, mg L^{-1}	-	50-100
Temperature, °C	20-27	20-27
Current density, $mAcm^{-2}$	15-20	25-100

2.2.4 Effect of additive and carrier

Additives are additional compounds, frequently employed in the semiconductor industry baths, to optimise the copper plating processes such as for TSVs. A list of additives, covered in patents granted in recent years, have been reported elsewhere [70]. Commercially available additives contain three main components: carriers (suppressors), additives (accelerators) and brighteners. Figure 2.1 shows schematics summarising their use in ECD. Carriers are typically polymers of PEG (polyethylene glycol) with molecular weights greater than 2000. These organic compounds are known to adsorb on the wafer surface and slow down Cu deposition in the adsorbed areas. Due to this reason they are also known as 'suppressors'. Moreover, an accelerator competes with the suppressor molecules for adsorption sites and accelerates Cu deposition in the adsorbed areas. Finally, levellers are strong secondary plating inhibitors, which typically co-function with brighteners to reduce copper growth at protrusions and edges.

The smoothing and grain refining tendency of additives has been associated with the formation of complex ions with copper or of colloids at the cathode interface. An example of an additive is gelatin or glycine which is known to form a complex ion with copper and for which ultramicroscope examinations

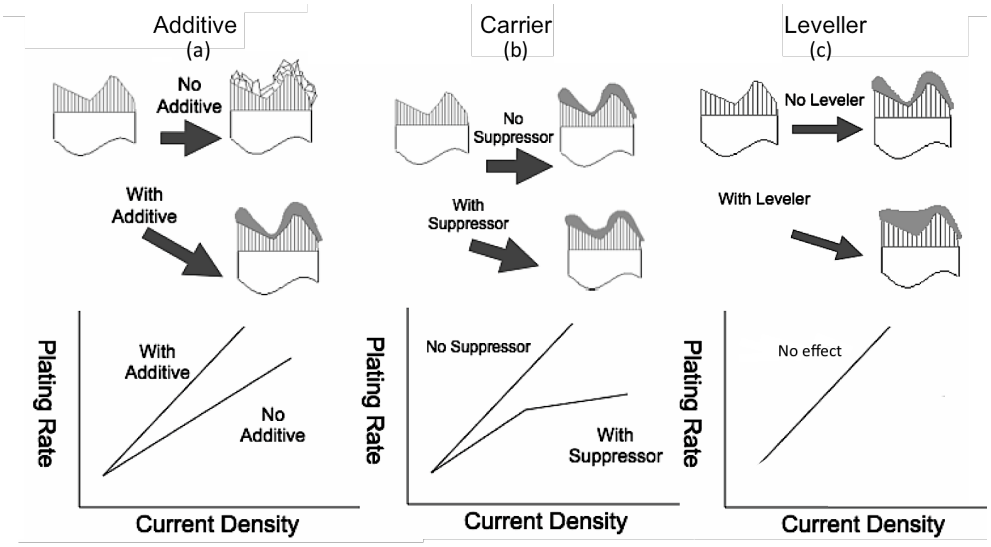

Figure 2.1: Schematics showing the effect of (a) additive (b) carrier and (c) levellers on the plating uniformity and trench filling properties in the electrodeposition of copper; Effect on the plating rates are also shown [1]

revealed its segregation at the cathode [71]. These have also have been reported to improve mass transfer to localised sites of the metal with lesser electric fields or feature height. Another example of additives are phenolsulfonic acid and phenol, when used together in a bath, they have been shown to produced harder and smoother films [72]. Excess inclusion of grain refiners such as thiourea produced smooth films but initiate nodulation which is associated with a large increase in overpotential of greater than 100 mV [73]. It can be seen that the choice and benefits of additives have been abundant and this has also led to proprietary and commercially available additive compounds, the chemical details of which are still undisclosed.

The effect of PEG and a carrier and 3-N,N-dimethylaminodithiocarbamoyl-1-propanesulfonic acid (DPS) as an accelerator (additive) on the residual stress of approx. 10 µm ECD copper has been recently studied by Kim *et al.* and Kobayashi *et al.* [74] [75]. They show that when added in the bath with PEG, DPS more effectively increased copper plating rates which Kim speculated as the displacement of PEG in PEG-Cl^- complex by DPS. The tensile residual stress has been shown to increase with PEG concentration while the compressive stress

increases monotonically with DPS. Residual stress is thought to originate from the entrapped impurities. Films were seen to relax with time, releasing stresses, with the outdiffusion of entrapped hydrogen in PEG and the incorporation of entrapped sulphur in DPS. They concluded that their importance in the baths were mutually dependent and the process window to obtain optimum films was narrow. Slight changes in concentrations of additive and carriers can therefore, effect the structural properties of the deposits and produce films with defects. This complex topic is however, of great interest, and is in need of an accurate method to characterise stress in ECD copper, which can then be used towards understanding the importance of these compounds in plating baths.

2.3 Electrodeposition of Nickel

Many nickel plating bath recipes have been employed successfully over the past few decades. Chlorides and sulphates of nickel have been the main provider of nickel dissolved in water. Philip and Nicol [76] conducted tests on the electrodeposition of nickel from a chloride solution containing 1 M $NiCl_2$, 0.1 M HCl, 53 °C and 22.5 $mAcm^{-2}$ and obtained a current efficiency of 94.3 %. They believed the presence of chloride ions played a catalytic role in nickel reduction, reducing the overpotential of nickel deposition without any simultaneous hydrogen evolution at the cathode. Finkelstein *et al.* [77] confirmed that a high current efficiency of nickel deposit can be obtained from chloride baths. It was also deduced that an improved nickel deposit can be achieved at higher nickel and chloride concentrations (1.5-3 M) and higher temperature (40 - 60 °C).

Internal stress has always been an issue with nickel deposits and Fujimori *et al* [78] pointed this out as a disadvantage for using a chloride bath. The addition of sulphate in the electrolyte produced films with lower internal stress but the mechanism remained unknown. The magnitude of stress increased with chloride concentration. Therefore, although high chloride concentration lowers the cell voltage due to the increase in the electrolyte conductivity, a compromised chloride

concentration must be chosen. It was also reported that the deposit stress became less severe as the temperature and pH rose. They attributed this to the generation of hydrogen at the cathode (which reduces the current efficiency), followed by its dissolution into the nickel film. Another hypothesis of internal stress inside the cathode deposit was the specific adsorption of chloride ions on the cathode surface and the occlusion of electrolyte at its surface [78].

To control the pH of the solution during ECD, boric acid has been found to be the most effective and has been used widely in the nickel electrodeposition. The purpose of using boric acid has been sketchy and controversial. It is widely known for buffering the pH near the cathodic surface resulting in an improved cathode quality [36], but its role as a surface catalyst has been questioned. The pK_a of boric acid ($B(OH)_3$) is around 9.2 [79][80] and nickel baths operate at pH of around 3. As pH<pK_a the source of H^+ increases with the presence of boric acid. To investigate the interaction of boric acid with nickel pH titration were carried out by Tilak *et al* [37] in a $NiSO_4$ - Na_2SO_4 - NaCl at 55 °C. Two experiments were carried out with varying boric acid (0.1 M to 0.5 M) in a fixed 0.97 M $NiSO_4$ concentration in one and varying $NiSO_4$ concentration in the other (0.1 to 0.5 M) in fixed 0.3M H_3BO_3. The buffering capacity of boric acid was observed to increase with both boric and $NiSO_4$. This effect showed the presence of a weak nickel-boric complex, $Ni(H_2BO_3)_2$, with log $K \approx$ -12.2 [37], but the pH of the bath was around 3.5. Besides the question of the reliability of the equilibrium constants used in the calculations, Tilak *et al.* did not consider the nickel-chloro complex and the formation of bisulfate. Although the complex of nickel with boric acid is likely to exist, the accuracy of the authors' calculations is questionable.

2.3.1 Effect of Hydrogen Evolution

The plating efficiency relies on the amount of hydrogen evolved at the working electrode which occurs simultaneously with nickel deposition [42]. This process is highly dependent on the initial pH and temperature of the solution and because of this process the hydrogen ion concentration is depleted near the cathode surface. This raises the pH near the cathode surface higher than the bulk electrolyte. Therefore, during the electrodepositon process the electrode activity is cathode surface pH dependent rather than the bulk electrolyte pH. Since the baths used are normally acidic (the reasons are discussed in latter sections), the reaction can be written as:

$$2\,H_3O^+ + 2\,e^- \longrightarrow H_2 + 2\,H_2O \tag{2.2}$$

Oxygen may also be dissolved in the solution which can affect the cathode surface pH:

$$O_{2(aq)} + 4\,H^+ + 4\,e^- \longrightarrow 2\,H_2O \tag{2.3}$$

To avoid the cathode surface pH rising during electrodeposition the reduction of hydrogen ions needs to be reduced. This can be achieved by vigorous agitation which will bring in the lower bulk pH towards the cathode while thinning the diffusion layer. The other resource could be a buffer acid like H_3BO_3 which can donate protons. Conversely, $NiOH^+$ and $Ni_4(OH)_4^{4+}$ can act as OH^- (hydroxyl) consumers and aid in lowering the surface pH. The following equilibrium reactions are expected to occur which will shift to the right when hydrogen evolution takes place:

$$Ni^{2+} + H_2O \longrightarrow NiOH^+ + H^+ \tag{2.4}$$

$$4\,Ni^{2+} + 4\,H_2O \longrightarrow Ni_4(OH)_4^{4+} \tag{2.5}$$

$$Ni^{2+} + 2\,H_3BO_3 \longrightarrow Ni(H_2BO_3)_2 + 2\,H^+ \tag{2.6}$$

With the continuous increase in pH in the case when the supply of H^+ ions is unable to meet the depletion rate then the reaction (2.5) will proceed to:

$$Ni^{2+} + 2\,H_2O \longrightarrow Ni(OH)_2(s) + 2\,H^+ \tag{2.7}$$

A sharp drop in the current density has also been observed when the potential becomes sufficiently negative. This phenomenon is called 'cathode passivation'. This is believe to be caused by the formation of insoluble nickel hydroxide on the cathode surface because of hydrogen evolution reaching a limiting condition [81][82][42][83]. This markedly reduces the nickel depositon efficiency. It is therefore thought to be important to use sufficiently acidic baths but prevent or at least lessen hydrogen evolution, otherwise the surface pH rises leading to the precipitation of insoluble nickel hydroxide. Some devastating physical effects of hydrogen evolution are metal embrittlement [84], pitting and tensile stress in the film [85, 86] which can all lead to poor device performance and ultimately failures [87].

2.3.2 Nickel-Iron Electrodeposition

ECD of 20 % iron and 80 % nickel alloy (permalloy) is of special interest because it exhibits low coercivity and high magnetisation saturation hence it is ideal as a magnetic core for the application of microinductor and microswitches [88]. However, slight changes in the film composition can effect the magnetic behaviour drastically. With increasing Fe percentage up to 20 % by weight the coercivity decreases and the permeability increases. For thin film the increase in film thickness reduces the speed of response to a magnetic field. Surface roughness, Fe %, film morphology and stress also played a role in the magnetic properties of permalloy [42][89]. These few physical properties mentioned can be controlled by careful adjustments to the plating conditions such as current density, convection, temperature, additive, carrier compositions. The most important challenge, however, is the fundamental understanding of the anomalous codeposition of NiFe, as the

less noble metal Fe, deposits preferentially to the more noble metal Ni [42]. This behaviour is abnormal, as nickel would plate at a faster rate in a typical aqueous solution when electroplated individually. As this phenomenon occurs, to achieve a $Ni_{80}Fe_{20}$, a plating bath is usually prepared with 40 times as much nickel as iron [90][42].

Many explanations were proposed for this anomalous codepositon of NiFe such as the continuous deposition of the lower work function alloy [91][92] and the adsorption of species suppressing the deposition of nickel [89], either additives or monohydroxides ($FeOH^+$ and $NiOH^+$) which act as the charge transferring species (or the pH of the cathode is not high enough the metal hydroxides $Fe(OH)_2$ and $Ni(OH)_2$ precipitate [82]). Bertazzoli *et al.* [93] reported the inhibition of the early stage nucleation and growth of the noble metal in the presence of the less noble metal. The additives and electrodeposition conditions also influence both the magnetic properties and the stress [94][95][96]. Most baths for this purpose use saccharin as an additive which results in a decrease in grain size and residual stress [96][97]. The reliability of a device, lies in the optimum properties of a plated film. In the MEMS industry, accurate characterisation of residual stress in these film is therefore important to successfully predict the final device performance.

2.4 Residual Stress in Plated Films

In MEMS, high stress can induce delamination and the peeling of thin films. The global stress variation in the ECD of NiFe thin films with varying bath Fe composition was investigated by Koo *et al.* [98]. The stress in pure Ni in his films was $\approx$ 150 MPa which was enhanced with increasing Fe% and reached a maximum stress of $\approx$ 330 MPa at $Ni_{60}Fe_{40}$. Pure Fe had 250 MPa stress, lower than when present in the alloy. This interesting trend in the polycrystalline film could be the effect of either composition or grain size, as both were also seen to be changing. It is not clear which of these two (or something else) was causing the change in stress. The correlation of grain size with Fe% was also measured

by Park *et al.* in 2006 [99] but without drawing any concrete conclusions. X-Ray Diffraction (XRD) measurements showed peak broadening with increasing Fe% which was taken as a strong evidence that the film was composed of finer grains or a larger number of grain boundaries.

The control of stress when electroplating permalloy layers was investigated by Zhang *et al.* [100]. The results revealed that a low concentration plating solution ($NiCl_2$ 23.5 g/l and $FeCl_2$ 1 g/l) helps to lower the internal stress of the deposited layer, and the stress could be further decreased with an increase of additive (saccharin) content. All these stress measurements were made using the wafer curvature technique (Section 2.4.1.1) which gives the overall value of stress in the wafer but spatially mapped stress measurements have not been made in detail in the past. The following section is therefore, designed to give a basic background on the development of stress measurement techniques previously employed. Their relative advantages and disadvantages have also been discussed.

2.4.1 Stress Measurement Techniques

2.4.1.1 Wafer Curvature

The wafer curvature method is widely used in the silicon industry for measuring stress in thin films [101]. It is a simple and non-destructive measurement technique first developed by Stoney in 1909 for electroplated beams and later modified by Hoffman in 1966 for plates [44]. In this technique the curvature of a bare wafer is first measured. This can be performed by either scanning along the diameter of the wafer with a DekTak or a laser. In the Frontier Semiconductor Measurement, FSM system, used in this work, the laser is scanned using a rotating mirror and the laser displacement, 'z', is measured as a function of position, 'x', with a precision photo detector, a schematic representation of which is shown in Figure 2.2[102]. The curvature is then determined by a 'least squares fit' approximation of $\delta z/\delta x$. The radius (R_1) of curvature of a substrate (thickness 'h') is determined by $R_1 = C / (\delta z/\delta x)$, where C is a constant (C = 2× beam path travel length). The wafer

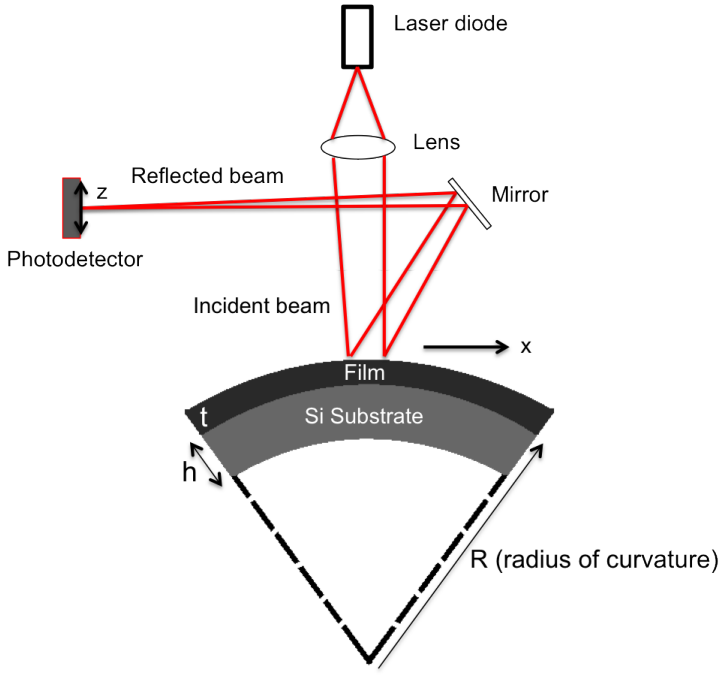

Figure 2.2: Schematic representation of wafer curvature

is then removed and the specimen film, of thickness 't', is deposited on it. The stress, σ, in the film will exert a bending moment on the wafer and changes the radius of curvature. The new curvature radius R_2 is determined using the same method, and σ calculated through Stoney's equation and can be written as:

$$\sigma = \frac{Eh^2}{6tR(1-\upsilon)} \tag{2.8}$$

where the change in radius of curvature caused by the film deposited is:

$$\mathrm{R} = \frac{R_1 R_2}{R_1 - R_2}$$

In Stoney's equation $\frac{E}{1-\upsilon}$ is the biaxial modulus of the wafer, where υ is the Poissons ratio of the substrate and 'E' the Young's modulus of the substrate. This method can also be used to measure the residual stress in the film on annealing to elevated temperatures. Although the technique is relatively simple there are some limitations. Firstly, the films are required to be on one side of the

wafer whilst the other side, usually polished for reflectivity, is scanned in the FSM. Secondly, the wafer bending decreases as the square of the wafer thicknesses, so the sensitivity to changes in stress in thin films decreases with larger wafers with greater thicknesses. Thirdly, this technique measures the sum of the stress induced by all films in the case where there are multiple layers. The thermal mismatch between all films will then have to be considered which adds to the complexity of analysing results. The wafers once replaced also have to be loaded in exactly the same position as the measurement system is incapable of rotating wafers in the chamber. This gives rise to errors as wafers seldom have a perfect symmetry.
A major issue is also that this method can only tell the overall (averaged) stress of monolayer blanket films on substrates. Spatial variations in stress due to non-uniform process factors therefore cannot be investigated using wafer curvature.

2.4.1.2 MEMS Stress Structures

Techniques based on the surface analysis of materials, such as those using Raman spectroscopy [103], Fourier transform infrared spectroscopy [104], and X-ray diffraction [105], have been investigated as potential spatial stress monitoring tools but these techniques have only provided moderate success. The spatial resolution of X-ray for example, is a few microns [106][107] and the line widths used in semiconductor devices are much smaller. They also require a number of simplifying assumptions about the texture, microstructure and defect density of the film, as well as the interaction between the film and the incident light. These assumptions are seldom accurate enough for quantitative measurement of thin films [108]. These techniques also require a long sampling time to collect a strong enough signal for analysis and as a result an established quantitative spatial non-destructive stress measurement, as a result does not exist.
The production of MEMS stress measurement devices started with the development of surface micromachining techniques about 20 years ago [109]. This method uses the strain (deformation) of the material to quantify stress. These MEMS sensors are designed to operate by undercutting the structures to free and then to

deform measurably under the residual stress of the material thereby indicating the degree of stress. The simplest test structures first employed were double-supported

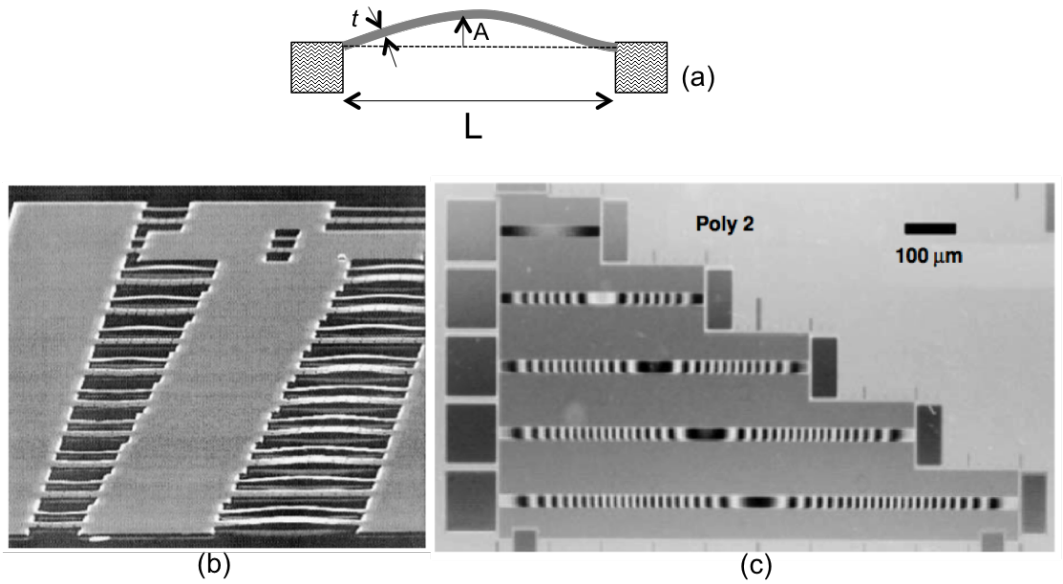

Figure 2.3: (a) Schematic layout plot of a fixed-fixed beam (b) SEM image o fan array of polysilicon beams made for characterising strain (beam lengths vary from 8-600µm) [2] (c) Interferometry measurement to indicate the buckling of beams [3]. Diamond shaped tensile stress sensors [4]

bridges proposed by Guckel *et al.* [2, 110] for strain measurements of poly silicon as shown in Figure 2.3. A schematic representation of a fixed beam is shown in Figure 2.3(a). Beams of different lengths were fabricated and a sacrificial layers underneath etched away to form a suspended structure. These beams bent under different stress conditions and the deflection was measured using an interferometer 2.3(c) . The problem with this simple technique was that these structures bent only if the compressive strain was above the critical Euler value [111]. Therefore a large number of bridges of different lengths had to be fabricated for a satisfactory resolution of strain and this consumed a large amount of wafer space (Figure 2.3(a)). The amplitude of deflection is sensitive to residual stress in the film, and this allows each buckled beam to be used for residual strain (ϵ_R) measurement through [3]:

$$\epsilon_R = \frac{\pi^2}{L^2}\left(\frac{A^2}{4} + \frac{t^2}{3}\right) \tag{2.9}$$

where A is the amplitude of the buckling deflection, L is the beam length and t is the beam thickness 2.3(a). Finite element analysis (FEA) was used to obtain the value of residual stress using the deflection data from all the beams. Unfortunately, because of the stress gradient and initial imperfections in the buckling behaviour of the beams due to uneven etch, there was a 10-20% difference between the analytical predictions and experimental results.

Guckel showed that if beams are clamped in the shape of a ring, Figure 2.4, then

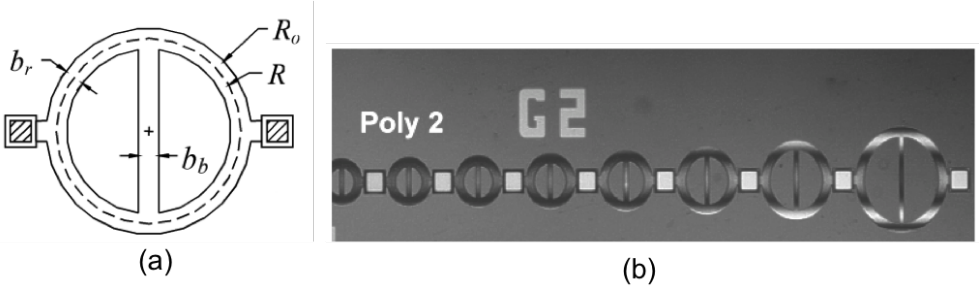

Figure 2.4: (a) Schematic diagram of the Guckel's ring (b) A series of Guckel's rings fabricated in polysilicon [3, 5, 6]

tensile stress could be converted to measurable compressive stress. The principal of these structures is such that, after release, the crossbeam gets compressed when the ring contracts if the structure has tensile stress. The crossbeam would buckle if the critical value of stress, σ, were reached [112, 6], and is given by:

$$\sigma = \frac{\pi^2 E t^2}{3.(2R)} . \frac{1}{G} \tag{2.10}$$

where t is the thickness of the ring, E is the Young's modulus of the material, R is the length of the crossbram and G is a constant determined by the specific geometry of the ring and the beam structure. This critical stress was calculated using finite element analysis using the material's Young's modulus and this is discussed in detail by Bounty and Masters *et al.* [113, 3]. This obviously solves the issue of quantifying both tensile and compressive stress, but this method also relies on strain data from a series of rings with different radii. Therefore the total area occupied by the micro-rings was 2.9 mm^2 and an array of 40 structures were required to quantify residual stress [3].

The second type of direct strain measurement system fabricated were the T and

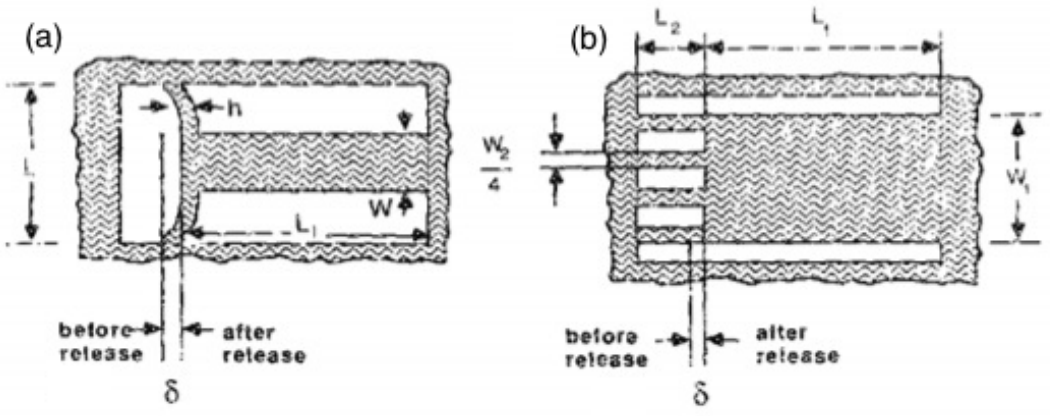

Figure 2.5: T and H-type strain sensors fabricated by Allen in 1987, image taken from [7]

H-type structures fabricated by Allen *et al* [7]. The T-type structure was designed such that upon releasing the T-structure, the residual tensile stress in the film would bend the stem of the T, which deflects (δ) at small strains as seen in Figure 2.5(a). The local residual strain in the film (ϵ_T) can be calculated as:

$$\epsilon_T = \delta\left(\frac{1}{L_1} + \frac{16}{W(L^3/h^3 - W^2L/h^3 + W^3/2h^3)}\right) \tag{2.11}$$

where L_1 and W are the length and width of the centre leg respectively and h is the beam width. In the H-type structure (Figure 2.5(b)) the residual stress causes an axial shrinkage of the wide part of the beam and a proportionate axial extension of the narrow neck upon release. The following formula was deduced for the residual strain of the H-type structure (ϵ_H) [114, 7].

$$\epsilon_H = \delta\left(\frac{W_1/L_1 + W_2/L_2}{W_1 - W_2}\right) \tag{2.12}$$

where δ is the displacement of the structure after release, L_1, W_1 are the length and width of the wide beam and L_2, W_2 are the length and width of the thin member of the beam. Both these types of structures yielded extremely small displacements, thereby making accurate measurements difficult.

These methods demonstrated MEMS techniques for material stress sensing on wafer but were prone to deflection extraction errors as a result of which scaling them down for spatial variations measurements were never attempted. The large uncertainty values of published results also suggested the need for improved methods.

2.4.1.3 Stress Relief Structures

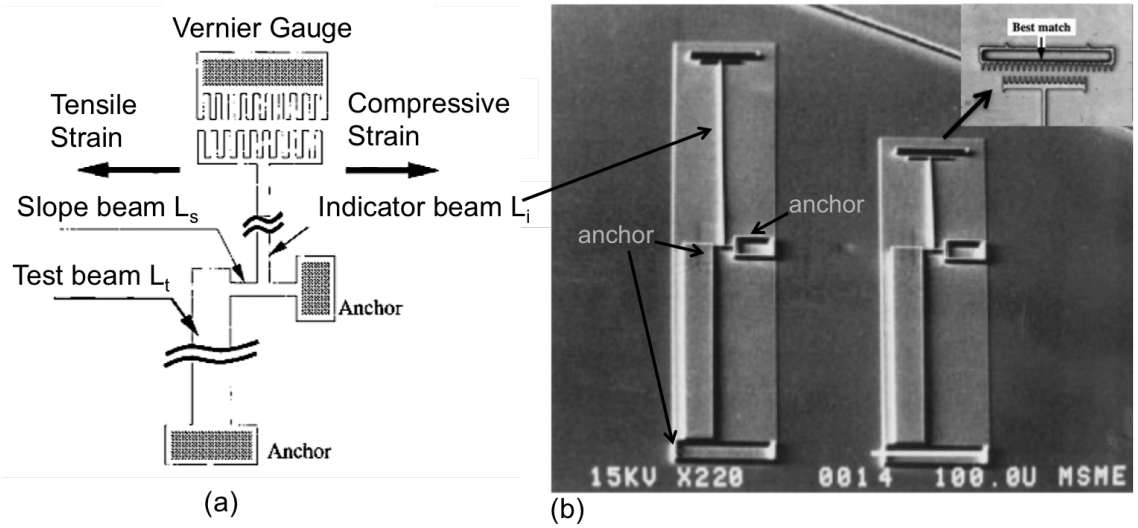

Figure 2.6: Schmatic plot of a vernier micro strain gages and fabricated device by Lin *et al* [8]

It was in 1993 when Lin and Goose *et al* [8, 115, 116] first devised the idea of stress relief mechanical devices that measured residual strain using an extension beam and a vernier scale, as shown in Figure 2.6. The structures were designed so that when the beam device is freed from an underlying sacrificial layer, the residual stress in the film is released leading to the deflection of the indicator beam. Consequently by employing many devices, residual stress can be evaluated at different locations on a silicon wafer. A single structure, was shown to be capable of determining both tensile and compressive stress under an optical microscope. In this particular case the test beam (L_t) expands or contracts, depending on the sign of the residual strain in the film, causing the compliant slope beam (length L_s) to deflect. The indicator beam (length L_i) attached to the deforming beam

at its point of inflection rotates and the deflection δ is read on the vernier scale. The residual strain ϵ_f is calculated as:

$$\epsilon_f = \frac{2L_s\delta}{3L_iL_tC} \tag{2.13}$$

where C is the correction factor due to the device geometry and can be expressed as:

$$\mathrm{C} = \frac{1-d^2}{1-d^3} \tag{2.14}$$

where d is the ratio of the width of the indicator beam over to length of the slope beam [115]. The length being much larger than the width can be neglected. This structure turns out to be very useful as by looking at Equation 2.13 it can be seen that the residual strain can be calculated without the knowledge of film thickness, which contributed to errors as seen in the other methods. Angled walls of high aspect ratio photoresists moulds (SU-8, NR2 and SPR-220) were also used to produce trapezium shaped electroplated beams but this irregularity in cross section was shown to also contribute negligible variation in measurements [117].

The approach was further modified by Gianchandani and Najafi [118] as shown

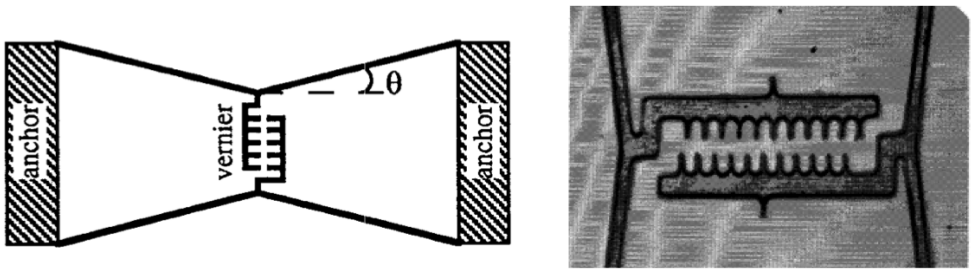

Figure 2.7: (a) Schematic of bent-beam strain sensor with vernier scale (b) SEM showing the deflection in vernier of the sensor fabricated in poly-silicon

in Figure 2.7. These sensitive passive strain sensors utilised a pair of narrow bent beams with an apex at their mid points. The narrow beams amplify and transform deformations caused by residual stress into opposing in-plane displacements of the apics, where vernier scales are positioned to quantify the deformation. Stress

was calculated using the displacement (strain) and Young's modulus of the bulk material taken from literature. It was shown that tensile and compressive residual stress levels below 10 MPa corresponding to strains below 6×10^{-5} could be measured in a 1.5 µm thick layer. The total area of the device was ∼0.23 mm^2. This achievement was significant as historical strain sensors like the T and H-type mentioned earlier were ∼ 4 mm in at least one dimension [7].

Elbrecht *et al.* [5] fabricated micromachined rotating indicator structures (Figure

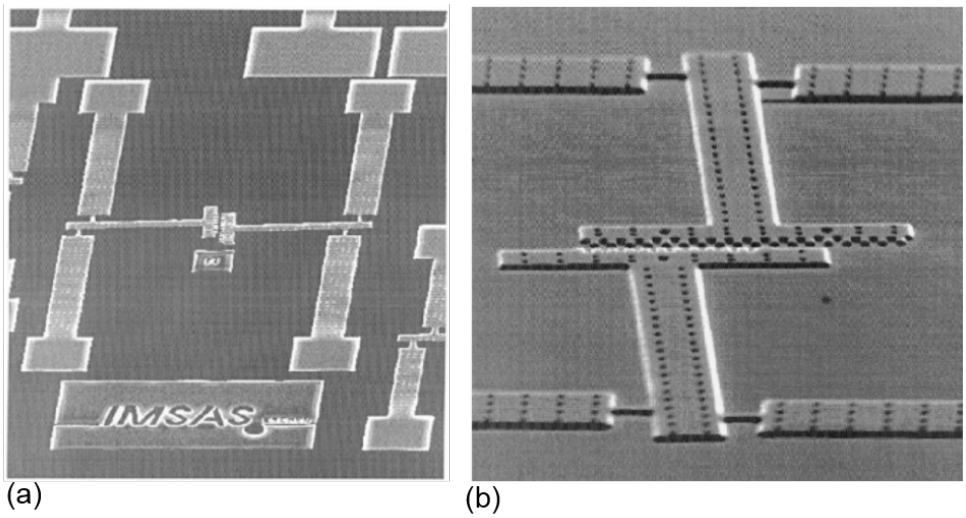

Figure 2.8: (a) Fabricated by Elbrecht *et al* [5] the SEM photograph of a micromachined indicator structure showing a tensile stress of about 300 MPa in a 1 um thick poly-silicon film (b) Detailed view of an indicator microstructure under tensile stress

2.8), in polysilicon, similar to those first presented by Goosen *et al.* [116]. In this design the pointer arm is supported by two anchor beams instead of one, which resulted in twice the sensitivity. Because of the offset between the anchor points, the stress developed in the beams was translated into the rotation of the pointer arm. These structures were shown to have a linear relationship between in-plane stress and indicator deflection, providing the bulk materials Young's modulus was uniform. The indicator rotation could be determined quite easily by means of inspection with an optical microscope using a vernier scale at the end of the indicator [119]. The edges of all joints were also rounded off to avoid cracking as the stress peaked in those areas. This also minimised processing induced variations

of the joint characteristics. Finite element analysis was used to deduce the value of stress, using fixed values of Young's modulus and Poisson's ratio. These strain sensors enabled measurement of stresses up to 600 MPa along with the smallest detectable stress variation (1.5 MPa) [5].

Xin Zing *et al.* introduced a simpler version of micro-rotating stress sensors, a

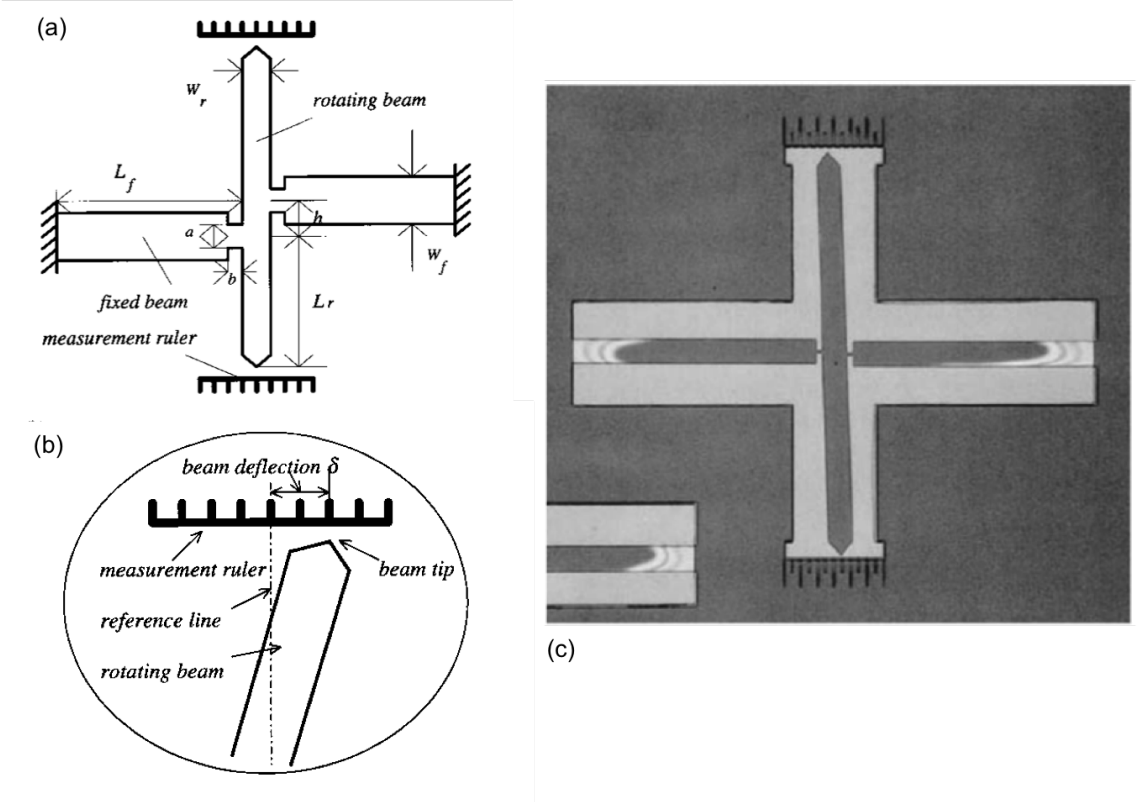

Figure 2.9: Schematic illustrations of the micro-rotating-structures by X.Zhang [9] (a) overall view (b) enlarged pointer tip (c) Photograph of the micro-rotating structures after releasing of the residual tensile stress in thin film

schematic of which is shown in Figure 2.9(a). Figure 2.9(b) shows the magnified deflection of the beam. As can be seen, the fixed beams, when detached from the underlying sacrificial layer, are free to extend or contract as a result of the released compressive or tensile stress. Necks (notches) were designed herein to narrow the connection between the rotating beam and the fixed beams and thus enhance the sensitivity of the structure. The two fixed beams are connected off-center to the opposite sides of the rotating beam. Thus, the displacement of the fixed beams due to the released residual stress leads to the deflection of the rotating

beam. To improve the performance of the structural design finite element analysis (FEA) was performed keeping the Poisson's ratio and Young's modulus constant. It was deduced, according to linear elasticity, that the residual displacement and hence the deflection was directly proportional to the residual strain. A formula for residual stress (σ_{res}) from this deflection was also proposed as:

$$\sigma_{res} = \frac{E\delta}{\alpha f_0} \tag{2.15}$$

where E is the Young's modulus, δ is the deflection of the rotating arm and the product of αf_0 (the length correction coefficient) was written as:

$$\alpha f_0 = \frac{L_r L_f}{L_{r_0} L_{f_0}} \tag{2.16}$$

where L_r is the rotating beam length, L_f is the fixed beam length and L_{r_0}, L_{f_0} are the initial values of the beam lengths. The experimental results indicated that the microrotating structures had the ability to locally measure a large range of tensile or compressive residual stress in thin films with high sensitivities. In particular, when the magnitude of the residual stress was small, the micro-rotating structures could still measure it with a high accuracy of ± 1 MPa [120, 9].

These techniques have many advantages over the wafer curvature method. Localised measurements can be performed on a wafer, using multiple beam systems, because of their small size. This can be employed to obtain useful spatial information about any abnormalities in the deposition process. MEMS strain sensors are also compatible with familiar CMOS technology, enabling measurements in real time during the wafer fabrication process cycle. Another major advantage, compared to the wafer curvature method was that, the relationship between the substrate thickness and stress can also be neglected. This means that devices can be designed to measure small changes in stress and elasticity without the information of any underlying layers, even if the specimen film is very thin ($\approx$ 1 μm). These films could be either sputtered, evaporated, electrodeposited or

spin coated. Also the fact that beam theory in MEMS is well defined ensures micomechanical pointer arms could be used to quantify strain and ultimately stress. This technique is therefore adopted in this thesis and discussed in Chapter 3.

2.5 Electrical Test Structures

2.5.1 Greek Cross Structures

The Greek Cross has been widely used as a test structure to measure the sheet resistance of thin films [121, 122, 123]. A schematic of this structure is shown in figure 2.10. The beauty of its design lies in the fact that the measurement is taken at the heart of the cross, which measures the resistance of a very small amount of material. This may carry information about the size and distribution of grains in that region[124]. Another attraction is that the resistivity does not depend upon the dimensions. Structure to structure variability has also been observed in Greek Crosses with narrow arms [125]. To keep the sheet resistance error less than 1 % the length of the arm (L) has to be greater than or equal to twice the arm width (W) [121, 126, 127]. It would be simpler to extract the sheet resistance from a

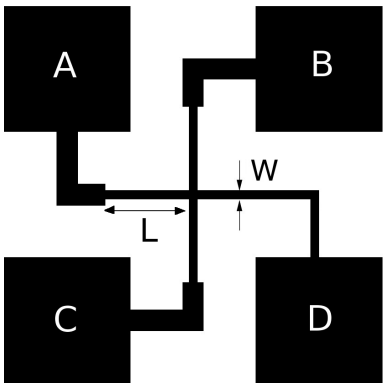

Figure 2.10: Layout of Greek cross sheet resistance test structure

single measurement, however in practice four measurements are required. Two

are at a static or (0°) position:

$$R_0(+I) = \frac{V_C - V_D}{I_{AB}} \tag{2.17}$$

where the current (I_{AB}) is applied between A to B and the potential drop (V) is measured between C and D. In the next measurement, the current I_{BA} is applied in reverse:

$$R_0(-I) = \frac{V_D - V_C}{I_{BA}} \tag{2.18}$$

Averaging these resistances would minimise uncertainty errors and is written as:

$$\mathrm{R}_0 = \frac{R_0(+I) \quad + \quad R_0(-I)}{2} \tag{2.19}$$

The next two measurements both forward and reverse arrangements are at "ninety degree" (90°) orientation. In that the current flows from pads A to C and the voltage is measured between B and D.

$$R_{90}(+I) = \frac{V_B - V_D}{I_{AC}} \tag{2.20}$$

$$R_{90}(-I) = \frac{V_D - V_B}{I_{CA}} \tag{2.21}$$

The mean of these resistances gives R_{90}, which is then averaged with R_0 from Equation 2.19 to yield the resistance:

$$R = \frac{R_0 + R_{90}}{2} \tag{2.22}$$

The sheet resistance (R_s) can then be calculated as:

$$R_s = \frac{\pi R}{ln(2)} \tag{2.23}$$

Any asymmetry in the structure is accounted for by the correction factor (f) which is given by the following relationship:

$$cosh\left(\frac{r-1}{r+1}\frac{ln(2)}{f}\right) = \frac{1}{2}exp\left(\frac{ln(2)}{f}\right) \tag{2.24}$$

where

$$r = \frac{R_0(+I) + R_0(-I)}{R_{90}(+I) + R_{90}(-I)} \tag{2.25}$$

More details on the effects of 'f' are given in reference [122]. In this work (F_A), the asymmetry factor is calculated from 'r' using

$$F_A = 2\frac{r-1}{r+1} \tag{2.26}$$

It was concluded that when $|F_A| \leq 10.74\%$, the correction factor can be approximated to unity. In this case, by using the four points measurement routines the sheet resistance equation is reduced to

$$R_s = \frac{\pi R}{ln(2)} \tag{2.27}$$

All sheet resistance measurements made in this study had calculated asymmetry factors of below 10.74%, therefore no asymmetry correction had to be made.
It was also important to consider the voltage offsets in the test system which can be highlighted from the measurements at forward and reverse currents at each orientation. If the zero-offset factor (F_0), calculated below, has a small value the measurement are more immune to the effect of voltage offsets in the test system.

$$F_0 = \frac{(|R_0(+I) - R_0(-I)| - |R_{90}(+I) - R_{90}(-I)|)}{2R(\pm I)} \tag{2.28}$$

To have a closer look at the heart of the Greek cross where the actual resistance measurement is taking place, the simulation and visualization software, COMSOL (Multiphysics 3.5a) was used. The electric currents module was employed on a Greek cross with dimension of L = 30 µm and W = 5 µm. A current of 0.1 A was

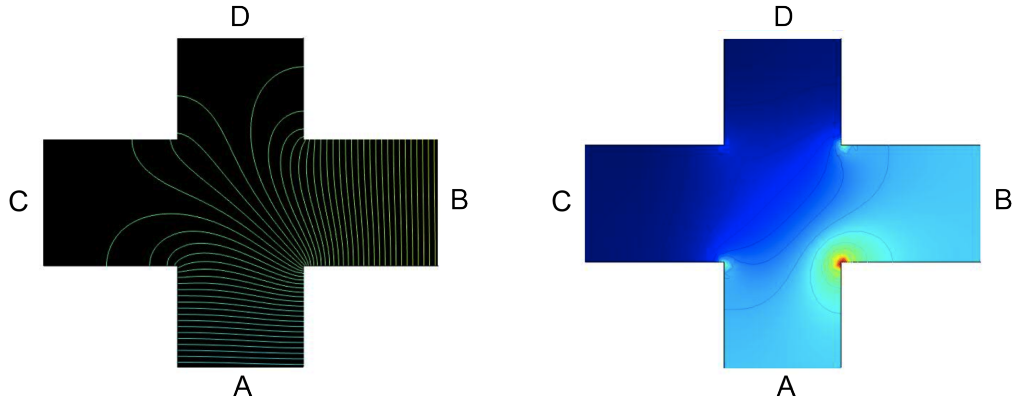

(a) Equipotential contour in Greek-cross

(b) Contours of current density for a Greek cross structure

Figure 2.11: Shows a COMSOL simulation of resistance measurement at the corner of a Greek-cross test structure, with current flowing from pads A to B and voltage measured between pads C and D

forced through the pads (A and B) and potential difference calculated between the opposite pads (C and D). The geometry of the cross is symmetrical along the dashed line which creates regions of equal potential, which are plotted as contours and shown in Figure 2.11(a). These potentials measured are the pads C and D should be the same as the small region at the inner corner of the cross between terminals A and B. The fact that Greek crosses can be used to measure sheet resistance at this small area might be useful in extracting information on individual grains or small grain populations of electrodeposited conducting films. Any non-uniformity in plating in those regions will be reflected in the resistivity measurements. The effect of different grain structures on a number of different cross geometries has been presented in reference [124]. It was deduced that variability of the sheet resistance increases with the cross size and the measurement region, as the probability of having a larger number of different grain orientations and boundaries will increase. This effect is also observed in the rounded corner Greek cross [121] where the voltage contours are closer over a larger area as illustrated in Figure 2.12. This would therefore provide the resistance averaged over a larger number of grains. It is also important to note

that fabrication processes such as wet etch removal of seed layers can attack the conducting metal layer and cause the edges to be rounded off in which case the results will vary from the expected ideal Greek cross structure.

A further issue with these structures is current crowding which can occur in the

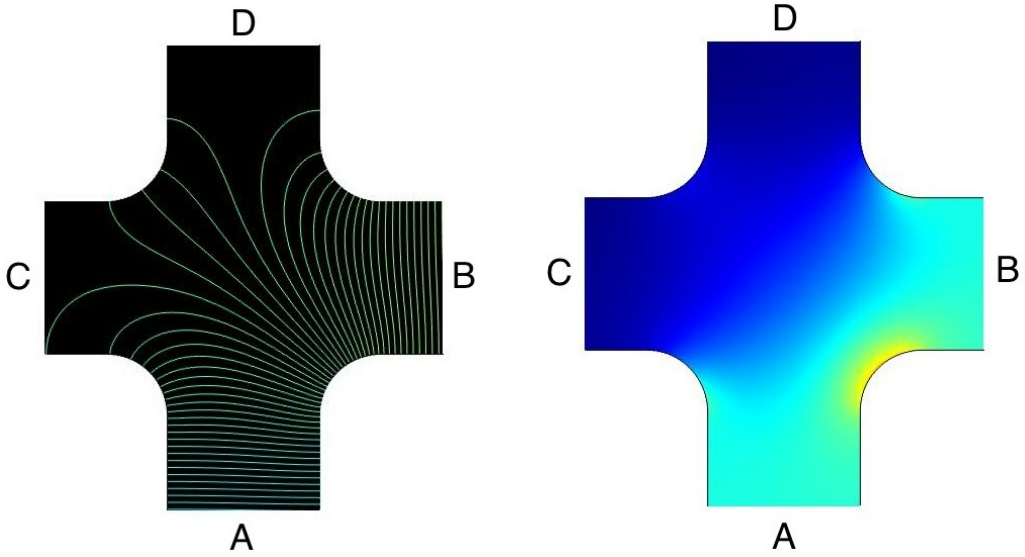

(a) Volage contour (b) Current density contour

Figure 2.12: COMSOL simulation with the same currents as in Figure 2.11 but the Greek-cross edges have been rounded

internal corner between the forced terminals of a small Greek cross. The scalar values of current at each node in a simulated structure can be plotted as contours in the same way as the potential. The current density is highest where the voltage contours are closest together as can be seen for both a Greek and a round cross structure in Figure 2.11.

In both structures the highest currents are observed at the internal corners between the forced terminals. If the current density in these areas becomes high enough this can affect the measurement especially in a Greek cross where the voltage is actually being measured in this area of maximum current. High currents in narrow armed crosses can also lead to Joule heating which will change the resistance of the conducting film [128, 129]. Reference [130] presents results showing

that there is an optimum value of current which gives the highest measurement repeatability. If it is too low, the resolution of the voltmeter will limit the accuracy whereas too high a current will tend to cause the effects which have been discussed above. Therefore it is important that the correct test structure and measurement strategy are determined for each application or process.

2.5.2 Kelvin Bridge Resistance Measurement (Linewidth)

Linewidth and resistance measurements are essential for the characterisation and control of the ECD copper windings, whose electrical properties are essential for defining the inductor's Q-Factor. However these become increasingly difficult as device dimensions reduce and hence the relevance of obtaining accurate CD measurements becomes important. The main methods for measuring linewidth are optical, scanning electron or probe microscopy and four-point-probe as an electrical technique. Unfortunately, there is no single metrology that can deliver all the required information. This section will discuss the use of a cross-bridge test structure which can be used to extract the sheet resistance, Kelvin resistance and line width of the conducting layer. The cross-bridge sheet resistor is a combi-

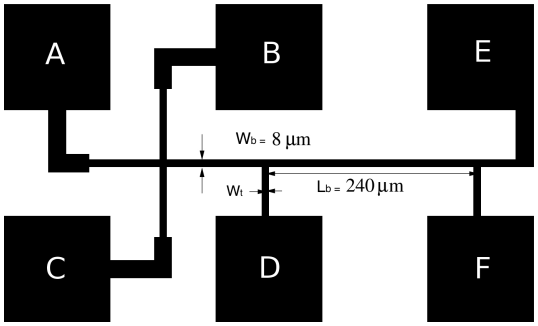

Figure 2.13: Diagram of cross-bridge electrical test structure for sheet resistance (few grains) and bridge resistance (more bulk material)

nation of a Greek or round cross and a four-terminal bridge resistor [131, 132]. A schematic diagram of such a structure is shown in Figure 3.10. The electrical width (W_b) of the bridge section between the voltage terminals B and F is calculated

from

$$W_b = \frac{R_s L_b}{R_b} \tag{2.29}$$

where L_b is the length of the bridge and R_s is the sheet resistance of the material which can be extracted from the Greek cross measurements and calculations shown in section 2.5.1. The value of W_b from equation 2.29 is the average value of the conductive width of the bridge section. To measure the bridge resistance (R_b) two measurements are made and the average resistance is calculated. Firstly a current (I_{CF}) is forced between terminals C and F and the voltage (V_{BE}) between terminals B and E is measured. The resistance is given by

$$R_b(+I) = \frac{V_{BE}}{I_{CF}} \tag{2.30}$$

The measurement is repeated with the current reversed and the resistance is once again determined

$$R_b(-I) = \frac{V_{EB}}{I_{FC}} \tag{2.31}$$

The average bridge resistance is then calculated by

$$R_b = \frac{R_b(+I) + R_b(-I)}{2} \tag{2.32}$$

There are two assumptions made in the calculation of the electrical linewidth. Firstly it is assumed that the sheet resistance is uniform, so the value extracted at the Greek cross section applies to the whole of the structure. Any error in the sheet resistance will be directly translated to an error in the calculation of the linewidth in equation 2.29. Therefore it is necessary that the accuracy of the sheet resistance measurements is the same or better than that required for the linewidth measurement. Errors may be introduced by limits in the resolution of the voltmeter used in the Greek cross measurement or by non-uniformities in the thickness of the material.

The second assumption is that the length L_b of the bridge section is the designed length between the centres of the voltage taps. However this is complicated by the

effect of the taps which effectively widen the bridge and lead to an over-estimation of the value of linewidth [133, 134]. The tap induced error can be minimised by using the design rules given in reference [126]. These are:

$$L_b > 150\mu m$$
$$L_b > W_b$$
$$W_b \geq W_t$$

2.6 Summary

The main challenge in the development of a microinductor is the use of low stress films using efficient and reliable processing technique compatible for its integration with IC technology. ECD has been chosen for the deposition of the magentic core (NiFe) and thick Cu windings, but internal stress within these films may develop due to variations in bath chemistries and other plating conditions and this poses a big issue for the reliability of the device.

To fully understand the origin of stress, the basic understanding of the ECD of these films is required and reviewed in this chapter. Present understanding on the effect of hydrogen evolution in Ni deposition and the anomalous codepositon of NiFe have also been discussed which can effect non-uniformities (voids) and hence stress within the film.

Many of the strain/stress characterisation techniques reported in literature have been reviewed. The advantages of MEMS stress structures over the conventional wafer curvature technique include its ability to be used for patterned films and extract not only average but spatial stress across the deposited film.

The following chapter aims to create a complete wafer level MEMS strain measurement system based upon the benefits of the techniques reviewed in this chapter.

Chapter 3

MEMS Strain Test Structure and Wafer-level Measurement Technique

3.1 Introduction

The spatial variation of material properties such as stress across a wafer is of great importance in MEMS, as this can be responsible for non-uniform device performance, yield losses and poor reliability. In extreme cases, it can cause layer delamination and substrate cracking [98]. Characterisation of stress in thin films is therefore of widespread interest across global foundries and research groups [100][135][36]. The wafer curvature technique (section 2.4.1.1) has been widely used in the semiconductor industry as a standard method for stress measurement. A major issue with this technique is that it can only provide the overall (averaged) stress of monolayer blanket films on substrates. Spatial variations of stress in patterned films, due to non-uniform process factors, therefore, cannot be investigated using wafer curvature.

The aim of this chapter is to develop a reliable spatial strain measurement system for electroplated films. Based on the knowledge gained from previous published techniques (section 2.4.1.2), MEMS based pointer arm rotating test structures have been employed to obtain quantitative and localised strain measurements. These values can then be used to geographically map the strain over the surface of the wafer.

In this chapter, a complete mask design, fabrication procedure and a in-house built measurement system devised, to successful extract spatial strain across a 200 mm wafer, is presented and the system used to spatially map strain on a *test* ECD Ni film.

3.2 Strain Test Structure

The strain sensor used in this work is a MEMS based pointer arm rotating structure, a schematic diagram of which is shown in Figure 3.1. These structures

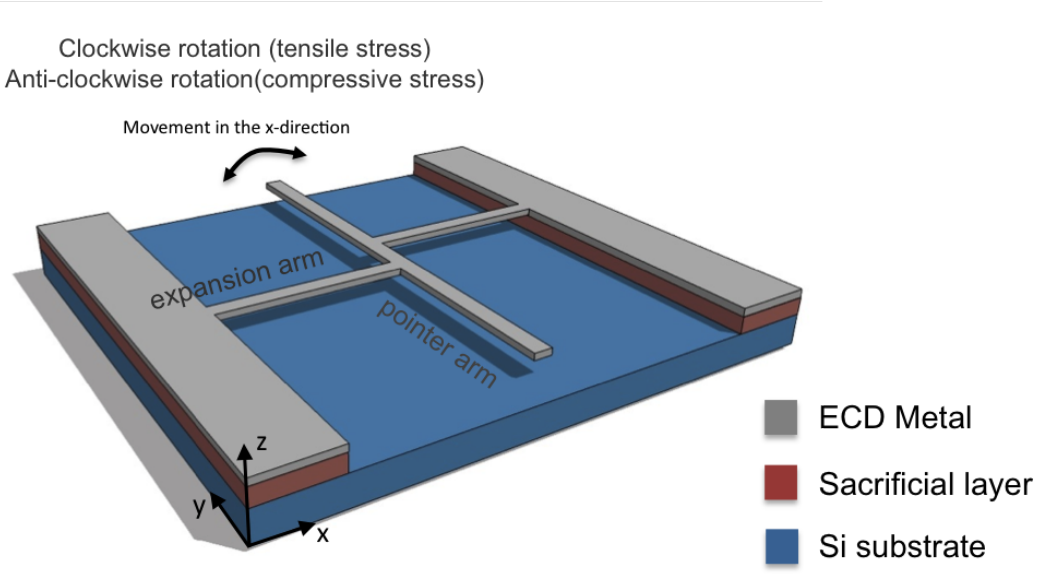

Figure 3.1: Schematic of the pointer arm strain sensor

are fabricated in the layer being characterised and consists of three main elements; two expansion arms anchoring a third pointer arm, with an offset in the center. An underlying layer is etched away to release (detach) the suspended structure, which releases any residual stress in the expansion arms. As the stress is relieved, any small deviation in arm length exerts a torque about the centre of the sensor which causes the pointer arm to rotate. The quantitative optical measure of displacement of the pointer arm (giving strain ϵ) can be used along with finite element analysis to determine the material's stress σ in a particular region. In the structure shown

in Figure 3.1, a clockwise rotation indicates tensile stress, while an anticlockwise rotation indicates compressive stress.

The schematic representation of the bending movement of the rotating arms experiencing compressive stress, is shown in Figure 3.2. Assuming ideal geometry

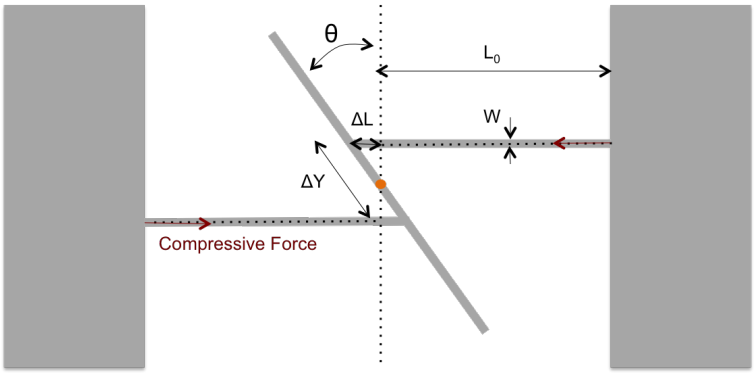

Figure 3.2: Schematic representation of the bending movement of the rotating structure under compressive stress

and rigid beams, the direct relationship between the pointer arm rotation (θ) and strain can be written, using simple trigonometry, as [136]:

$$\theta = \tan^{-1}\left[\frac{2\Delta L}{\Delta Y}\right] \tag{3.1}$$

where, L_0 is the arm length without stress, ΔL is the change in length of the stressed expansion arm and ΔY is the arm separation (assuming $\Delta Y \gg$ arm width, W). For, rotations $< 10°$ (small angle approx, $\tan(\theta) \approx \theta$ can be applied) to give:

$$\theta = \epsilon \frac{L_0}{\Delta Y} \tag{3.2}$$

where strain ($\epsilon = \Delta L / L_0$). From this relationship, if the structure geometry is kept constant and no bending movement of the arm occurs, then, the local strain can be considered to be directly proportional to the pointer rotation.

3.3 Design Optimisation

The sensitivity of rotation in these devices relied on the following parameters: the arm length L, the arm separation ratio ΔY, the arm width W and the material's elastic properties (Young's modulus). These have been investigated previously, using Finite Element Analysis [10][137]. This model used thermal strain to extract the rotational response of the structure which could be arbitrarily converted into stress, upon solution using Young's modulus (E) from the literature.

$$\sigma = \mathrm{E} \times \epsilon \tag{3.3}$$

Firstly, the effect of arm separation ratio ΔY on the pointer rotation was investigated, for an arm width W = 8 µm (lithography value). Figure 3.3 presents the simulated rotations as a function of the ratio of extension arm separation and arm width (ΔY/W) for increasing values of stress, assuming Young's modulus = 200 GPa for NiFe [138, 139].

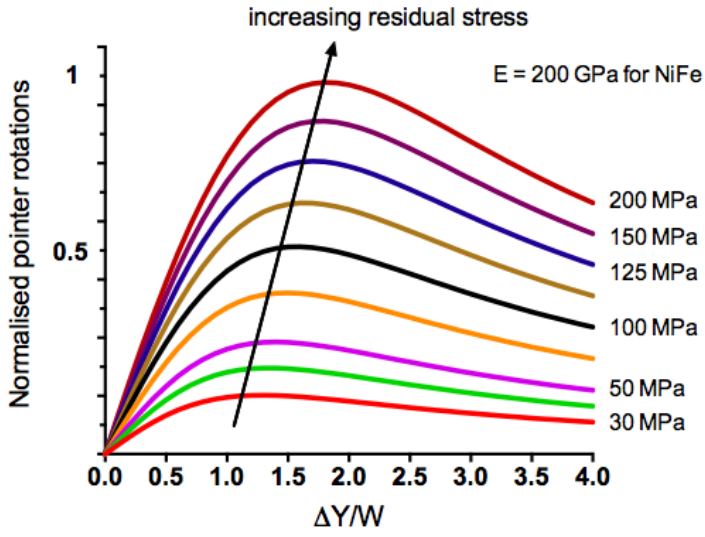

Figure 3.3: Simulated pointer rotation as a function of arm separation : width ratio (ΔY/W) for increasing values of stress (0 - 300 MPa), assuming Young's modulus = 200 GPa for NiFe [10]

The range of interest for the residual stress in electroplated NiFe films have been reported to be less than 300 MPa [100, 33] therefore, these plots were simulated for stress values between 0 to 300 MPa. A plot reveals a sensitivity area where the rotations peaks. This occurs for two reasons. Firstly, when $\Delta Y/W = 0$, the expansion arms would be aligned and the structure would act as one long suspended bridge. Any stresses would be translated directly into the buckling motion in the z-direction, without giving any rotational torque in the x-direction. Alternatively, at higher $\Delta Y/W$, the expansion arms would be separated at a longer distance from the central torque point, thus decreasing the sensitivity of the hinge. Therefore, an optimum point where the rotation is maximum was obtained, which depends on the material stiffness and geometry of the hinges. Figure 3.4 shows the extracted values of $\Delta Y/W$ as a function of the input residual

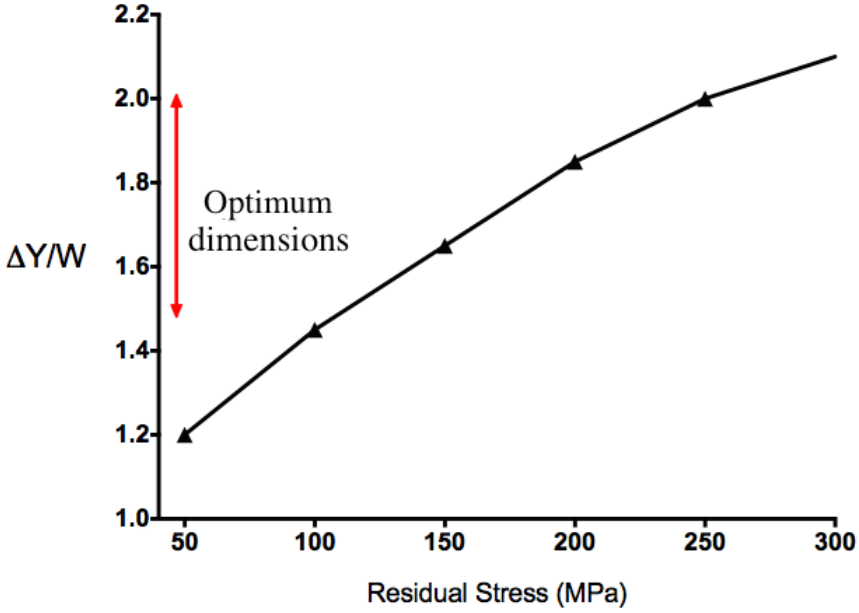

Figure 3.4: Optimum pointer arm rotation geometries as a function of the input residual stress. This curve was used for the dimensioning of the structures by identifying a stress range of interest and designing test devices with the corresponding optimum geometry.

stress. With the range of interest for the residual stress in ECD NiFe films it is consequently possible to design the structures accordingly with $\Delta Y/W$ ratios ranging from 1.5 to 2.

Assuming only a small variation in stress, the optimisation of the structure dimensions W and L can be considered. Figure 3.5 shows the predicted maximum pointer rotation as a function of feature width for different arm lengths using the fitting stress from Figure 3.3. This demonstrates that the sensor must be optimised to maximise the sensitivity, as the small variations in geometrical parameters do not give a sufficiently large difference. The feature width is the most sensitive parameter to increase rotation [10], following a negative power relationship with stress. However, depending on the process it may be easier to increase the arm length L, which also increases the rotational sensitivity to stress, following a power relationship.

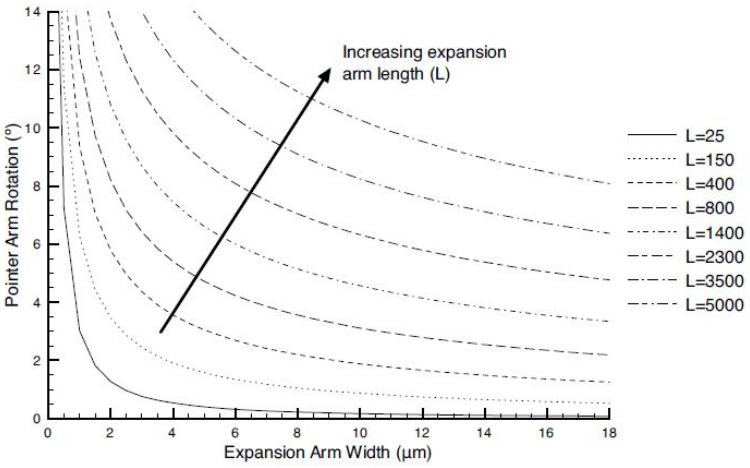

Figure 3.5: Simulated pointer rotation as a function of arm separation ratio (ΔY/W) for increasing values of feature length (L) [10, 11]

A design variation was also introduced by designing notched expansion arms, as shown in Figure 3.6(b). The notch has been designed to relieve the stiffness of the joint with the pointer arm and reduce the buckling effect to help avoid any out of plane (vertical) displacement of the beam.

Figure 3.7 shows the improvement in the response of the devices if notched arms are used for arm length of 800 µm. The rotation of the pointer arm is enhanced by about 30% if the arm width is reduced from 8 to 5 µm, at the expense of a

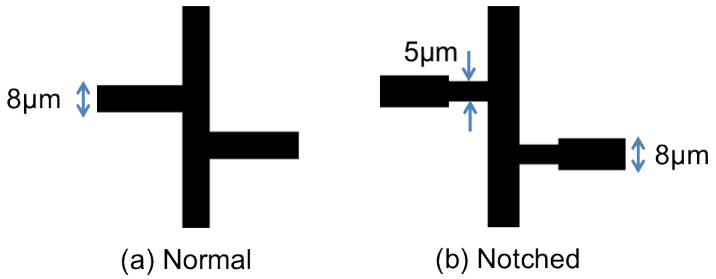

Figure 3.6: Pointer arm variations showing the difference between normal and notched structures

higher mechanical fragility and possibility of failure.

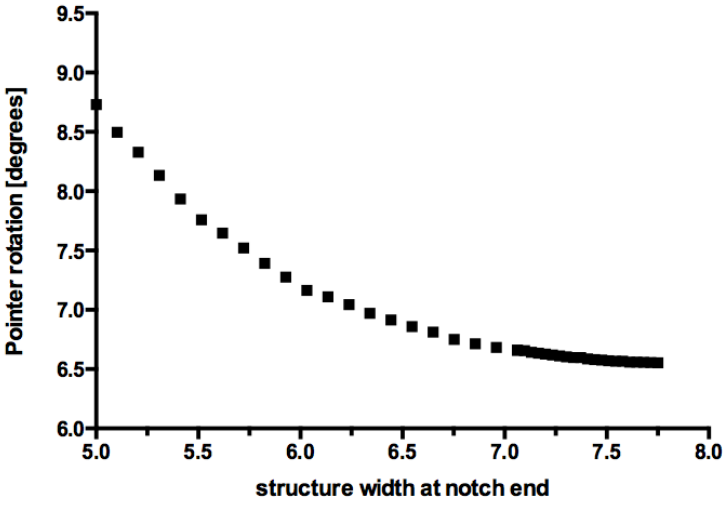

Figure 3.7: Simulated rotations with expansion arm notch width anchoring the pointer arm as shown in Figure 3.6(b)

3.4 Test Structure Chip and Mask Layout

Based on the results described in the previous section, a test mask was designed that consisted of an array of stress test structures with $L = 850$ μm, $W = 8$ μm and $\Delta Y/W = 1.50$, 1.75 and 2.00. One of these structures is shown in Figure 3.8 and the test die is shown in Figure 3.9. Each die in the test mask design has 32 test structures which includes seven structures with $\Delta Y/W = 1.50$, seven with $\Delta Y/W = 2.00$, and fourteen with $\Delta Y/W = 1.75$. In addition, there are four

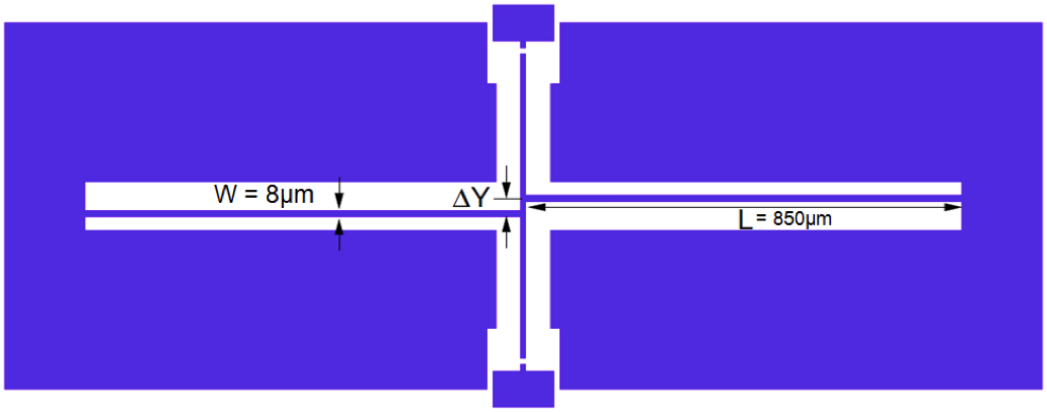

Figure 3.8: Model of the pointer arm strain sensor

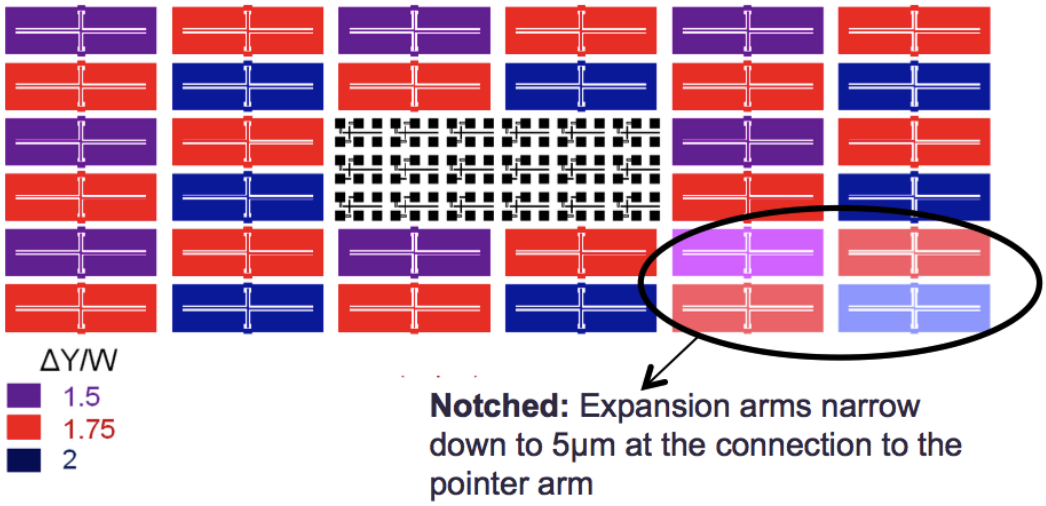

Figure 3.9: Chip layout with 32 pointer arm strain sensors of three different ΔY/W ratios (colour coded) surrounding a matrix of 6×3 electrical test structures in the center

'notched' structures where the expansion arms narrow to 5 µm where they attach to the pointer arm (Figure 3.6).

In the centre of the strain structure chip is a matrix of 6×3 identical Greek and Kelvin bridge resistance test structures for local sheet resistance and linewidth measurements. This is shown in Figure 3.10 and it worth noting that W for these test structures is also 8 µm (same as the rotating test structure). The mask layout of the electrical test structure matrix is presented in Figure 3.11.

The test structure chip was populated on the floorplan for a full 9" photomask, as shown in Figure 3.12. There are 384 dies giving a total of 12,288 strain test

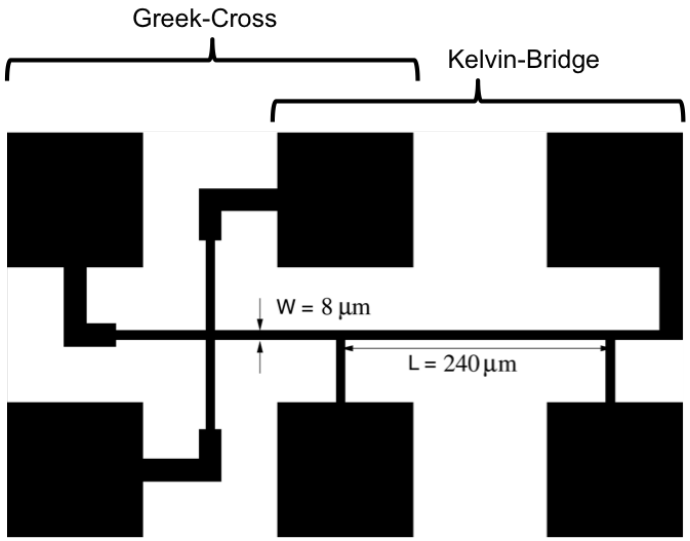

Figure 3.10: Diagram of combined cross-bridge electrical test structure for sheet resistance (few grains) and Kelvin-bridge resistance test structure (bulk material)

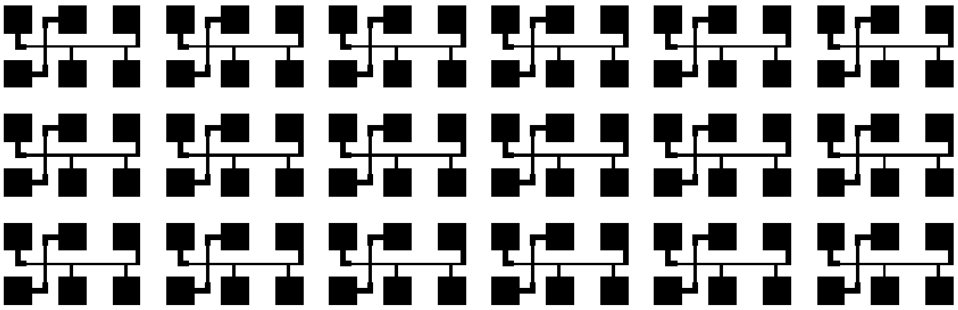

Figure 3.11: 6×6 matrix of combined Greek-cross and bridge structures chip

structures on the wafer. The mask was intended to be used to pattern these structures in a single photolithography/patterning step on a 200 mm wafer. After successful fabrication and release, variation of stress and sheet resistance with position could then be quantified.

3.4.1 Fabrication and Release Techniques

This section outlines the complete fabrication and release procedure of the strain test structures fabricated on wafers using a test NiFe ECD film. The basic schematic of the fabrication process is shown in Figure 3.13. The steps were as follows:

Cleaning: Starting from a bare silicon wafer, the substrate was cleaned using

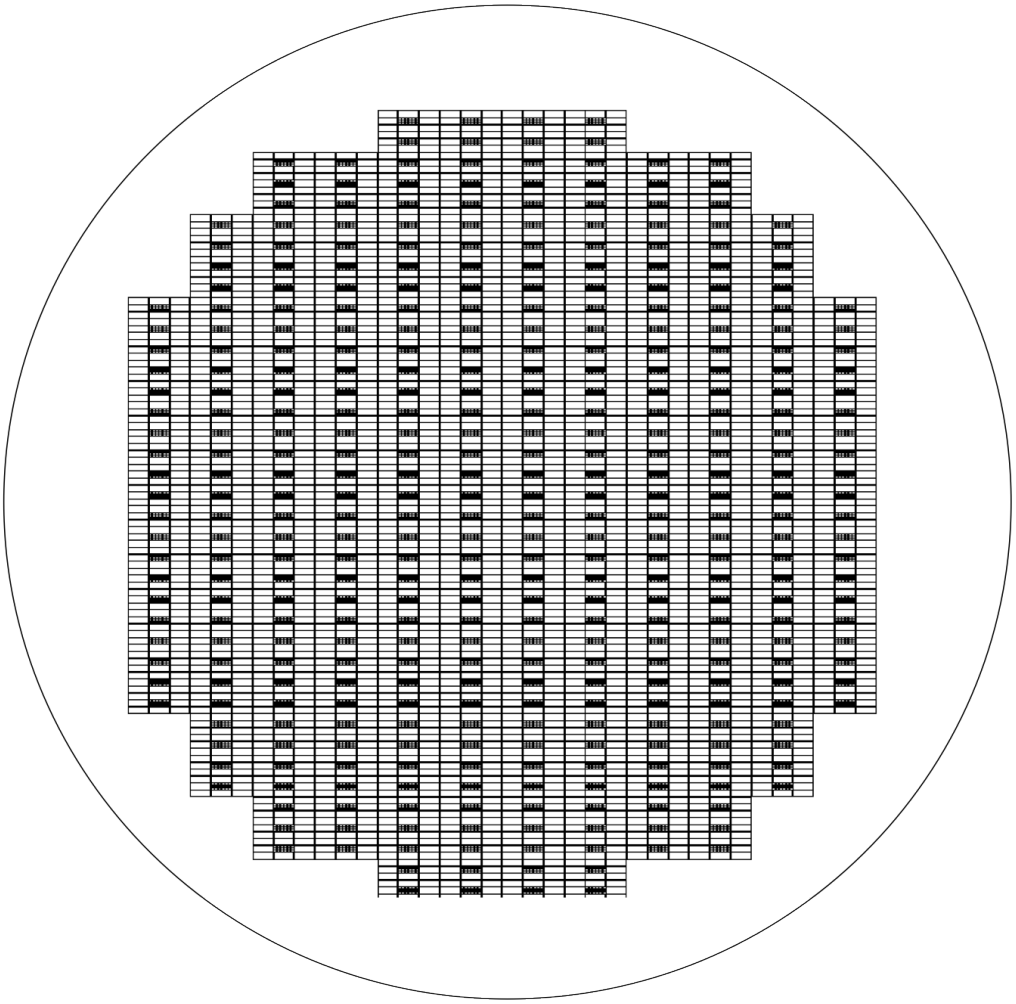

Figure 3.12: Shown is a complete 9" mask layout, for 200 mm wafers populated with the identical test structure chips; the mask designed was designed with a 10 mm edge exclusion

acetone, in an ultrasonic bath, for 10 mins. The wafer was then rinsed with isopropanol alcohol (IPS) and DI water to dissolve any traces of acetone.

Sacrificial Silicon Dioxide layer: [Figure:3.13(a)] To passivate the silicon for electrical measurements and also to act as a sacrificial layer for the release of the strain sensors, silicon dioxide (SiO_2) was deposited by plasma enhanced chemical vapour deposition (PECVD), in a Surface Technology Systems (STS), tool. The thickness varies with deposition time and for this procedure a 0.7 µm thick oxide (20 mins deposition) was deposited as the release layer. After deposition, the

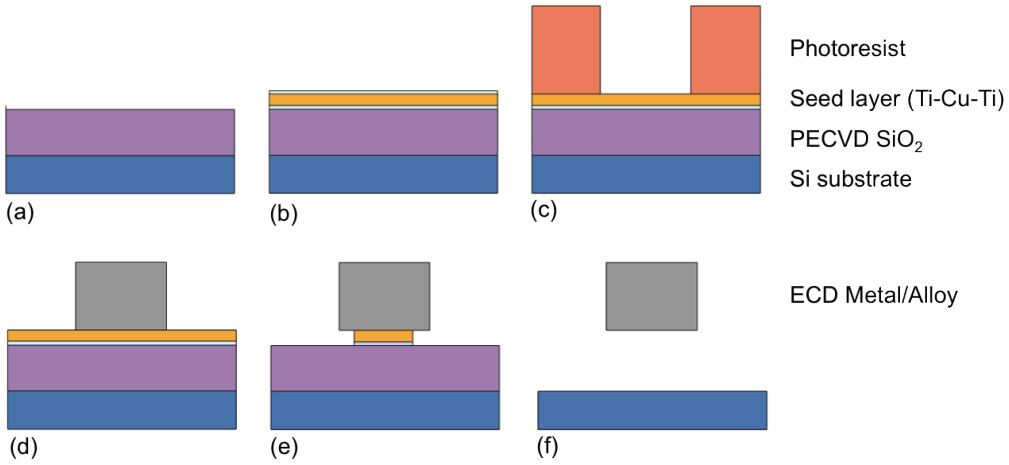

Figure 3.13: (a-f) Schematics of the fabrication procedure for the strain test structure

oxide thickness was verified using a reflectometer (Nanospec 3000).

Seed ECD layer: [Figure:3.13(b)] A 200 nm layer of sputtered copper was used as the blanket seed layer, for ECD. To ensure it adhered well to the oxide underneath, a thin layer (50 nm) titanium was deposited first. To protect the copper seed from oxidation in air, a 30 nm titanium layer was also resputtered on top of the copper. The 200 nm copper seed was therefore sandwiched between the two 30 nm titanium layers.

Photoresist Coating: Hexamethyldisilazane (HMDS) [140] is a common primer used before spin coating photoresist, that serves as an adhesion promoter. Therefore, prior to photoresist coat, the wafer was vapour primed in HMDS for 10 mins. The positive photoresist mould chosen to achieve 8µm thickness was Shipley^{TM} Megaposit^{TM} SPR220-7 [141] which was spin coated (at 2000 rpm) on to the 200 mm wafer and soft baked on a hotplate at 115 ℃ for 90 seconds.

Edge Bead Removal (EBR) During the spinning of photoresist, there is an

accumulation of resits at the wafer perimeter. In order to get the best resolution using contact lithography, it was necessary to have an intimate contact between the substrate and the photomask. Therefore, a 10 mm photoresist edge was removed from the perimeter of the wafer, using propylene-glycol-monomethyl-ether-acetate (PGMEA) on an automated Brewer CEE wafer track system.

Patterning: [Figure:3.13(c)] The 9" mask shown in Figure 3.12 was used to pattern the 200 mm wafer using a Karl Suss MA / BA8 Mask Aligner with a 50 sec exposure dose (hard-contact). A post exposure bake (PEB) of 115 ℃ for 90 secs was also performed. After baking the wafer was developed using Microposit MF-26A at room temperature in a beaker. The wafer was finally inspected under the microscope, and the critical dimension (CD) and resist thickness measured using a Veeco Dektak 8000 surface profiler. In this case the CD was the 8 µm pointer arm width.

Electrochemical deposition (ECD): [Figure:3.13(d)] The protective Ti layer was removed by wet etching in a dilute 1 % HF solution to expose the Cu seed layer for ECD.

A custom 35 L plating tool was used for ECD, equipped with a DC power supply and a jet agitation system. The wafer was securely placed in a sealed 200 mm wafer holder and plated for the designated current/time, as determined by the target film thickness. Detailed description of bath chemical composition, recipes and plating conditions are discussed in the proceeding chapters. After ECD the wafer was rinsed, dried and the photoresist stripped using acetone. The wafer was inspected again and the plating thickness confirmed using the Dektak.

Seed Layer Etch: [Figure:3.13(e)] To gain access to the sacrificial layer (for release), the seed layers (Ti-Cu-Ti) stacks have to removed. The titanium seed layer was first removed by submerging the wafer for 10 secs (or until the titanium

was visibly etched), in a diluted 1 % HF solution. At such a low concentration the corrosion of the exposed metals (Cu, NiFe) [142] towards HF was minimised. The three copper seed etchants commonly used are 20 g/l ammonium persulfate,

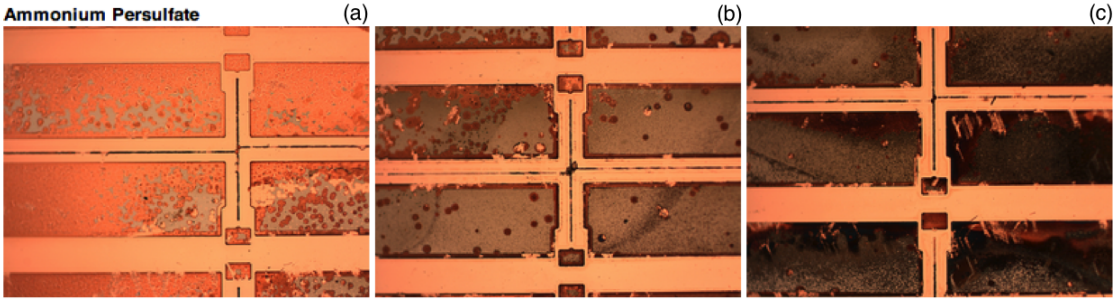

Figure 3.14: Microscope images of structures with copper seed layer etched in a solution containing 20 g/l ammonium persulfate after (a) 60 s (b) 120 s (c) 200 s

5 % HNO_3 and $HCl/FeCl_3$ solutions. Conventionally, in industry, ammonium persulfate has been optimised for use with ECD Ni. However, upon testing with

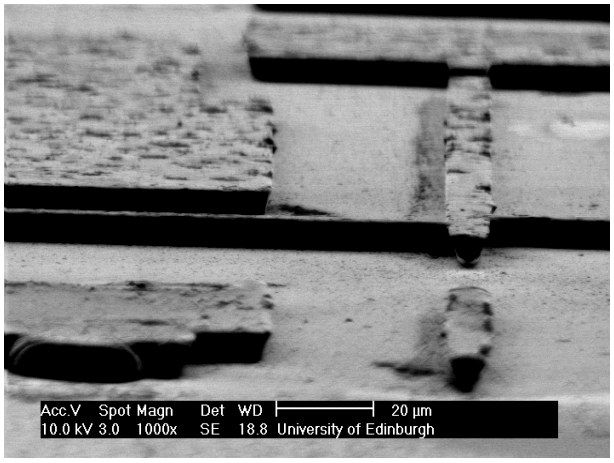

Figure 3.15: SEM image of NiFe corrosion after etching Cu seed layer

ECD NiFe alloy (Figure 3.14), corrosion of the metal was apparent. An SEM image of a corroded tests structure is also shown in Figure 3.15 confirming the chemical attack. This undesired effect was eradicated by developing a unique selective metal etchant. In contrast, Figure 3.16 shows results from the improved etchant which consisted of: 20 g/l ammonium persulfate, 50 g/l sodium citrate and 1 M sodium hydroxide (or ammonium hydroxide) to maintain a high pH value > 12.

Observed here are three different regions of the wafer etched with this new recipe.

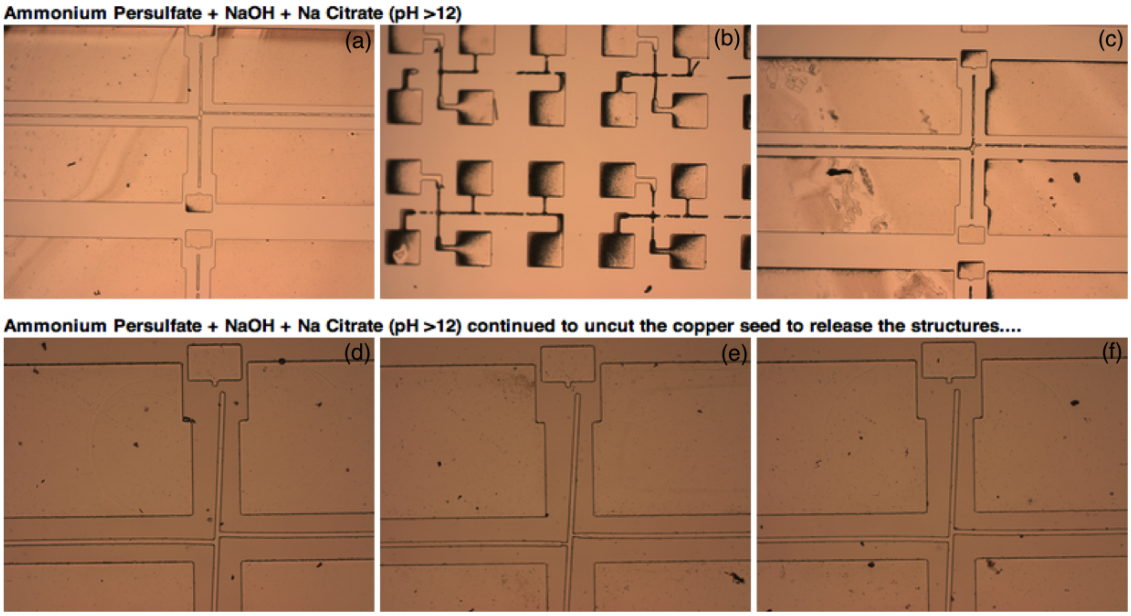

Figure 3.16: Microscope images of selectively etched copper seed layer sample in a solution containing ammonium persulfate + NaOH + sodium citrate for (a-c) 3 mins (d-f) 6 mins

NiFe corrosion was minimised and the seed layer was completely etched. The total process time to etch 200 nm of copper on a 200 mm wafer was approximately 3 mins. Continuing the etch for another 3 mins started to undercut the pointer arm test structures, releasing them temporarily as shown in Figure 3.16(d,e,f).

After a successful copper seed etch, the bottom Ti layer was removed with 1 % HF solution, leaving the sacrificial layer exposed for vapour etch.

To this point the wafer was always processed using an aqueous medium. The test structures were observed to have been released but were expected to stick down to the substrate due to a surface force called 'stiction'. This occurs when a liquid meniscus, formed on hydrophilic surfaces, pulls the microstructure towards the substrate where they stick indefinitely. However, this problem can be alleviated by etching the sacrificial layer using a vapour etch technique.

3.4.1.1 Vapour Etch

To successfully release the structure it was critical to use a highly controllable and repeatable process which could isotropically etch away the underlying material, without attacking NiFe. The underlying material employed was silicon dioxide (SiO_2), as mentioned earlier, which acted as a insulating layer for the electrical measurements and also as a sacrificial layer to release the rotating test structures [Figure:3.13(f)].

A MEMSSTAR Sentry Platform (vapour HF etcher) was employed for this task, in which hydrofluoric acid (HF) was used in its vapour phase to etch SiO_2. It has been reported previously, that nickel and its alloys are less prone to corrosion in the HF vapour [143] therefore, the overall reaction of vapour HF with the sacrificial layer, SiO_2, can be written as [144]:

$$SiO_{2(s)} + 4\,HF_{(g)} \longrightarrow SiF_{4(g)} + 2\,H_2O_{(l)} \tag{3.4}$$

The temperature and pressure of the chamber also plays an important role in governing the kinetics of the reaction [145]. At the beginning of the process, water vapour is pumped into the chamber at low pressure, which condenses on the oxide surface, and initiates the etching process. With time, more water is generated, as seen from the overall reaction 3.4, which further catalyses the reaction and increases the overall rate [146] (Eq: 3.5 and 3.5).

$$SiO_{2(s)} + 2\,H_2O_{(l)} \longrightarrow Si(OH)_{4(aq)} \tag{3.5}$$

giving:

$$Si(OH)_{4(aq)} + 4\,HF_{(g)} \longrightarrow SiF_{4(g)} + 4\,H_2O_{(l)} \tag{3.6}$$

With large undercut lengths, excess water generated, can cause stiction to the rotating arms, which has to be avoided. Therefore, the etch rate has to be monitored at all times, during the process.

In this particular etching tool, a galvanic sensor [147] was used to detect small

amounts of SiF_4 (g), extracted from the etching chamber, which can be used, reliably, to estimate the etch rate. A typical etch rate curve for etching 0.7 µm oxide on a 200 mm substrate, is shown in Figure 3.17. The first half of the plot

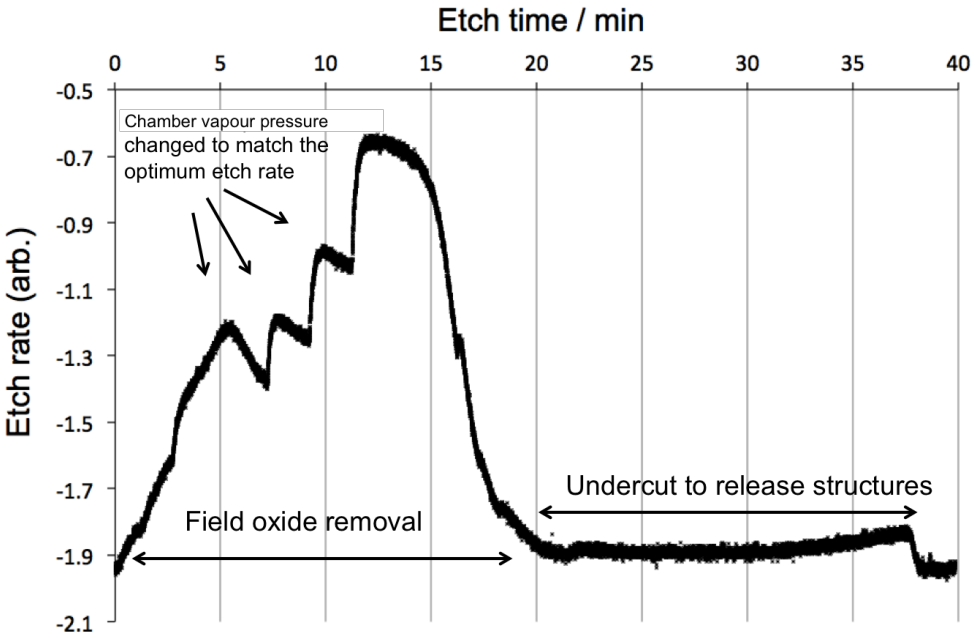

Figure 3.17: HF vapour etch progress (obtained from MEMSTAR HF etch tool) showing the removal of field oxide and undercut to release test structures

shows the field oxide being removed, and the second half shows the undercut and release of the test structures. The vapour pressures were changed numerous times during the field oxide etch to match the optimum etch rate. This would however depend on the exposed oxide area (substrate size etc.). A schematic drawing representing the HF vapour etch mechanism is shown in Figure 3.18. Arrows indicate the etch direction. During the field oxide etch, 3.18(b), the undercut would also proceed but the etch would be expected to accelerate inwards proceeding the complete removal of the field oxide 3.18(c). During the first run, the wafer was inspected every 5 mins, to confirm release. The total etch time for a 0.7 µm oxide etch was 45 mins. An SEM image of a fully released 5 µm thick NiFe strain test structure is shown in Figure 3.19. This same process recipe was also tested and verified for ECD Ni, later used in this work.

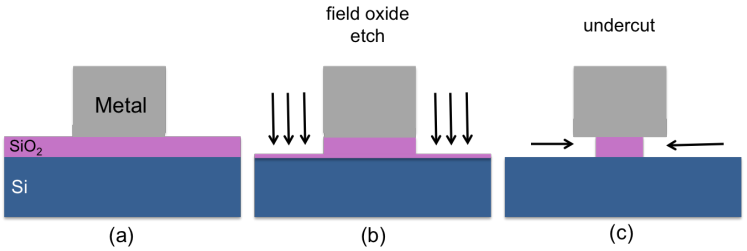

Figure 3.18: Schematic representation of an isotropic HF vapour etch mechanism to release a MEMS device showing (a) Before etch process (b) during field oxide etch and (c) during undercut

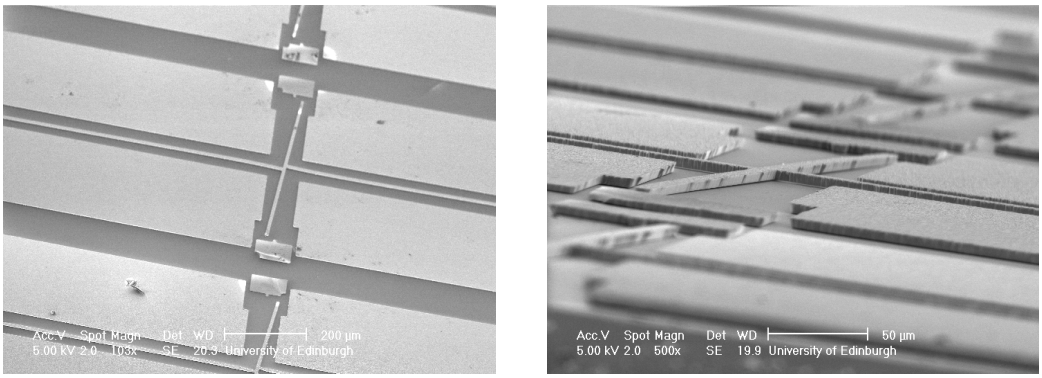

(a) (b)

Figure 3.19: ECD NiFe (5µm thick) SEM image of top view (a) and side view (b) showing the rotation of pointer arm after HF vapour release

3.5 Development of Localised Strain Measurement System

As there were over 12,200 released test structures on each wafer, an automated system was required, which was quick and could robustly extract the angles of rotations from all the pointer arms. Therefore, the next section details the working of an in-house built measurement system, capable of automatically wafer mapping strain from a 200 mm wafer in less than 30 mins.

The first test wafer fabricated using this design used 5 µm thick electroplated nickel. The film was deposited, at 20 $mAcm^{-2}$ DC, on a copper seed layer using an 8 µm thick mould of SPR220-7 photoresist. After plating, the resist was removed

by rinsing with acetone and the excess seed layer was removed with the wet etch process, described in Section 3.4.1. The structures were fabricated on 200 mm silicon substrates coated with a 0.75 µm thick sacrificial layer of thermal SiO_2. The stress structures were released from the substrate by the dry HF vapour etch step detailed in Section 3.4.1.1. After release the stress structures were free to rotate, but there was little or no deflection of the pointer arms on any structures which indicated a low level of stress in the as-deposited Ni film.

Subsequent processing and packaging typically involves multiple heating steps, for example to cure photoresist, glues used in packaging and soldering during assembly. To assess the effects of such heat treatment, the wafer was heated to 150 °C for 10 minutes on a hot plate. Figure 3.20 shows a released test structure before and after this heat treatment. After this heat cycle all of the structures showed a clockwise rotation indicating the development of tensile stress in the nickel film. This interesting observation was on eye level but to fully characterise spatial

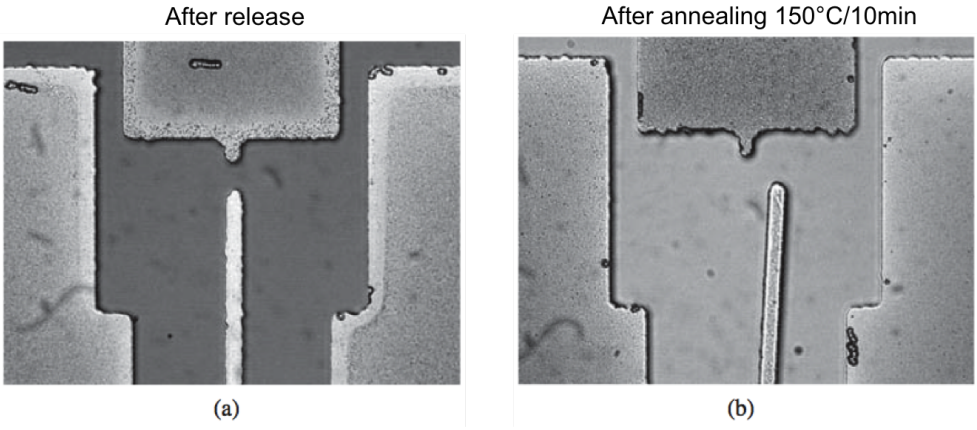

Figure 3.20: Optical microscope images of the pointer arm tip of stress sensors (a) before and (b) after heating to 150 °C for 10 minutes, taken from the center of the wafer

strain on an automated measurement system was developed with the capability to exact pointer rotation from the 12,228 structures on the wafer.

The following section explains the working of this system which was used to fully scan this wafer, results of which are discussed later in this chapter.

3.6 The Measurement System

The measurement system, which was developed consists of three major components; a camera, which captures the image of the stress test structure, a prober which scans the camera over the wafer and a computer, which analyses the image and determine the angle of rotation. Figure 3.21 shows photographs of the hardware and the following sections detail and discuss the system requirements

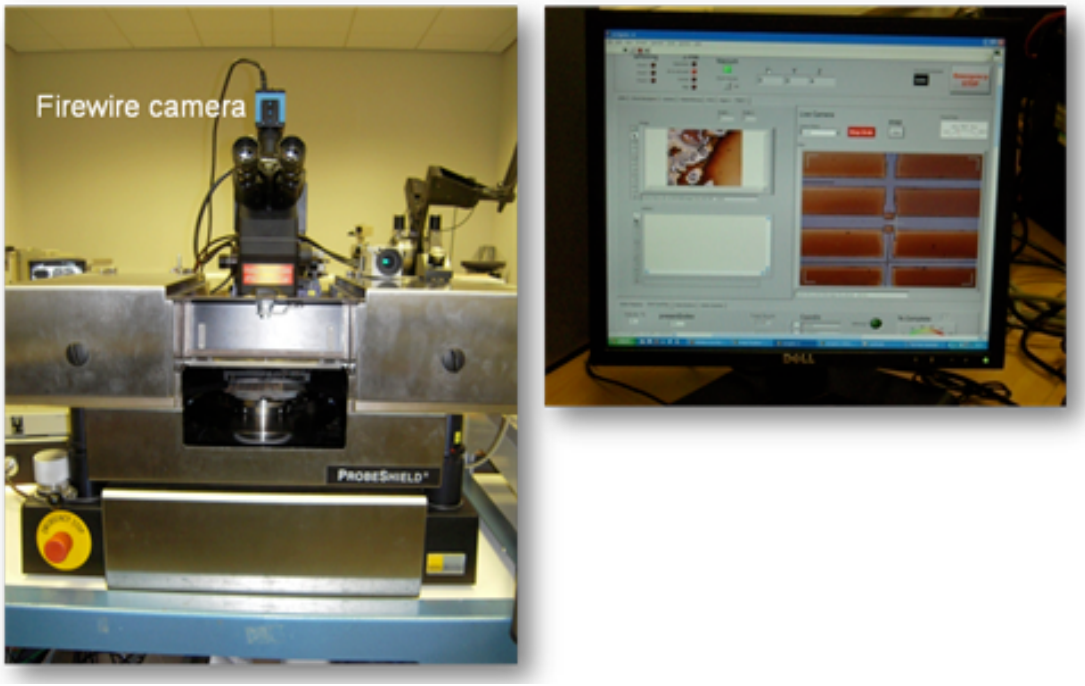

Figure 3.21: The measurement system consisting of a semi- automatic prober to scan the test structures and a PC running Labview, which controls both the prober and camera

and the development of the system created in Labview 8.6 to perform these functions. Figure 3.22 shows the measurement flow for the system.

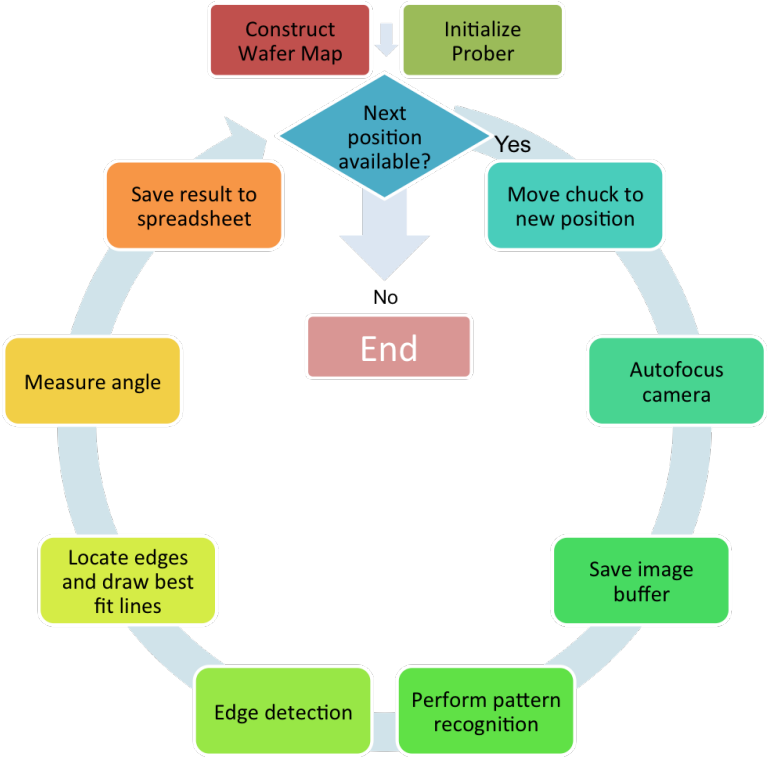

Figure 3.22: Measurement flow of the characterisation system

3.6.1 System Requirements

The requirements for the automated stress structure measurement system were that it should provide:

- Rapid and accurate measurements
- Deliver a robust measurement even when broken structures are present.
- Be simple to use and require minimal set-up.

The setup was designed to be fully automated and a graphical user interface (GUI) based wafer mapping tool (Figure 3.23), formed an integral part of the system, which enabled the mapping of individual elements to sub-micron accuracy across a complete wafer. This also provided a click and drag option, which allowed the user to initially set the system up to select the dies for scanning. After creating the measurement coordinates, the software translated the test structure coordinates on each chip into a prober based compatible coordinate array. This array could then be rearranged so that the wafer was scanned either 'chip by chip' or the

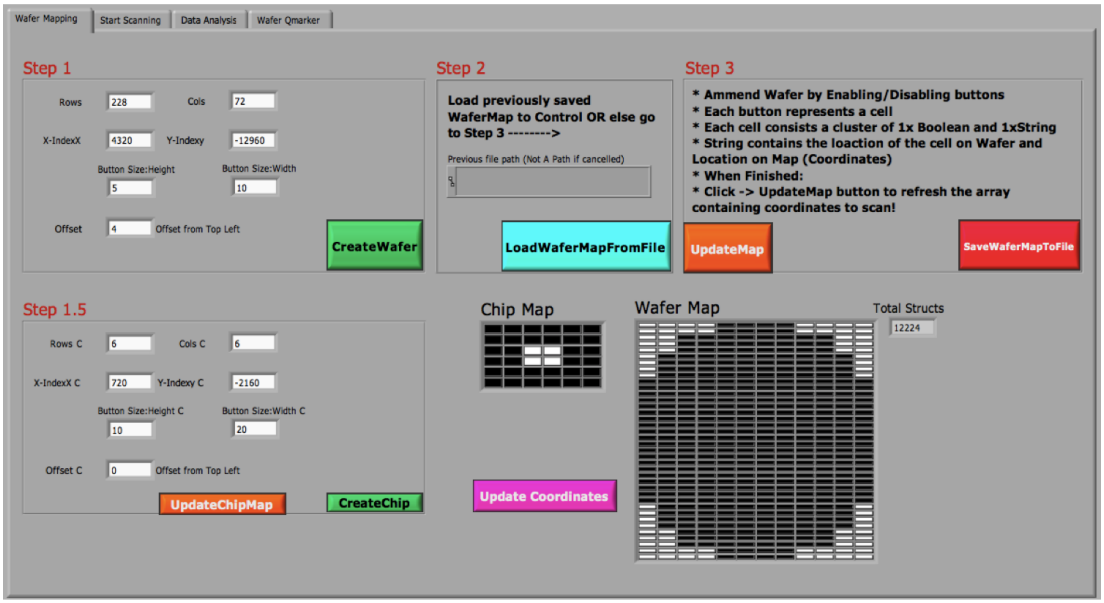

(a) Wafer mapping

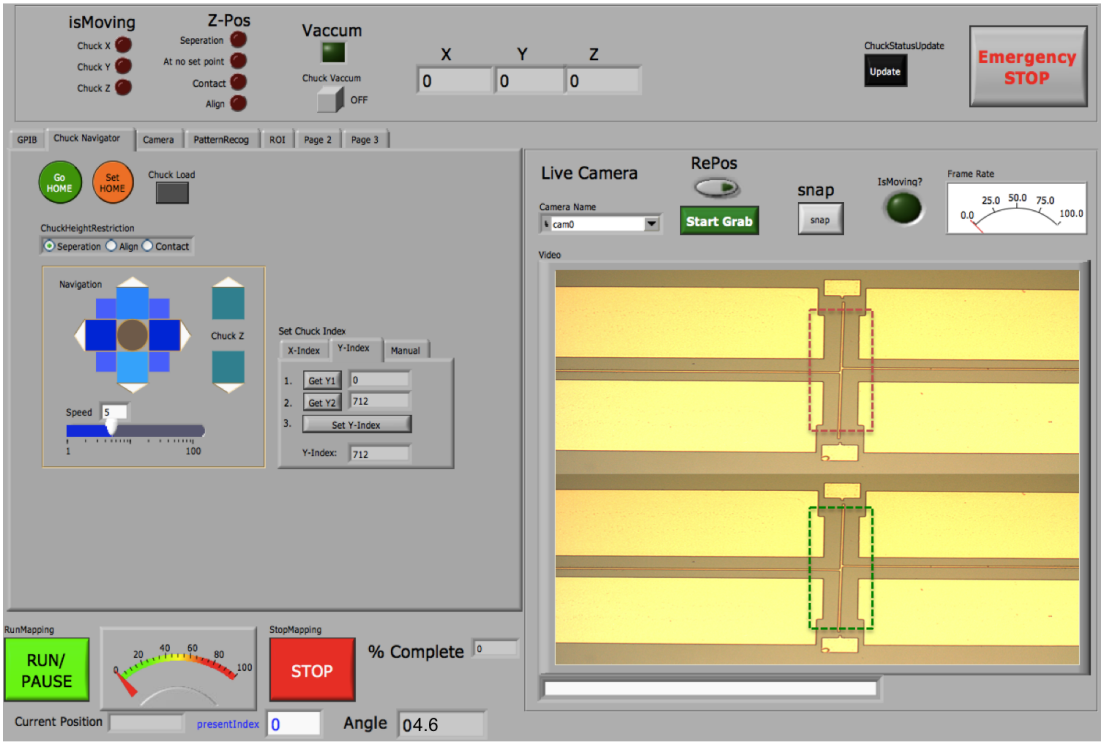

(b) Image acquisition/processing

Figure 3.23: Screenshot images of the measurement software created in Labview

'nearest structure first'. This latter option captured the image and extracted the results considerably faster, as the system did not have to wait for the prober to step between dies.

3.6.2 Device Initialisation

In an automated system it is important to perform initialisation checks before any measurements commence. As the system was designed for acquiring accurate measurements at high speed, the following parameters were monitored both initially and during the measurements process. These were; the prober general purpose interface bus (GPIB) read/write check, chuck related settings (vacuum, offsets, XYZ-axis crash control) and finally the initialisation of the camera (firewire port, image buffers, autofocus thresholds, image brightness, contrast, gamma auto adjustments) to optimise the performance of the image processing and pattern recognition.

3.6.3 Data Acquisition

Once the wafer stepping pattern was set, and the preliminary checks were performed, the automated measurement proceeded. The scan started either from a predefined home position (position of the first chip/structure) or from where the scan was paused manually or from an unexpected interrupt such as one caused by a communication port read/write failure.

A single scan involves a number of routines. It starts with smoothly moving the chuck from one structure to another, ensuring that the suspended rotating arms are not jolted when the chuck stopped. The camera is then automatically initialized and an initial low resolution image of the structure captured though the microscope mounted on the prober. A software routine checks the focus of the camera by taking an average SNR (signal-to-noise-ratio) of the image. The SNR for the image is the ratio of the mean pixel value to the standard deviation of the pixel values and was used to check the contrast of the edges. The camera

was then focused by adjusting the chuck height until the value was within a set SNR threshold (value depends on the material surface texture colour). A higher resolution image was then captured and further processed for pattern recognition, edge detection and angle extraction.

3.6.4 Pattern Recognition

To perform pattern recognition on images of the stress structure's thin pointer arms, a camera with a suitably high resolution was required. The camera used was from Imaging Source (with a firewire interface). The captured images were 1024 $\times$ 768 pixels with 96 dpi (dots-per-inch) and the camera refresh rate (20 fps) was considerably higher than the scan rate (6 structures per second). The high resolution image also enabled more than one structure to be captured and detected simultaneously thereby speeding up the measurement. Finally, all images were saved to disk for future reference and analysis.

There were numerous pattern recognition routines available, written in Matlab and Vision Assistant (Labview). Their usefulness for this application depended upon the ease of integration with Labview. Initially the pattern recognition code was written in Matlab, but this proved to be too slow when it came to acquiring the image data from Labview. Since speed was an important consideration for the overall measurement system, the built-in image acquisition and processing capabilities in Labview were selected. The system was setup such that it first, acquired an RGB image from the firewire camera, which was converted into binary (IMAQ extract single color plane). Once the image was converted into binary (intensity), this image was passed onto the pattern recognition function. A template of the rotation arm pivot (cross) was used to match similar a pattern in the image. This resulting system can efficiently detect a number of identical or different predefined patterns in a binary image. A rotation tolerance of $\pm$ 45 $^\circ$ to the pattern was used to detect dislocated or broken structures. The final system was implemented so that the camera captured a high resolution image containing

two structures at a time, which were readily detected and further processed for angle extraction.

3.6.5 Image Processing using Pattern Recognition

One of the important elements related to the measurement was the ability to identify both working and missing structures so that undesirable data could be reliably eliminated. As the Ni process qualification wafer used had many over etched and broken structures, this wafer was used to develop the image processing algorithm. The conventional edge detection algorithm detected both the intact and broken structures, which posed a challenge to differentiate between the two. In contrast to many edge detection algorithms, the system uses the Hough Edge / Rake Detection scheme [148] and traces along the pointer and extension arm within a set region of interest looking for discontinuities or breakages/missing elements. Figure 3.24 shows example of a number of different faulty/broken structures with the (red) box correctly identifying the centre of the pointer arm. However, having done this the software was able to identify these as non

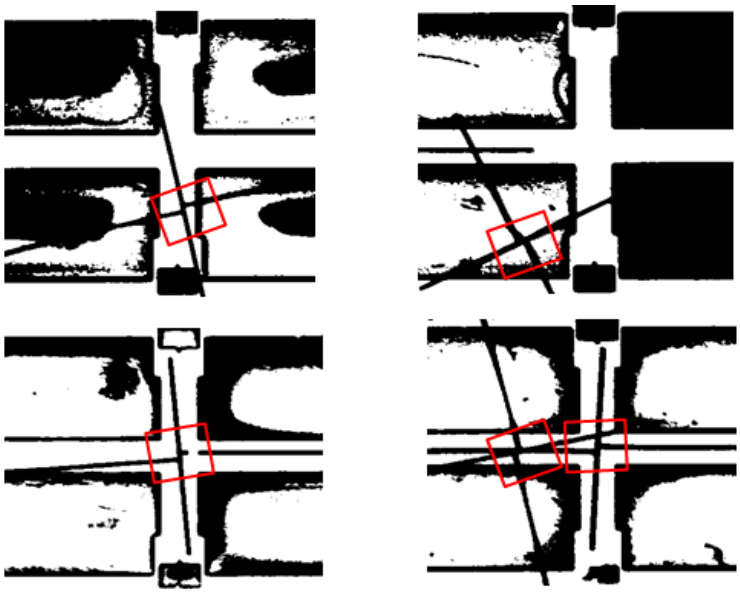

Figure 3.24: Broken structures detected by pattern recognition but neglected in edge detection

functioning structures by following the edge of each structure and analysing the

trace looking for any unexpected corners. Figure 3.25 shows an example of a structure where the pointer arm is missing.

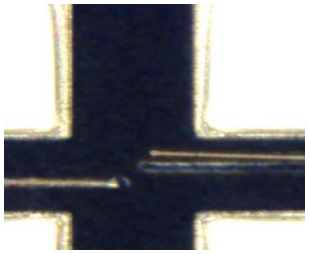

Figure 3.25: Missing pointer arm after overetching during Cu seed removal

The edge detection routine used in the system was able to distinguish between functional and broken structures and hence eliminate false results.

The acceptable test structure image is now passed onto the angle extraction algorithm which identifies the edges of the pointer arm and the surrounding sidewall. The software is able to identify the central portion of the pointer arm and from this reference coordinate performs 65 horizontal scans along the width of the image. An example of the scan area and the resulting edge detection of the Ni pointer arm and its sidewalls is shown in Figure 3.26. Four edges are identified,

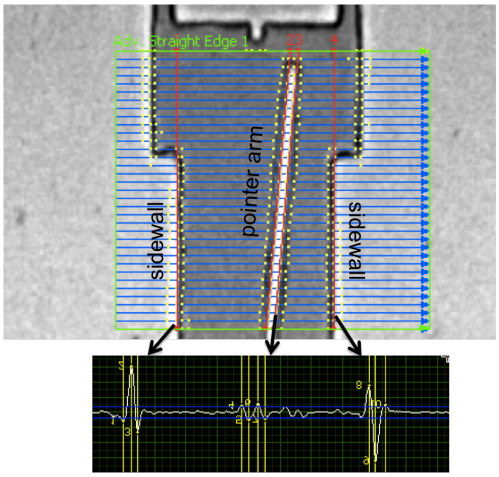

Figure 3.26: Actual Labview output of pointer arm and sidewalls edge recognition using Hough Edge Rake detection algorithm

two sidewalls and two edges (sides) of the pointer arm. The lines of best fit were applied to these edges and the slope relative to the sidewalls used to calculate the

angle of the pointer arm (Figure 3.27). The intensity of the edges (also shown in

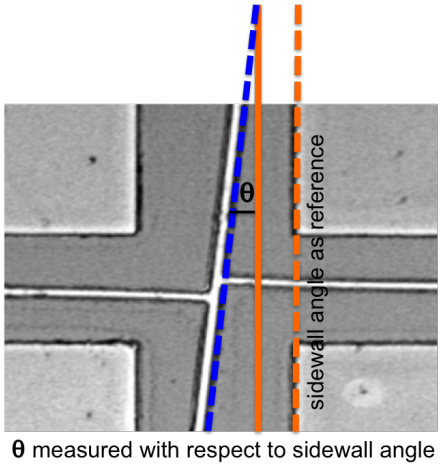

Figure 3.27: Pointer image with Hough / Rake edge detection transform applied to identify straight edges with coloured lines representing the angle extraction from the sidewall and pointer arm

the figure) can be modified to make the edge extraction more sensitive depending on the material texture.

3.6.6 Angle Extraction

The resulting automated high speed optical measurement system is capable of extracting angles of over 12,000 microrotating test sensors on a 200 mm wafer in less than 30 minutes. This makes it ∼600 times faster than a laborious manual measurement procedure.

The power of the measurement system described in this chapter is that it moves MEMS based stress characterisation devices from interesting structures that provide limited quantitative information on to another plane. It translates them into a tool that can not only provide quantitative information but also increases the volume of data that can be routinely extracted to provide stress wafer maps at densities which have not been previously available. An additional appeal of the system is that it is completely non-contact and simply relies on an optical image which has the attraction that no area is required for probe pads.

3.6.7 Statistical Analysis of Strain Measurements

For this test Ni wafer, two complete sets of structures on a chip were measured, one in the centre of the wafer and one near the edge. The corresponding results are presented in Figure 3.28, where each data point represents the average rotation for the set of structures with a given value of ΔY/W and the error bars indicate the standard deviation. Statistical tests were performed to confirm, with a 95% confidence, that there was a significant difference between the two sets with greater rotation in the centre of the wafer. These results could occur if difference

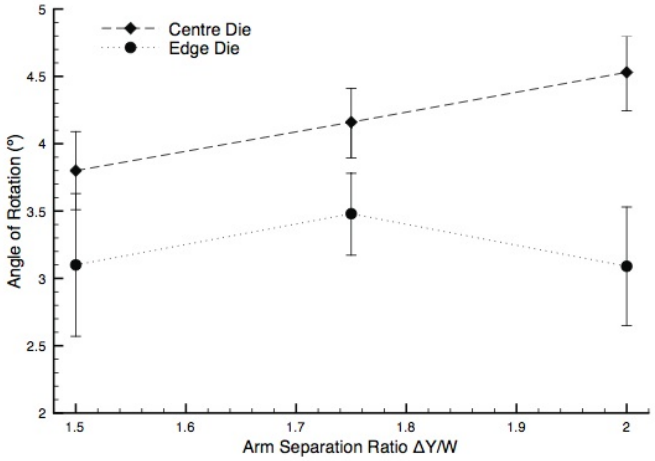

Figure 3.28: Pointer rotation plotted against ΔY/W for nickel test structures

in the geometry of the test structures, particularly in terms of the expansion arm width exist. To be able to determine whether this was the case, the test dice also includes a set of eighteen cross-bridge electrical linewidth test structures, as shown in Figure 3.11. To investigate any dimensional differences between the structures, one set at the centre and one at the edge of the wafer was measured and the results are presented in Table 3.1. The difference between the mean values

Table 3.1: Electrical linewidth results for Ni test structures

Position	**Mean Linewidth (μm)**	**σ (Linewidth) μm**
Center	5.31	0.12
Edge	4.86	0.22

of linewidth at the centre and edge was around 2%, with wider structures in the centre. If the stress structures show similar dimensional bias then it would be expected that the rotation of the pointer arms, for a given value of stress in the film, should be reduced for the wider expansion arms. In addition, and referring back to Figure 3.5, simulations suggest that the observed change in linewidth would lead to a change in rotation of less than 0.1°. This result suggests there is a difference in the level of stress in ECD nickel between the centre and the edge of the wafer.

Figure 3.29 shows the complete spatial rotation map of the nickel stress structures

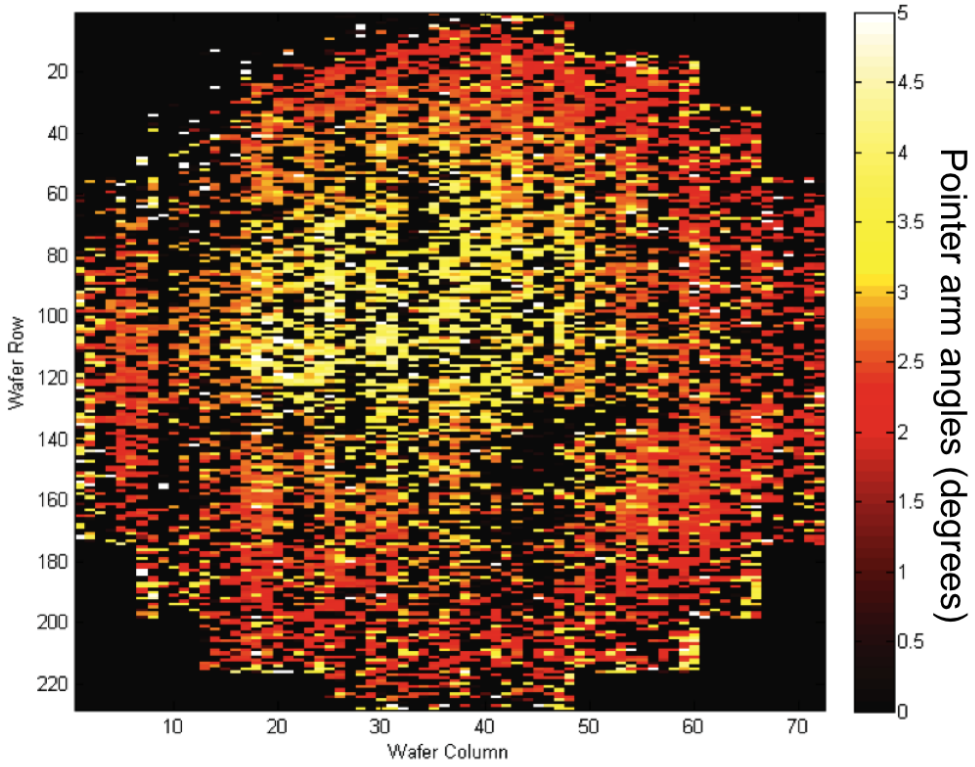

Figure 3.29: Wafer map of rotation for the 5μm electroplated Nickel film

extracted from the automated pointer rotation measurement system described in the previous section. Where the structures were damaged and could not be measured, a value of 0 is used which shows up as black. There is a clear pattern to the data with greater rotations near to the centre but the variability is quite large and there are also structures with large rotations around the edge. The poor

yield also leads to many empty spaces in the map which can make it difficult to interpret the pattern. The problems with yield was mainly caused by the wet etch process used to remove the copper seed layer before release as this also tends to attack nickel and this was not optimised at that time (etched with 20 g/l ammonium persulfate only - section 3.4.1).

By taking an average value of rotation for each die it was possible to reduce the granularity of the wafer map and get a more useful picture of the variation. This large scale map is presented in Figure 3.30. The average rotation was greater in

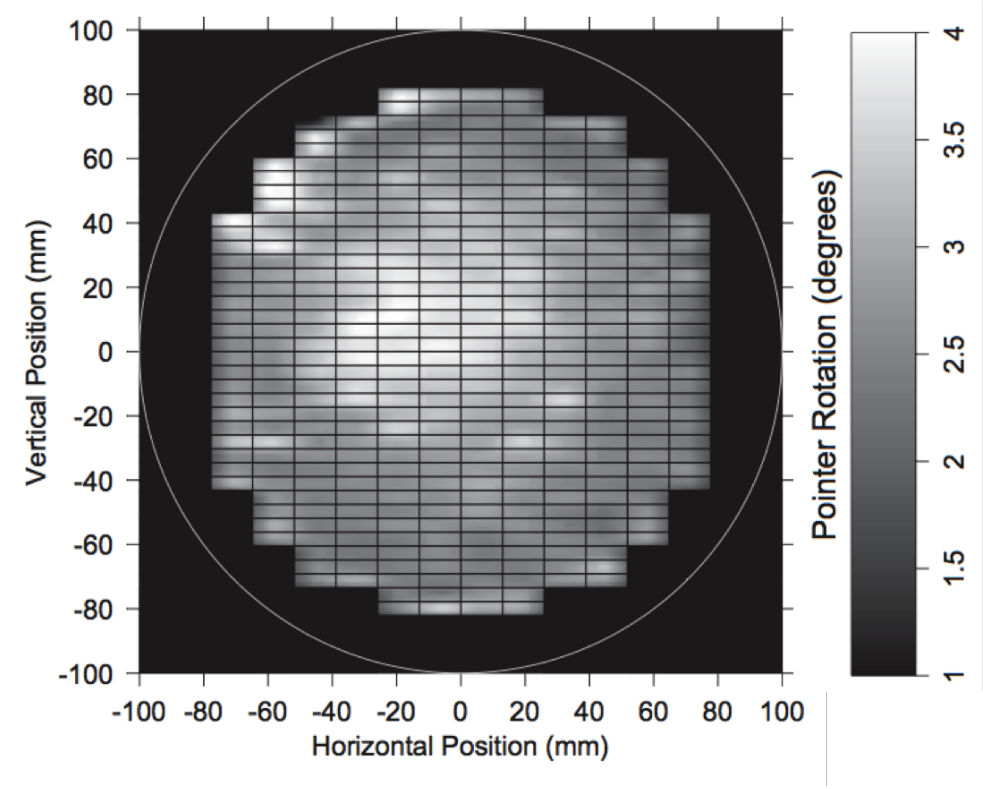

Figure 3.30: Wafer map of the average rotation for each die on the 200 mm wafer

the centre of the wafer at around 3.5 ° while it was closer to 2.5 ° at the edge. The large rotations near the edge in the upper left quadrant of the wafer were a result of measuring one or two structures in each die which show very large rotations. The automated measurement was able to determine if a structure was broken and it is clear from Figure 3.29 that the yield is particularly low in this area.

Figure 3.30 shows the average for all the structures in each die, but as was

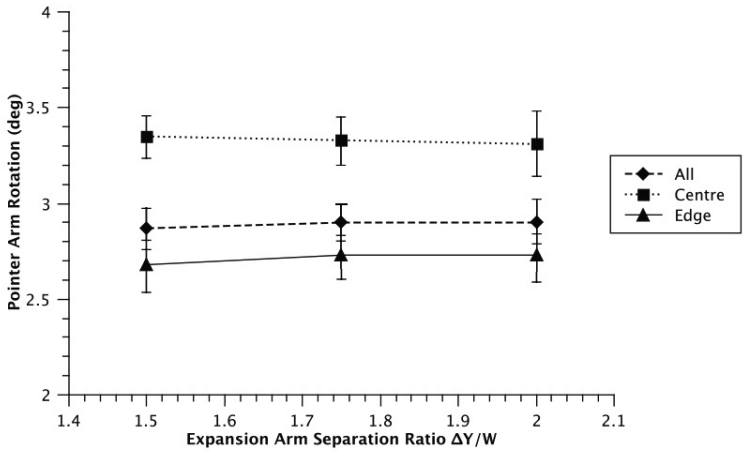

Figure 3.31: Average pointer arm rotations plotted against expansion arm separation ratio of standard (non-notched) structures

mentioned previously there were a number of different structures with a range of expansion arm separation ratios. The average rotation for each value of ΔY/W has been calculated for each die and is plotted in Figure 3.31. In addition, the averages for a block of 6 $\times$ 18 dice in the centre of the wafer and the remaining structures around the edge have also been calculated and are plotted on the same graph. Each point represents the mean value while the error bars show the standard deviation (2 σ) with 95% confidence. The total number of structures that were measured to produce each mean value varies due to the yield issues mentioned previously but there are generally a few hundred results associated with each point. Although the standard deviations are quite large the differences between the structures near the centre and those around the edge have been shown to be statistically significant. Interestingly there is no obvious trend in rotation with ΔY/W, unlike the initial FEA results. Either this is very small and is being masked by the variation across the wafer or there is no dependence on ΔY/W , which suggests the structures were operating around the peak of the curve in Figure 3.3. Figure 3.31 shows the results for the standard test structures while Figure 3.32 presents the results for the structures where the expansion arms narrow to 5 µm where they meet the pointer arm. These rotation results show very

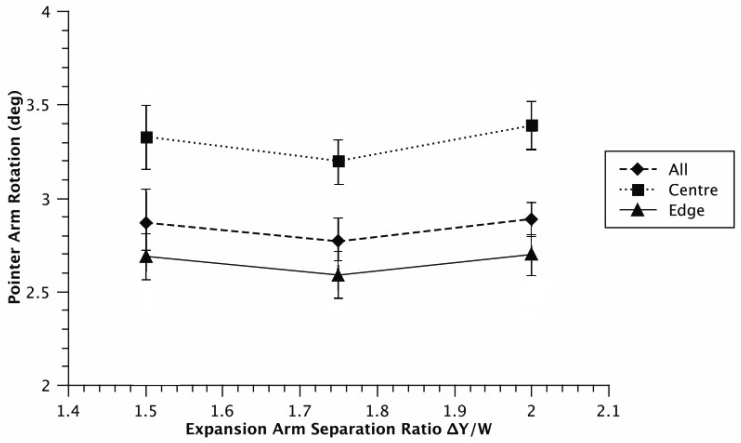

Figure 3.32: Average pointer arm rotations plotted against expansion arm separation ratio for narrowed structures with 95% confidence

similar, statistically significant, differences between the centre and the edge of the wafer and similar variabilities in the rotation for each value of ΔY/W. There is more variation in rotation with expansion arm separation but this is insignificant in comparison to the overall variability. Within the standard deviation there is also no significant difference in rotation between the standard structures and those with the narrowing of the expansion arms.

Simulations of the strain/stress as a function of a test structure with W = 5, L = 850 can be seen in Figure 3.33. A typical value for Young's modulus of 200 GPa was used to convert the simulated strain into a stress value. Even if the change in rotation between the centre and edge of the wafer is as low as 0.5° that equates to a change in stress of around 20 MPa. Using strain (rotation) values of 2.5 ° and 3.5 ° residual tensile stress values were seen to range from 75 - 110 MPa at the edge and center respectively. An approx. 36% change in the spatial variation was observed which has shown to demonstrate the importance of wafer mapping stress in ECD films. However, these results have assumed the elastic modulus is constant over the entire surface which still needs to be confirmed and further studies have been presented in the following chapters concerning this issue.

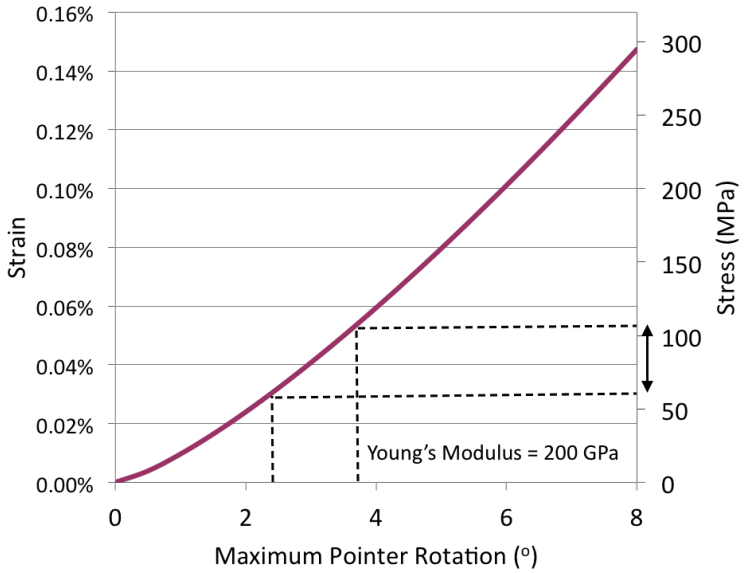

Figure 3.33: Simulated stress and strain figures plotted against maximum pointer rotation angle for the Ni structures with W = 5 µm and L=850µm and Young's modulus assumed to be 200 GPa

3.7 Conclusions

Mechanical pointer arm test structures have been used to develop a complete spatial strain/stress measurement system for 200 mm wafers. The optimum dimensions for device sensitivity, were chosen based on a FEA [149]. A full mask design (comprising 12,228 pointer arm strain test structures) and fabrication procedure with ECD films has been demonstrated with the addition of a novel selective copper seed layer etching technique. With over 12,000 structures the need for an automated arm rotation measurement system is self-evident. This was developed in-house and is capable of extracting rotation data and plotting a complete strain map in less than 30 minutes. This technique made it feasible to comprehensively wafer map the stress over many wafers when developing new processes, which is a significant advance over the manual extraction of the rotation angle which is both error-prone and laborious.

The capability of the resulting system has been demonstrated by measuring the pointer arm rotation fabricated from 5μm thick electroplated metallic Ni film.

Initially, no obvious rotation were observed after release. However, after heating the wafers to 150 °C the structures rotated to indicate tensile stress. A full set of structures at the edge and at the centre of the wafer were measured and the results showed a significant difference in rotation. This cannot be accounted for by differences in the widths of the expansion arms in these structures and so the results indicate a difference in stress with position. Wafer map was obtained which showed $37\% \pm 5\%$ more stress in the center of the wafer, therefore, demonstrating the potential of the system to extract spatial variation in 200 mm wafers.

This technique has successfully made use of MEMS tests structures to spatially characterise strain assuming a constant Young's modulus. The spatial variation of strain observed in the ECD film could suggest variations in the structural properties of the plated film, and this would also effect the Young's modulus. Therefore, spatially mapping Young's modulus with strain would be required to create stress maps (demonstrated in Chapter 5). Moreover, as mentioned before, the Ni bath used to fabricate the structures for developing the measurement system was non-optimised. To plate NiFe (preferentially permalloy) with low stress for microinductor cores, optimum bath composition and conditions must be employed and this procedure has been discussed in chapter 4 using the same test structure chip employed in the above system developments.

Chapter 4

Chip Level Metal Electrochemical Studies of NiFe

4.1 Introduction

The as-deposit properties of ECD NiFe films such as alloy composition, film thickness, magnetic properties and intrinsic stress [150] are widely known to be dependent on plating variables such as, plating current density, bath temperature, pH and chemical concentrations [151, 152, 153]. However, the interdependence of these properties, particularly towards the evolution of stress in NiFe, is not fully understood, and needs further clarification.

The mechanism of NiFe electrodeposition, is notorious for its ambiguous characteristics. The less noble metal Fe, compared to Ni, is known to be deposited preferentially and this phenomenon is called the, 'anomalous codepositon' of NiFe [153]. The change in pH near the cathode surface, occurring from the evolving hydrogen, has been postulated to cause this effect [154]. Hydrogen evolution is also known to govern the overall plating efficiency and quality of deposits, but little work has been published towards confirming its effect on film stress.

This chapter investigates the effect of hydrogen evolution on the development of intrinsic stress in Ni and NiFe films using the test structures described previously in chapter 3.

4.2 Fabrication of Strain Test Structure Chip

The effect of bath parameters such as concentrations of ions and additives on stress is problematic to study on 200 mm wafers, as this exercise would require numerous bath changes, with each setup, potentially utilising over 30 L of electrolyte, which would be both expensive and time consuming, not to mention wasteful on chemicals. As an alternative, beaker level electroplating was considered more suitable using smaller substrates consisting of test chips diced from a 200 mm wafer having the same sacrificial layer and seed stacks as described in section 3.4.1 and patterned using the masksets shown in Figure 4.2). The patterning process has been modified, such that the original test structure mask layer 1 is overlayed with an acetate mask layer 2 to expose every other row of test structure chips. These masks are removed and the acetate layer 3 is introduced which exposes small regions for the ECD electrical contact.

Following these two exposures, the wafer is developed in acetone and the underlying titanium layer is etched using 1% HF. This step exposes the underlying copper seed layer to be used for ECD. Finally the wafer is diced which delivers around 190 dies. Each die measures 13 × 17 mm and contains 64 strain test structures and a schematic drawing of the resulting die is shown in Figure 4.2.

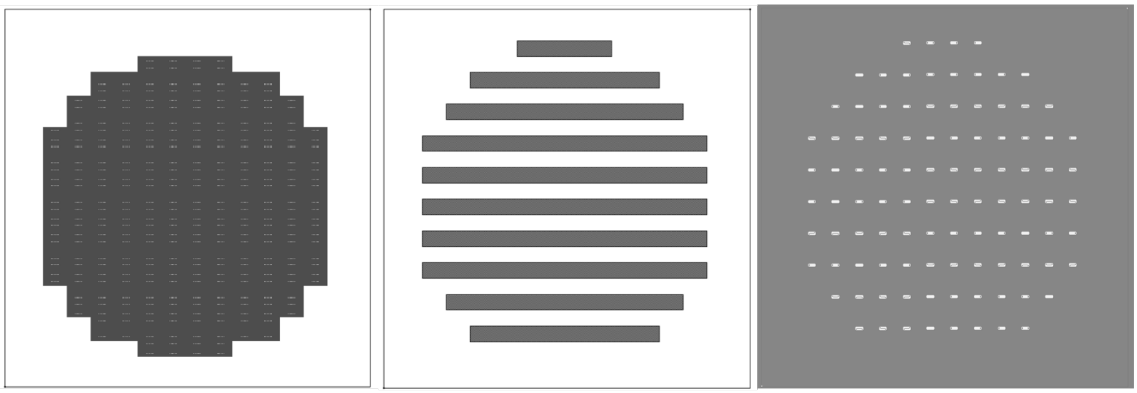

Figure 4.1: 9" masksets used to pattern test structure chips on a 200 mm wafer; the resulting die after singulation is shown in Figure 4.2

The black region represents the copper seed and the grey region represents the photoresist acting as an insulator and mould for the bottom-up plating process.

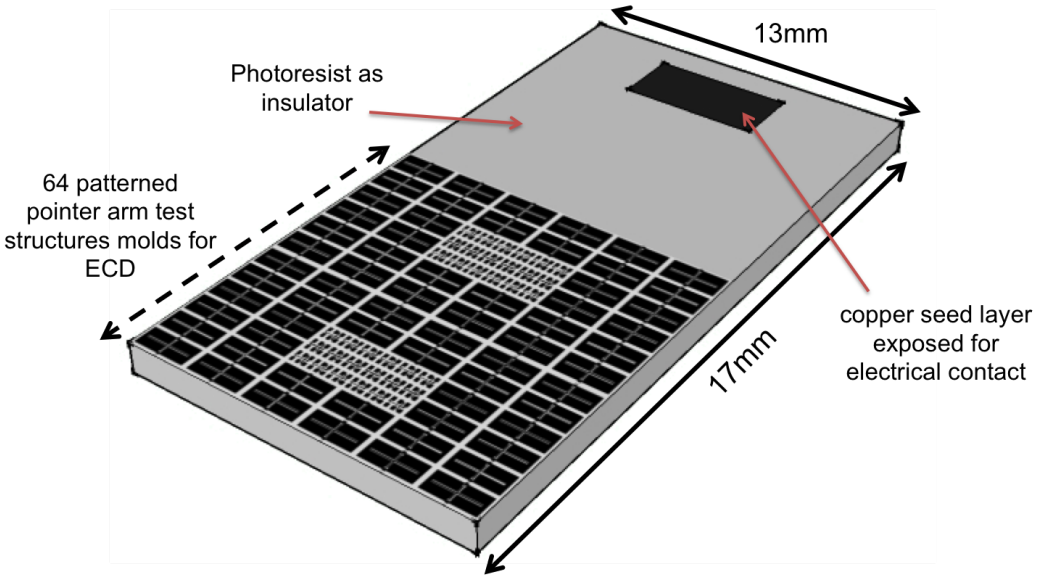

Figure 4.2: Schematic drawing of a diced test structure die with 64 strain sensors and 36 electrical test structures giving a total active area of 0.765 cm^2 (measured from the mask design CAD software)

4.3 Experimental Setup and Procedure

The apparatus and experimental setup used for the beaker level ECD of Ni/NiFe is shown in Figure 4.3. The plating system consists of a computer controlled potentiostat/galvanostat (Metrohm Autolab PGSTAT302), pH meter (Mettler Toledo), digital thermometer and a three electrode system with SCE[1] as the reference electrode (RE), a pure nickel pellet with surface area $\approx$ 3 cm^2 as the counter electrode (CE - Anode) and the test structure chip (Figure 4.2) as the working electrode (WE - Cathode). Theory of the 3 electrode system analytical technique can be found in Appendix A.1.

A nickel anode was used instead of inert platinum to maintain consistency with

1. SCE = Saturated Calomel Electrode with cell notation $Cl^{-}(sat'd)|Hg_2Cl_2(s)|Hg(l)|Pt$ where $E^0_{SCE}|E^0_{SHE} = +0.244V$

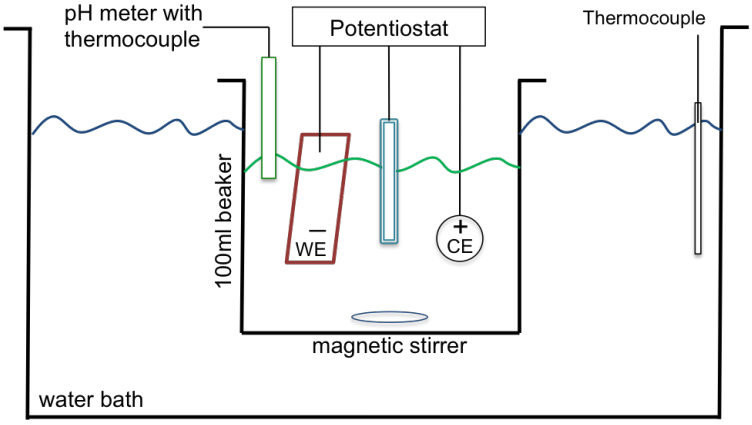

(a)

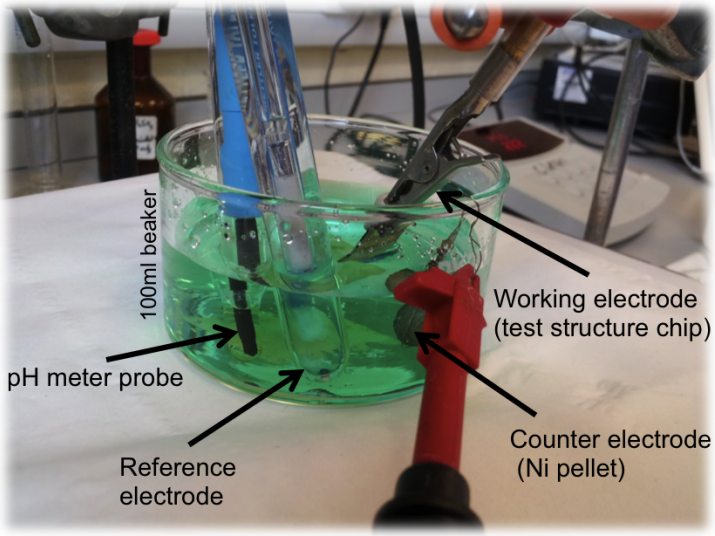

(b)

Figure 4.3: (a) Schematic drawing of the 100 ml beaker level bath setup for fundamental ECD study (b) photograph of the actual laboratory setup (water bath not shown)

industrial wafer plating procedures. This setup was kept identical for each experiment, with the spacing between the CE and WE set at 2.5 cm. The electrochemical cell was a 200 ml beaker filled with 100 ml of electrolyte under investigation. The temperature was controlled using a water bath and agitation induced using a magnetic stirrer, with a magnetic flea inserted in the solution. Adequate stirring

was performed at a medium rate (position 3 from a scale of 1 to 5) and was kept consistent for all experiments. Unless otherwise stated, each solution was purged, to remove dissolved air, by bubbling Ar gas for 20 minutes. For most tests the current density applied ranged between 5 and 40 $mAcm^{-2}$, the temperature was 25 °C and pH of the electrolyte was between 2.4 and 2.6. As the pH tends to increase after ECD due to hydrogen evolution at the cathode surface, this was adjusted by adding 1% HCl solution.

The following baths were investigated in this study:

1. $NiCl_2$
2. $NiCl_2$-boric acid
3. $NiCl_2$-$FeCl_2$-boric acid
4. $NiCl_2$-$FeCl_2$-boric acid-saccharin

These baths were prepared using commercially available semiconductor grade $NiCl_2$ and $FeCl_2$ solution (Dow Chemicals^{TM}), analytical grade boric acid (Sigma-Aldrich^{TM}), sodium saccahrin (Sigma-Aldrich^{TM}) and deionised (DI) water of 18 MΩcm resistivity. A fresh bath was used for each experiment's batch of chips and the plated sample rinsed with deionised water and dried using nitrogen gun, before any further analysis.

The plating current efficiency of each sample is obtained from the mass gained after ECD (described in Appendix A.2.1.8). Following this measurement, the photoresist is stripped, seed layers are etched and the test structures released as described in section 3.4.1. The pointer arm rotations were measured using the image analysis algorithm described in section 3.6). Strain comparison between plated samples has been undertaken in this study by only analysing structures with separation ratio $\Delta Y/W = 1.75$. Magnetic hysteresis of some plated films were also obtained using BHL described in Appendix A.2.5.

4.4 Effects of Plating Conditions and Additives

4.4.1 Effect of pure nickel concentration on plating

A number of ECDs were performed at room temperature with the aim of investigating the effect of nickel(II) concentrations on both plating efficiency and the resulting film strain. For this evaluation the bath was kept free from additives and surfactants.

Three sets of test structure chips were plated galvanostatically in fresh $NiCl_2$ solutions (0.1 M, 0.4 M and 1.0 M) using a range of current densities (5, 7, 10, 20, 40 $mAcm^{-2}$). The time required to achieve a target plating thickness of 5µm (assuming 100% efficiency) for each of these plating current densities were calculated using Equation A.15 in Appendix A and these are shown in Figure 4.4.

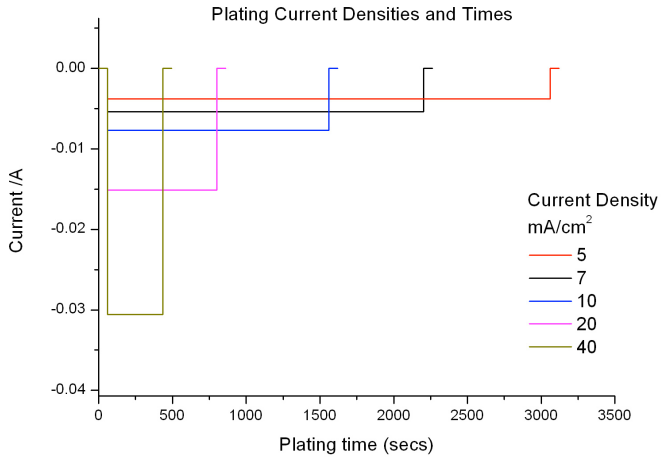

Figure 4.4: Plot shows the time required to electroplate 5µm of Ni at different current densities

4.4.1.1 Analysis of cathodic potential

Figure 4.5 shows potential versus time plots of the first batch of samples plated in 0.1 M nickel(II). At lower plating current densities (5, 7 and 10 $mAcm^{-2}$)

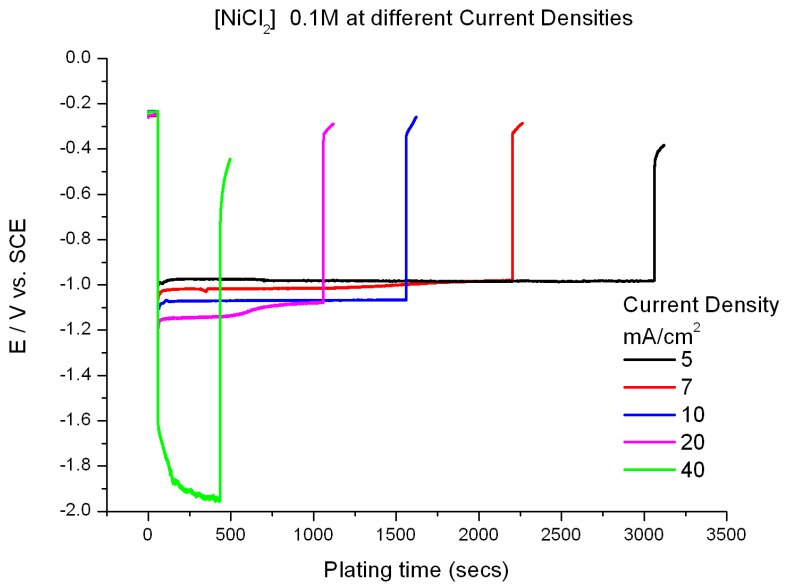

Figure 4.5: Potential vs. time plots of samples plated in 0.1 M $NiCl_2$(aq) using various current densities

there is a slight drift in potential at the start of plating, which is expected during the transition of Cu (seed layer) to Ni. A steady state potential is reached when depositing Ni on Ni. The plating potentials were also observed to change linearly for each current density 5, 7, 10 and 20 $mAcm^{-2}$. However, at 40 $mAcm^{-2}$ a major potential drop is recorded, which is significantly different to the other samples. This potential drop can be regarded as the domination of hydrogen evolution reaction at high currents ($H_2O + e^- \rightarrow 1/2\ H_2 + OH^-$) over nickel deposition which has also been reported by Song [155] . Hydrogen bubbles were also visually observed on all plated samples. An example chip being plated is shown in Figure 4.6 for which bubbles adhered to the surface and gradually increased in diameter during the course of plating. At 40 $mAcm^{-2}$, bubbles evolved most vigorously, and compared to previous samples, did not adhere to the surface. The consequent deposit consisted of a green/white powder, which got removed after rinsing in DI

water. Test structures were deformed on this particular sample which was not measured further.

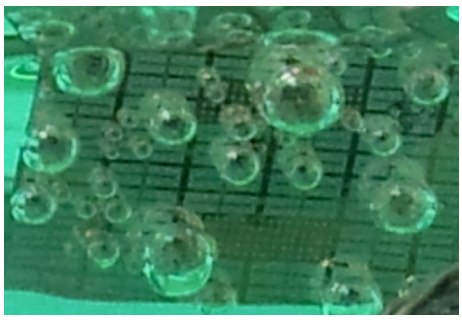

Figure 4.6: Image of a test structure chip being plated (at 10mAcm^{-2}) showing hydrogen bubbles evolving during deposition

Figure 4.7 shows potential versus time plots of samples plated in 0.4 M Ni(II). The plating potential at 5 mAcm^{-2} current density is observed to be steady, while

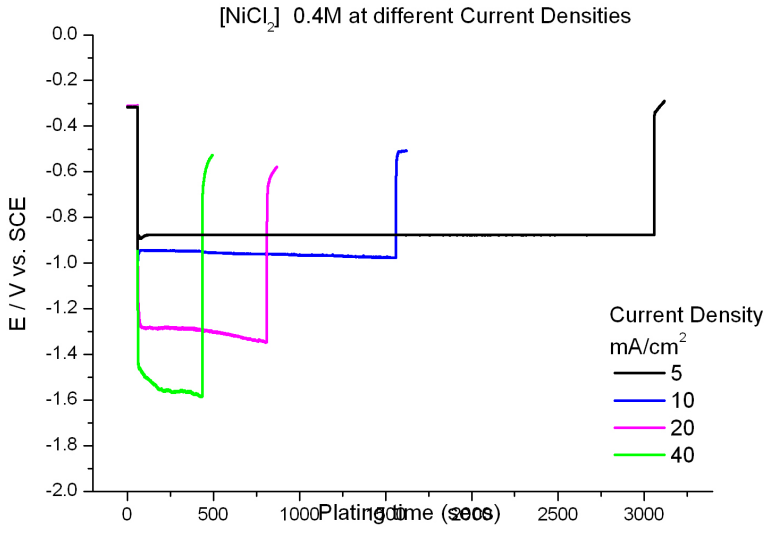

Figure 4.7: Potential vs. time plots of chip samples plated in 0.4 M $NiCl_2$(aq) using various current densities

at 10 mAcm^{-2} it decreased slightly through the duration of plating. A potential difference of -0.08 V between the 5 and 10 mAcm^{-2} samples, suggests efficient plating, while a significant drop (greater than -0.35 V) observed for 20 and 40

$mAcm^{-2}$, indicates excessive hydrogen evolution, besides nickel reduction. Compared to the previous bath, 0.1 M Ni(II), the hydrogen evolution contribution is more prominent even at lower current densities. The vigorous hydrogen evolution observed at 20 and 40 $mAcm^{-2}$ also led to the delamination of the photoresist. The deposited film, again, consisted of loosely bound green deposits which were removed upon rinsing in DI water. These two samples were not measured further. Similar results were also observed after increasing the Ni(II) concentration to 1.0 M (Figure 4.8). The difference in plating potential for 5, 7 and 10 $mAcm^{-2}$ were

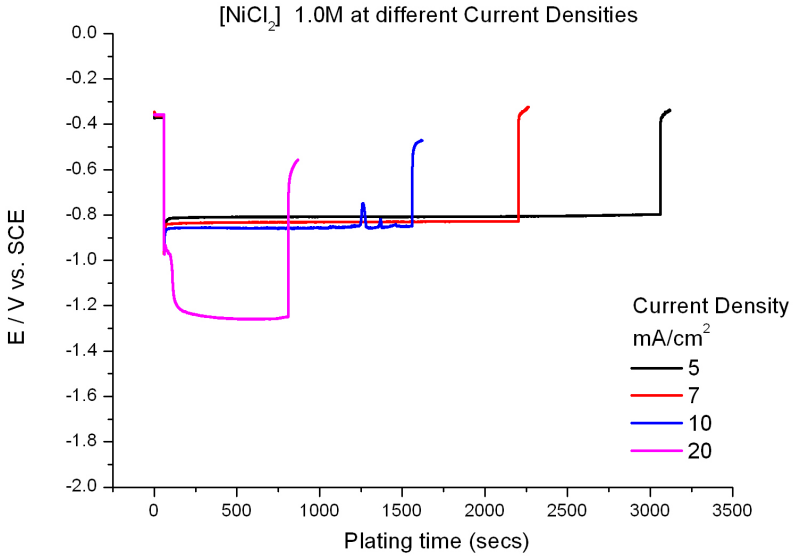

Figure 4.8: Potential vs. time plots of chip samples plated in 1.0 M $NiCl_2$(aq) using various current densities

significantly smaller compared to the drop recorded for 20 $mAcm^{-2}$. With the inability to deposit Ni efficiency, this sample was discarded for further measurements.

Potential plots of the three baths at 10 $mAcm^{-2}$ have been compiled in Figure 4.9. The initial OCPs were observed to become more negative, however, these are hard to predict using Nernst equation as the electrode would required to be made of the same metal (Ni) as the ions (Ni^{2+}) in the solution. Moreover, the possible reactions together with their potential expressions at 25∘C listed below can be

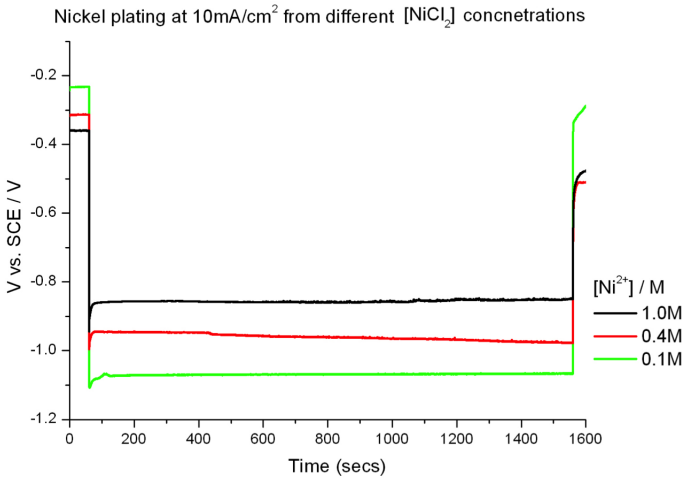

Figure 4.9: Potential vs. time plots of samples plated at 10 $mAcm^{-2}$ in various $[NiCl_2]$ baths

used to compare the final OCPs, post deposition, in which case the electrode is transformed to nickel. For easy comparison these potentials have been expressed versus SCE [2] [156].

$Ni^{2+} + 2e^- = Ni$

$$E_{Ni^{2+}/Ni} = -0.498 + \frac{0.059}{2} log[Ni^{2+}] \tag{4.1}$$

this would equate to - 0.57 V at 0.1M, -0.52 V at 0.4 M and -0.50 V at 1 M of Ni^{2+}.

The second possibility could be: $Ni(OH)_2 + 2H^+ + 2e^- = Ni + 2H_2O$

$$E_{Ni(OH)_2/Ni} = -0.125 + \frac{0.059}{2} log[H^+]^2 \tag{4.2}$$

this equates to -0.125 + 0.059(-pH) = -0.28 V at pH = 2.6.

The third possibility could be: $H^+ + e^- = 0.5H_2$

$$E_{H^+/H^2} = -0.241 + \frac{0.059}{1} log[H^+] \tag{4.3}$$

this equates to -0.241 + 0.059(-pH) = -0.40 V at pH = 2.6

2. The difference between SCE and H_2 electrode potentials is 0.241 volt at 25°C

Looking at these values of electrode potentials at pH = 2.6 (post plating) and for the concentrations of Ni(II), it can be seen that only the 0.4 M and 1 M Ni(II) potentials are close to the calculated $E_{Ni^{2+}/Ni}$, but the 0.1 M solution's potential was surprisingly approaching $E_{Ni(OH)_2/Ni}$. This could indicate the presence of $Ni(OH)_2$ in the film or variations in the surface morphologies such as roughness, polycrystalline lattice configurations and voids could contribute to the final OCPs being so different. Magnified images, focusing on the film texture (Figure 4.10) supports this hypothesis, as it is apparent that the films textures changes with [nickel(II)]. The inclusion of an insoluble nickel compound in the film (such as the green powder observed) may have also contributed to the variation in grain morphology and film appearance. Further analysis is therefore, required to confirm these findings.

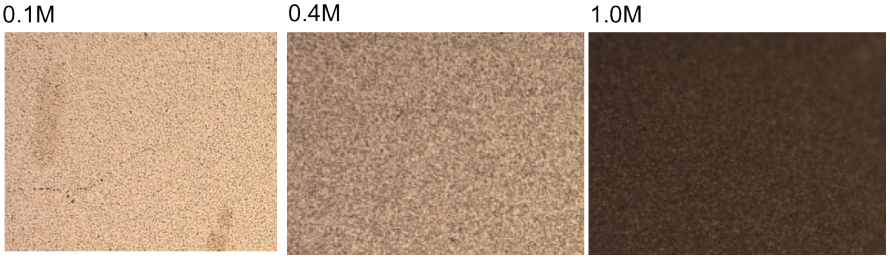

Figure 4.10: Magnified microscope images showing the texture of samples plated at 10 mA/cm^2 from pure $NiCl_2$ solutions with concentration 0.1 M, 0.4 M and 1.0 M respectively.

4.4.1.2 Plating Efficiency

Each chip was weighed before and after plating and the plating efficiency was calculated. Figure 4.11 shows the plating efficiency plotted against the plating current density. An interesting observation is that the efficiency can be seen to increase with plating current density until it falls sharply to <40% for all three nickel baths. A peak value of (85 ± 8)% between 10 and 20 $mAcm^{-2}$ is also observed. Overall, the efficiency trend is seen to drop with increasing nickel concentration. Correlating this with the potential plots analysed earlier, and the

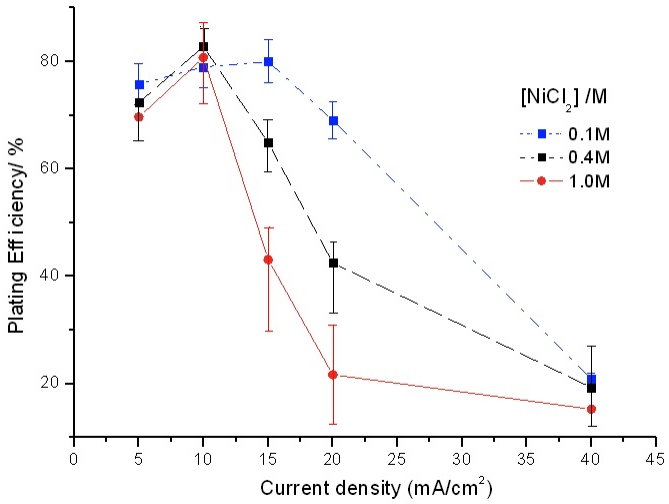

Figure 4.11: Plating efficiency of nickel from baths composed of different $NiCl_2$ 0.1 M, 0.4 M and 1.0 M at pH of 2.6

visible bubbles during ECD it was evident that hydrogen evolution was the root cause. To further investigate, an SEM image of a structure plated in the 0.4 M Ni(II) bath at 10 $mAcm^{-2}$ is shown in Figure 4.12. This image shows part of a test structure, where a hydrogen bubble was seen trapped. A clear circular depression is visible with little or no nickel deposited. This suggests that the presence of a stationary hydrogen bubble on the surface inhibits nickel deposition and also lowers the overall plating efficiency of the bath.

4.4.1.3 Pointer arm rotation (strain) measurements

Microscope images of the Ni test structures are shown in Figures 4.13, 4.14 and 4.15 for the three baths under investigation. As mentioned earlier, successful plating could only be achieved at current densities less than 20 $mAcm^{-2}$. At higher currents the influence of hydrogen evolution was more profound during the plating process leaving the test structures damaged. Therefore, these samples were not included in the release process. After release, pointer arm rotation (strain) values were extracted from structures with arm separation ratios of 1.75, and these have been collated in Figure 4.16. A clockwise rotation, indicating tensile stress was

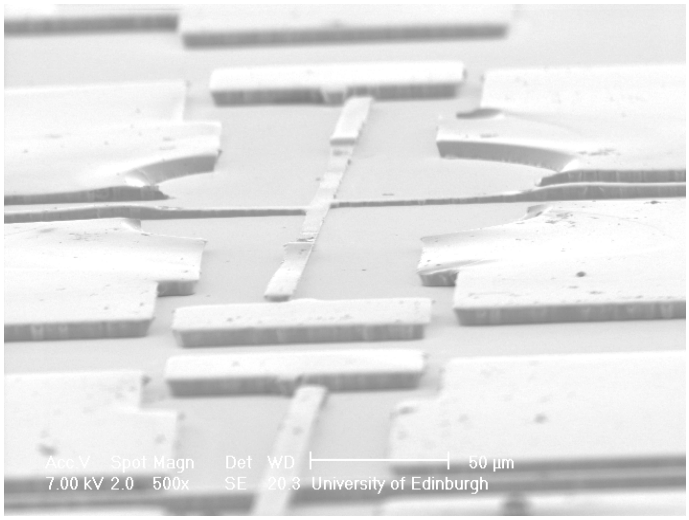

Figure 4.12: SEM image of the region of the test structure (after stripping photoresist) where a hydrogen bubble was seen trapped

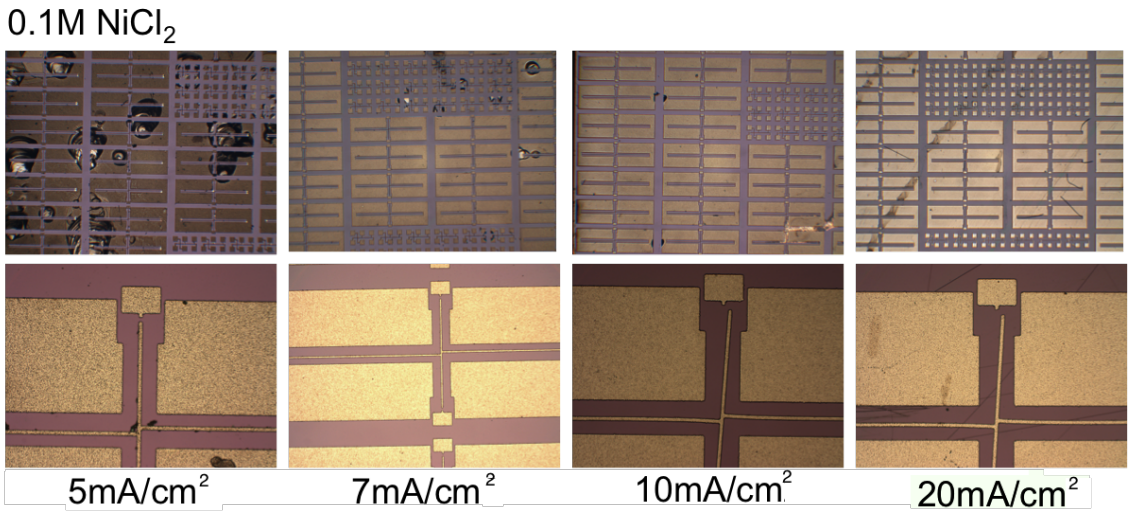

Figure 4.13: Microscope images of the dies with released test structures plated in 0.1 M $NiCl_2$ at various current densities (columns) and rows shows the same chip but at different magnifications ($\times 2$ and $\times 10$)

observed from all samples. The highest rotation of $\sim 6°$ was measured for the 1.0 M Ni(II) bath at 10 $mAcm^{-2}$, while the lowest rotation of 2.6° was obtained for 5 $mAcm^{-2}$ plated in a 0.1 M Ni(II) solution. On average, rotations increased both with nickel(II)chloride concentration and the plating current density, and this clearly indicates how plating parameters can influence the development of intrinsic stress.

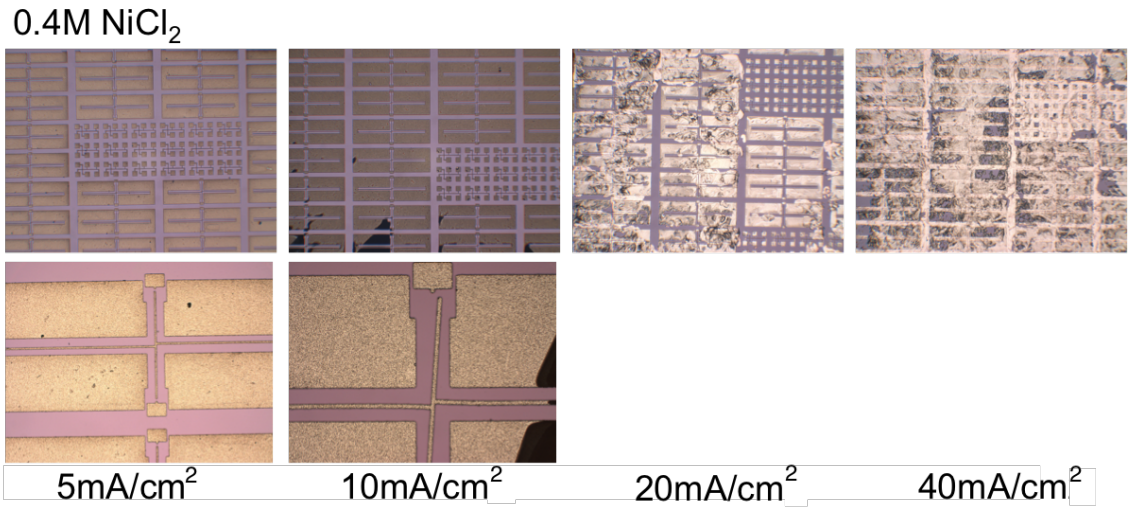

Figure 4.14: Microscope images of the dies with released test structures plated in 0.4M $NiCl_2$ at different current densities

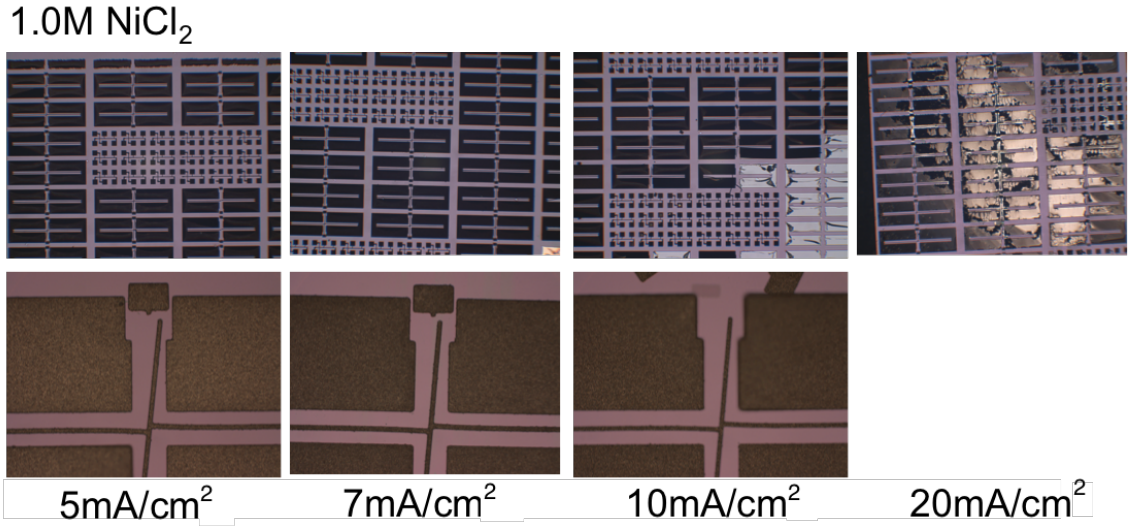

Figure 4.15: Plated samples

The magnetic hysteresis of the chips is presented in Figure 4.17. As the chips were non-continuous (patterned), the hysteresis data can only be used for qualitative comparison between individual samples. Taking this into account it can be noticed from the shape of the curves that the samples do not reach saturation magnetisation when plated at lower current densities, however, this increases in magnitude which is important when considering its use in a microinductor, as higher permeability materials are desirable for this application. Another factor

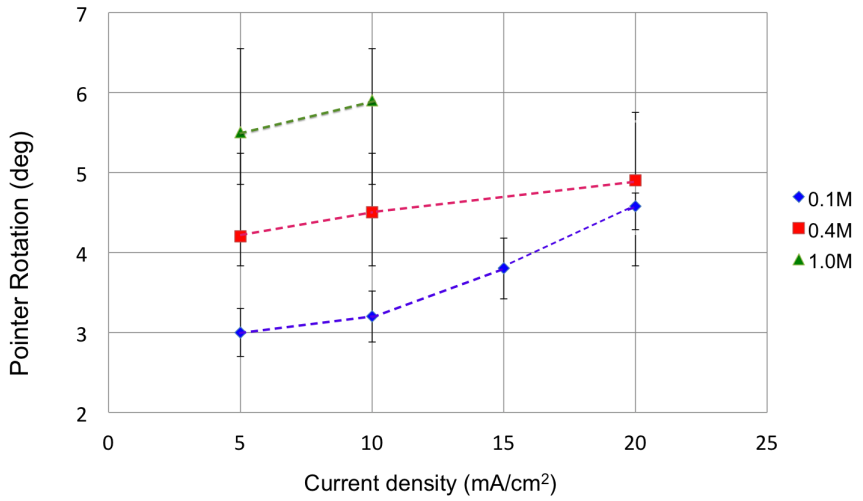

Figure 4.16: Pointer rotation of nickel test structures plated in different nickel(II)chloride compositions 0.1 M, 0.4 M and 1.0 M at pH of 2.6

of primary importance is the total area inside the hysteresis which corresponds to the magnetic energy stored in the core. The higher this area, the more the material would act as a hard magnet and greater the energy is lost due to the changing magnetic energy in the core during the inductor switching cycle. Such materials would not be ideal for high frequency applications. It can be noticed that this area is smallest when plated below 10 $mAcm^{-2}$, whilst the coercivity remained the same for all samples. At these lower current densities it was also observed that, changes in nickel(II) concentration in the bath did not seem to have any significant effect on the hysteresis.

4.4.1.4 Discussion

The effect of nickel concentration in the bath can be postulated to have two effects on the deposition of nickel. Firstly, the activity of the solution is raised, as the number of charge carriers increases. With this increase in activity of nickel ions, the activity of hydrogen ions is affected which alters the level of hydrogen evolution for a given pH. If the hydrogen reduction dominates the overall plating mechanism, the suppression of nickel is expected which results in a lower plating efficiency. Films plated at such low efficiencies may have hydrogen incorporated

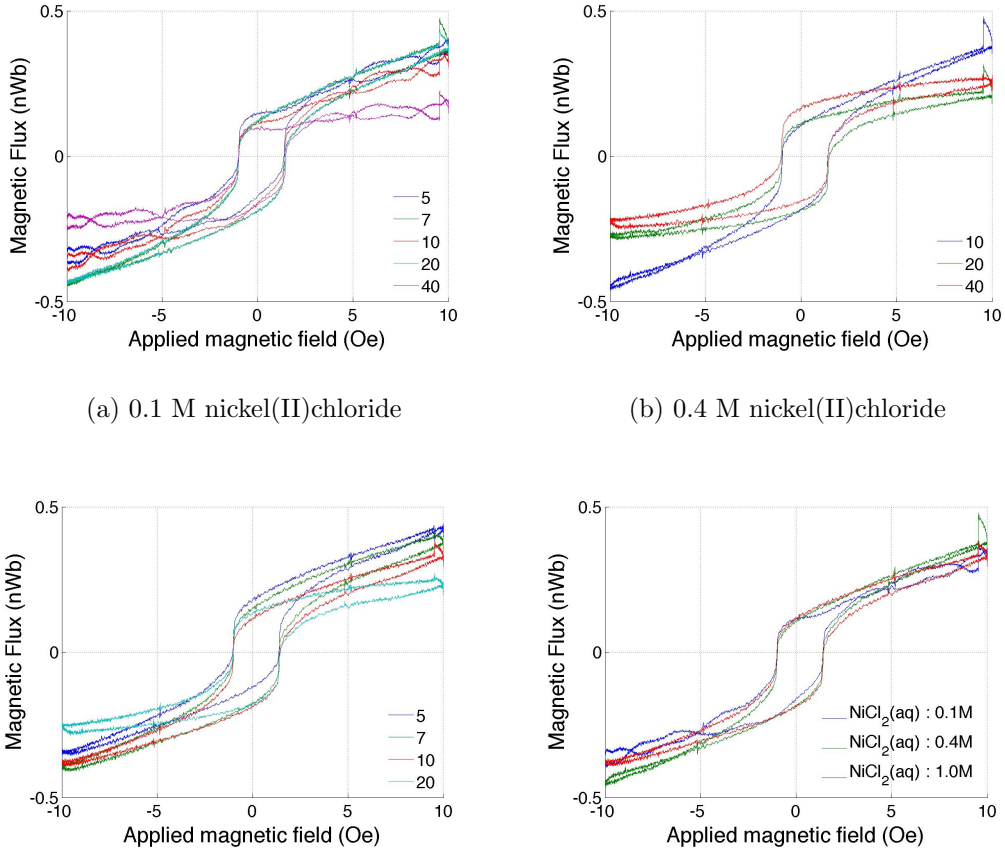

(a) 0.1 M nickel(II)chloride

(b) 0.4 M nickel(II)chloride

(c) 1.0 M nickel(II)chloride

(d) Compiled samples from $NiCl_2$(aq) concentrations plated at 10 mA/cm^2

Figure 4.17: Magnetic hysteresis loops of thin films plated in pure nickel(II)chloride at various current densities

within the film growth and this could leave voids, deformities and a coarse grained finish. Such films would tend to relax by relieving their energies in the form of high tensile stresses. Secondly, the existence of an insoluble powdery deposit found on most of the samples plated at elevated current densities, may also contribute towards deformities in films. In higher nickel baths, Davalos and Jili *et al.* [40, 83] also observed a familiar green deposit which they confirmed was, $Ni(OH)_2$ (s). High pH readings, near the cathode surface were also observed to correlate directly to the hydrogen evolution reaction in their study. Combining this information along with the strain results reported in Figure 4.16, it may be the case that the

insoluble compound could have been absorbed in the deposits producing a film with a defective grain morphology and higher intrinsic stress.

This initial study has highlighted the benefits of using MEMS test structures when characterising intrinsic strain in ECD Ni films plated from an additive free bath. From the results presented, it can be concluded that both low strain film and high efficiency plating precess can be obtained from a pure nickel bath with concentrations between 0.1 M and 0.4 M, plated at current densities ranging between 5 and 20 $mAcm^{-2}$.

The effect of hydrogen evolution has shown to be a prominent factor influencing the plating efficiency and also the resulting structural properties of nickel. However, it should be noted that the inclusion of boric acid has been reported to depreciate hydrogen evolution [40] but its influence of stress is still unknown. Addressing this question has been the motivation behind the work reported in the next section.

4.4.2 Effect of boric acid in pure nickel solution

4.4.2.1 Introduction

The mechanism of Ni^{2+} reduction from an acidic bath is known to occur in several steps, in which two successive Faradic reactions have been suggested. The first is the formation of Ni^{+}_{ads} ion and the second is its following reduction to Ni. However, in the presence of freshly deposited Ni, H^{+} is reduced to H^{ads} which strongly bonds to the the electrode surface which inhibits further reduction of nickel. Hydrogen evolution is caused by the reduction of this H_{ads} [157] [158].
Boric acid has been used in nickel/nickel-iron plating for decades and many researchers have studied its effect with various different views. The general conclusion can be summarized as follows [36]:
(i) Boric acid acts as a pH buffering agent [159][83]. The practical pH range of a buffer is $pK_a \pm 1$, and in the case of aqueous boric acid at 25°C the origin of its acidity has been controversial. Raman spectroscopy of strong alkaline solutions has shown the presence of $B(OH)_4^-$ ions leading to the conclusion that the acidity is exclusively due to the abstraction of OH^- from water [160][161] giving a pK of 9.14. Another source suggests that boric acid is also a tribasic Brϕnsted acid, with successive ionization steps[80]:

$$\begin{aligned} B(OH)_3 &\rightleftharpoons BO(OH)_2^- + H^+ (pK_{a1} = 9.24) \\ BO(OH)_2^- &\rightleftharpoons BO_2(OH)^{2-} + H^+ (pK_{a1} = 12.4) \\ BO_2(OH)^{2-} &\rightleftharpoons BO_3^{3-} + H^+ (pK_{a1} = 13.3) \end{aligned} \tag{4.4}$$

These pK_a values are too high when considering the fact that the bulk pH of a typical nickel bath is < 3.0. Some suggest that a weak complex with nickel exists which acts as a pH buffering reagent [37]. However no concrete existence of any complex could be proved experimentally.
(ii) Boric has also been claimed to act as a catalyst for nickel reduction [38]. It has also been reported that when the boric acid concentration increases the rate

of nickel deposition increases, relative to the rate of hydrogen evolution.

(iii) Horkans *et al.* suggested that boric acid absorbs on the nickel surface during deposition significantly suppressing hydrogen evolution [90]. A contrasting theory, presented by Yin, states that boric acts as a surfactant which prevents the electrode from passivation during nickel deposition [39].

(iv) Abyaneh *et al.* [162] reported that boric acid acts as a buffer and increases both the thickness and the lateral growth of nickel deposits.

(v) In a recent EQCM study by Davalos *et al.* in 2013, it was observed that in the absence of boric acid an insoluble specie $Ni(OH)_2(s)$ (also observed by Yin [158]) was formed due to hydrogen evolution. In the presence of boric acid it was argued that boric acid (or its compound) adsorbs on the nickel and stops H^+ reduction resulting in H_{ads} (the cause of hydrogen evolution) [40].

Clearly the influence of boric acid on nickel deposit is complicated and still remains unclear.

The aim of the following work is to observe the effect of boric acid on nickel deposition efficiency and at the same time monitor the corresponding development of intrinsic strain.

4.4.2.2 Experimental setup

Table 4.1 summaries the bath composition and condition examined in this set of measurements. The first batch of samples were plated with nickel from a bath

Table 4.1: Ni/boric acid bath composition and conditions

Bath contents	**Concentration/M**	**Concentration/(g/l)**
$NiCl_2.6H_2O$	0.4	95.2
Boric Acid (varied)	0.2, 0.4, 0.6, 0.8	12, 24, 37, 49
Current Density (mA/cm^2)	10, 20, 30, 40	
Temperature (°C)	24 ± 1	
pH	2.6 - 2.8 (adjusted with HCl)	

containing 0.4 M nickel(II)chloride and 0.4 M boric acid, at different current

densities (10, 20, 30 and 40 mAcm^{-2}). The second batch was plated at 20 mAcm^{-2} but with varying boric acid concentrations (0 - 0.8 M). The target film thickness for all samples was again 5µm, assuming 100% plating efficiency.

4.4.2.3 Analysis of cathodic potentials

Figure 4.18 presents the potential vs. time plots obtained for the first batch of samples which shows that a steady plating potential was achieved for all four current densities. The highest negative cathodic potential was recorded for the

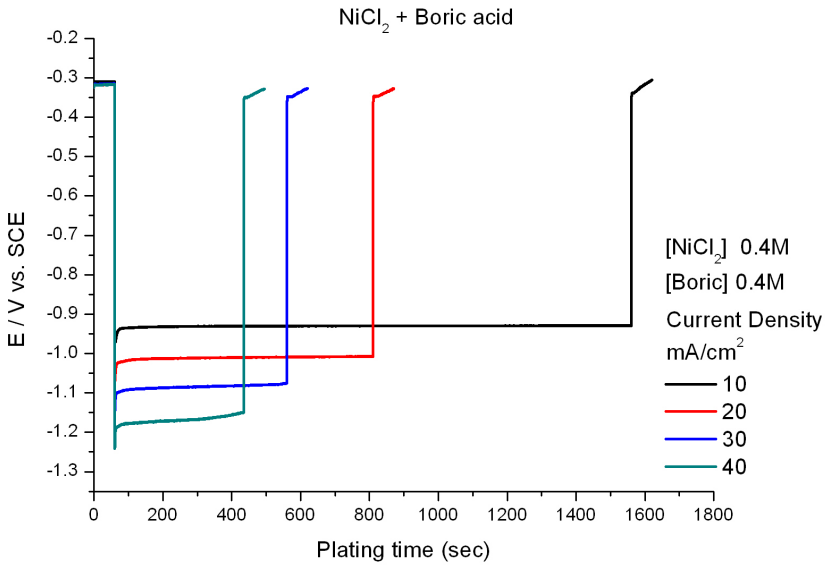

Figure 4.18: Potential - time plots: (a) The effect of current density on Nickel plating from a bath containing nickel(II)chloride 0.4 M and boric acid 0.4 M

sample plated 40 mAcm^{-2} which essentially reached -1.17 V. The initial OCPs were consistent for all plating samples (-0.32 V) for Ni(II) alone and with boric acid. There was a transient observed in the final OCP just after plating and the potential was observed to get more positive with time. However, the trends and values of the final OCP were consistent, unlike the observations in pure Ni(II) (Figure 4.7). There were also far less hydrogen bubbles seen evolving during deposition in the nickel/boric bath. The presence of boric acid clearly shows the ability to plate at higher current densities which could not be achieved in its

absence (pure $NiCl_2$(aq)).

A comparison between the steady-state cathodic potential (E/V vs. SCE) at different plating current densities for pure Ni and Ni-boric baths is presented in Figure 4.19. The potentials at low current densities (5 and 10 $mAcm^{-2}$)

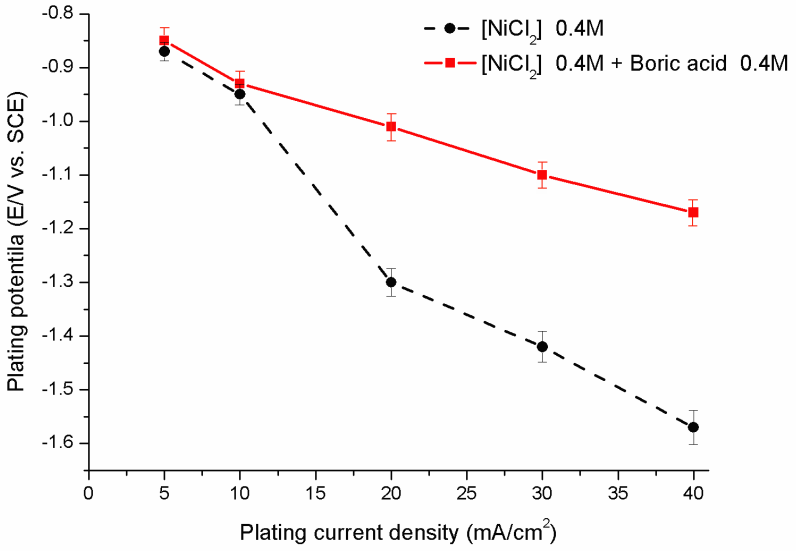

Figure 4.19: A comparison of the steady-state plating potential vs. plating current density of baths containing $NiCl_2$ and $NiCl_2$ (0.4M) + boric (0.4 M)

were similar. While at plating current densities higher than 10 $mAcm^{-2}$, a large potential drop ($\sim$ 0.3V) was observed for the pure Ni(II) bath because of hydrogen evolution. In the presence of boric acid, no such potential drops exists which suggest the suppression of hydrogen formation.

The effect of boric acid concentration on the plating potential is shown in Figure 4.20. The OCP (-0.33 V) and plating potential (-1.1 V) show no significant change between samples. The cathodic potential in the absence of boric acid is $\sim$ 33% more negative which demonstrates that at elevated current densities, boric acid inhibits the hydrogen reduction to enhance Ni deposition. The fact that no potential change in the OCP is observed, with and without boric acid, also suggests the non-existence of any nickel-boric complex in the bath.

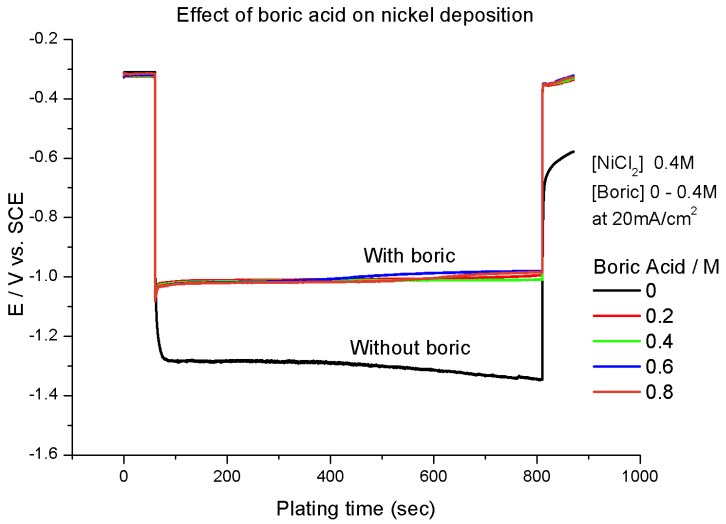

Figure 4.20: Potential-time plots of samples plated in different boric acid concentrations ($[NiCl_2] = 0.4$ M)

4.4.2.4 Correlation of strain and plating efficiency

Photoresist and seed layers were later stripped and the strain test structures released. Optical images of the sample plated at different current densities are shown in Figure 4.21. It can be observed that films have a shinier finish when

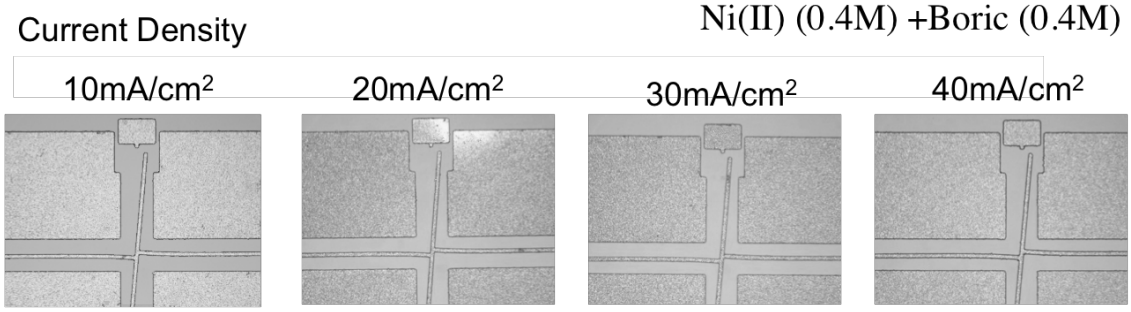

Figure 4.21: Microscope images of Ni test structures plated at different current densities

plating at 10 $mAcm^{-2}$, while higher current densities display a slightly darker finish.

Pointer rotations were extracted from these images and correlated with the plating efficiency as shown in Figure 4.22. A maximum efficiency plateau (92± 3)% for 20-30 $mAcm^{-2}$ is observed, followed by a slight decline (81± 4)% at 40 $mAcm^{-2}$.

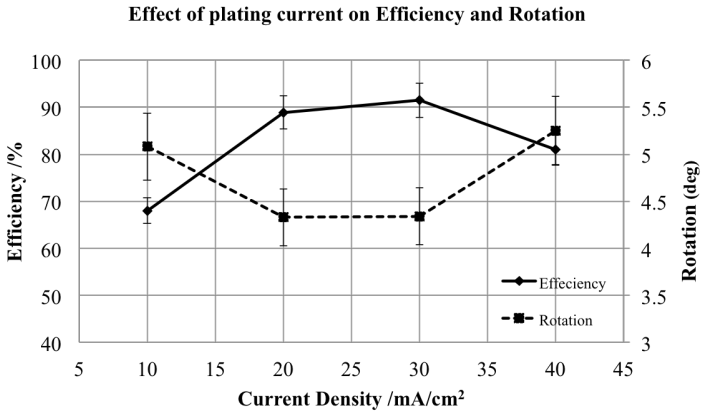

Figure 4.22: Plated efficiency and reciprocal of strain with current density for a solution containing 0.4 M $NiCl_2$ and 0.4 M Boric acid

An inverse correlation is clearly visible between the efficiency and strain with minimum rotations of 4.3° acquired when the plating efficiency was high. These plots suggest that the deposition of nickel is diffusion-limited below 30 $mAcm^{-2}$, which surprisingly could not be obtained from the galvanostatic plots (Figure 4.18). In the absence of boric acid, a large drop in potential corresponded to the evolution of hydrogen which also reflected upon the efficiency data. However, in the presence of boric acid, no such potential drops were recorded at e.g. 40 $mAcm^{-2}$ but the corresponding decrease in plating efficiency may suggest hydrogen being absorbed in the film (instead of evolving and escaping as a bubble). These conclusions are speculative and need further analysis for confirmation.

Next, the effect of changing boric acid concentration on intrinsic strain was investigated using the optical images of the released nickel test structures shown in Figure 4.23. The obvious observation is that the film texture and appearance changed from a darker (grainy) to shinier finish with the increase in boric concentration. Pointer rotations were extracted from these images which been correlated with the change in plating efficiency as shown in Figure 4.24. In the absence of boric acid the plating efficiency is lower than 60% but with concentrations greater than 0.4 M the efficiency seems to stabilise at 90%. An initial observation is that there is inverse correlation between these two quantities could be suggested, which is confirmed by compiling all the data from both

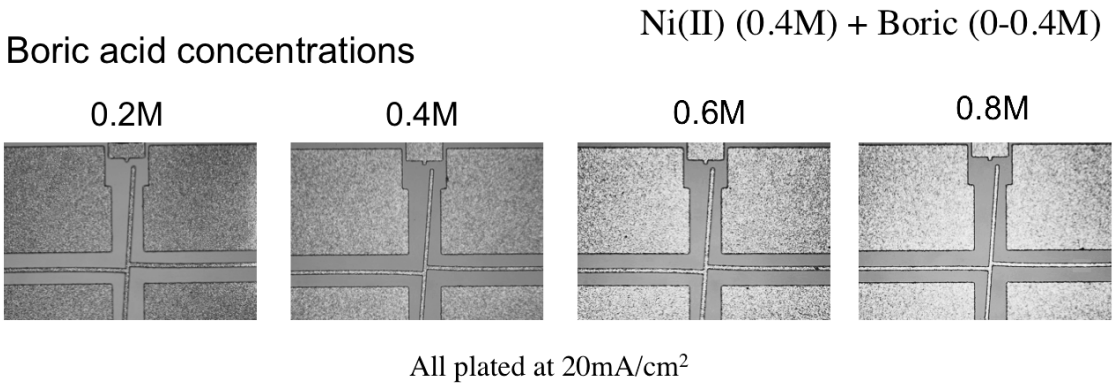

Figure 4.23: Microscope images of Ni test structures plated in different boric acid concentrations

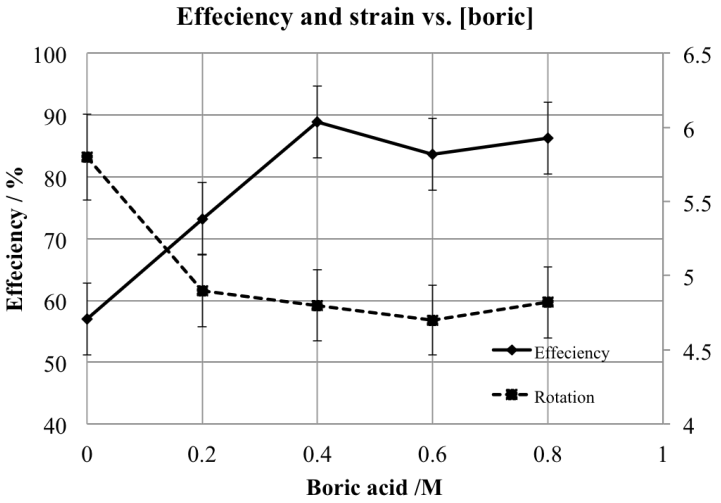

Figure 4.24: Plated efficiency and reciprocal of strain with different boric acid concentrations for a solution containing 0.4M $NiCl_2$ and plating current density of 20 mA/cm^2

batches in Figure 4.25. This dependency of strain with plating efficiency suggests that hydrogen evolved during nickel deposition may be absorbed within the plated film creating defects and changes to the film morphology. Armyanov [163] has also claimed that the desorption of hydrogen codepositon in the nickel film from a Watts bath was responsible for high tensile stress in the film. However, another study by Raub *et al.* confirmed the existence of nickel hydride (NiH) deposits, using X-ray diffraction measurements [164] which appeared after the phase transformation of nickel into unstable nickel hydride, during deposition in

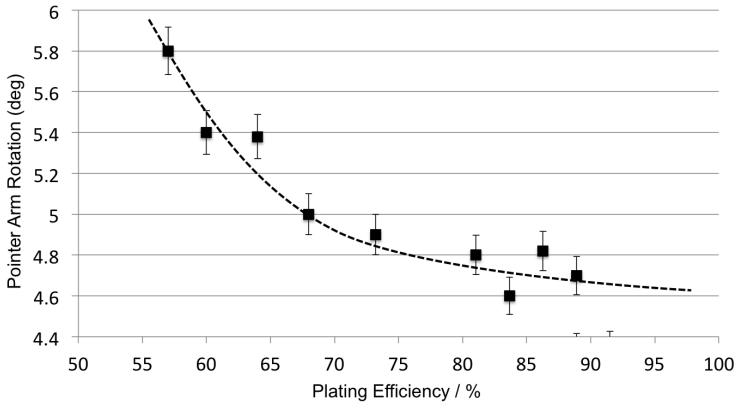

Figure 4.25: Plot of pointer rotations against plating efficiency for a pure nickel bath containing boric acid

an acidic bath [165, 166].

Based on these findings, the optimum plating current densities, to achieve maximum efficiency and the low film strain, are within the range of 20-30 $mAcm^{-2}$ in a Ni(II) + boric bath. Higher concentration of boric acid (greater than 0.4 M) may also be beneficial to achieve bright deposits and low stress (considering the low solubility of boric acid in wafer (47 g/l [167]) this might not be optimal).

It can be concluded from this section that boric acid effectively suppresses hydrogen evolution, enhancing both nickel deposition and the overall plating efficiency. It was also shown, with the aid of MEMS test structures, that strain and plating efficiency are mutually dependent and that the eradication of hydrogen evolution/absorption is necessary to produce low stress Ni films.

The final application of a microinductor requires the magnetic core fabricated using ECD NiFe (permalloy), therefore the next section investigates the effect of boric acid on the anomalous codepositon of the alloy.

4.4.3 Effect of boric acid in nickel-iron solution

4.4.3.1 Introduction

The first explanation for the anomalous codeposition, observed in the nickel-iron system, was provided by Dahms and Croll in 1965 [154]. Their data indicated that ferrous ions in the bath increased the deposition overpotential for nickel. It was recognised at the time that, hydrogen ions are reduced at the cathode, and that this half-reaction increases the pH at the surface of the deposit. However, Dahms and Croll attributed the overpotential to the formation of an $Fe(OH)_2$ precipitate film on the deposit. Some years later Hessami and Tobias [168], suggested that the increase in cathode pH was only sufficient to produce the soluble iron hydrolysis product $FeOH^+$. A mathematical model of anomalous codepositon based on the adsorption of this species on the cathode successfully predicted Ni-Fe deposit compositions. Shortly after the Hessami-Tobias model was published, Deligianni and Romankiw [169] experimentally verified that the increase in cathode pH was modest, compared to the bulk solution pH. Furthermore, it was noted that the pH increase was similar to that observed with ferric ion solutions, suggesting that ferric ion (present in the bath as the result of the air oxidation of ferrous ion) was controlling the cathode pH. Thus, they attributed anomalous codepositon in the nickel-iron system to the adsorption of the hydrolysis products of ferric ion [170]. As the evolution of hydrogen during electrodeposition can increase pH at the cathode surface or cause hydroxide formation, it is believed to be a dominant factor in determining the composition and structural properties of NiFe thin films. Boric acid has been used extensively in NiFe plating baths, as an attempt to control the pH rise and eliminate the hydrogen evolution on the surface of the cathode [89]. However, little work has been reported on the characterisation of intrinsic stress in these films.

The aim of this work is to examine the effect of boric acid on the NiFe deposits and compare its performance with a nickel only bath. Therefore, the following study was carried out at the same temperature and agitation conditions used for

the previous experiments. To achieve a nickel-iron alloy (target $Ni_{80}Fe_{20}$), 3 g/l iron(II)chloride tetrahydrate was added to the original nickel solution and the effect on plating with and without boric acid investigated.

4.4.3.2 Experimental setup

Table 4.2 details the bath composition and parameters employed for the preparation of the electroplated samples. Cathode potential was recorded (vs. SCE) for each plated sample. Plating efficiency, strain (pointer arm rotation) and magnetic hysteresis were also recorded and analysed. Before any Fe(II) was added, the pH

Table 4.2: Ni/Fe/boric acid bath composition and conditions

Bath contents	**Concentration/M**	**Concentration/(g/l)**
$NiCl_2.6H_2O$	0.4	95.2
$FeCl_2.4H_2O$	0.015	3.0
Boric Acid (varied)	0 - 0.4	12, 24, 37, 49
Current Density (mA/cm^2)	20	
Target thickness (µm)	5	
Temperature (°C)	24 ± 1	
pH	2.6 ± 0.2	

of the nickel bath solution was reduced from 4.4 (fresh bath pH) to 2.6 by adding 1% HCl. The first sample was plated with 0.4 M Ni(II), 0.015 M Fe(II) and no boric acid. As soon as the plating commenced, the cathode chip was observed to become covered in a black deposit, accompanied by excess hydrogen evolution and the flaking of a powdery deposit. The efficiency of this plated sample could not be obtained as most of the loosely deposited material was removed, during the DI rinse after plating. A microscope image of the die is shown in Figure 4.26. The next sample was plated with the addition of 0.2 M boric acid and less hydrogen bubbles were observed. However, flaking of the unknown black deposits continued. Similar effects were observed with the addition of boric acid upto 0.8 M. All the samples were carefully rinsed and weighed to obtain efficiencies less than 30%.

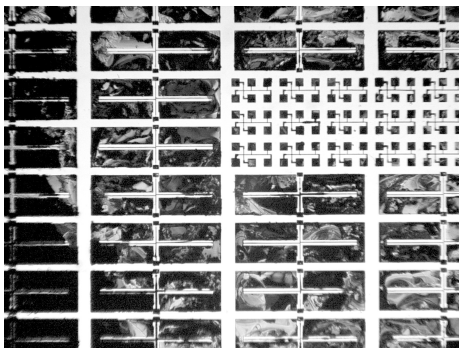

Figure 4.26: Image of sample plated in solution containing 0.4 M nickel(II) and 0.015 M iron(II)chloride only

These initial observations suggests that the inclusion of iron has clearly altered the deposition mechanism to such an extent that even the effect of boric acid (as hydrogen suppressor) has ceased to exist. The corresponding galvanostatic curves obtained for each sample, are presented in Figure 4.27.

4.4.3.3 Galvanostatic analysis

The OCPs between samples were consistent with and without boric acid ($\sim$ -0.05 V). No significant changes were observed in the plating potentials in different boric concentrations (averaging $\approx$ -0.95 V), which suggests that its presence does not contribute towards the deposition of the NiFe alloy. A further comparison of plating potentials of pure Ni and NiFe alloy with and without boric acid have been compiled and are shown in Figure 4.28.

Firstly, a clear distinction between the initial OCPs can be observed which is related to the inclusion of iron in the bath. This change of -0.28 V implies the existence of the Fe^{2+} / Fe^{3+} redox couple, which has been reported in the literature [171]. Secondly, no significant change in OCP before and after the addition of boric acid suggests the non-existence of either Ni - boric or Fe - boric complexes.

Comparing the steady state plating potentials at 400 s a few conclusions can be drawn: Hydrogen evolution occurs in a pure nickel bath which favours the overall reaction and drives the overpotential up to -1.3 V. The addition of boric acid however, inhibits the production of hydrogen and encourages nickel reduction

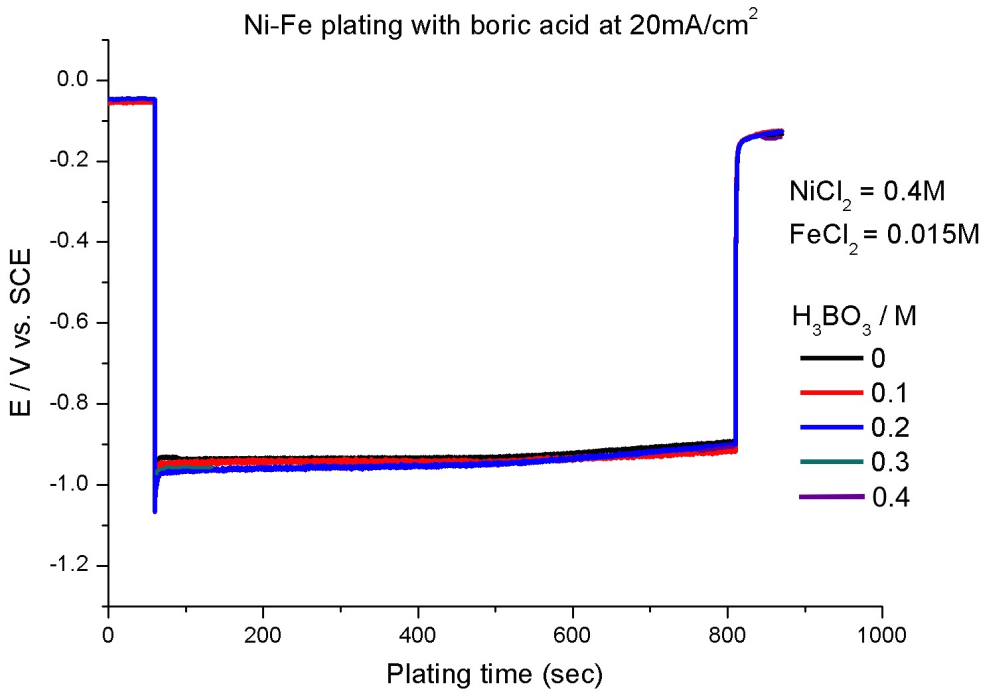

Figure 4.27: Galvanostats of nickel/iron alloy plating with changing boric concentrations, plated at 20 $mAcm^{-2}$

which lowers the plating potential to -1 V. The presence of iron lowers the plating potential even further to -0.93 V suggesting the overall reduction reaction favours iron more than nickel (anomalous codepositon of NiFe). Finally, adding boric acid to this bath makes no significant difference.

A further analysis of the structural properties of the plated film was carried out and compared with these glavanostatic results.

4.4.3.4 Strain measurements

Figure 4.29 shows microscope images of the plated samples for different boric acid concentrations. It can be observed that the plated material near the pointer arms had delaminated and buckled up, which is why they appear darker and out of focus and this is the case for all samples. Pointer arm rotations were extracted from these images and are presented in Figure 4.30(a).

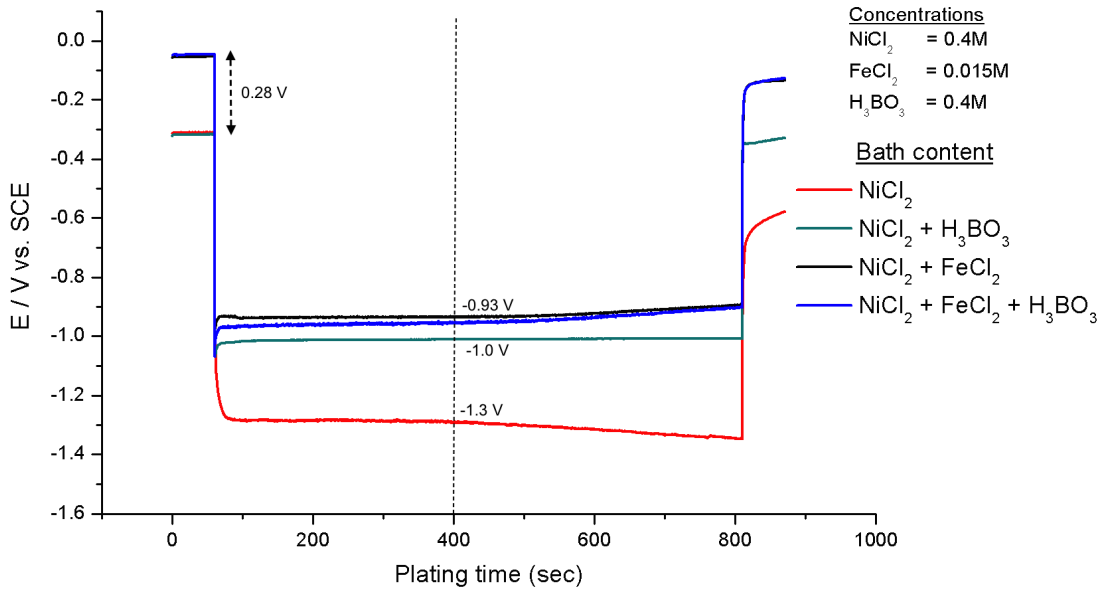

Figure 4.28: Shows galvanostats obtained from plating samples at 20mAcm^{-2} in different bath chemistries

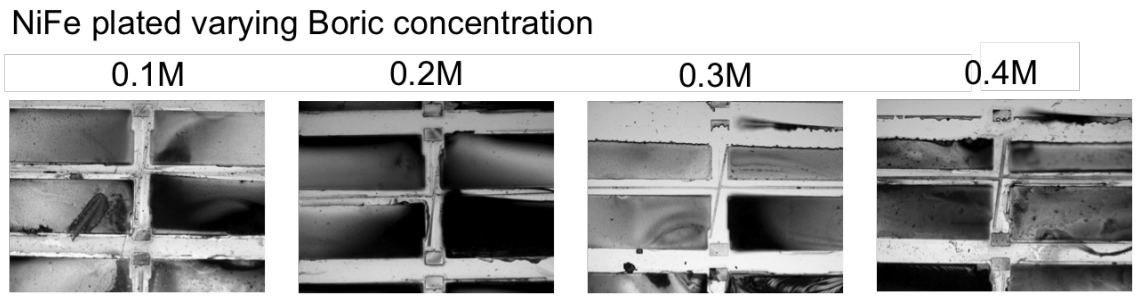

Figure 4.29: Microscope images of the test structures plated in a bath containing 0.4 M Ni(II), 0.015 M Fe(II) and varying boric acid

A closeup image of a pointer arm (Figure 4.30(b)) shows the arms had rotated clockwise to its maximum limit, which was observed for all plated NiFe samples, with and without the boric acid. The inclusion of iron has, therefore, drastically changed the plating dynamics and increased the intrinsic strain of the films by more than 130%.

Plated Fe% compositions with respect to the boric concentration in the bath are

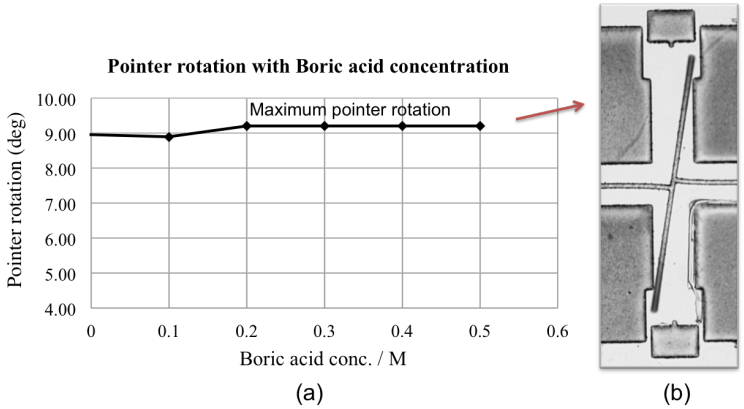

Figure 4.30: Bath: $NiCl_2$, $FeCl_2$ and H_3BO_3 (a) Pointer rotation vs. boric acid concentration (b) Microscope image of one of the test structures from the batch reaching its maximum rotation limit

shown in Figure 4.31, measured using XRF (Appendix. A.2.4) and a general trend

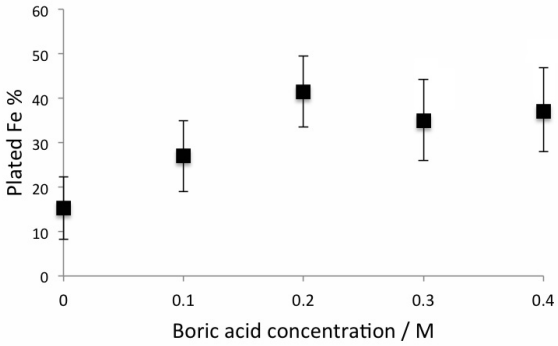

Figure 4.31: Effect of boric acid concentration in plating bath on plated nickel-iron composition

of increasing Fe% with boric acid is observed. The large variation in iron (±15%) was due to the XRF's inability to focus on the delaminated plated structures as seen from the microscope images in Figure 4.29 however, a general trend is evident. A proposed hypothesis for this behaviour could be the absorption of boric on the electrode, which completely blocks the nickel ions but partially allows the ferrous ions to penetrate through and deposit on the cathode. This surface coverage mechanism of boric acid has also been proposed by Yin and Lin [39] which supports this theory.

Figure 4.32 shows the magnetic hysteresis of the NiFe alloy which seems to act

more like a paramagnetic material with increasing boric acid concentrations. It can be observed that the applied magnetic fields are incapable of saturating the domains of the magnetic material which could be caused by the mechanical defects/impurities (black deposits) incorporated within the film during deposition. It should also be noted that the character of magnetisation depends on the shape and volume of the sample, so this would change if the sample is for example, low yielding or delaminating.

The coercivity is seen decreasing with increase in boric acid which could correlate with the material becoming soft with more iron being incorporated within the film, which is desirable for microinductors however, these films also have high residual stress and this plating recipe cannot be employed for production. Further improvement to lower the material stress will therefore be required, which has been reported in the next section.

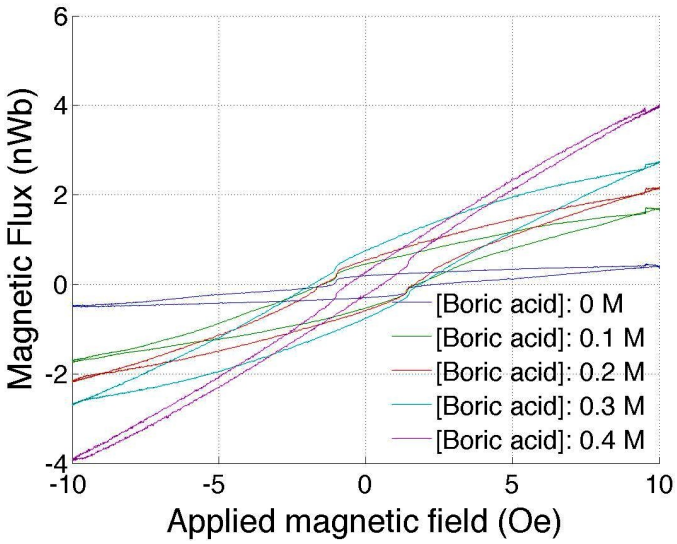

Figure 4.32: Effect of boric acid concentration on the plated films magnetic hysteresis

4.4.3.5 Summary

In nickel bath, the addition of boric acid (upto 0.4 M) was observed to improve the plating efficiency, but this could not be achieved in the presence of iron. All NiFe films showed signs of delamination which confirmed very high tensile stress levels through the pointer arm rotations. However during their deposition, less bubbles with the addition of boric acid was observed which could suggest that boric is trying to suppress hydrogen evolution but the presence of iron hinders nickel reduction, producing films with high stress and less than 30% plating efficiency. This observation also backs up previous studies reported in the literature [90][172], where the addition of boric acid in permalloy plating solutions was not found to eliminate anomalous codeposition but rather induce more stress in the plated NiFe film which also suggests its inclusion in the film during deposition causing deformities.

4.4.4 Effect of Saccharin in nickel/iron/boric baths

Table 4.3: Ni/Fe/boric acid/saccharin bath composition and conditions

Bath contents	**Conc./M**	**Conc./(g/l)**
$NiCl_2.6H_2O$	0.4	95.2
$FeCl_2.4H_2O$	0.015	3.0
Boric Acid (varied)	0.4	24
Na-Saccharin	0 - 0.02	0 - 4
Current Density (mA/cm^2)	20	
Target thickness (µm)	5	
Temperature (°C)	24 ± 1	
pH	2.6 - 2.8 (adjusted with 1% HCl)	

One approach known to reduce the stress in electroplated films is the addition of saccharin to the electrolyte. Hence the effect of saccharin, on films strain, has been investigated. Different concentrations of saccharin were added to a bath containing Ni(II) + Fe(II) + boric acid and table 4.3 summarises the bath compositions employed. Five bath samples were prepared with increasing saccharin bath concentrations. Figure 4.33 shows the plating potentials recorded for the

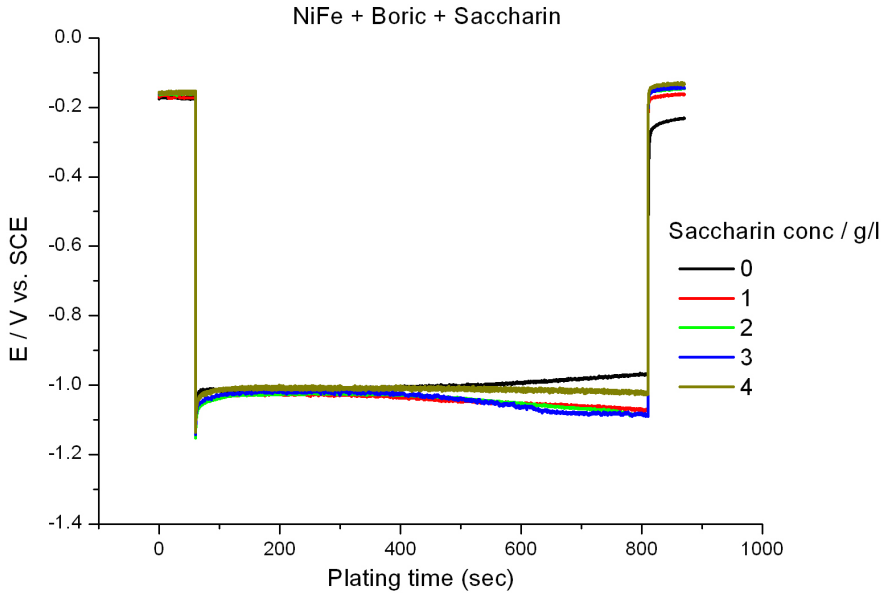

Figure 4.33: Galvanostats of nickel/iron alloy plating with bath containing boric acid but changing saccharin concentrations, plated at 20 $mAcm^{-2}$

test structure chips plated with NiFe for a target thickness of 5 µm.

The initial OCPs for all samples were roughly -0.16 V. During deposition it was interesting to see a steady potential of -1.02 V, lasting 340 s, which then drifted to a slightly more negative value until the end.

During deposition less hydrogen bubbles evolved and there was no flaking or delamination. Deposited films also had a bright shiny finish. The chips were then further processed to release the test structures and microscope images of the these are shown in Figure 4.34. It can be clearly seen the stress in the films

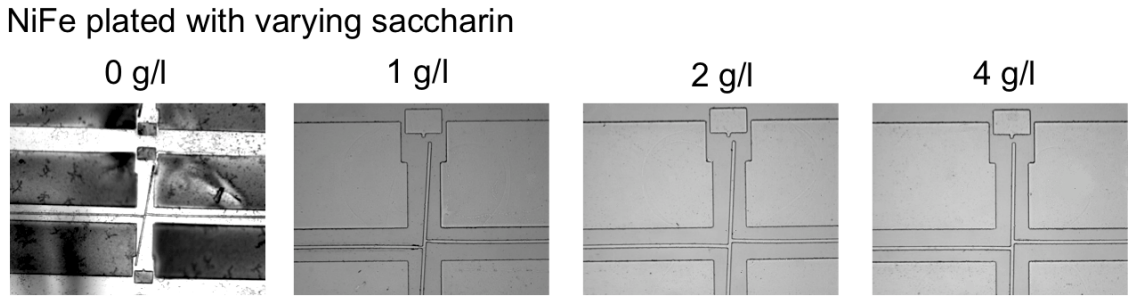

Figure 4.34: Microscope images of NiFe samples plated in bath containing $NiCl_2$, $FeCl_2$, H_3BO_3 and Saccharin (varying) - concentrations shown in Table 4.33

has been significantly reduced as a result of introducing saccharin into the bath. Pointer arm rotations were extracted from the plated chips and these have been plotted in Figure 4.35 which shows the correlation of strain (pointer rotation) with plating efficiency. The plating efficiency increased from 17% (without saccharin) to

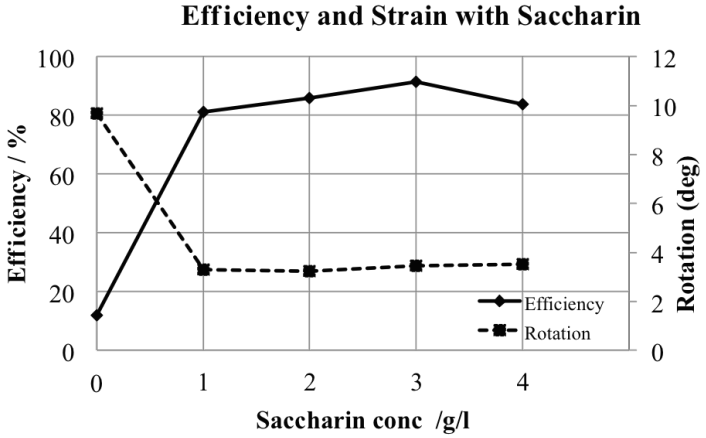

Figure 4.35: Effect of saccharin on plating efficiency and strain of NiFe films; Bath: $NiCl_2$, $FeCl_2$, H_3BO_3 and saccharin (varying)

around 90% with the addition of 3 g/l of saccharin. Pointer rotations (strain) also significantly decreased with the addition of saccharin. The increase in saccharin concentration from 1 - 4 g/l did not appear to show a noticeable change in either the appearance or strain of the film.

The magnetic hysteresis of the samples are presented in Figure 4.36. The mag-

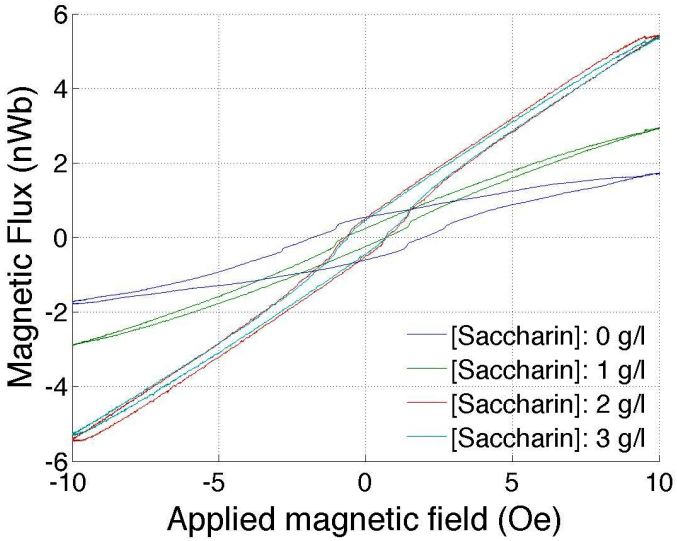

Figure 4.36: Effect of saccharin on magnetic hysteresis of NiFe films

netic flux at any applied magnetic field is shown to increase while the coercivity decreased significantly in the presence of saccharin. It was also observed that the hysteresis was near identical for the 2 and 3 g/l saccharin. When comparing the hysteresis of plated nickel samples where the magnetic flux at 10 Oe was < 0.5 nWb (Figure 4.17), the 10 times increase in magnetic flux is correlated to the increase in the Fe% in the film making the material softer.

Table 4.4: Ni/Fe/boric acid/saccharin bath composition and plating current densities investigated

Bath contents	**Concentration/M**	**Concentration/(g/l)**
$NiCl_2.6H_2O$	0.4	95.2
$FeCl_2.4H_2O$	0.015	3.0
Boric Acid	0.4	24.0
Na-Saccharin	0.005	1.0
Current Density (mA/cm^2)	10, 15, 20, 30, 40	
Target thickness (µm)	5	
Temperature (°C)	24 ± 1	
pH	2.6 ± 0.2	

The effect of plating with different current densities was investigated using the bath composition detailed in Table 4.4. All samples were plated to the same target thickness of 5µm and the corresponding (potential vs. time) plots obtained are shown in Figure 4.37.

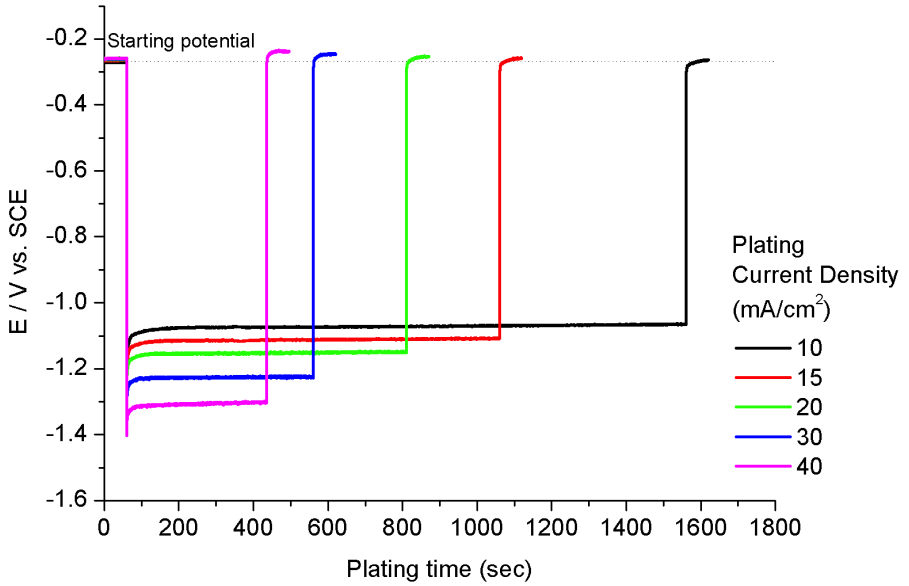

Figure 4.37: Potential vs. time plots of NiFe plating with different current densities (10 - 40 $mAcm^{-2}$); Bath: $NiCl_2$, $FeCl_2$, H_3BO_3 and saccharin (1 g/l)

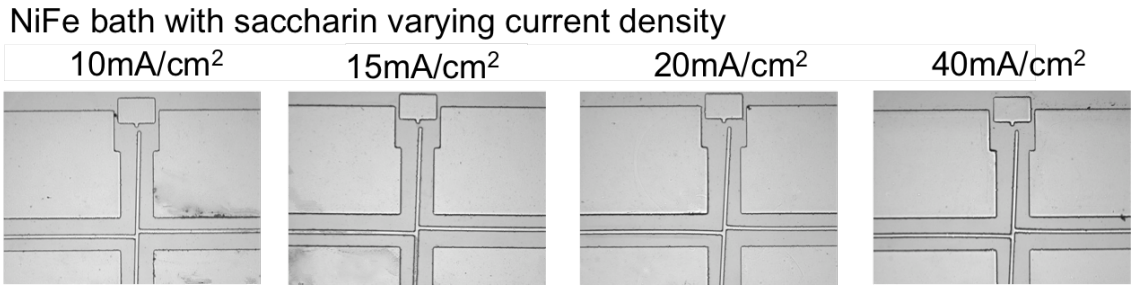

Figure 4.38: Microscope images of NiFe released test structures plated in bath containing saccharin and boric acid

The first observation is that little or no hydrogen gas bubbles were seen evolving from the surface and the plating potentials were steady throughout the deposition. The samples also had bright and shiny finish with no film delamination at any plating current density. Microscope images of the released test structures are shown in Figure 4.38 and a low pointer rotation was observed compared to samples plated with bath not containing saccharin.

The plating efficiencies and strain (pointer rotations) with respect to plating

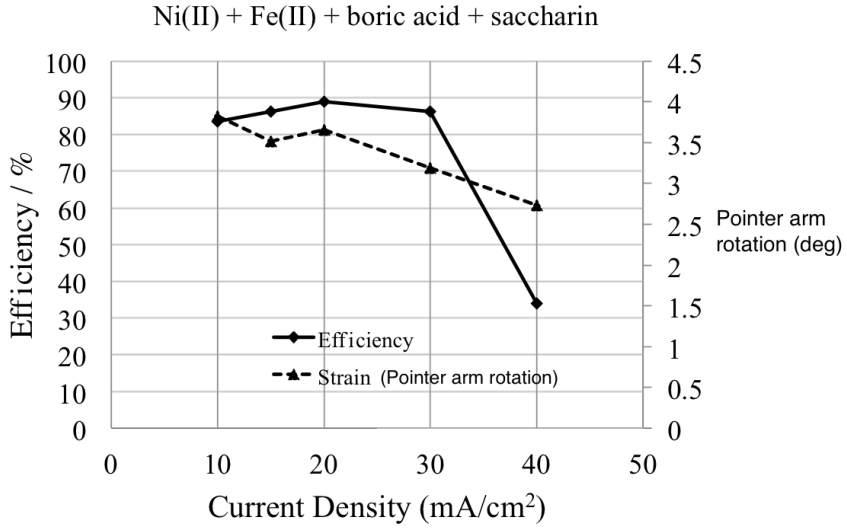

Figure 4.39: Bath: $NiCl_2$, $FeCl_2$, H_3BO_3 and saccharin. The effect of plating current density on strain (pointer arm rotation) and plating efficiency

current density is shown in Figure 4.39. The efficiency was shown to increase to a maximum of 90% at 20 $mAcm^{-2}$ which then decreased for higher plating

current densities (diffusion limited). With saccharin in the bath it was interesting to note the effect of efficiency on strain did not correlate inversely as observed in its absence (compare Figures 4.22 and 4.24). Pointer rotations decreased with decreasing efficiency which was interesting as the strain in film was observed to increased with low plating efficiency for all samples plated previously. Therefore, to investigate further film iron composition was measured and it can be observed to be correlated with strain in Figure 4.40. The correlation between the strain

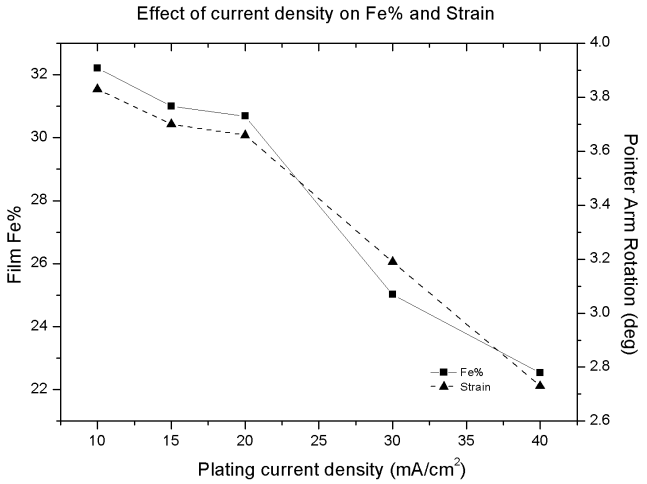

Figure 4.40: Plot showing the effect of plating current density on the film Fe% and strain (Bath: Ni(II), Fe(II), boric acid and saccharin)

and Fe% was calculated as 0.98 which shows a strong relationship between the two parameters. The Fe% in film was also observed to change linearly with the plating current density. 32% Fe was achieved at 10 $mAcm^{-2}$ and 22% Fe at 40 $mAcm^{-2}$ which yields an approximately 3.3% decrease in iron with every 10 $mAcm^{-2}$ increase in current density for a bath containing 0.4 M $NiCl_2$ and 15 mM $FeCl_2$.

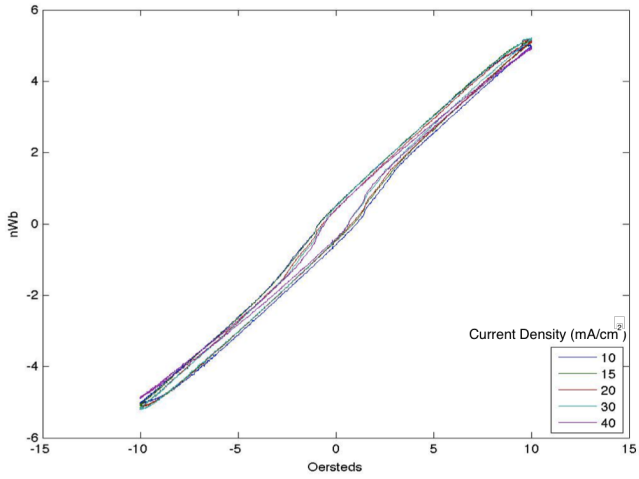

Figure 4.41: Bath: 0.4 M $NiCl_2$, 15 mM $FeCl_2$, 0.4M H_3BO_3 and 5 mM (= 1 g/l) Saccharin. Magnetic hysteresis of films plated at different current densities.

The magnetic hysteresis of each sample was plotted and is shown in Figure 4.41. Very slight or no change in the magnetic response with the applied external magnetic field was observed between samples. This is unexpected as a 10% change in Fe% would be expected to alter the material softness and ferromagnetic responses but this was not observed in the magnetic hysterysis plots.

In this study the addition of saccharin (1 g/l) in a NiFe bath has shown to reduced strain levels by $\approx$ 70%, yielding films with a bright and smooth finish. The effect of saccharin composition has also been investigated which showed no variation in plating efficiency and strain. Maximum efficiency (90%) was obtained from 3 g/l saccharin which also produced a film with the highest magnetic saturation. Lowest stress was also achieved at plating current density of 40 $mAcm^{-2}$ while the highest efficiency (>90%) was obtained at plating current density of 20 $mAcm^{-2}$.

4.5 Summary

MEMS test structures have been fabricated on 1.3 × 1.7 cm Si chips which have shown to be capable of characterising strain in Ni and NiFe films plated in a beaker level setup. Numerous bath chemistries have been investigated to show that small changes in the plating conditions can lead to changes in film characteristics such as intrinsic stress, texture and magnetic properties.

The effect of hydrogen evolution has been shown to be a prominent factor influencing the plating efficiency and also the resulting structural properties of nickel plated from a pure nickel bath. Low stress nickel films were achieved from low concentration of nickel(II) (0.1 M to 0.4 M) plated at low current densities (5 - 20 $mAcm^{-2}$).

The effect of boric acid and saccharin on NiFe was investigated and the following table summarises the optimum bath parameters and conditions to achieve low stress NiFe films:

Table 4.5: Recipe for achieving low stress NiFe films

Bath contents	**Concentration**
$NiCl_2.6H_2O$	0.4 M
$FeCl_2.4H_2O$	3 g/l (depends on film target Fe%)
Boric Acid	0.4 M
Saccharin	3 - 4 g/l
HCl (aq)	(variable) for pH adjustment
DC Plating current density / ($mAcm^{-2}$)	20 - 30
Expected film Fe composition	20 - 25 %
Temperature (°C)	24 ± 1
pH	2.6 ± 0.2

This work provides the platform for further optimisation and demonstrates an increased understanding of processes windows which have been employed in further chapters where industrial scale baths have been employed to achieve low stress and high efficient NiFe films.

Chapter 5

Wafer-level Strain Measurements and Correlations with other Properties of NiFe Films

5.1 Introduction

Nickel-iron alloys are of increasing interest in MEMS technology because of their excellent magnetic properties, which have applications related to magnetic actuators, integrated microscale inductors and transformers, where high magnetic flux densities are required. For typical applications, thicker films result in improved performance, although the stress developed during deposition and other process steps can potentially result in unacceptable wafer bows and, in extreme cases, cracking and delamination. Therefore, understanding the mechanisms of stress development within plated films, with the aim of optimising process conditions to minimise induced stress, is of great interest [135, 100, 173, 152].

MEMS strain test structures with small scale beaker level experiments, has been used to characterise plated Ni and NiFe films, as described in the previous chapter 4. It was shown that even minor changes in plating parameters affected intrinsic strain in the deposited film. This data was correlated with other measured quantities such as film composition, plating efficiency and plating potentials which proved to be an important aspect of understanding the origin of stress in the deposited film. However, this ECD study was carried out on smaller chips, and so the results will not necessarily directly transfer to wafer deposition as, for

example, the current crowding effect will be significantly different. Hence, a full wafer comparison is required and this chapter, reports the spatially mapping of stress in NiFe films on 200 mm wafers. It also investigates for the first time the spatial correlations between parameters such as Young's modulus, film thickness, film composition and sheet resistance. This technique of visualising variations on wafer level helps facilitate multi-parameter optimisation in order to achieve ECD films with ideal characteristics.

5.2 Experimental

The aim of this study was to compare the effect of different thermal annealing procedures on the stress developed in NiFe films plated on 200 mm wafers.

Two double side polished[1] wafers (W1 and W2) were patterned with 7.5 µm thick

Table 5.1:
Ni-Fe bath composition and conditions

Parameter	**Value**
$NiCl_2.6H_2O$ (g/l)	110 or 0.4 M (98.9%)
$FeCl_2.4H_2O$ (g/l)	1.0 or 5 mM (1.1%)
Boric acid (g/l)	25
Saccharin (g/l)	1
Na dodecyl sulphate (g/l)	0.1
NaCl (g/l)	5
Bath volume (litre)	35
Bath temperature (°C)	24 ± 1
pH	2.6 ± 0.2
Anode material	Solid Ni pellets
Agitation method	Pump with adjustable nozzle spray
Plating current density	20 $mAcm^{-2}$

1. Wafer curvature measurements were also obtained for these wafers which required the backside surface to be highly reflective for the laser in the FSM system (section 2.4.1.1)

photoresist (SPR220-7) and NiFe strain test structures were electroplated using the bath recipe detailed in Table 5.1. The electroplating regime (20 $mAcm^{-2}$) was selected as it reflects the requirement in manufacturing for high deposition rates and hence any resulting wafer level non-uniformities would be of significant interest. After ECD and seed layer stripping, the test structures on W1 were released first and subsequently heated to 150 °C for 10 mins on a hot plate, while the second wafer (W2) was annealed using an identical temperature-time profile and then test structures released by the HF vapour etch. Wafer curvatures have also been measured for both wafers after each process step. Details of the fabrication procedure can be found in section 3.4.1. Besides plating these patterned wafers another blanket film was deposited using identical plating conditions and wafer bow was measured before and after the anneal step as part of the comparison.

5.2.1 Wafer plating tool

The plating tool was custom built [2] (Figure 5.1(a,b)), being specifically designed for process development, as it allows quick bath changes and can accommodate wafers of different sizes, from 75 mm to 200 mm diameter, in sealed wafer holders as shown in Figure 5.1(c). This tool has two 35 L tanks that can host two different chemistries (namely NiFe and Cu), with connections to a single current-controlled DC rectifying power supply with 2 independent channels, each capable of supplying a maximum of 20 A / 16 V.

Sufficient agitation is performed using a pump which, for this experiment, sprays a stream of electrolyte vertically upwards from bottom to top directed towards a point above the centre of the cathode (wafer). Figure 5.2 shows a schematic image of the agitation setup during the plating process of W1 and W2.

The geometry and the characteristics of the tool introduce a number of non-uniformities in the processing conditions, which are then reflected on the electrodeposited films. Although not ideal for production, this configuration is useful

2. Built by Plating Engineering Ltd, Unit 9 Poplar Drive, Witton, Birmingham, B6 7AD, http://www.pe-limited.com/

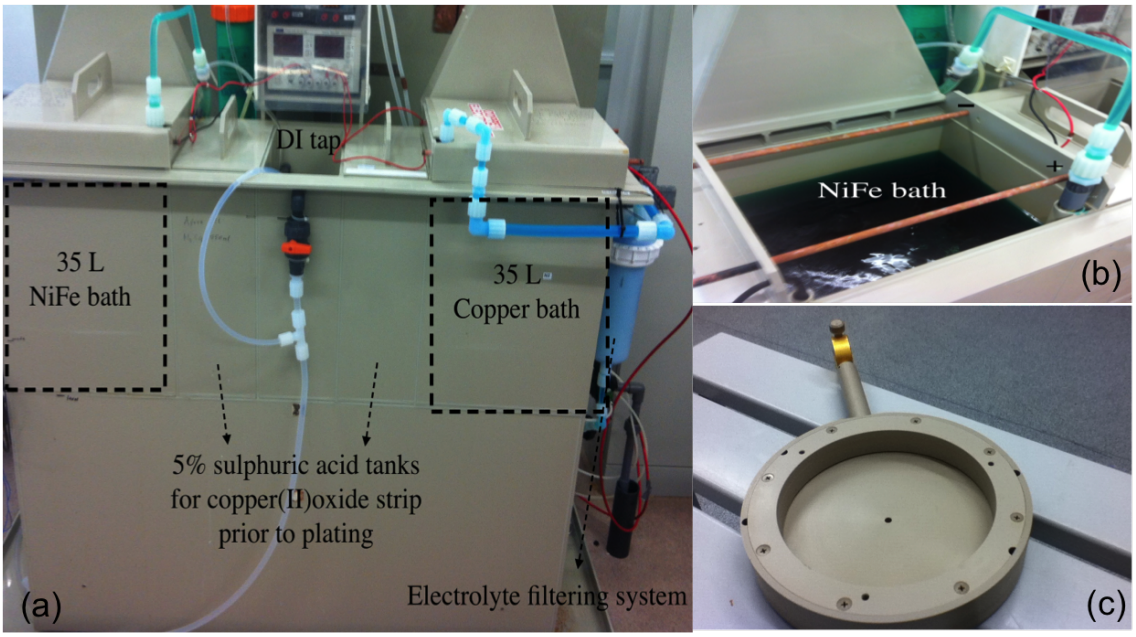

Figure 5.1: (a) SMC plating tool (b) NiFe plating tank showing the electrical contact rods (c) 200 mm wafer holder for plating

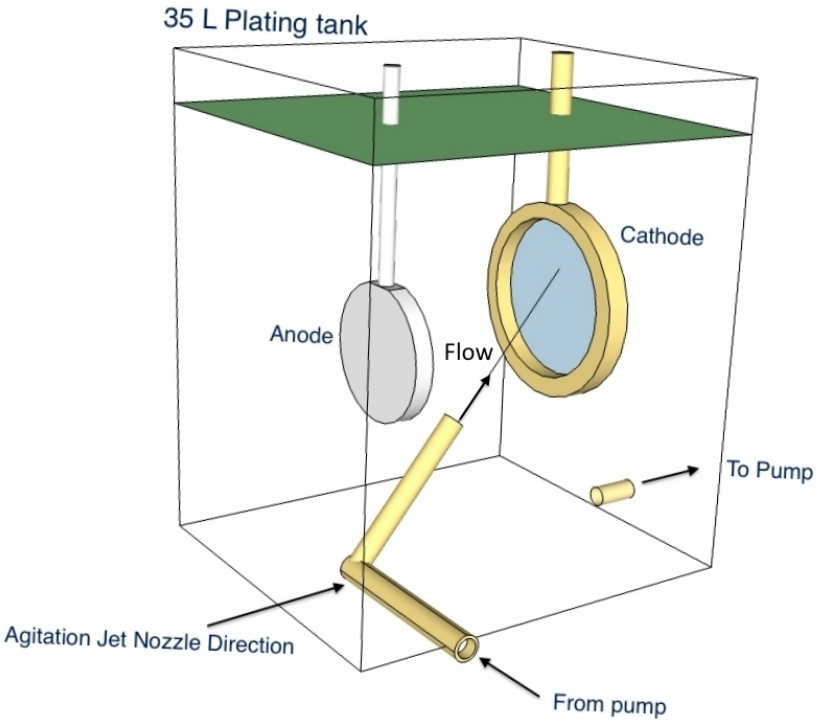

Figure 5.2: Schematic of agitation setup used for plating W1 and W2. Jet nozzle is directed just above the center of the wafer.

to determine the effects of different processing parameters on the electroplated films.

5.2.2 Measurements

Strain measurements were made on the suspended rotating strain structures along with parametric electric measurements such as sheet resistance and linewidth on the Greek-cross and suspended bridge test structures (see sections 2.5.1 and 2.5.2 for details). Film thickness and compositional ratio of the plated films were wafer mapped using X-ray fluorescence (see section A.2.4).
Specific attention was paid to the effect that different heating regimes had on the development of stress within the NiFe film, with stress and resistance measurements made before and after the high temperature steps.

5.3 Results and Discussion

5.3.1 Pointer Arm Rotation Measurements

Figure 5.3 shows the pointer arm rotation (strain) map of W1 which was annealed after release. A spatial pattern can be observed, suggesting ∼50% more rotation in the top middle part of the wafer. Closer to the bottom half, lower rotation values range from 0.3° - 0.8°, forming a crescent shape. Rotations from 200 test structures located in these regions (marked with a cross on Figure 5.3) have been analysed and plotted with respect to the arm separation - linewidth ratios in Figure 5.4, with a 2σ standard deviation. Trends show that the sensitivity of the arms peaked at a separation ratio 1.75 where the pointer rotation is $(60 \pm 5)\%$ greater. Test structures with the separation ratios 1.5 and 2.0 show similar rotations, within the standard deviation. A clear differentiation between the edge and top section of the wafer confirms the pattern observed in the wafer map.

Figure 5.5 presents the pointer arm rotation (strain) map of W2 which was an-

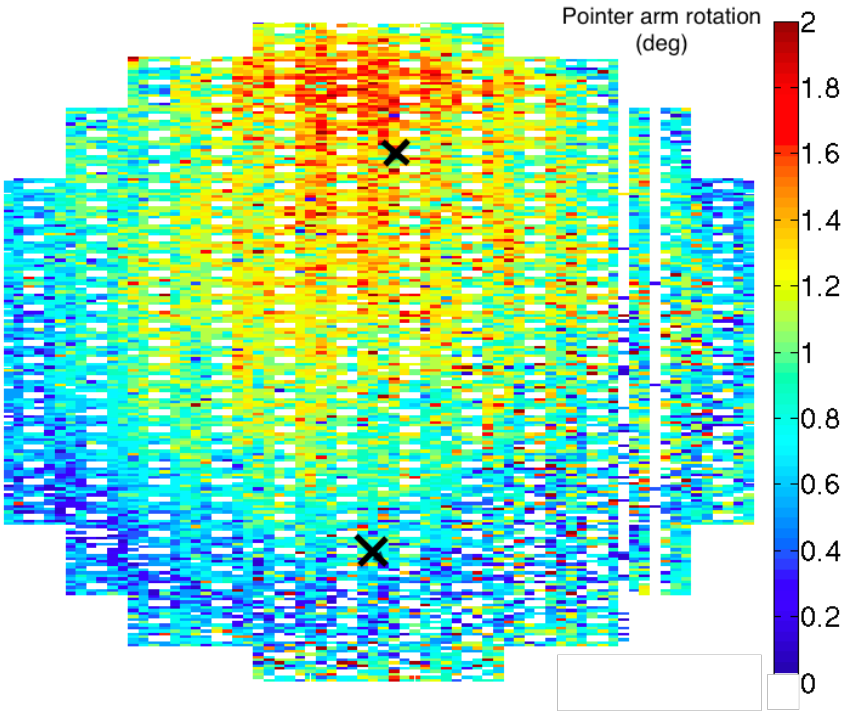

Figure 5.3: Pointer arm rotation map (strain) of W1 showing the spatial variation around the 200 mm wafer. No structures were present in the region marked in white.

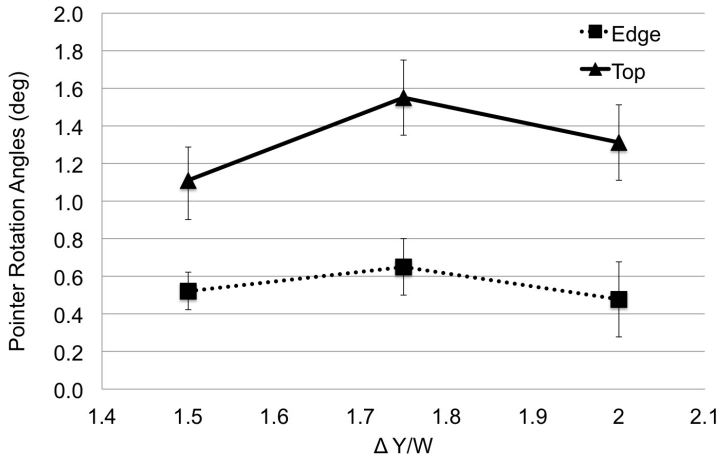

Figure 5.4: Average pointer arm rotations from W1 plotted against arm separation ratio taken from middle and edge of wafer (positions marked with a cross in Figure 5.3)

nealed before release. Significantly higher rotations compared to W1 are observed.

Strain variation is greater on W1, with W2 having a more uniform spread.

Figure 5.6 presents rotations plotted with respect to the arm separation:arm

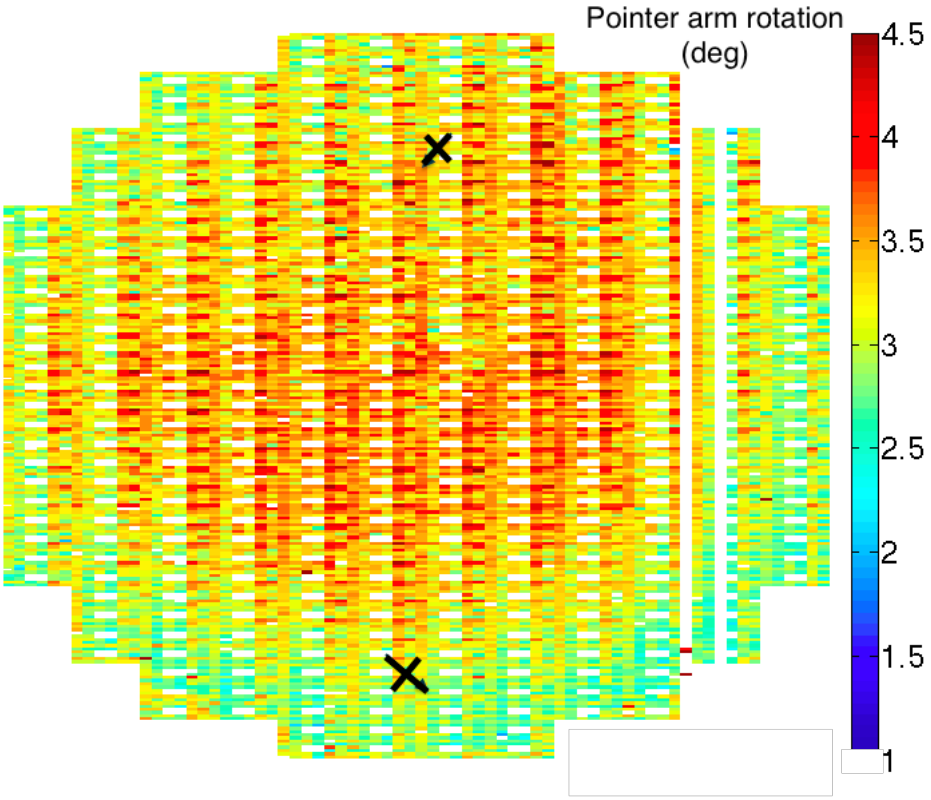

Figure 5.5: Pointer arm rotation map (strain) of W2 showing the spatial variation for the 200 mm wafer. No structures were present in the region marked in white.

width ratios also with a 2σ standard deviation. A maximum rotation of $\simeq 4.5°$ can be observed for $\Delta Y/W$ of 1.5 and 1.75. Higher rotations were also observed around the top section of W2. These results suggests that ECD NiFe retains more stress if heated before release. This observation could potentially be useful in the correct placement of thermal annealing steps within the process flow, if suspended NiFe structures, such as micorswitches, are required.

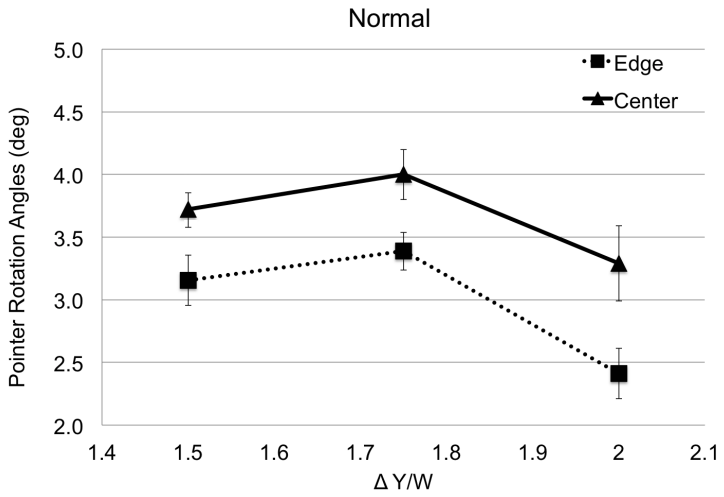

Figure 5.6: Average pointer arm rotations from W2 plotted against arm separation:width ratio taken from middle and edge of wafer (positions marked with a cross in Figure 5.5)

5.3.2 Young's Modulus

To further understand the differences in the mechanical properties of the two films, nanoindentation measurements[3] were conducted on the Permalloy used for the rotating pointer arm structures (method described in appendix A.2.3). This employed a Hysitron triboindenter tool with a Berkovich diamond tip which indents through the surface of the material using a controlled force regime, while measuring the response of the film. The wafer chuck of the indenter could not accommodate a 200 mm wafer, therefore both wafers were cleaved to quarters.

Figure 5.7 shows the spatial distribution of the Young's modulus across the entire surface of W1 and W2. These were obtained by divided the surface into 65 locations where individual nano-indentation measurements were performed. Each of the coloured squares in the figure represents the average of 4 indentation measurements taken on 4 points on the anchor areas of the electroplated film. The measured values for W1 (left) cover a range from 60 to 110 GPa, which is significant, given the statistical variation within each set of 4 measurements of

3. Nanoindentation measurements were performed in collaboration with co-worker, Giuseppe Schiavonne, and the obtained results have been jointly published [174]

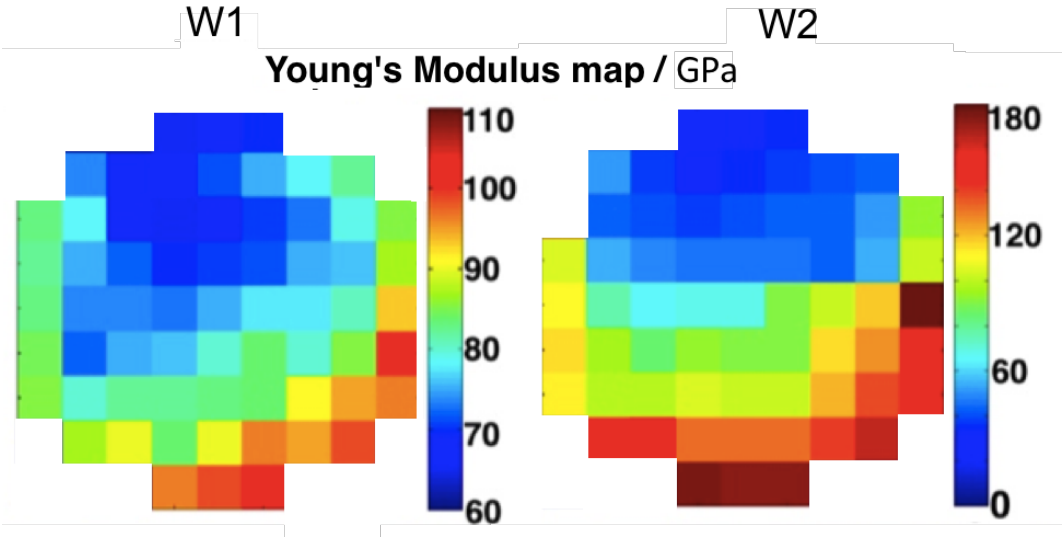

Figure 5.7: Shows the wafer maps of Young's modulus for W1 and W2 obtained using nano-indentation

3 to 10%. Smaller, but still significant variations were observed for W2 (right), with Young's modulus ranging between 30 and 180 GPa, with similar tolerances. The nominal value of Young's modulus for NiFe alloys is reported in the literature is around 200 GPa [175]. Electroplated film properties such as Young's modulus significantly differ from bulk materials, and reporting correct values for their properties is a challenging task as a huge number of parameters that describe the growth process have to be taken into consideration. In particular, the expected values for Young's modulus are significantly lower than the reported bulk values because the electroplating process causes organic molecules from the bath additives, as well as voids, to be included in the film while it grows, affecting primarily the grain structure and therefore the material density [70]. Furthermore, the films characterised in this work have been deposited by DC electroplating, in a high current density regime ($\sim$ 20 mAcm^{-2}). These conditions are known to result in less uniform deposition dynamics, with relatively little grain rearrangement and the presence of a higher number of defects in the film, which again reduced the value of Young's modulus.

5.3.3 Spatial Stress Maps

Finite element analysis curves of simulated pointer arm rotations corresponding to the specific Young's modulus values were then created for different stress ranging from 25 MPa to 400 MPa and this is shown in Figure 5.8(a). Using this alonf with the measured pointer rotation data (Figures 5.3 and 5.5) and the Young's modulus (5.7) obtained from nano-indentation, a residual stress map was constructed which is shown in Figure 5.8(b). It can be observed that these values range between 60 and 150 MPa for W1, and from 50 to 220 MPa for W2. It is satisfying that these residual stress levels fall within the ranges reported in the literature for similar films [139] [138]. It is interesting to note that the higher stress areas do not correspond to areas with higher pointer rotation; on the contrary the associated wafer maps indicate these to be the least subject to stress. The highest stress levels are found for the stiffest portions of films localised on the lower right edge of both wafers, where slightly lower rotation angles are observed. A comparison of these results with the conventional wafer bow method is presented in the following section for further verification.

5.3.4 Stress Comparison with Conventional Wafer Bows

As mentioned earlier in this chapter, a non-patterned wafer (blanket) was plated under the same plating conditions as W1 and W2. This wafer had bow measurements conducted after annealing. A final bow height of 187 µm was obtained, which translates to 194 MPa residual stress. This value is similar to the mean stress calculated for W2 (172 MPa) which was annealed before release. However, due to large spatial differences of stress on the patterned wafers, W1 and W2, a mean value cannot be used to compare with the blanket wafer curvature measurements.

During the processing of the above wafers (W1 and W2) the wafer bow was also monitored at each stage in the process and these results are shown in Figure 5.9. Comparing this set of data with the blanket deposited film confirms that the

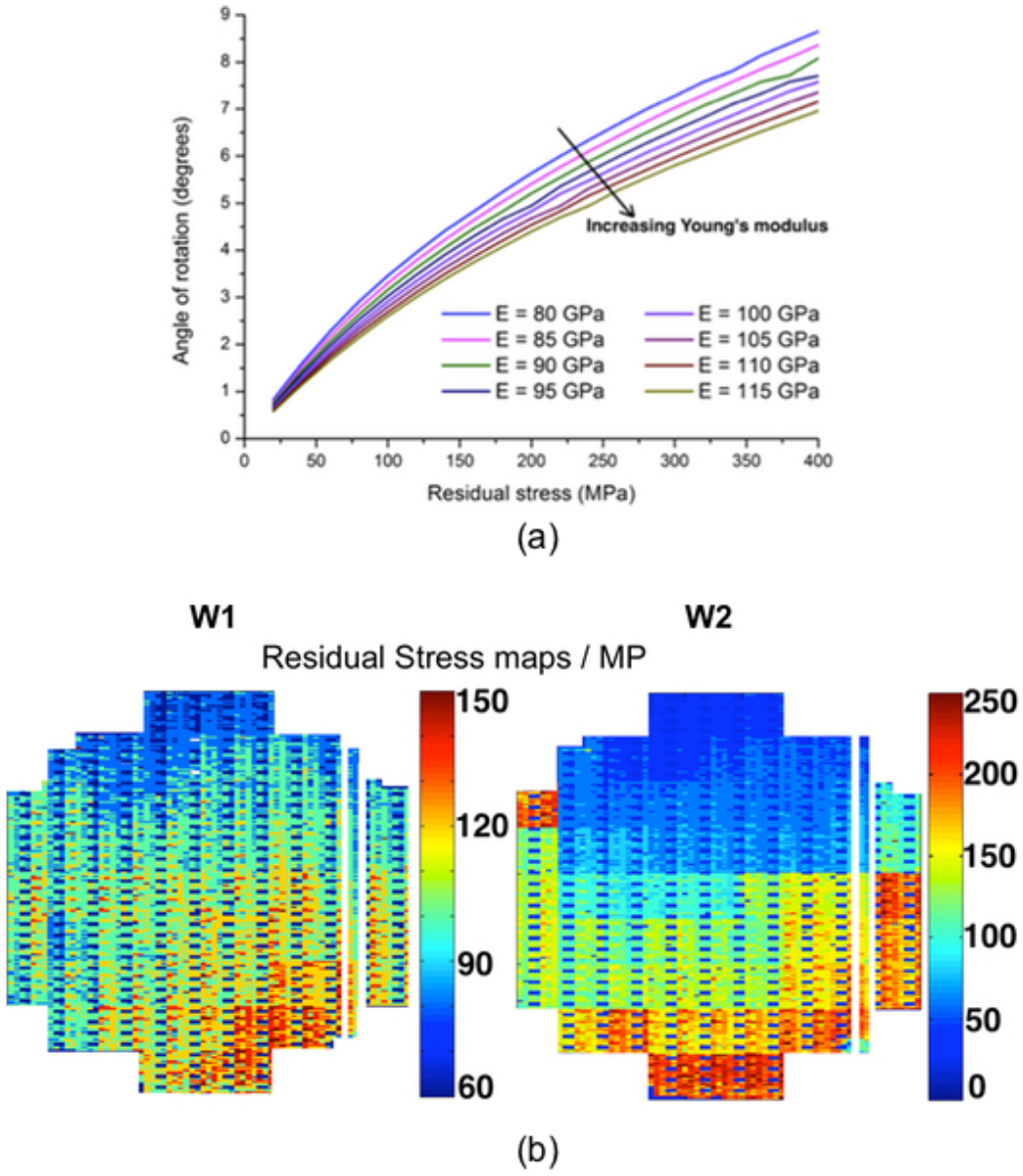

Figure 5.8: (a) FEA curves simulating the pointer arm rotation angle in response to the relief of tensile residual stress for various YoungâĂŹs modulus values (note that the graph shows only part of the complete plot for ease of viewing) (b) Stress maps calculated from pointer rotation (strain) map and local Young's modulus map

patterned wafers have less overall bow than the blanket deposited wafer, which indicates that patterning relieves some of the stress in the NiFe film.

Figure 5.10 illustrates the bow heights for W1 and W2, going through different process stages. It can be seen that every fabrication step contributes to the overall stress of the wafer and for the recipes used, each wafer is converted from a negative

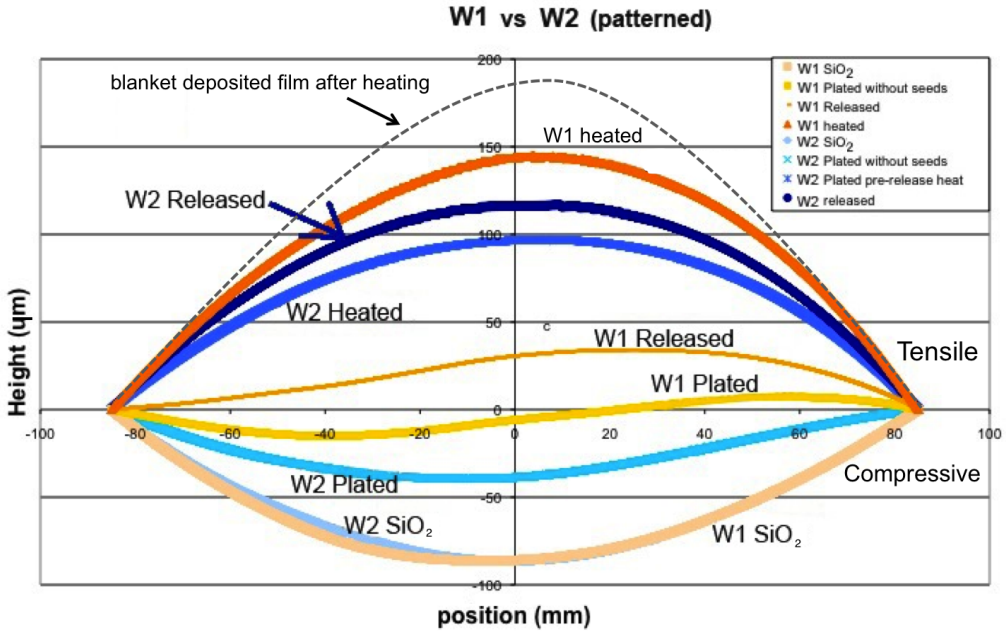

Figure 5.9: Wafer bows for the patterned wafers measured after each fabrication stage

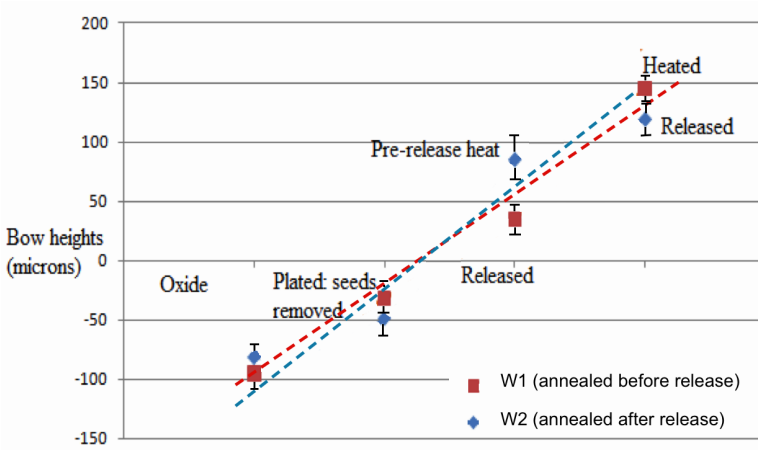

Figure 5.10: Maximum bow height for the patterned wafers

to a positive bow height, indicating a change from an overall compressive to tensile stress.

It is important to remember that a wafer bow measures the overall stress, which is the combined sum of all stresses contributed by the individual layers stacked on the wafer being studied. Hence, the resulting bow depends on the effect of process conditions and variations on each layer. In this case, for example, W2 exhibits a lower final curvature compared to W1 (although not too different), which is

in contradiction with the results illustrated in Figure 5.5, where the rotation maps show lower strain in W1 compared to W2. Wafer bow can therefore, be misleading as the observed change in wafer bow may not be due to the ECD film under investigation. This observation illustrates the greater potential of the test structure approach compared with the more conventional wafer bow measurements.

5.4 Correlation of wafer maps

5.4.1 Iron Composition

To understand the origin of the spatial stress patterns on the two wafers, iron composition was measured (using XRF), on one structure per chip. The maps obtained were correlated with the strain map and these are presented in Figures 5.11 and 5.12, for W1 and W2 respectively. It can be observed that the spatial strain map for both wafers follow a similar pattern to the iron composition of wafers (especially W1). Correlation numbers greater than 0.8 for both wafers are obtained, which indicated that stress is correlated with the percentage of iron deposited. It should be noted that the wafer was located in the holder shown in Figure 5.1 and its recessed position may affect the flow dynamics of the electrolyte (Figure 5.2). Hence, regions (top-middle) of the wafer that received a direct jet of electrolyte would have a vigorous or turbulent flow pattern, affecting the iron distribution and structural properties of NiFe. This particular observation has been confirmed by changing the bath agitation setup which is discussed later in the chapter.

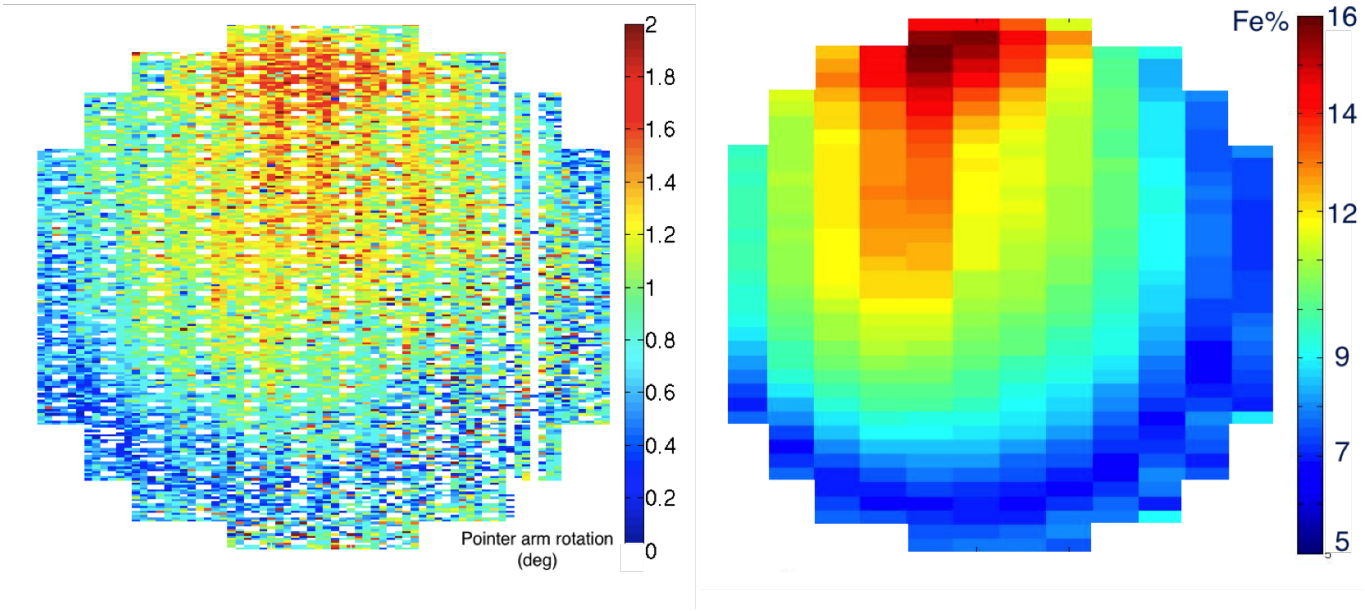

Figure 5.11: Correlation between pointer arm rotation (strain) map and iron composition for W1. Correlation number = 0.87 was calculated which shows a strong relationship between the two quantities

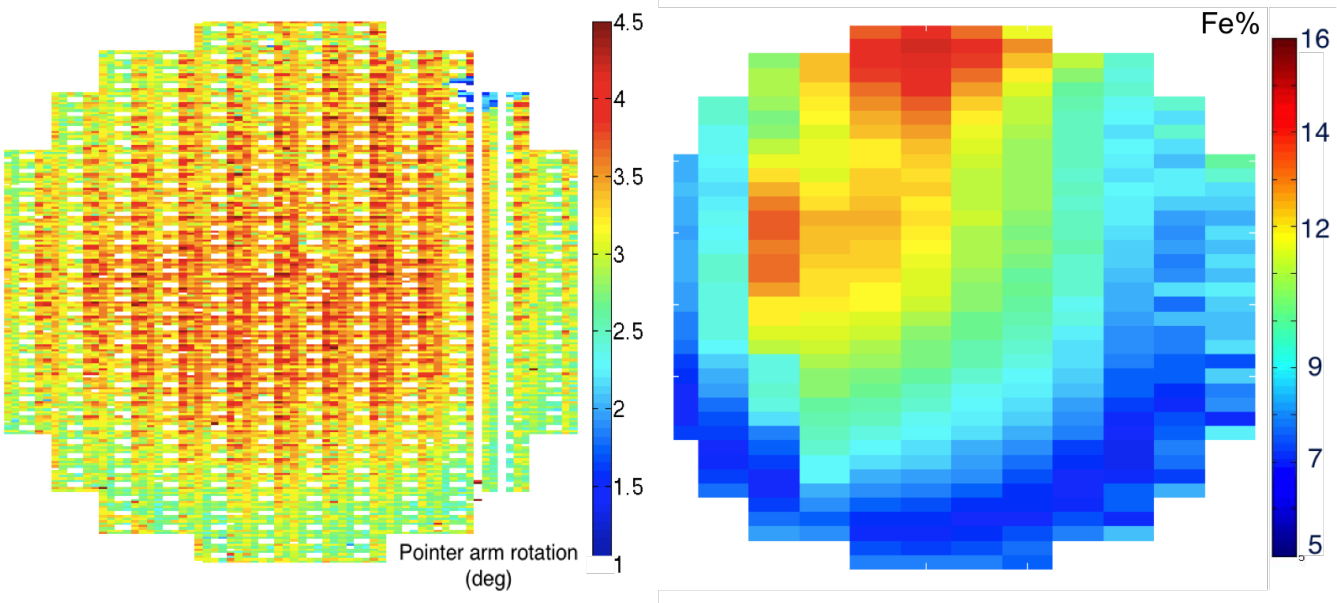

Figure 5.12: Correlation between pointer arm rotation (strain) map and iron composition for W2. Correlation number = 0.81

5.4.2 Film Thickness

Figure 5.13 presents the spatial distribution of film thickness for W1 and a clear radial pattern can be observed, with 5 µm with thick layer at the centre increasing to 6 µm at the outer edge. The average film thickness measured for W1 was 5.3µm. The thickness gradient from edge to center could arise from the current crowding or the low plating efficiency caused by the absorption of hydrogen in the metal which may be inhibiting the nickel deposition. Non-uniform agitation may contribute to the plating efficiency drop, as observed by Andricacos *et al.* [176], and this may lead to thickness and composition variations. A correlation factor of 0.63 was obtained between the stress pointer rotation and film thickness maps which is less than that observed with the iron composition map.

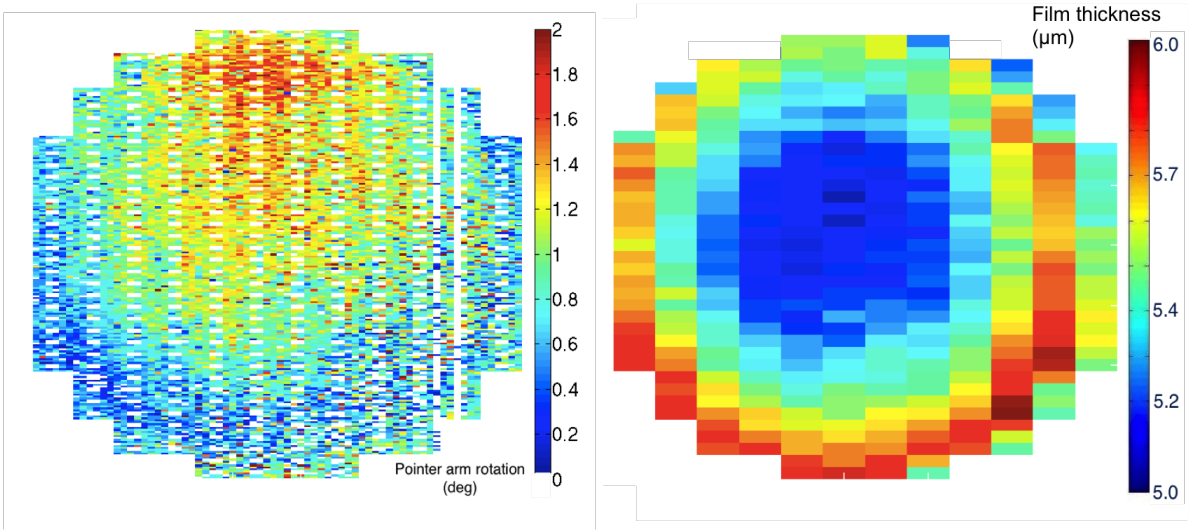

Figure 5.13: Correlation between pointer arm rotation (strain) map and film thickness for W1. Correlation number = 0.63

A very similar radial pattern of thickness variation was observed for W2, which is shown in Figure 5.14 which shows a lower correlation (0.52) with rotation compared to that observed with W1. With W2 showing a thinner film in the center $\sim$ 4.75µm and thicker around the edges (5.5µm - 6.0µm) the similar profiles of both wafers suggest the thickness variation results from the same causes.

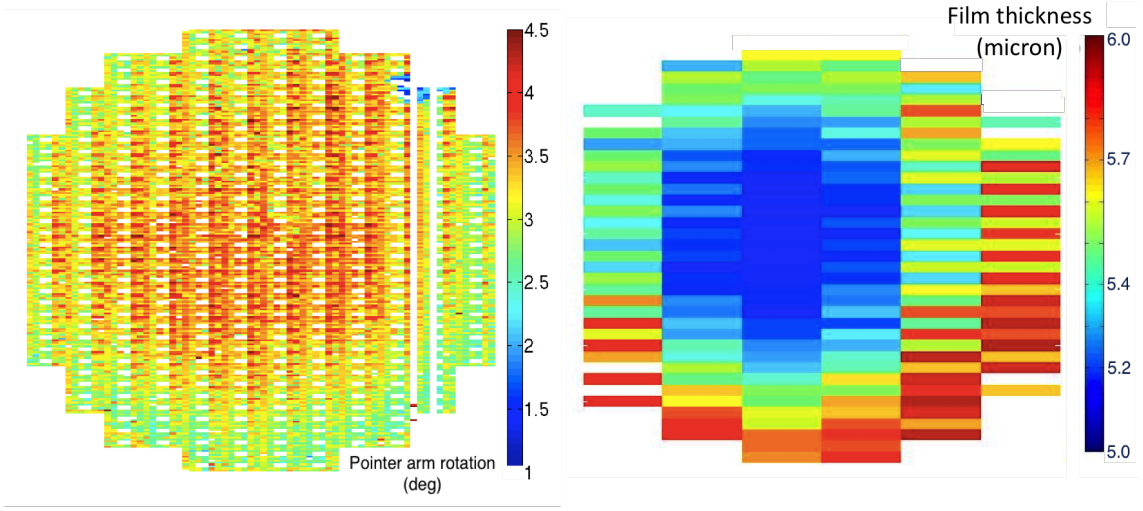

Figure 5.14: Correlation between pointer arm rotation (strain) map and film thickness for W2. Correlation number = 0.52

Electrical cross-bridge test structures were also measured and wafer maps obtained for W1 and W2 at 23°C and in the absence of any magnetic fields. The correlation with film thickness is shown in Figure 5.15. The correlation numbers for W1 = -0.82 and W2 = -0.86 were obtained which were expected as the electrical resistance of metal is inversely proportional to its thickness ($R = \rho\frac{l}{A}$). Negative correlation number therefore appear as the thinner regions have higher resistance. The radial patterns observed show a lower resistance around the perimeter of both wafers. Film thickness, linewidth, bridge resistance and the length of the bridge (240µm) were used to calculate the electrical resistivity (ρ) of the plated films and spatial maps were obtained and are shown in the third column of Figure 5.15. Observing the different sets of spatial measurement together makes it easy to correlates the different parameters. It can be seen that the resistivity of the film is much higher in the center (2.8 - 3.0 $\times 10^{-7}\Omega m$) than the sides ($2.2-2.4\times 10^{-7}\Omega m$). The resistivity peaks ($3.2\times 10^{-7}\Omega m$) at the top of the wafer where the strain and %Fe is maximum. From these observations, the structural properties of the material are clearly influenced by the alloy composition which is expected, although its origin is still unclear.

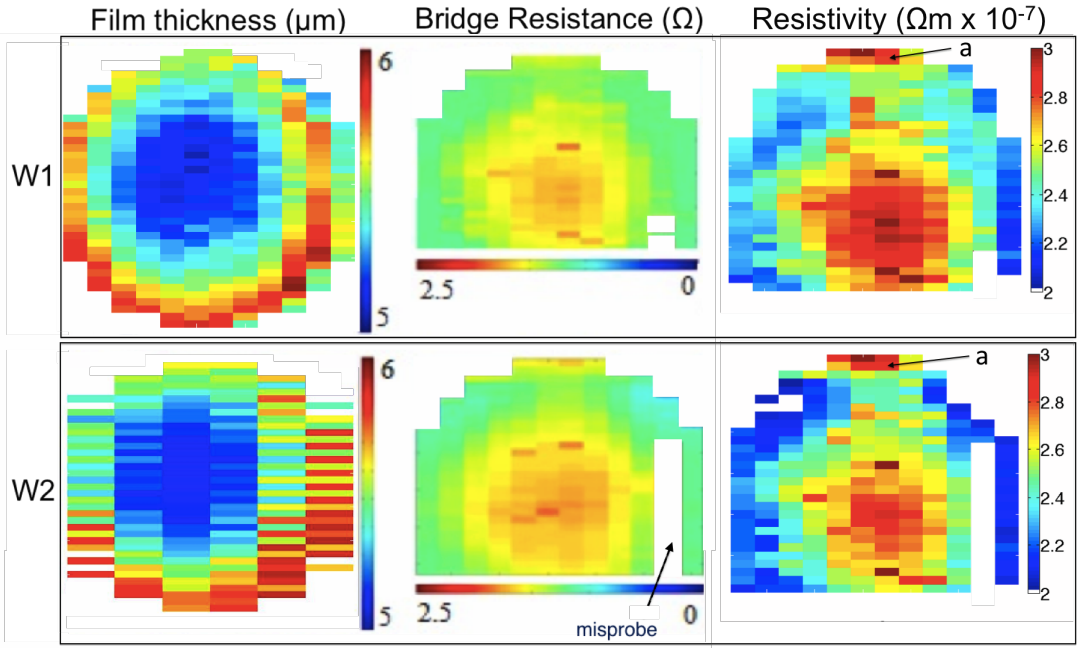

Figure 5.15: Plots of the spatial variations of film thickness, bridge resistance and electrical resistivity for W1 and W2

5.4.2.1 Spatial strain in plated nickel

To further investigate the effect of Fe% on strain, a fresh nickel bath was prepared in the adjacent tank, with the aim to characterise spatial strain in a nickel only film. The concentrations of $NiCl_2$(aq) and other additives were as detailed in Table 5.1, except that there was no $FeCl_2$ in the bath. Nickel was plated and annealed under the same conditions as the NiFe wafer (W2). Test structures were released and pointer rotations (strain) measured before and after anneal.

Figure 5.16 shows the resulting strain maps and there are some prominent features worth further discussion. Clockwise rotations were found everywhere on the wafer indicating tensile stress. The strains before annealing shows a prominent pattern with more rotation in the top-middle of the wafer. A radial ring pattern around the perimeter of the wafer comprised of structures with lower rotations. A similar pattern was observed for the NiFe wafer (W1). After annealing the rotations increased considerably and the strain patterns appear more prominent. Further statistics on 200 test structures were carried out and the resulting rotations were

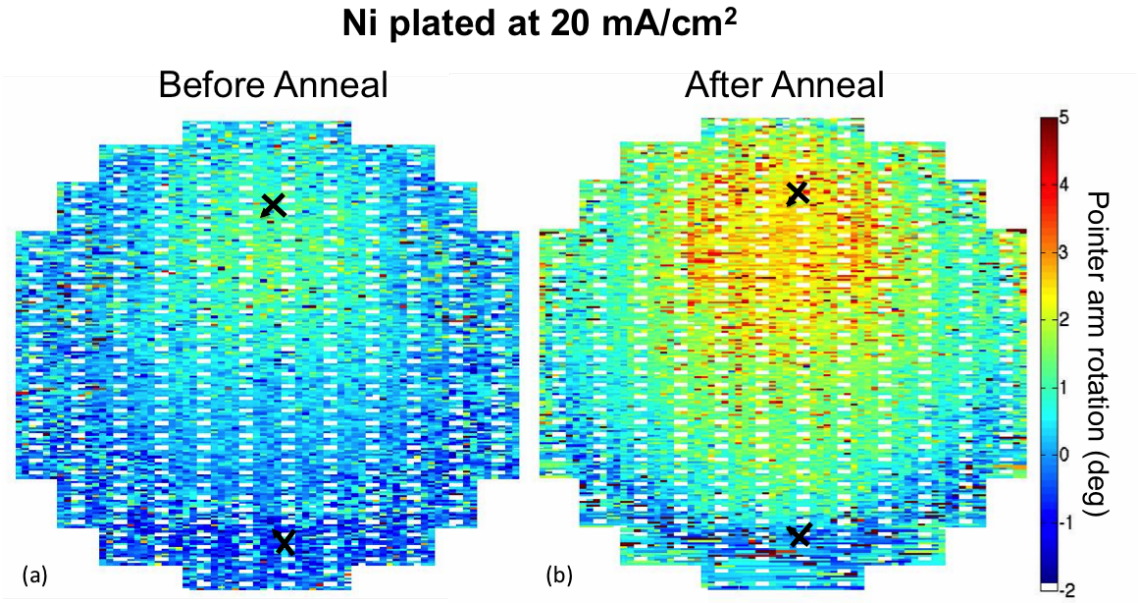

Figure 5.16: Wafer maps of pointer arm rotation (deg) plated in Ni (W0), before and after annealing

plotted against the arm separation:width ratio (Δ Y/W), shown in Figure 5.17. The pointer rotations show no trend with separation ratio within the standard deviations. Around the top-middle of the wafer, average rotations of $0.75° \pm 0.4°$ and around the edges $0° \pm 0.5°$ were observed before annealing. The increase in rotation upon annealing is observed and again the consequence of the flow pattern

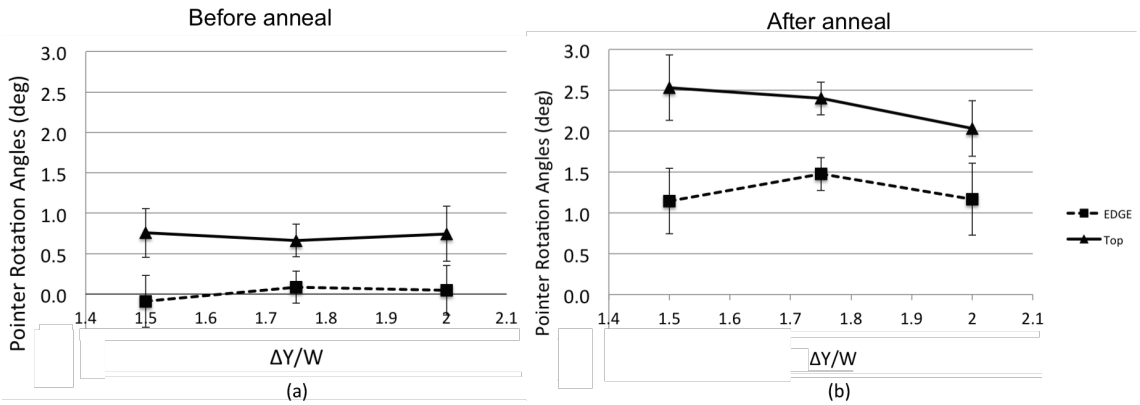

Figure 5.17: Average pointer arm rotations from nickel test structures plotted against arm separation ratio taken from middle and edge of wafer (positions marked with a cross in Figure 5.16)

is clearly visible in terms of non-uniformity in strain in different parts of the

wafer. The non-uniformity in agitation across the film surface has been shown to produce a film with higher strain in regions receiving the direct flow of electrolyte from the jet nozzle. The influence of hydrogen evolution on plating efficiency was examined previously on chip level experiments (Section 4.4.2) and a inversely proportional relationship was observed between strain and the plating efficiency. The reduction of Ni^{2+} and H_2O to nickel metal and hydrogen gas is known to occur simultaneously, within the same potential regimes. Hydrogen could either evolve from the newly deposited nickel surface and escape the solution as a gas bubble or it could absorb in the deposition irregularly forming voids and cracks. In various studies it has also been shown that in an inadequately agitated nickel bath, films produced are dull with streaks and pits mainly due to hydrogen bubbles adhering to the surface during deposition [177][178][179][180]. In another study by Hovestad *et al.* the rate of agitation has shown to affect the codepositon in two opposite ways. Increased agitation, with laminar flow, results in a larger particle composite content by enhancing the particle transfer, from bulk of the electrolyte to the cathode surface. Conversely, too much agitation (turbulent flow) may decrease the particle composite content because particles are ejected from the surface before being incorporated [181][182][183]. A well agitated bath will facilitate the removal of hydrogen adhered to the cathode, which is essential to produce bright and shiny films [184]. However, agitation alone might not block the hydrogen ions penetrating and absorbing into the metal film. The high strain pattern in the regions with direct nozzle flow (Figure 5.16) may suggest this phenomenon. Upon release the film may still contain entrapped hydrogen embedded in the nickel film thus showing low strain value. Soon after annealing, hydrogen entrapped within the metal diffuses out, relaxing the film, thus increasing its tensile stress. This is possibly the reason why a change in rotation was observed in regions with a more vigorous agitation.

The next set of experiments were carried out to qualitatively verify the effect of changing the bath agitation on the film spatial properties such as Fe% and strain.

5.5 Effect of Film Thickness and Agitation

Three more wafers were processed in the original Ni-Fe bath with chemical compositions summarised in Table 5.1. The current density was fixed to 20 mAcm^{-2} for these three wafers, while the plating times set at 12, 24 and 36 mins to achieve a target plating thickness of 2.5, 5 and 7.5 µm respectively (Table 5.2). The

Table 5.2: Thickness and agitation parameters for plated NiFe films

Wafer ID	Plating time (mins)	XRF measured thickness (μm)	Agitation
W3	12	2.5±0.5	Yes
W4	24	5.0±0.5	Yes
W5	36	7.5±0.5	No

agitation in the plating bath has also been changed with respect to the previous experiment. On this occasion, the jet nozzle has been directed diagonally towards the top left for W3 and W4 (shown in Figure 5.18). W5 has been plated without

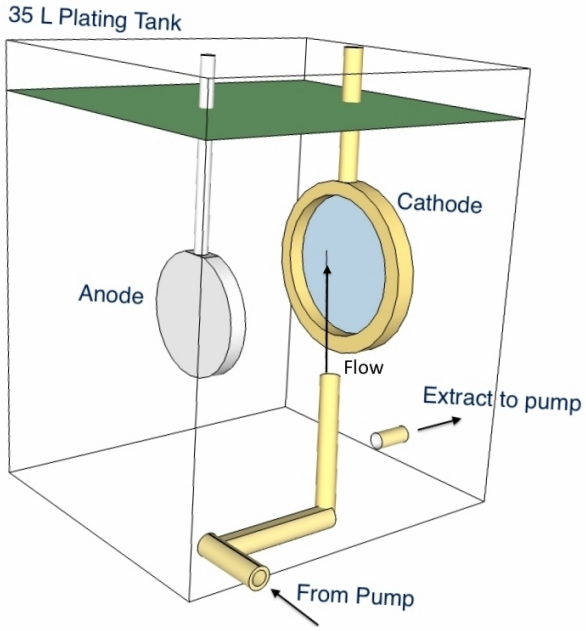

Figure 5.18: Schematic of agitation setup used for plating W3 and W4. Jet nozzle is directed to the top-left of the wafer, also note the angle of the nozzle has changed compared to the previous setup shown in Figure 5.2

agitation to gather additional information about the influence of zero flow on the

properties of the films. All wafers had the test structures released prior to a 10 min / 150°C anneal. The corresponding strain maps and alloy composition are presented in the following section.

5.5.1 Pointer rotation maps

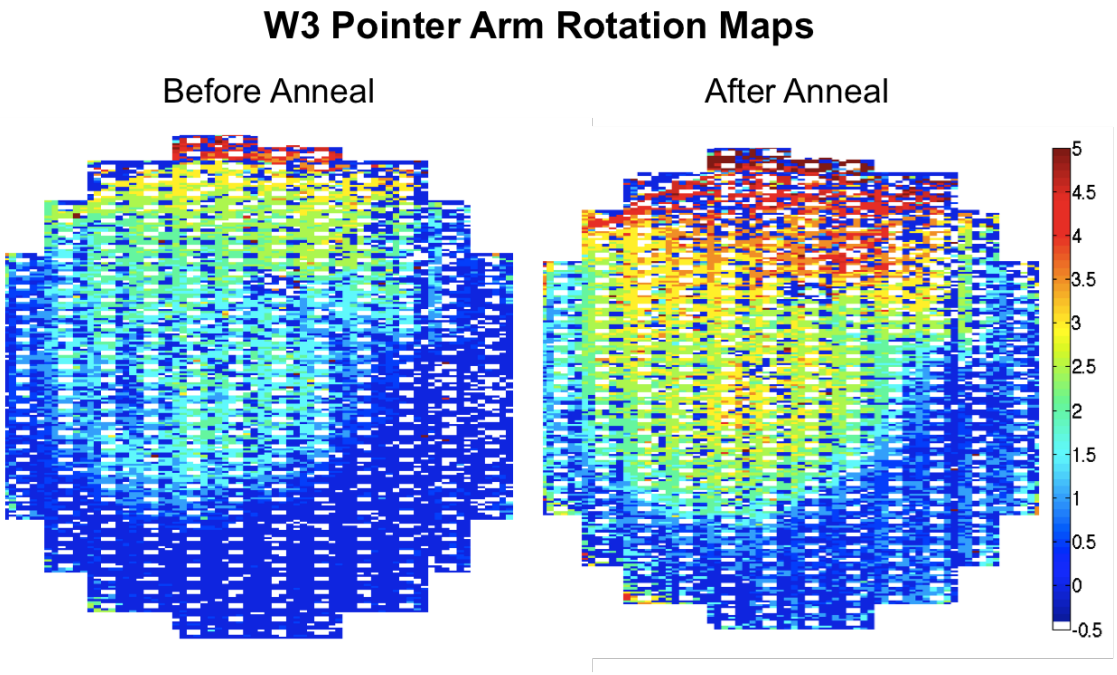

Figure 5.19: Pointer rotation maps of W3 (film thickness 2.5 ±0.5µm) before and after anneal

Figure 5.19 shows the strain (pointer arm rotation) maps of W3 (2.5 µm) before and after annealing. With the direction of agitation nozzle changed, the strain pattern is clearly noticeable. As mentioned previously the wafer is recessed in the holder, and with the fluid flowing upwards there is a high turbulence flow expected at the top of the wafer. This region produced films with different strain levels compared with the levels observed at the bottom perimeter. The pointer rotation varied from 2° at the center to 4.3° at the top with the bottom half of the wafer surprisingly having very low rotations (0° - 0.5°). Upon annealing at 150°C for 10 mins, stress is seen to increase.

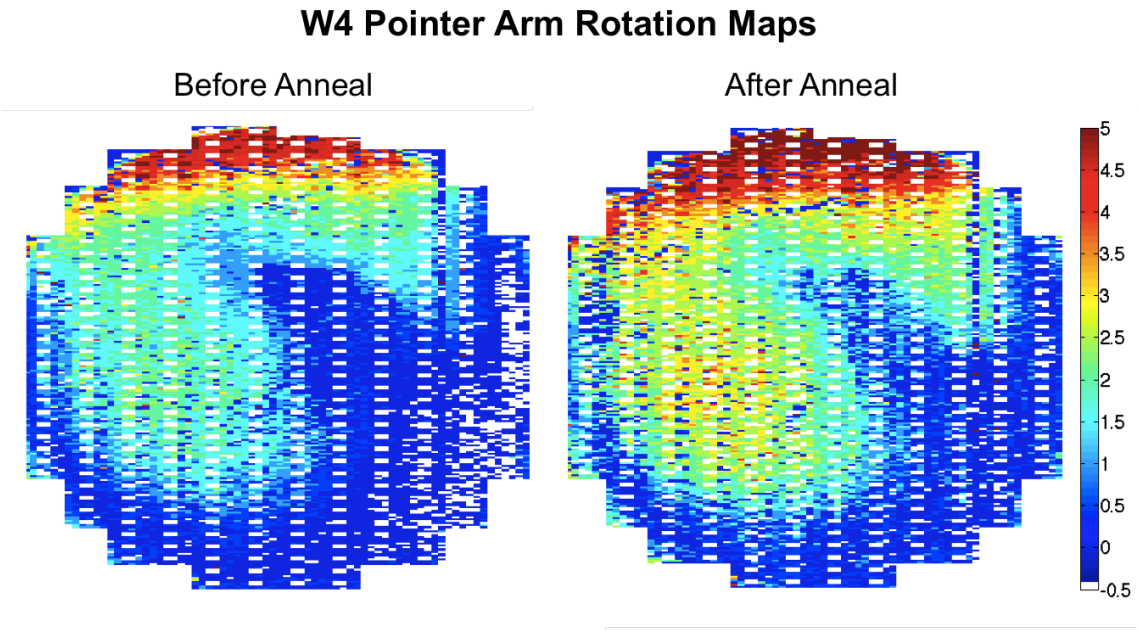

Figure 5.20: Pointer rotation maps of W4 (film thickness 5.0±0.5µm) before and after anneal

W4 plated with NiFe film thickness (5 µm) underwent the same annealing process and the strain maps obtained are shown in Figure 5.20. Identical strain pattern can be observed, which surprisingly are more prominent in this case. The angles ranged from 2.0°-2.5° close to the center, while maximum strain can be observed at the top of the wafer (5°-7.5°). A slight increase of rotation (≈1°) with respect to thickness has been recorded but with a measurement uncertainty of ±0.5°, this change is insignificant.

Figure 5.21 shows the comparison of the film Fe% for W3 and W4. It was observed that the depletion of Ni $^{2+}$ enhances the proportion of Fe^{2+} reduced in that region, where the agitation jet nozzle stream was directed (turbulent), with around 35% iron observed with respect to the rest of the wafer. Regions, where it is postulated that the agitation was more effective, plated only 8-10% iron. A direct correlation between the film strain and iron composition has been observed yet again, which has been discussed earlier in Chapter 4.

AFM scans were performed on W3 to investigate any tangible difference in the topology. Figure 5.22 shows morphology profiles of the electrodeposits, taken at

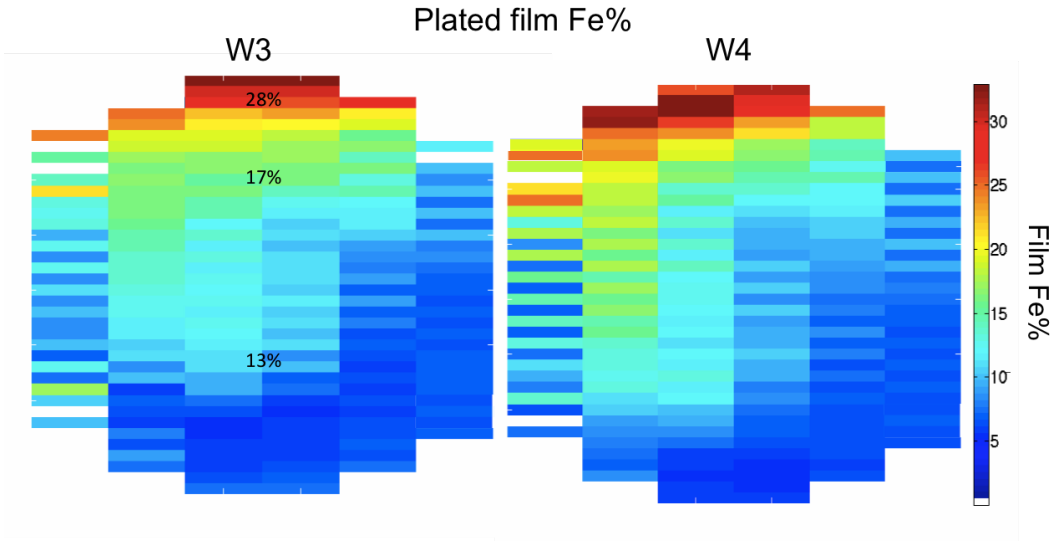

Figure 5.21: Spatial variation of film Fe% for W3 and W4 obtained using XRF

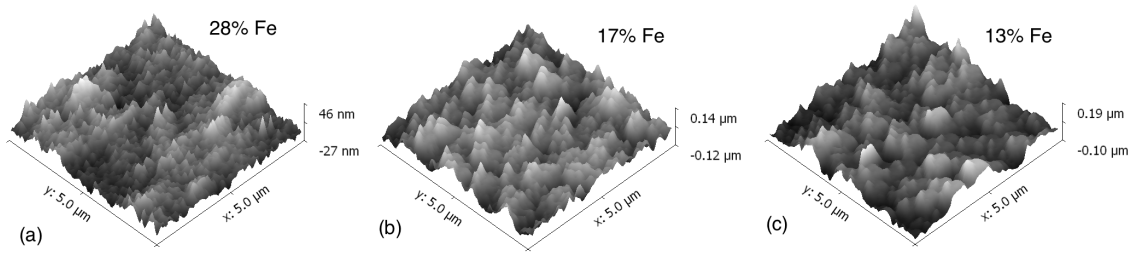

Figure 5.22: AFM scan of three different regions on wafer W3 after annealing where the iron compositions were (a) 28%, (b) 17% and (c) 13% respectively

the top, middle and bottom of the wafer where the average iron compositions were 28%, 17% and 13% respectively. The surface roughness increases from top to bottom, with measured values of 46 nm, 140 nm and 190 nm respectively, as a results of the non-uniformities introduced by the agitation in the bath.

Figure 5.23 shows maps of W5 which looks very different from those discussed previously. This was the wafer plated with no agitation and it can be seen that the film strain is very low and far more uniform over the surface. Annealing does not change the rotations, which may suggest that the film is already relaxed as it may have been deposited will a low hydrogen inclusion within the grains. The Fe% distribution on this wafer is much lower ($\approx 7\%$) but more uniform compared to the previous wafers.

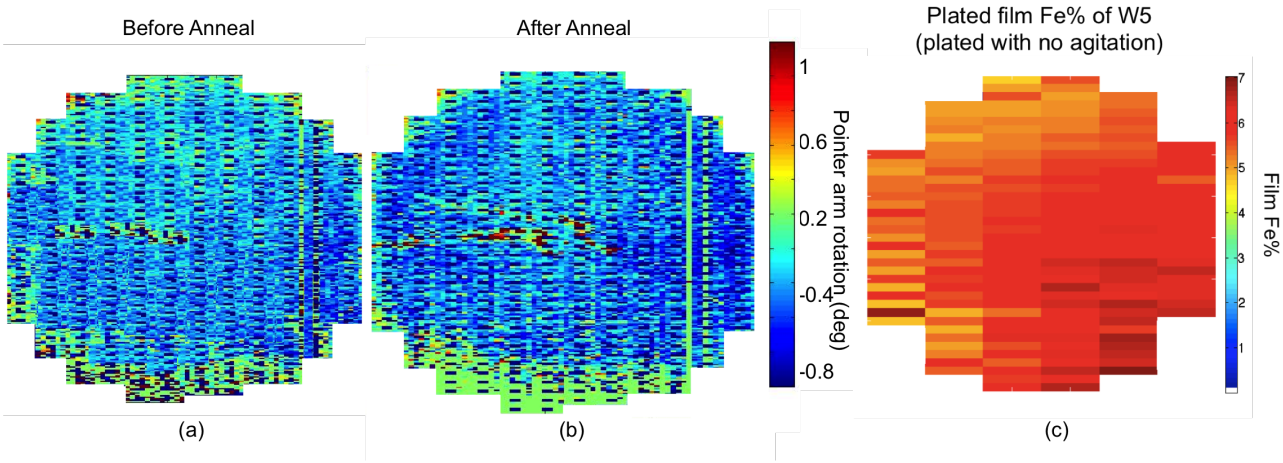

Figure 5.23: W5 Strain map (a) before anneal (b) after anneal (c) Spatial maps of film Fe%. W5 was plated at 20 mAcm^{-2} to achieve a 7.5µm thickness and NO agitation was used

In summary, the rotation pattern of the stress structures reflected the fluid flow pattern in the bath, following a similar distribution to that seen for iron composition and less prominently for the overall film thickness. Due to the high density of stress test structures on the wafer the pointer arm rotation maps shows a more detailed stress pattern in the NiFe film. The maps also illustrate that annealing uniformly increases the rotation angles over the wafers, adding an additional 1.5° on average for W3 and W4. By comparing results for the two wafers we see that before annealing the rotation was greater for the thicker deposits (W4). W5 was plated in a stagnant bath which produced a film with low compressive stress, which may suggest that the film is less defected and the grains are already in a relaxed state. No significant change in rotation was observed after annealing. The most uniform film iron composition was also achieved in the absence of agitation.

In a previous study of nickel deposition on rotating disc electrodes conducted by Andricacos *et al.* [176] the data showed that in a nickel only bath there was no effect of agitation on the nickel deposition reaction. At two different rotating disc speeds (100 and 1600 rpm) the Tafel plots exhibited the same slopes. But in the presence of Fe^{2+}, the polarisation curves are shifted more negative (cathodic)

which may indicate that Ni deposition is inhibited when Fe is codepositing. Another observation was that at a low rpm the Tafel slopes were similar to that of pure nickel. Increased agitation accentuated the inhibition effect, but only in the potential region where the Fe deposition reaction was mass-transfer influenced. As the Fe(II) in the bath is just 1.1%, compared to Ni(II), this observation could suggest that the inhibition effect is primarily dependent on the flux of Fe^{2+} to the electrode surface. This may explain the high iron content in regions with a direct jet spray as can be observed in Figures 5.11 and 5.12.

5.6 Conclusions

The key properties of electroplated NiFe films for MEMS applications have been spatially investigated using a combination of test structure measurements and other characterisation techniques. The power of the approach presented in this work is the wafer mapping of all the important performance parameters of the electroplated film, thereby providing an excellent visualisation of their variation and interactions.

This approach can potentially be applied to any micromachined material using test structures and can be employed to optimise processes by providing a means to monitor residual stress non-uniformities resulting from specific process steps used during the microfabrication process. The measured tensile residual stress was mapped at the wafer scale for two NiFe films electroplated on 200 mm Si wafers, yielding values ranging from ∼50 MPa to ∼220 MPa. Blanket wafers were also plated and Stoney's equation was used to calculate the overall stress of this wafer which matched the stress values obtained from the test structures.

This work has also highlighted that the sheet resistance wafer map, as should be expected, correlates with the current density distribution during the electroplating process and therefore the thickness of the plated film. Wafer mapped XRF measurements have indicated that stress in NiFe films correlates with the electrolyte agitation in the bath. This study also indicates that the stress test structure

results are consistent with other measurements, and have advantages over wafer bow measurements which are globally confounded with stresses contributed by other layers.

The importance of agitation on iron composition and stress has been demonstrated and is clearly an aspect of the ECD process that needs to be carefully considered when electroplating permalloy. The relationship of plating efficiency with hydrogen absorbing which may cause voids and ultimately more stress in regions where there is turbulent agitation. Increasing the agitation increases the probability of a lower concentration of metal ions reducing at the cathode surface, while removing the agitation, at the chosen current density produces a more uniform alloy film with low stress.

Chapter 6

Self-Annealing Studies of Electrodeposited Copper Films

6.1 Introduction

Electrochemically deposited (ECD) copper is known to undergo room temperature recrystallisation. This is known as self-annealing and was initially observed in 1944 [185]. ECD copper, patterned using the damascene process, is widely used in the semiconductor industry for interconnects [186], and in this application it is important to be able to characterise and ultimately control changes in film characteristics which arise during self-annealing from the changes in microstructure and grain growth with time. These changes can modify device behaviour, but their effect can be largely controlled by performing high temperature annealing of the interconnect copper.

More recently, however, copper has been employed for other applications, such as through silicon vias for 3D integration and the windings in microscale inductors [187]. In some of these processes high temperature annealing of the ECD copper is not possible and self-annealing has become an important issue which can potentially affect the reliability of circuits and devices. This room temperature phenomenon is known to be initiated by dislocation and the diffusion of grain boundaries [188][189] and the metallurgical term 'self-annealing', is used to describe the entire process [185].

Three stages with respect to time have been identified in this self-annealing process, namely the incubation period, which shows little changes in the film

characteristics, the transition period during which the film characteristics change and the stable period, where there is no further change in film characteristics [190]. Film resistivity and strain are the most important global parameters for documenting the progress of self-annealing as the change in resistivity is closely connected to microstructure evolution. These have been measured, in this work, using test structures to characterise for the first time their variation both with time and spatially across the wafer surface, to gain an insight into the rate and spatial distribution of the self-annealing process across the wafer.

6.2 Experimental Technique

The aim of this study was to compare the effect of different plating conditions such as plating current density, bath additive:carrier ratio and film thickness, on the self-annealing rates of ECD copper.

Three 200 mm wafers named (W1, W2 and W3) were prepared, with Cu electro-

Table 6.1: Copper bath composition and conditions for plating on 200 mm wafer

Bath contents	**Concentrations**
Dow Intervia $CuSO_4.5H_2O$	120 g/l
Sulphuric acid	190 g/l
HCl	50 mg/l
InterVia Cu 8540A (Additive)	5 ml/l
InterVia Cu 8540C (Carrier)	5 ml/l
Temperature (°C)	24 ± 1
pH	1.0
Anode Bag	Polypropylene
Agitation	Spray nozzle agitation

plated using a bath with the chemical compositions shown in Table 6.1. Details of the fabrication process are given in section 3.4.1. The test structure mask, previously presented in Figure 3.12, was used to pattern 7.5 µm thick photoresist

which acted as a mould for ECD. The first part of this study investigates the effect of plating current density shown summarised in Table 6.2. The automated

Table 6.2:
Copper plating parameters

Wafer No.	**Wafer diameter (mm)**	**Plating rate (µm/min)**	**Current density J (mA cm^{-2})**
W1	200	0.11	5.00
W2	200	0.22	10.0
W3	200	0.44	20.0
Target thickness for all wafers 3.5 μm			

measurement system used to monitor the changes in copper strain and resistivity over time consisted of a Suss Microtech PA200 semi-automatic prober, HP4062UX based semiconductor parameter analysis equipment and a camera on the wafer prober, all of which was controlled by a PC based LabView system. In addition to electrical measurements the system captures images of the strain test structures (see Chapter 3.8) and has been explicitly configured to ensure the reliability and robustness of critical time sensitive measurements by removing any user interaction during the process.

Figure 6.1 shows the location of the 190 structures that were measured on each wafer. The choice of current for Greek-cross and bridge resistance measurements was critical, as higher values can induce Joule heating which could escalate the self-annealing process. Therefore, a series of currents were applied continuously and the resistance change measured on a dummy wafer and the optimum currents chosen were 100 mA for the Greek-cross and 0.05 mA for the Kelvin bridge resistance measurements (detailed method described in [191][122]). The pointer arm angle of rotation were recorded simultaneously with the resistance measurements every 15 minutes for a total period of 45 hours.

After ECD, seed etch and test structure release the wafer was transferred to the test tool where it was aligned and the test procedure executed within 15 mins.

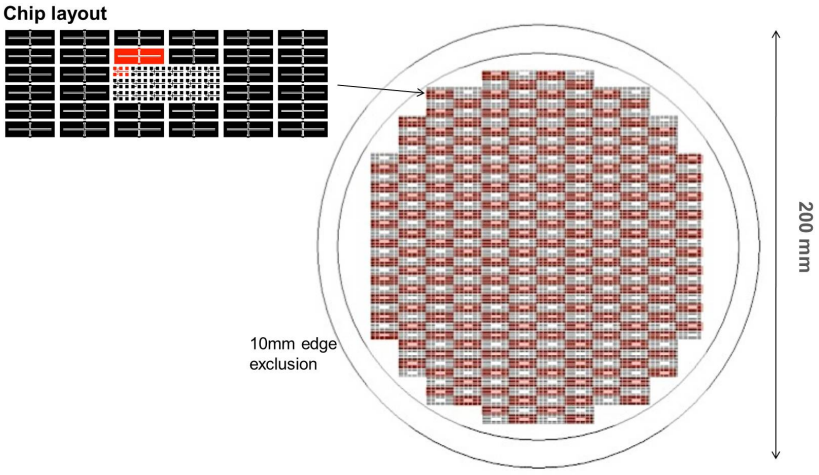

Figure 6.1: Chip and wafer layout of the 200 mm wafer with the 191 structures shown in red

At this point the total time elapsed since the start of the copper deposition was ∼60 mins (15 mins for plating, 5 mins for seed removal and 40 mins for the release process). This delay before any measurements, needs to be considered in the presentation of results, assuming that copper starts recrystallising as soon as it is electroplated.

6.3 Results and Discussion

6.3.1 Resistance change

Figure 6.2 presents the three phases of recrystallisation namely incubation, transition and stabilisation which were observed from the resistance measurement of a structure on W2. The incubation period can be seen as the constant initial resistance, at the beginning, which stays constant for $\sim$ 5 hours, before leading into the transition regime where a $\sim$ 20% resistance drop is observed. A steady state resistance is finally achieved 14 hours later, which represents the end of recrystallisation and is known as the stabilisation period. Having reached the final resistance, identified as a dotted line in Figure 6.2, its magnitude has been confirmed by re-measuring the same value on the structure 6 months later. These

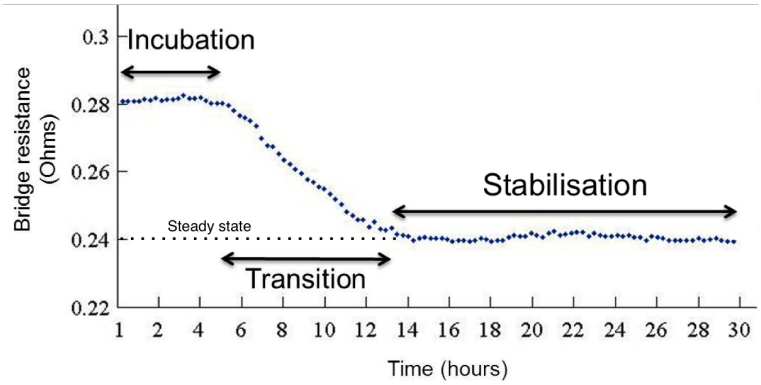

Figure 6.2: Resistance change of a copper test structure showing the three periods of self annealing

three periods, identified in Figure 6.2, are of interest in defining the self annealing characteristics of electroplated copper.

Figure 6.3 shows the change in bridge resistance for the top and middle structures on the three wafers. The slowest decrease in resistance (0.115% per hour) can be observed for W1. The exact period of recrystallisation for this wafer cannot be judged from the 20 hours measurement, but a steady decrease was apparent. A cross chip variation in the initial resistance value was also observed which suggests non-uniformity in film thickness. W2 plated at twice the current density (10 $mAcm^{-2}$) annealed at a much faster rate with the bridge resistance decreasing more than 1.50% per hour, while for W3 (plated at 20 $mAcm^{-2}$) this drop was the largest at 3% per hour during transition period. Unfortunately, there were large variations between resistance of structure and also annealing rates, and quantitative analysis could not be conducted on this data. Thickness measurements were performed, using Dektak on six structures in the top and middle of the wafer and 23.2% variations were obtained which could explain the above anomaly. Upon further investigation, the additive and carrier concentrations in the bath were measured (method described in Appendix B.4), which were 1 ml/l and 3 ml/l respectively, while the expected concentrations were 5 ml/l for each. This decrease in concentration with time of both additive and carrier would have caused the film texture and thickness to vary for each plated wafer and therefore

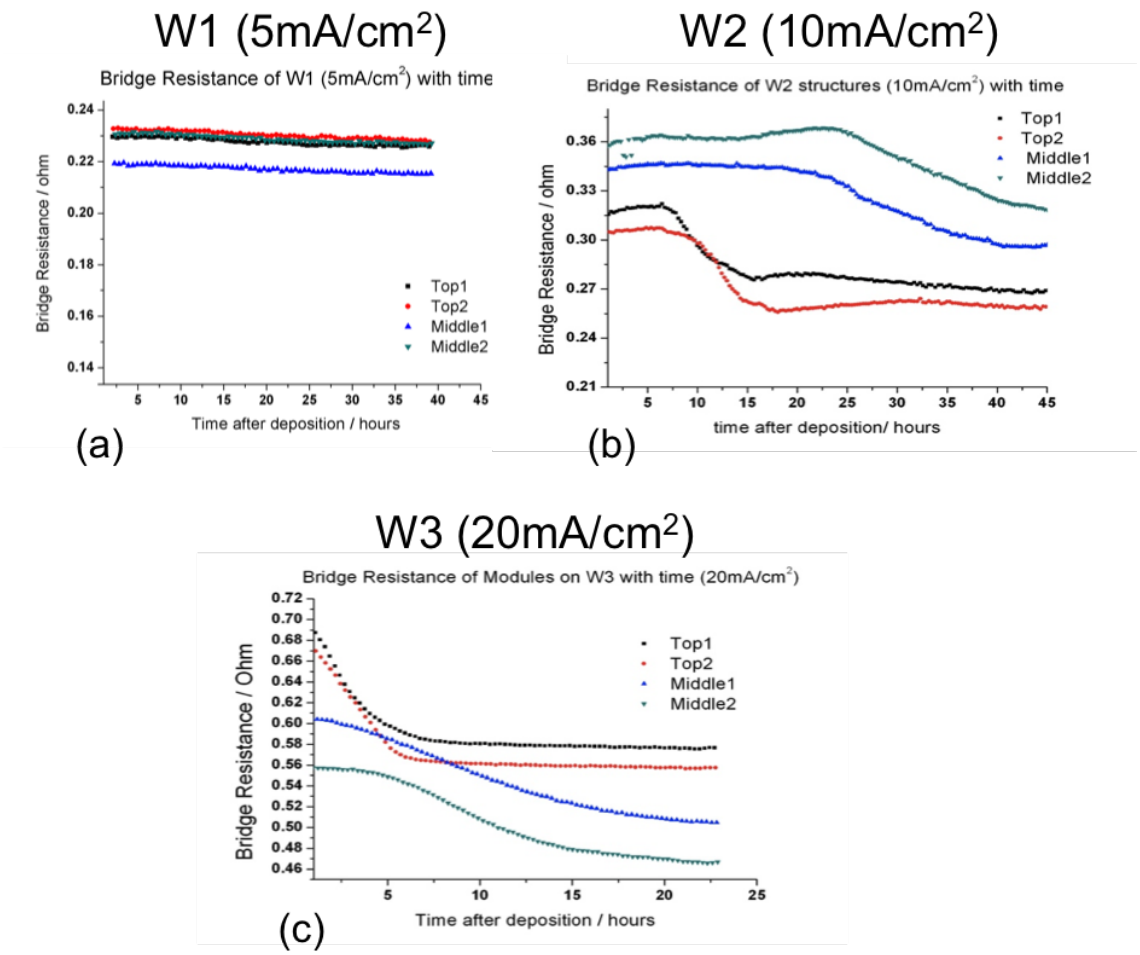

Figure 6.3: Variations in bridge resistance measurements taken from test structures located at different locations on the wafers (a) W1 (5 $mAcm^{-2}$) (b) W2 (10 $mAcm^{-2}$) and (c) W3 (20 $mAcm^{-2}$)

had to be considered for future experiments.

6.3.2 Stress Test Structure

The strain test structure release process achieved a poor yield with 15% because of stiction. Compared to nickel whose Young's Modulus is $\sim$ 200 GPa [192], copper has a value ranging from 110-128 GPa [193]. This means that nickel is $\sim$60% stiffer than copper and the chances of copper buckling after release and sticking to the substrate is much higher. Full wafer maps could not be obtained for any wafer, however, results from some functioning structures are shown in Figure 6.4. An

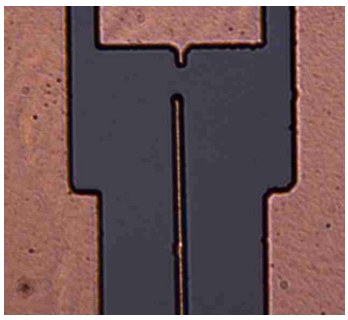

Figure 6.4: Pointer arm after release showing 0.5°anticlockwise rotation indication compressive stress in W1 (5mA cm^{-2})

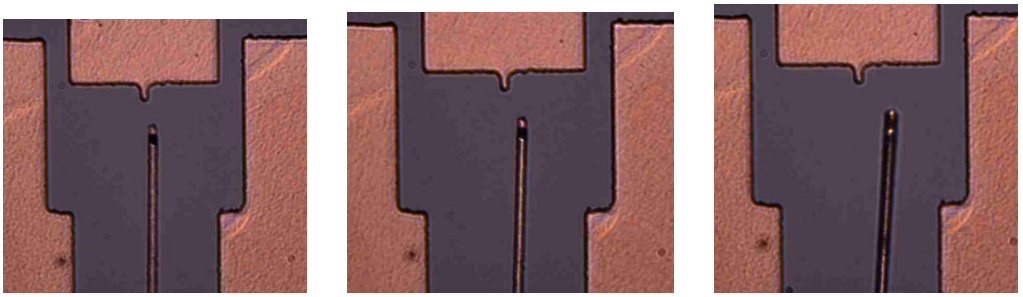

Figure 6.5: Pointer arm position of a plated a test structures from the perimeter of W3 (20mA cm^{-2}) at times 1, 5 and 20 hours (from left to right)

anticlockwise rotation of 0.5° was recorded for W1 which indicates compressive stress. Figure 6.4(a) shows the test structure after 30 hours which recorded no change in rotation. Interestingly, a transition from compressive to tensile was observed for W2, with angles changing from -0.3° to +1.6° during 30 hours. Finally, W3 recorded the highest change in strain, from +0.2° to +2.3° within 20 hours, which can be observed in Figure 6.5. The pointer tip, for this structure, can be observed to have buckled upwards after 20 hours which indicates an out of plane distortion due to an additional stress gradient through the thickness of the copper film. These strain test structures are well suited to measure both tensile and compressive strain, provided that the expansion of strain is translated into in-plane rotation and not buckling.

Both electrical and optical measurements were carried out simultaneously, but only the electrical results have been wafer mapped, as the yield of the released structures were poor as mentioned earlier. Figure 6.6 show the change in Kelvin-bridge resistance for wafers W1, W2 and W3 measured 1, 5 and 20 hours after

plating. Higher resistance around the perimeter of W1 is observed, however no

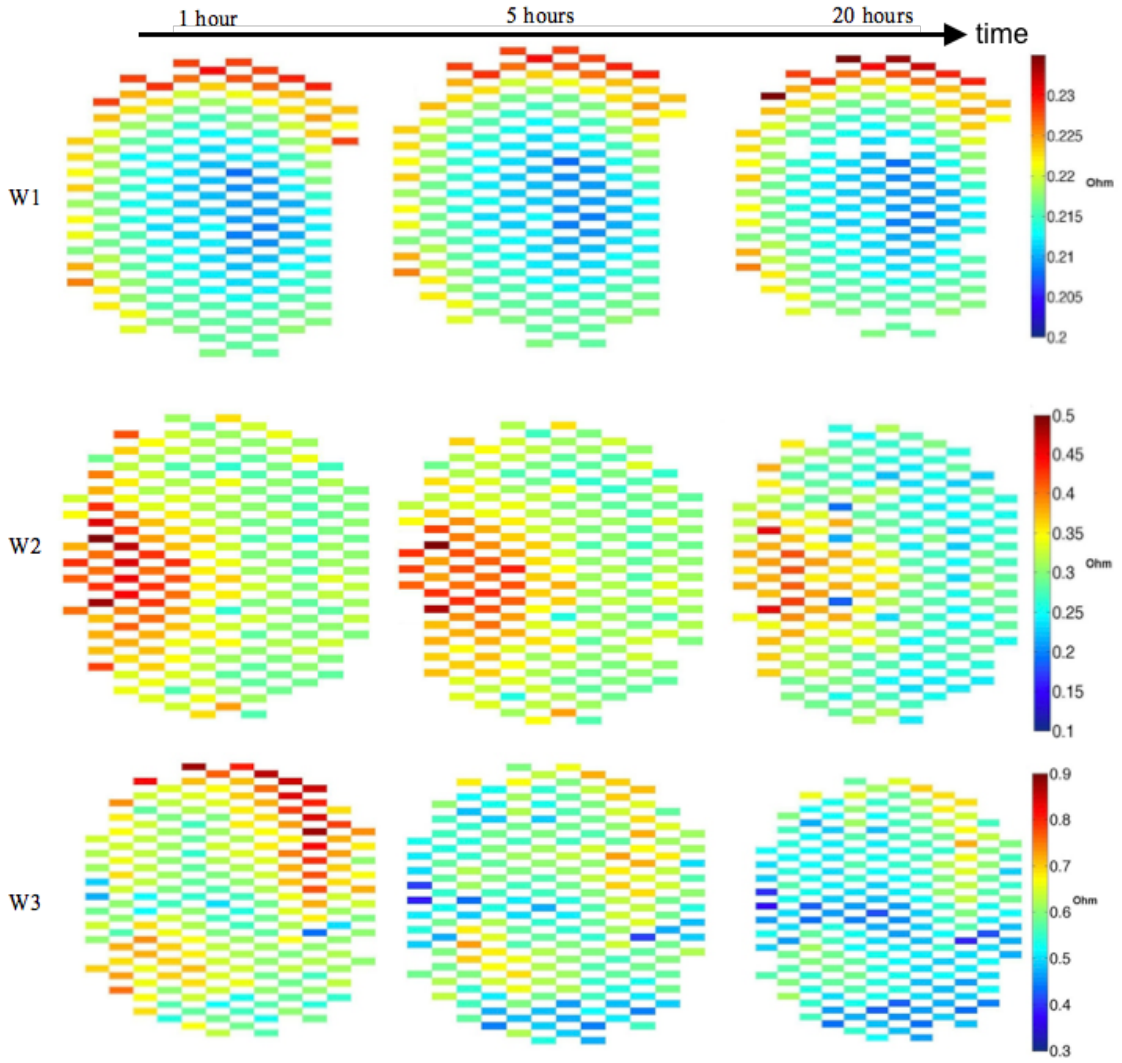

Figure 6.6: Resistance maps (from *bridge test structures*) for the 200 mm wafers (W1, W2 and W3) for times of 1, 5 and 20 hours after electroplating

significant change in the pattern is recorded within the 20 hours. W2 however shows a different resistance pattern compared to W1 with higher values recorded in the left half of the wafer. A drop in resistance can also be observed after 20 hours. A different resistance pattern can be seen for W3 which changes as the resistance drops 5 hrs and 20 hrs after deposition. It was surprising to see these different variation across the three wafers, which could be because of the non-uniform agitation and distribution of additives around the wafer surface which caused the film thickness to vary considerably, however the exact reason was

unclear.

Although this experiment proved to be successful, as a system in observing resistance and strain changes simultaneously, it highlights the need to more rigorously maintain bath additive/carrier concentrations to better understand the effect of various parameter settings.

Summary of experimental issues:

- Each wafer sample was plated and tested individually, with at least 2-3 days difference between successive samples.
- Bath conditions (additive/carrier concentrations) were not monitored for each plated wafer.
- Strain structure release was not optimised for copper, resulting in a poor release yield ($< 25\%$) on all wafers.
- For best results, all wafers should have been plated with the same bath conditions and tested simultaneously to rule out any temperature or humidity variations in the test lab.

6.4 Plating under controlled additive/carrier concentrations

6.4.1 Improved experimental setup

Based upon the results from the initial experiment, the following approach was applied to eradicate the issues identified above. Firstly, the copper bath was re-prepared, and a system was setup to monitor the additive and carrier concentration using a Titraplate CVS analyser (method described in Appendix B.4). In addition, the effect of these additives on the re-crystallisation of copper and the non-uniformity in the deposited layer has also been taken into account. To make sure the experiment proceeded under the same conditions, smaller 75 mm wafer substrates were plated consecutively, but released and measured simultaneously. The release method was optimised, in the Memsstar HF tool, to process four 75 mm wafers at the same time. It was also decided to deposit a thicker (1.5 µm) sacrificial layer on each 75 mm wafer to make the release process more robust. Finally, the HF vapour chamber pressures were also precisely monitored so to minimise generation of water which could facilitate stiction during release.

The test prober was setup to measure four 75 mm wafers simultaneously to obtain both electrical and optical properties. This was achieved by first aligning and then physically glueing the 75 mm wafers on a larger dummy 200 mm wafer. This wafer was mounted on the prober chuck and the test system run for 30 to 90 hours, depending of the experimental requirements.

6.4.2 The effect of plating current density

Table 6.3: Plating current densities investigated for Cu self-annealing

Wafer	Plating rate (µm/min)	Current density J ($mAcm^{-2}$)	Plating thickness µm	A[Additive] (ml/l)	C[Carrier] (ml/l)	A:C
1	0.11	5	2.5	5	5	1:1
2	0.22	10	2.5	5	5	1:1
3	0.44	20	2.5	5	5	1:1
4	0.66	30	2.5	5	5	1:1
Bath temperature = 23° C						

In this study, four 75 mm wafers were plated with 2.5 µm Cu using the current densities summarised in Table 6.3. The bath additive and carrier concentrations were both kept constant (5 ml l^{-1}). After plating, the test structures were released and measured for changes in the resistance and strain.

Figure 6.7 shows the decrease in resistance with increasing current density obtained from the as-deposited Cu films. This can be explained from the principle

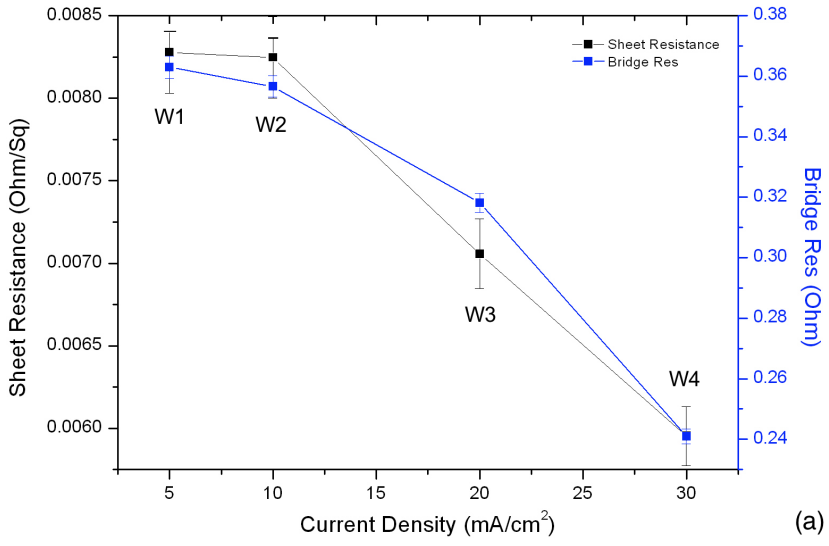

Figure 6.7: Sheet and bridge resistance of as-deposited Cu films

of electrocrystallisation where the rate of nucleation (ω) [1] on the electrode surface is exponentially related to the squared cathode polarisation (η) [195]:

$$\omega = \mathrm{B} \exp\left(-\frac{K}{\eta^2}\right) \tag{6.1}$$

where B and K are constants for a given metal at steady state conditions. This suggests that the increase in cathode polarisation (which increases with the plating current), will result in a large number of newly formed nuclei, producing a denser film with a uniform grain distribution and a lower resistivity [196, 197]. Another factor is the possibility of organic impurity incorporation in the film as a function of current density which can also effect the arrangement of the grains and the corresponding sheet resistance.

The wafers were measured for a further 90 hours, for changes in microstructure evolution, and the average bridge resistance with time has been plotted in Figure 6.8. The three phases of recrystallisation can be clearly observed for the wafer samples plated at low current densities (5 and 10 mAcm^{-2}). While for 20 and 30 mAcm^{-2} the incubation period have already passed during post-plate processing (etch/release), so only the transition and stagnation periods were captured. Another interesting observation was the rate at which recrystallisation was taking place during the transition period. Slope of the sigmoid, representing the rate of self-annealing during the transition period, has been calculated and represented on the same figure indicated with an arrow. The slowest transition was for W1 which occurred between 18 and 65 hrs with the resistance decreasing at a rate of 0.52% / hr (1.9 mΩ / hr). The largest change was observed for W4 where the resistance decreased at 5.90% / hr ($\simeq$ 14.2 mΩ / hr). This clearly

1. *Nucleation* is the process of forming a nucleus and is considered to be a very important process in metal deposition. The competition between growth and nucleation determines the granularity of the deposit. The higher the nucleation rate during deposition, the finer are the crystal grains of the deposit. On the other hand, the forms of the growing crystals determine the general appearance and structure of the deposit. With a higher growth rate of the crystal grains normal to the substrate surface, for instance, a fibrous structure of the deposit is obtained. Or, with large developed crystal faces parallel to the substrate a brightening effect can be achieved [194]

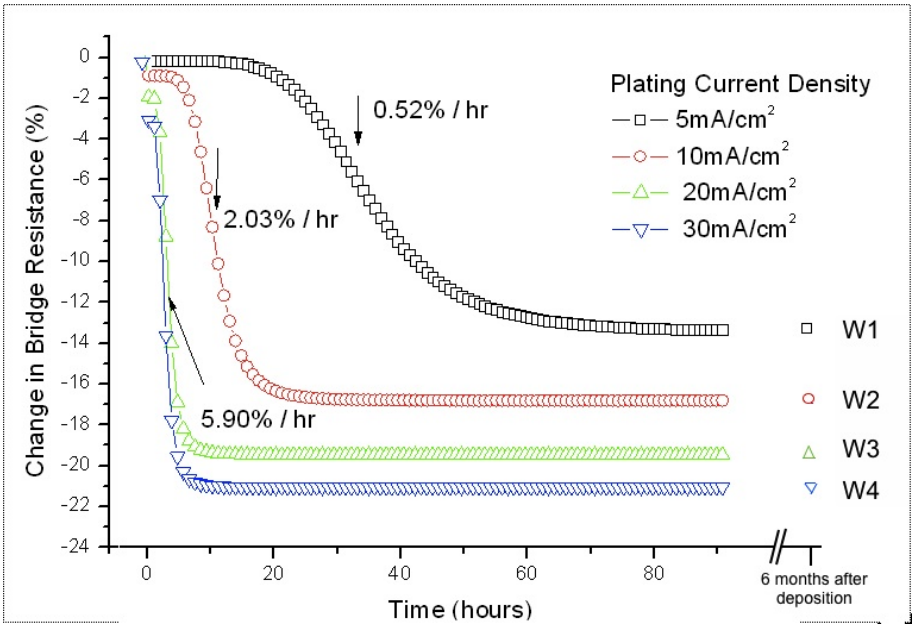

Figure 6.8: Normalised change in bridge resistance with time of samples plated at different current densities

suggests that the self annealing rate increases with the plating current density. The incubation and transition periods have been extracted from these plots and an exponential relationship with current density was achieved as seen in Figure 6.9, which may correlate with the exponential formation of nucleation sites with cathode polarisation. The acceleration in self-annealing observed here is expected

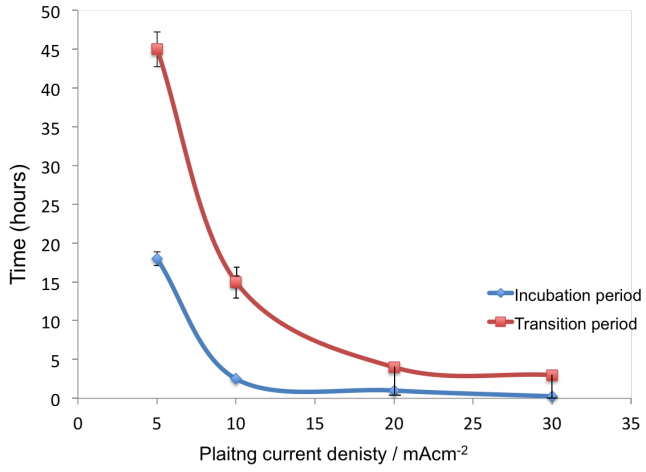

Figure 6.9: Incubation and transition periods extracted from the plots in Figure 6.8

as the crystalline defect density increases, when Cu^{2+} ions are forced to reduce at

a fast rate, causing the Cu to segregate randomly around protrusions or corners especially where the electric fields are high [196]. This would ease and speed up the transformation process. It is also interesting to note that the incubation period is always smaller than the transition period which also scales down with increased plating current densities.

The randomness of copper reduction around protrusions as described above was investigated by measuring the variations in resistances of a few individual grains packed at the center of closely located Greek-cross test structures on W1, shown in Figure 6.10(a). These have been compared with the standard bridge resistances of

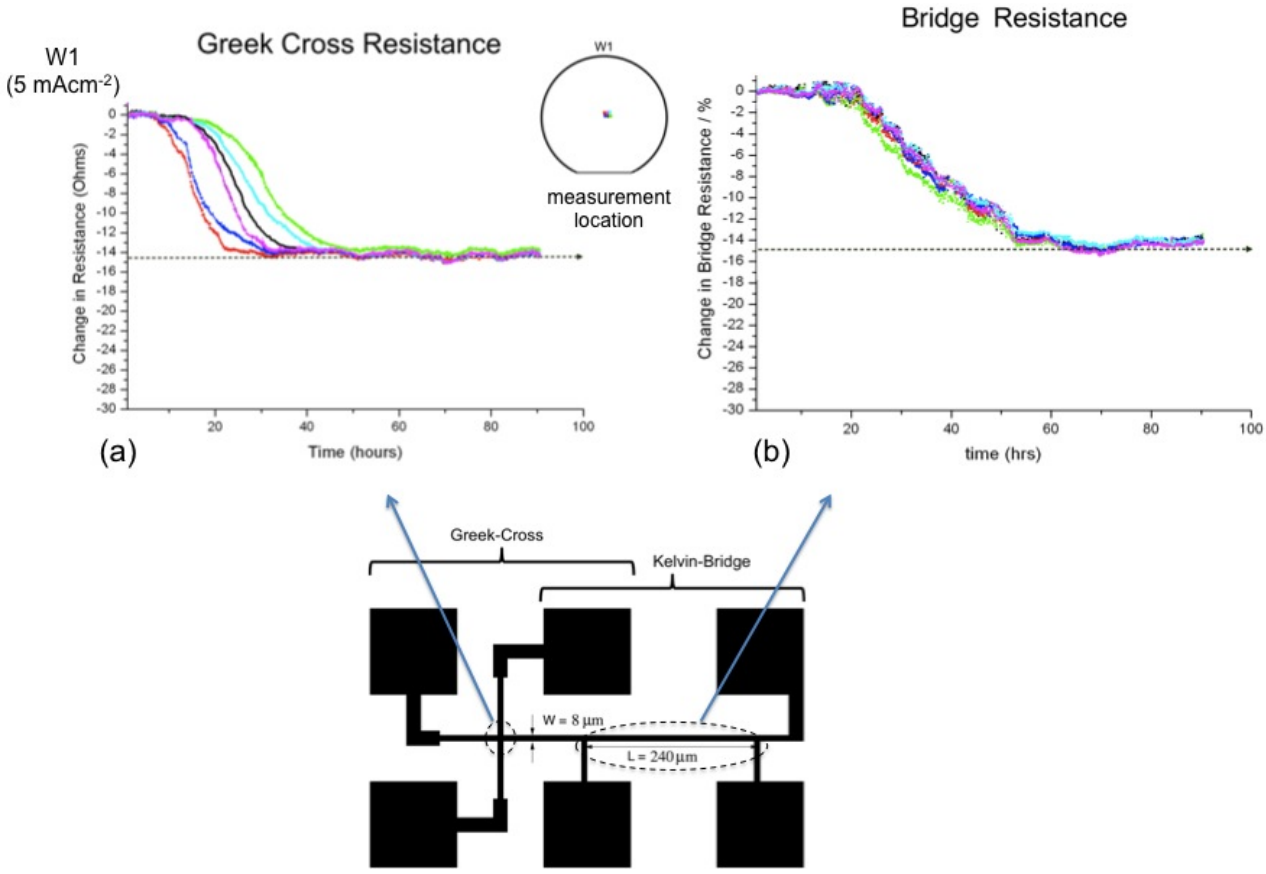

Figure 6.10: (a) Greek-cross and (b) Kelvin bridge resistance measurements with time obtianed from six tests structures located in the center of W1. The dashed lines indicate the stabilised resistance measured 6 months after deposition

the same test structure in Figure 6.10(b)) and a variation in incubation period is clearly visible, which suggests that the defect density of packed grains in the small

geometrical area (8 × 8 µm) varies from structure to structure. The probability of having an identical grain distribution on all the structures in this area is very low, therefore variation in self-annealing rates are expected.

Conversely, on the Kelvin bridges structures, the resistance is measured over a longer length (240 µm), which averages the resistances of all the grain configurations in the path, hence providing a stable measurement of self-annealing rate over time. From these observations and the discussion it can therefore be suggested that both the initial nucleation process and the packed density of electrodeposits determine the rates of self-annealing.

The bridge resistances were also mapped for the four wafers and are presented in Figure 6.11. There was a peculiar high resistance patch on the bottom left region of W1,W2 and W3. Upon investigation a small leak was found in the wafer holder which may have caused an uneven current crowding, resulting the film to be 5% thinner in this region. The average film thickness obtained of all four wafers was 2.3 µm with $\sigma = 3.7\%$, with films being slightly thicker in the center. However, these films were more uniform compared to the previous experiment where the additive (brighteners and levellers) concentrations were not monitored prior to plating. The change in resistance at times 1 hr, 30 hr and 80 hr for W1 and 1 hr, 8 hr and 20 hr can be clearly seen from the colour change of all the wafer maps.

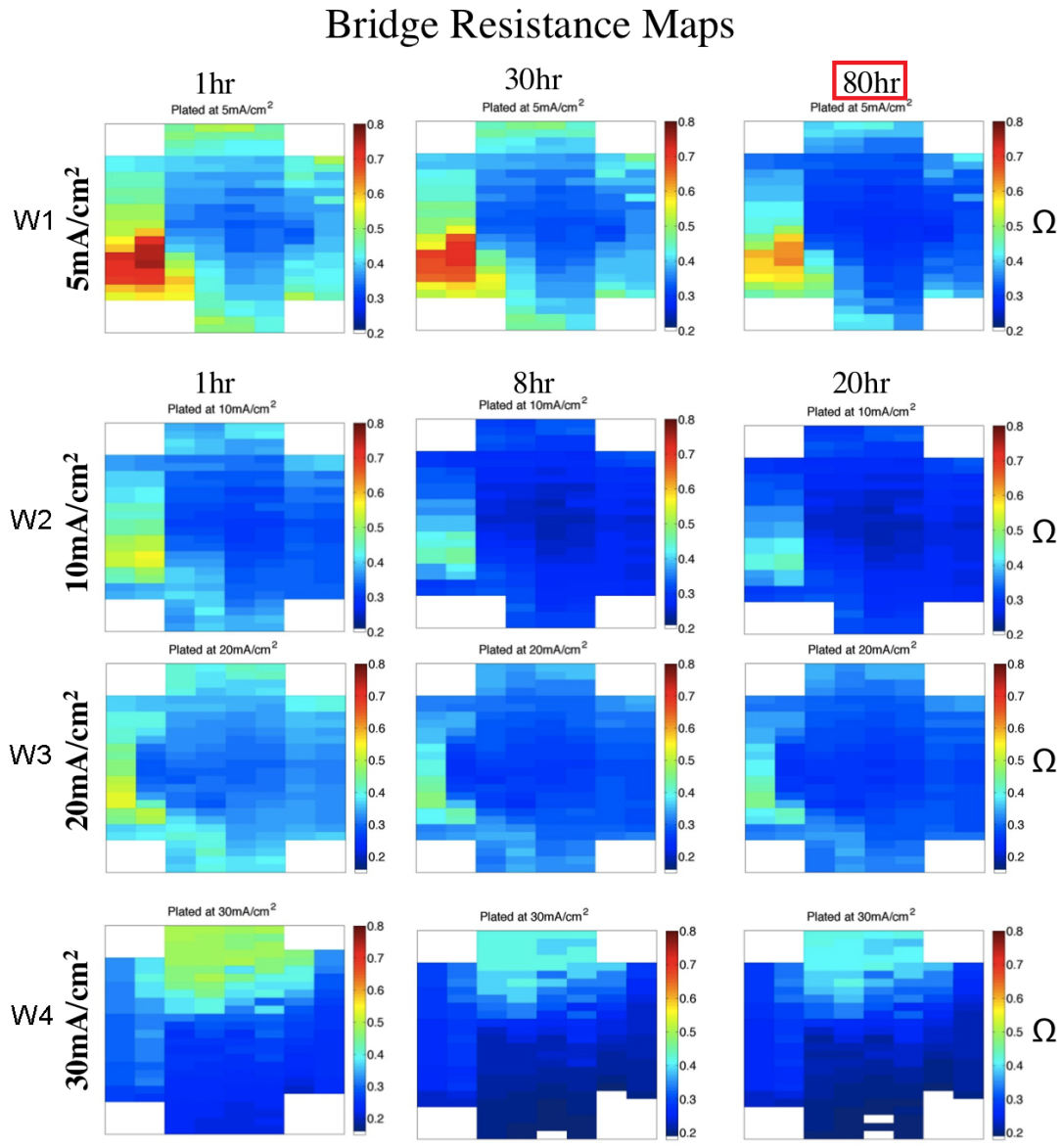

Figure 6.11: Spatial variation of bridge resistance of W1-W4 plated at different current densities, measured 1 hr, 30 hrs and 80 hrs for W1 and 1 hr, 8 hr and 20 hr for W2-W4 after deposition

Correlation of resistance with strain

The strain test structures on all wafers had a high release yield of greater than 98% and the average pointer arm rotations with time are shown in Figure 6.12. Due to low initial stresses only the notched structures have been included in the

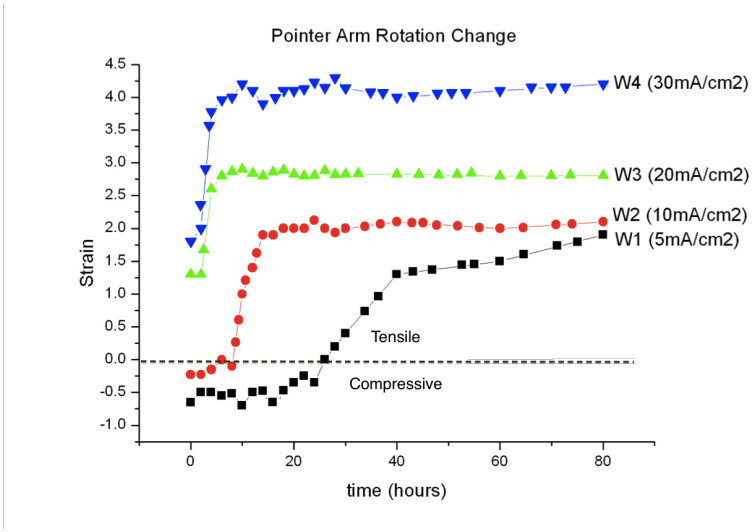

Figure 6.12: Average pointer arm rotation (strain) changing with time for wafers plated at different current densities

analysis as they have increased sensitivity. W1 showed an initial negative pointer arm rotation of -0.5°(indicating compressive stress), which changed to positive rotation (tensile stress) in a period of 27 hrs. After 80 hrs the final pointer arm rotation recorded was 1.9°. Six months after deposition, the average rotation for W1 was measured to be 2.1° suggesting that stabilisation to be attained between 80 - 90 hrs. W2 plated at 10 $mAcm^{-2}$ showed a similar behaviour to W1, with stress changing from compressive to tensile. It was interesting to observe that the final stress values of W1 and W2 matching at around 2°. W3 and W4 recorded a tensile stress at the beginning, with a clockwise pointer rotation (1.7°), which increased with time to stabilise at 2.75° for W3 and 4° for W4. The results suggest that film stress increases with plating current densities, which also correlate well with the time scales of the bridge resistance measurements for all wafers.

It is well known that the electrodeposited copper is in the thermodynamic metastable state soon after the electrodeposition process completes [198] which is followed by

microstructural evolution occurring at room temperature. As mentioned earlier, higher current density would result in a high crystal nucleation rate that lead to a fine-grained structure. The fine-grained structure would produce a large amount of grain boundaries which can be assembled by impurities from the organic additives present in the bath. This has been reported previously [199][200] where the deposited film were analysed over time for carbon incorporation (indicating organic impurities) using radio frequency glow discharge optical emission spectrometry (RF-GD-OES) [201]. It was observed that during incubation period C impurities diffused towards the metallisation surface leaving the Cu layer. It can be attributed from this and the strain plots shown in Figure 6.12 that soon after the impurities diffuse the grain boundaries are unpinned releasing tensile stress in the film which depicts film relaxation occurring during the transition period. It can be concluded from this that the different current densities led to the difference of impurities and grain boundary density, thus the diffusion rate was different at varied conditions. The higher the current density, the denser the film in terms of grain boundaries, resulting in a film with a low level of impurity, which diffuse faster, accelerating the self-annealing process of ECD copper.

Figure 6.13 shows a further comparison of the spatial strain with bridge resistance at t = 1 hr. Regions with a lower copper resistance arising from a thicker film exhibit larger strains. A high correlation between the patterns can also be observed on each wafer suggesting that the thickness dependence on stress is apparent. The overall stress levels on each wafer are also observed to increase from being compressive to tensile with the increase in the plating current density which can be attributed to be arising from the differences in defect density, as mentioned earlier.

Thickness variations in the film, as observed from the spatial bridge resistance maps, is also known to impact the self-annealing process [190]. Therefore a rigorous analysis on the change in bridge resistance trend has been performed on each structure extracting the total self-annealing time (incubation + transition period) which has been presented in Figure 6.14. A cross-wafer variation in self-annealing

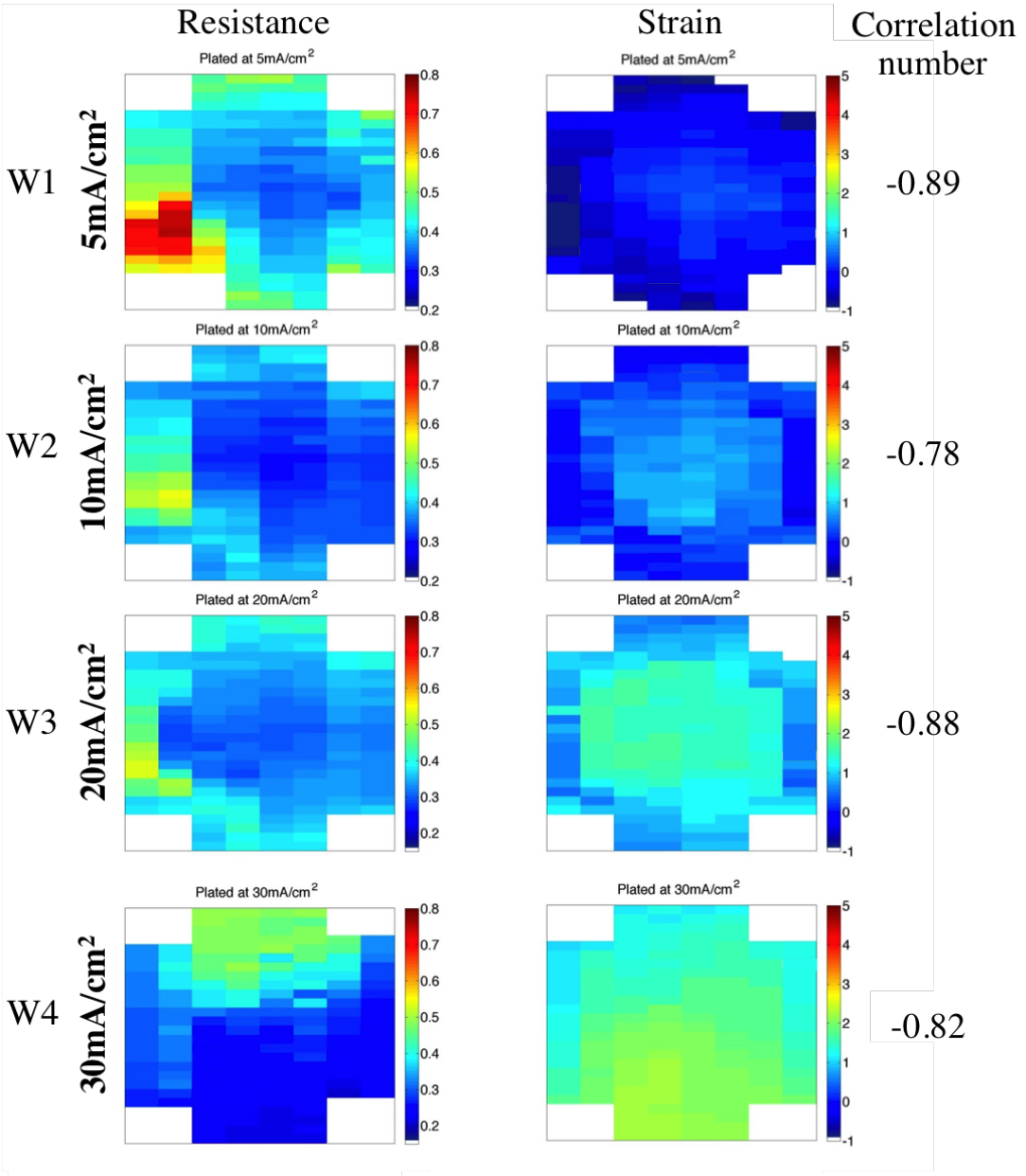

Figure 6.13: Correlation of bridge resistance with pointer arm rotation map

periods is clearly observed on each wafer which can be correlated directly with the spatial resistance maps in Figure 6.13. For W1 the right half of the film is seen to anneal much slower than the rest of the wafer with stagnation achieving greater than 30 hours. W2 showed a similar pattern which was more prominent especially around the wafer periphery where copper is seen annealing slower than the middle. Spatial variations can also be seen vaguely on W3 and W4 as these

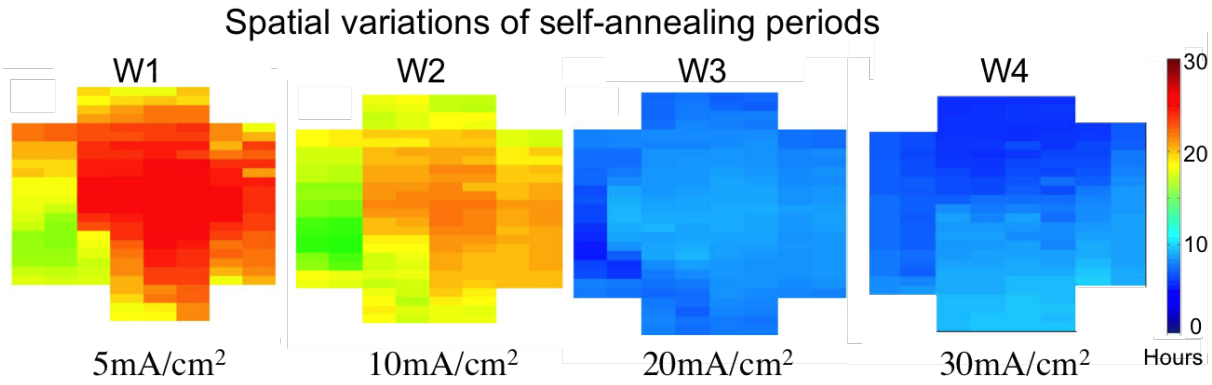

Figure 6.14: Spatial variations of total self-annealing periods (incubation + transition) plotted for W1, W2, W3 and W4

self-annealed much faster (< 5 hrs) compared to W1 and W2.

Observing the cross wafer variation of copper self annealing, using MEMS test structures, is a novel approach which has been employed in this work to investigate the effect of parameters such as the plating current density. With the strain and electrical test structures located on the same chip it was possible to perform simultaneous measurements which resulted in obtaining a direct correlation between the spatial evolution of the two quantities over time, which has never been reported before. The high interest in the topic of copper recrystallisation especially in the semiconductor industry where the performance of devices depend heavily on the RC delays contributed by the ECD Cu interconnects, the characterisation of these films is critical. However, employing the curvature method to perform stress measurements, can provide only the average values which can be misleading, as process non-uniformities can often cause variations in deposited film which has been observed in this study. Tackling this issue using the test structure technique has certainly provided an interesting insight on the recrystallisation of ECD copper and has been employed further to study other bath parameters which can influence this effect.

6.4.3 The effect of additive and carrier

An acid copper sulfate system operated without organic additives yields deposits of poor physical properties. Proprietary organic additives, such as Intervia 8540 manufactured by Dow Chemicals, are used to modify deposit characteristics in semiconductor industry, with the particular type and concentration of these components selected to enhance specific deposit attributes [202]. These organic additives are employed to improve grain refinement, increase throwing power, thickness uniformity and brightening of the deposit. Generally, there are three basic types of additives used in acid copper plating: carriers, brighteners, and levelers. (i) Carriers, also referred to as suppressors, are typically large molecular weight polyoxy-alkyl type compounds [202][203]. Carriers adsorb at the surface of the cathode and, in concert with chloride ion, act to suppress the plating rate. (ii) Brighteners, also referred to as accelerators, are typically organo-sulfur compounds [204] that increase the plating reaction by displacing adsorbed carrier. Brightener compounds may exist in several forms in electrolytic working baths. (iii) Levelers are typically nitrogen-bearing aromatic compounds that act by displacing brightener species in high current density sites (for example, at protrusions). Adsorption of these additives at protrusions reduces the plating rate in those regions [202].

This next set of experiments, therefore, involves investigating the effect of proprietary accelerator and suppressor Intervia 8540 A(additive[2]), C(carrier[3]) manufactured by Dow Chemicals, which are widely employed in industrial plating systems. These two components respectively promote or inhibit deposition and are active at different current density regimes. The operation of the bath in fact requires a fixed current density regime (e.g. 20 $mAcm^{-2}$) set by the power supply. The uniformity of the current density however suffers from irregularities

---

2. This chemical is improperly labelled as 'Additive' by the manufacturer is basically an accelerator/brightener and should not be confused with the generic term also 'additive' which is used for all types of organic species that are used to promote plating in baths.
3. Also known as suppressors and levellers

introduced by substrate topologies. The consequent effects are mitigated by the additive and the carrier by respectively enhancing the deposition at slightly lower current densities or inhibiting the deposition at slightly higher current densities. This greatly improves the profile uniformity of the electroplated structures. It is possible to balance the concentration of the additive and the carrier to achieve improved results for radically different applications, such as via filling (high-aspect ratio topologies) or blanket depositions (substrate with rather planar surface). It is quite clear that these species may be absorbed in the film and can effect the recrystallisation property of copper, and this has been investigated in this section. One barrier to undertaking this work on wafer scale is that the additives, once included in the 35 L plating bath, cannot be removed/filtered and therefore a new bath would have to be prepared each time which is time consuming, costly and environmentally undesirable. Therefore, it was decided to perform this investigation at beaker level using the same test structure but fabricated on chips as previously described in Chapter 4. Table 6.4 shows the parameters used. Bath samples were prepared with a combination of additives and carriers

Table 6.4: [Additive:Carrier] investigated in a copper bath

Bath sample	A [Additive] (ml/l)	C [Carrier] (ml/l)	A:C	Figure label
1	0	0	1:1	A0C0
2	5	0	1:0	A5C0
3	10	5	2:1	A10C5
4	0	5	0:1	A0C5
5	5	10	1:2	A5C10

Bath temperature: 23°C
Plating current density: 20 $mAcm^{-2}$
Target plating thickness: 2.5 µm

while keeping the copper(II) and acid contents the same. All chip samples were plated and measured simultaneously for consistency. Twelve test structure, per chip (Figure 6.15), were monitored for resistance changes for a period of 90 hours. Results show the resistance variation with time for different [additive] and [car-

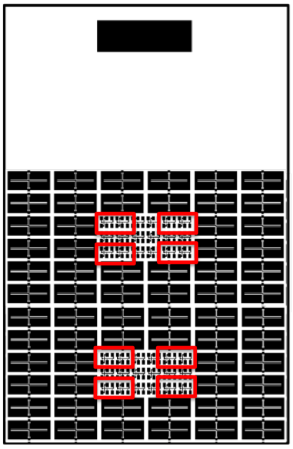

Figure 6.15: Eight Greek-cross and Kelvin bridge structures on a chip which were monitored to investigate the influence of [additive/carrier] on self-annealing of Cu

rier], presented in Figures 6.16 and 6.17 respectively. The convention used to mention the figures are e.g. A5C5 with 5 ml/l [additive] and 5 ml/l [carrier]. All plots have a dotted line which is the stabilised resistance value measured 6 months after deposition.

The first two plots (Fig 6.16 a,b) show that with the absence of both additive and carrier (A0C0), no change in resistance occurs during the 90 hours scan, except for the odd spikes occurring due to misprobing errors (between t = 30 - 50 hrs) in which case the probes had to be realigned and measurement procedure was restarted. The plated film from this bath sample was also non-uniform in thickness and grainy, which is expected in the absence of levellers and grain refiners. Considering this, it can be hypothesised that the films have no impurity inclusions and are purely copper, because of which no self-annealing is observed. It was interesting to see the same effect with an addition of 5 ml/l accelerator (A5C0) (Figure 6.16(c,d)) and the film showed no change in resistance. The film grains were smaller and yielded a shinier finish which suggested that the additive was acting but and does not get included in the film during deposition.

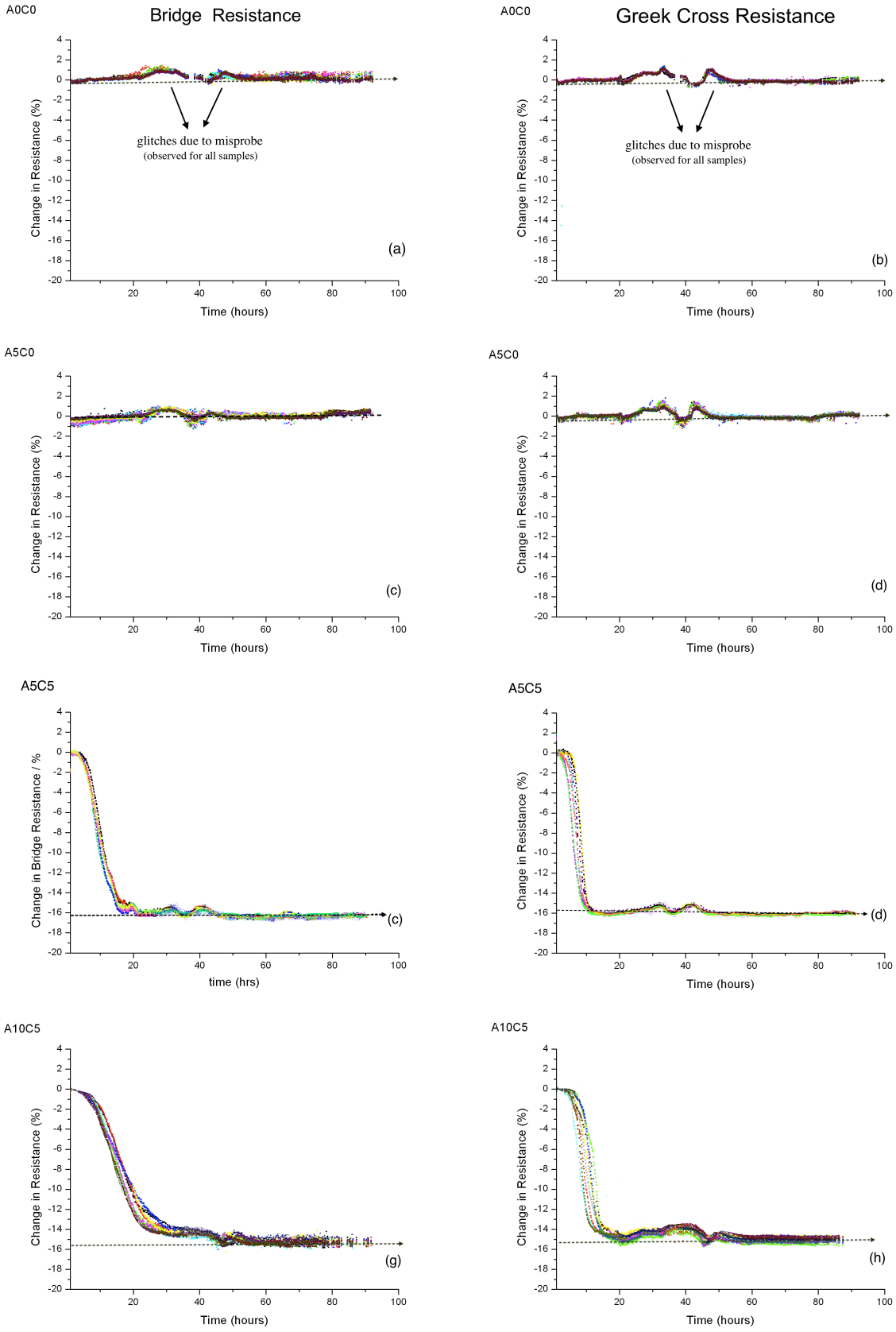

Figure 6.16: Effect of additive(brightener): Bridge resistance plotted with time for structures in 6.15. Dashed lines indicate the stabilised value of resistance measured 6 months (4000 hours) after deposition.

It has also been reported that brighteners are negatively charged and their function is to affect the surface morphology by changing the transport property of other chemical species in a solution and are not adsorbed on the cathode surface [205][206] which suggest why no self annealing was observed in its presence.

Bath with the same additive but with 5 ml/l carrier (A5C5) (Figure 6.16(e,f)) also produced a bright film, however it shows a transition period lasting 18 hours, identical to results from the 75 mm wafers plated in the previous experiment. The Kelvin resistance measurement are consistent for all samples however, more variations in the Greek-cross measurements can be seen, as would be expected. The presence of carrier is highlighted here which is known to be diffused-absorbed in the high current density regions of the film. Its inclusion in the film is inevitable, which suggests the mechanism by which its diffusion towards the film surface during incubation occurs, unpinning the grain boundaries and forcing copper grain growth to proceed which reduces the film resistance until stagnation [200].

Bath with excess additive (A10C5) also produced a bright and shiny film however, the decay during transition period is slightly slower than A5C5 suggesting the film has finer grains with a large number of grain boundaries which can house considerably more organic impurities, the diffusion of which would tend to be much slower hence, decelerating the overall self annealing process.

It can be concluded from this data that self annealing is only observed when carrier is present in the bath and the hypothesis of its absorption-diffusion within the film [200] may be related to the grain growth mechanism of copper. Figure 6.17 shows the effect of changing carrier concentration on the change in resistance with time. Bath with 5 ml/l carrier and no additive produced a film with a much darker finish. No significant change in bridge and greek-cross resistance can be observed suggesting that in the absence of additive, the grains are larger with a comparatively less number of grain boundaries which can result in a lower amount of carrier impurities incorporated within the film.

Bath with more carrier (A5C10) but less additive produced a shiny finish and the variations in the transition rates are identical to the A5C5 sample suggesting that

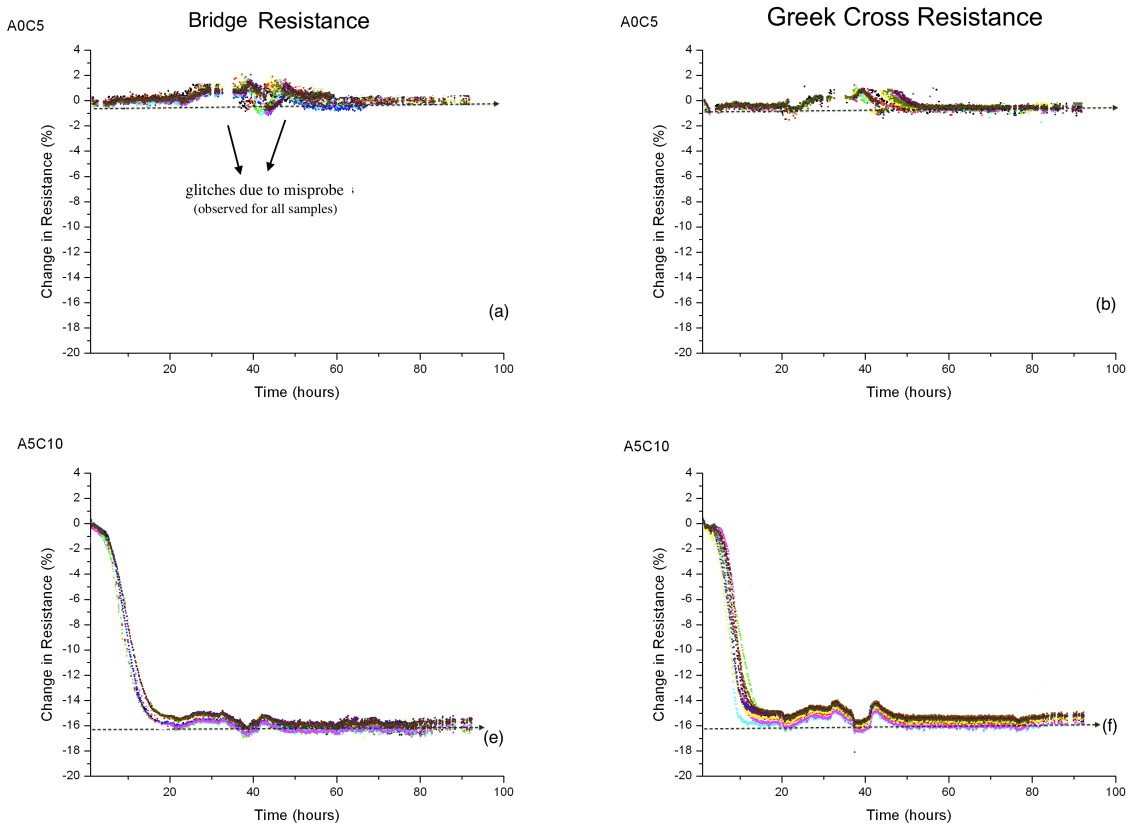

Figure 6.17: Effect of carrier(suppressor): Bridge resistance plotted with time for structures in 6.15. Dashed lines indicates the stabilised resistance values measured 6 months (4000 hours) after deposition

the higher concentration of carrier did not affect the self annealing of copper. It can be summarised from this data that the presence of both additive (brightener) and carrier (suppressor) together influences the grain growth mechanism of the electrodeposited copper.

The last sample, shown in Figure 6.18, was plated with the same additive and carrier as A5C10 but with half the thickness (1.25 µm). The slowest bridge resistance drop was recorded for this sample which did not reach the stabilisation stage within the 90 hours measurement. At this slow rate, this sample was expected to self-anneal within 1 or 2 weeks. The effect of film thickness on self annealing has been hypothesised previously in numerous publication [207][190][208] which are also in agreement with the result shown in Figure 6.18. It has been suggested that

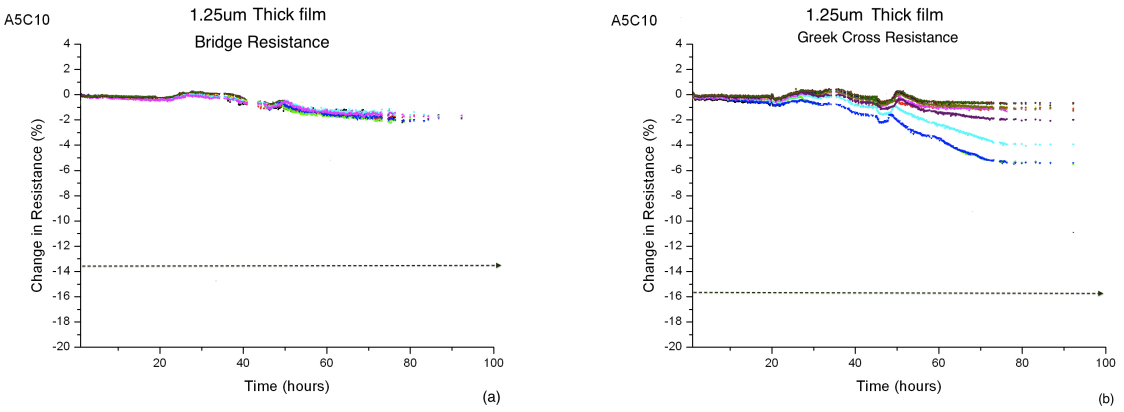

Figure 6.18: Bridge resistance change shown for a film with 1.25 µm thickness

physical restriction on grain growth comes into play especially when reducing the film thickness closer to the size of the crystallised copper grain clusters which can force the growth to advance in two dimensions, therefore increasing the transition period.

The effect of A:C concentration on the cross-chip variation in resistance is presented in Figure 6.19. Films had the largest cross-chip resistance variation which

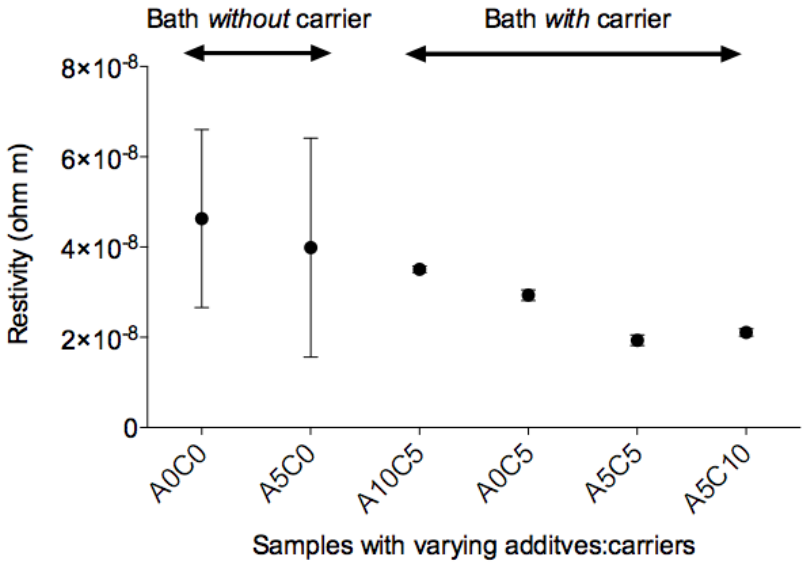

Figure 6.19: Variations in film properties with the effect of additive and carrier in the electroplating bath

were plated without any carrier in the bath. It can be seen that the inclusion

of carrier predominantly effects the uniformity of the films which is expected as carriers are known to suppress the current densities in regions with high current crowding (in protrusion), hence, producing features with a more uniform thickness. Conversely, additives are species that are known to promotes the reduction of Cu^{2+}, and ultimately contribute in brightening and softening the copper deposits. They, however, do not alters the uniformity of the film [209].

It was evident from these observations that carrier is important if the thickness uniformity across a wafer is required. Therefore for a shiny film with uniform thickness and low resistivity, carrier should be present with concentration higher than or equal to the additive concentration.

6.5 Conclusions

Test structures have been used to characterise the self-annealing of electroplated copper. Resistance measurements have been correlated with the rotation observed in strain structures using a custom built system that can perform optical and electrical measurements in parallel, which also enables different time lapsed measurements to be correlated and wafer mapped. The effect of different current densities on 75 mm and 200 mm wafers has been investigated.

It was observed that wafers plated at lower current densities anneal slower compared with wafers plated at higher current densities. An exponential decrease in transition period with plating current density was observed. Results from the wafer mapped quantities revealed a spatial distribution of self annealing rates across the wafer as a function of plating conditions. This result has never been reported before and it clearly portrays the importance of employing test structures for material characterisation which can be useful for optimising processes.

The influence of proprietary additive and carrier (Intervia 8540 A,C) concentrations on the self annealing were also investigated, but on beaker level experiments. Samples plated from an additive/carrier free bath produced films which showed no signs of self annealing. However, a change was apparent only when the additive

was used together with the carrier which suggests that the impurity absorption-diffusion mechanism through finely packed grains could be responsible for the delay observed in the self annealing of ECD copper. Furthermore, it was also found that the rate of self-annealing depended on the concentration of additive used in the bath.

Chapter 7

Characterisation of Stress in SU-8 Films

7.1 Introduction

The epoxy based negative photoresist polymer SU-8 is an important material used in the manufacture of MEMS [210]. Applications of SU-8 range from the production of microfluidic systems [211] to the formation of molds for electroplating of thick metal patterns [212]. However, when SU-8 is cross-linked by exposure to UV light and subsequent postexposure baking, it tends to shrink, which introduces tensile stress [213]. This can lead to problems with cracking [214] and adhesion, particularly when it is deposited on metal layers to act as a template for electroplating copper in the fabrication of microinductors [215]. The purpose of this work is to adapt the pointer arm test structures, developed in Chapter 3.5 and use them to characterise the spatially evolved stress in patterned SU-8.

7.2 Fabrication

Figure 7.1 shows the generic process flow for patterning thick SU-8 on a 200 mm Si substrate and then selectively removing sacrificial material under some of the SU-8 to create structures such as strain indicators.

First, the wafer is first cleaned for 10 minutes in "Piranha" solution (3:1 H_2SO_4:H_2O_2)

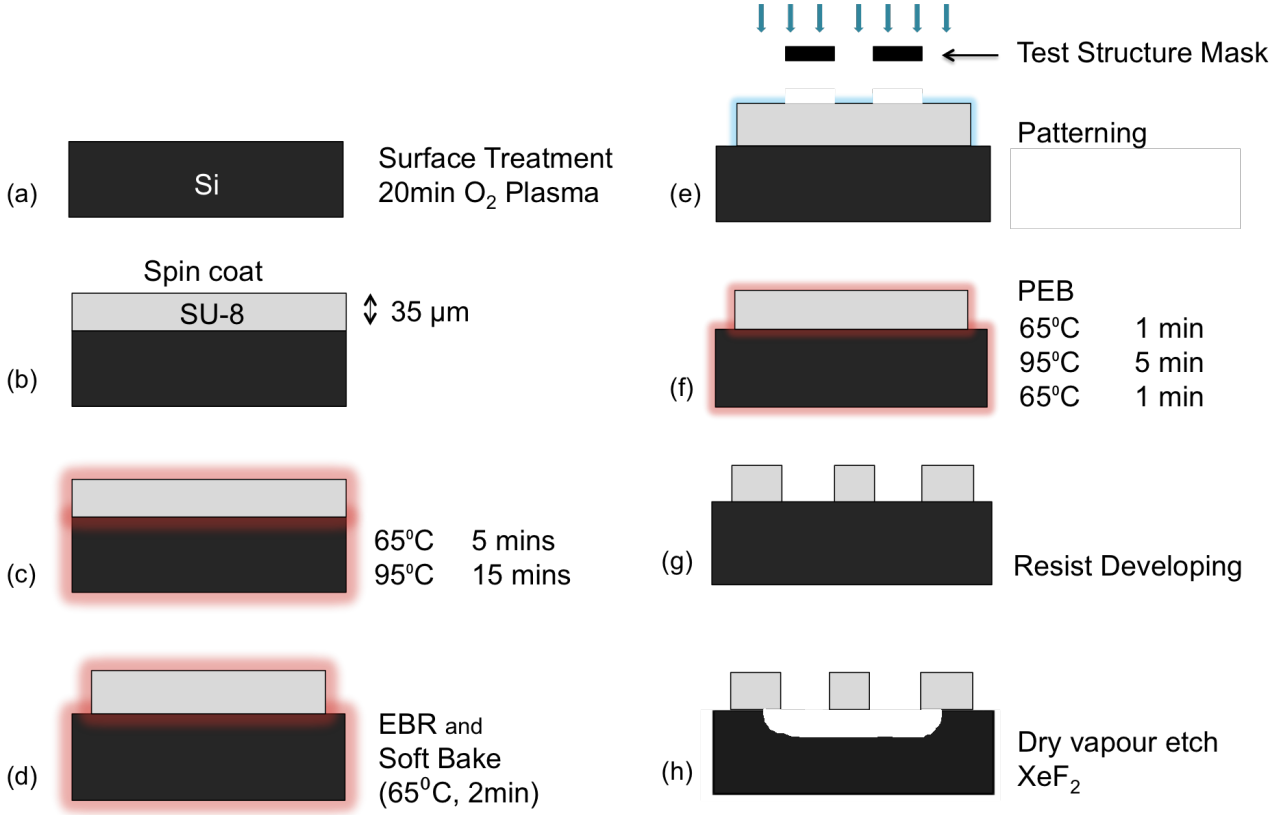

Figure 7.1: Schematic of the fabrication processes of SU-8 test structures wafer

before rinsing in deionized water (Caution: Piranha solution is highly corrosive and reacts violently with organic matter - check safety information before using). The wafer is dried by baking on a hot plate at 200°C for 20 min. This is followed by an oxygen plasma treatment in a reactive ion etch tool (STS Multiplex RIE Etcher or Barrel Asher) for 30 mins to promote adhesion (Figure 7.1(a)). It is then placed on a spin coating tool (POLOS MCD Spin Coater) and 20 ml of SU-8 3035 puddle is dispensed by hand to prevent bubble formation. Each wafer is spun up to 500 rpm for 10 s to spread the resist, then at 3000 rpm for 30 s, which created a nominal layer thickness of around 35µm (Figure 7.1(b)). This is subsequently followed by two steps of soft bake, first lasts 5 min at 65°C, followed by a second 15 min bake at 95°C (Figure 7.1(c)). The wafers are allowed to cool down before an automated edge bead removal (EBR) process is performed, using a stream of propylene glycol/methyl ether acetate (PGMEA) solvent, on Brewer

CEE Wafer Track spin coating system. This process removes a 10 mm ring of the resist from the wafer perimeter to ensure even contact between the wafer and mask during photolithography. A further short baking step at 65°C for 2 min is performed to ensure the wafer is completely dry before exposure (Figure 7.1(d)). The SU-8 is exposed with the test structure pattern using a UV mask aligner (Figure 7.1(e)). The wafer is postexposure baked (PEB) at three steps of 65°C for 1 min followed by 5 min at 95°C and a further 1 min at 65°C, before cooling to room temperature (Figure 7.1(f)). The resist is developed in a spin and spray developer tool using PGMEA for at least 6 min before rinsing in isopropyl alcohol and drying (Figure 7.1(g)). At this stage, the underlying Si is etched with dry XeF_2 vapour to release the desired structures using a Memsstar SVR XF etch tool. This process isotropically etches the exposed silicon substrate and releases the suspended test structures as seen in Figure 7.1(h). Being a vapour based process this release etch has no problems with the stiction that can occur with wet release processes [216]. The initial release etch used was somewhat uneven on the initial test wafer but this was addressed by the use of a very short (5 mins) oxygen plasma etch or de-scum, prior to vapour etching, which greatly improved the etch uniformity as can be observed in Figure 7.2. A short dip in

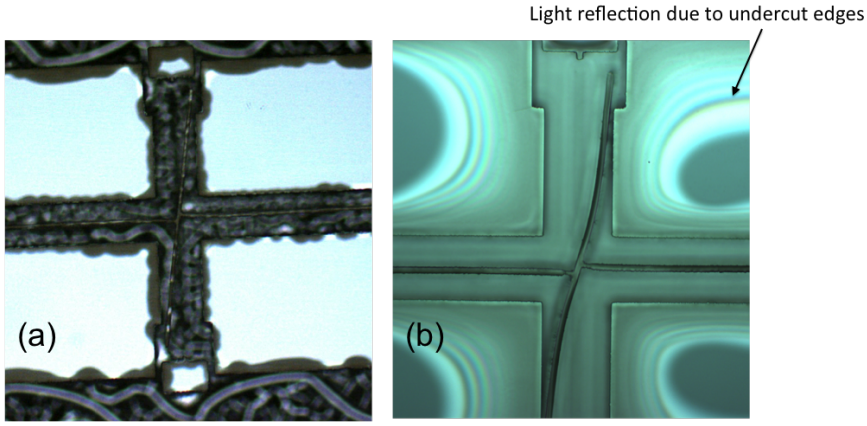

Figure 7.2: Microscope images of structures showing the effect of O_2 plasma treatment before release (a) Without de-scum unwanted SU-8 is seen on Si (b) After de-scum Si is completely exposed for etching

48% HF solution was also investigated in order to determine if the release-etch

problems were related to the native silicon oxide on the wafer, but unfortunately, this tended to result in partial delamination of the structures from the substrate and so this was not used in future processing. It should be noted that the SU-8 strain sensor pointer arms in Figure 7.2(b) have hit the anchor material and any rotation angle measured in cases such as this will clearly be compromised.

7.3 Experiment and Results

The aim of this work is to investigate the effect of exposure dose on the shrinkage of SU-8 caused by the cross-linking of the photoresist film resulting from the exposure. For this purpose two wafers were exposed with the test mask (Figure 3.12) using a UV mask aligner with the "long pass" filter selected. This attenuated light with a wavelengths below 350 nm, which could cause problems with the sidewall angle of printed features. One test wafers (W1) was exposed with a dose of 400 $mJcm^{-2}$ while the other (W2) with a dose of 320 $mJcm^{-2}$.

Both wafers were successfully released with a uniform silicon etch while W2 was only partially released as the etch was performed without the de-scum step.

Figure 7.3(a) and (b) shows an SU-8 stress sensor before release while Figure 7.3(c) and (d) shows a similar test structure after XeF_2 etching. The clockwise rotation of the pointer arm in the released structure clearly indicates significant tensile stress in the exposed and developed SU-8 film.

The stress pointer arm sensor structures have been characterized visually using the same procedures described in details in Chapter 3.5. After the images were acquired, pattern recognition analysis is performed using the in house code written in Labview. An image template file is used to locate the pivot point of the rotation arms in the stress structures as shown in Figure 7.4(a). Since the silicon underneath is etched isotropically, it typically leaves an etch mark, as indicated by the 'arrow' shown in Figure 7.4(a), which the software can falsely identify as the pointer arm.

A modified Hough edge detection transform [148] is used to determine the edge

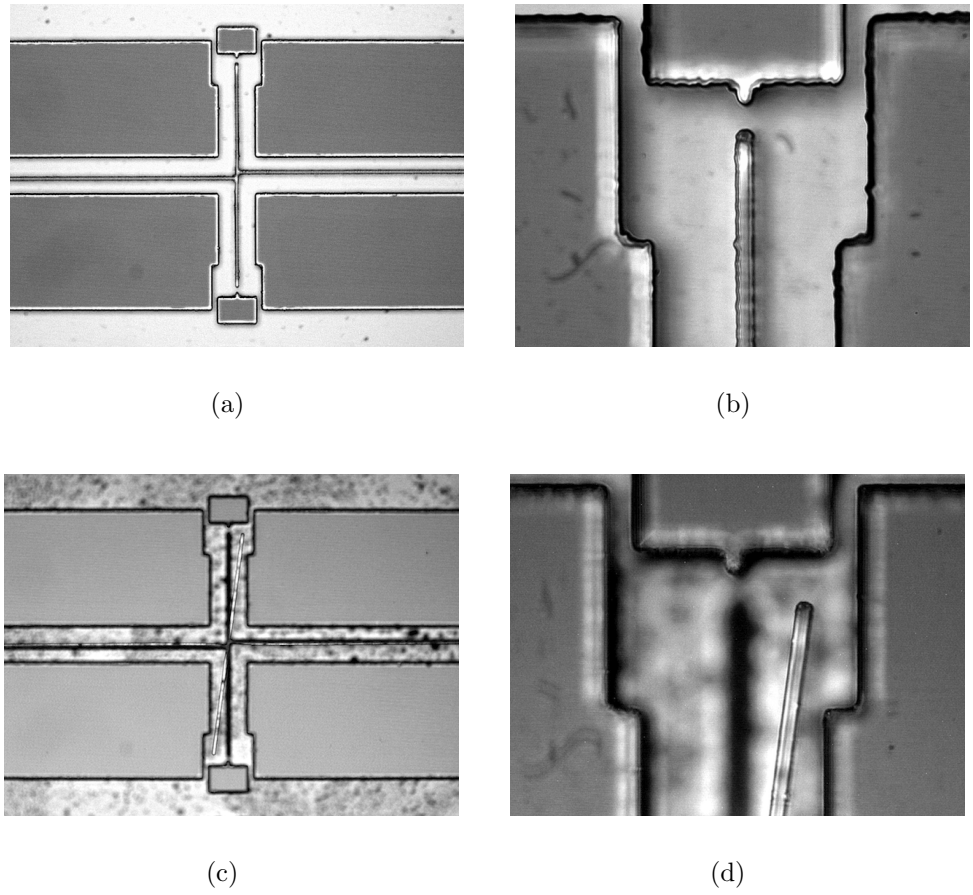

Figure 7.3: (a) Unreleased stress sensor structure (b) Magnified image of the same structure (unreleased) (c) Released stress sensor structure (d) Magnified image of the same structure (released)

of the pointer arm, starting from the pivot. This technique allows the correct identification of the arms as well as any broken structures. Figure 7.4(b) shows the results of the algorithm applied to identify the different edges located in the image. After edge detection, a line of best fit to the pointer arm is drawn and the relative slope used to calculate the angle of rotation. Figure 7.5 shows the complete edge detection process algorithm being applied and it can be noted that in this case the rotation is so large that the pointer arm has hit the surrounding SU-8 that forms the support for the structures and acts as a reference line to extract the rotation. These particular structures were designed with the minimum process dimension for the hinge connecting the expansion and alignment arms

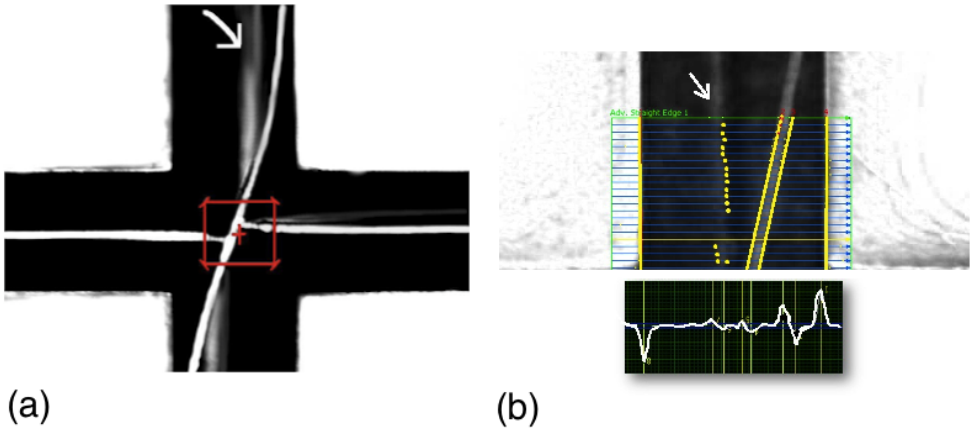

Figure 7.4: (a) Image captured by the measurement system identifying the pattern recognition routine (marked in red) has located the pivot of the stress structure. The arrow indicates the etch mark left after release (b) Etch marks detected using the Hough edge detection algorithm discussed in Chapter 3.6.6

(see Chapter 3), which helps to prevent the expansion arms becoming bowed and distorted. It is clear from Figure 7.5 that the angle of rotation would be greater if the structure sidewalls were not limiting the degree of rotation. Clearly, if quantitative values of stress are to be calculated this must be avoided [11].

The rotation data was used to obtain full wafer maps from wafers W1 and W2

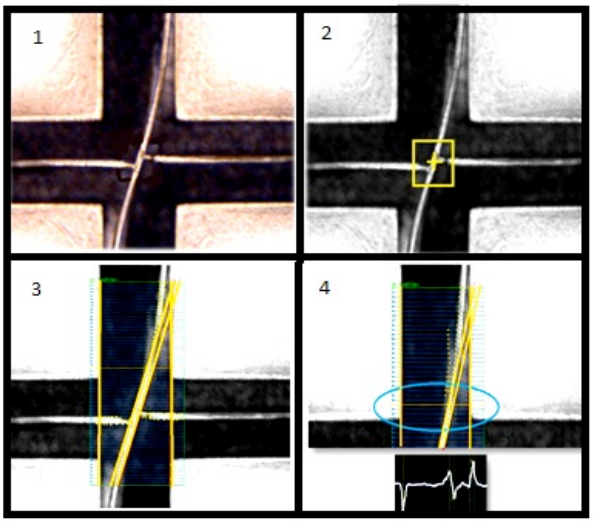

Figure 7.5: Determination of the angle of rotation for the stress test structures. (1) Capture of image, (2) Identification of the centre of the expansion arm, (3) Horizontal intensity scans to identify the edges of the pointer arms and the reference material, (4) Example of an intensity scan for the circled scan

which are presented in Figures 7.6(a) and (b), respectively.

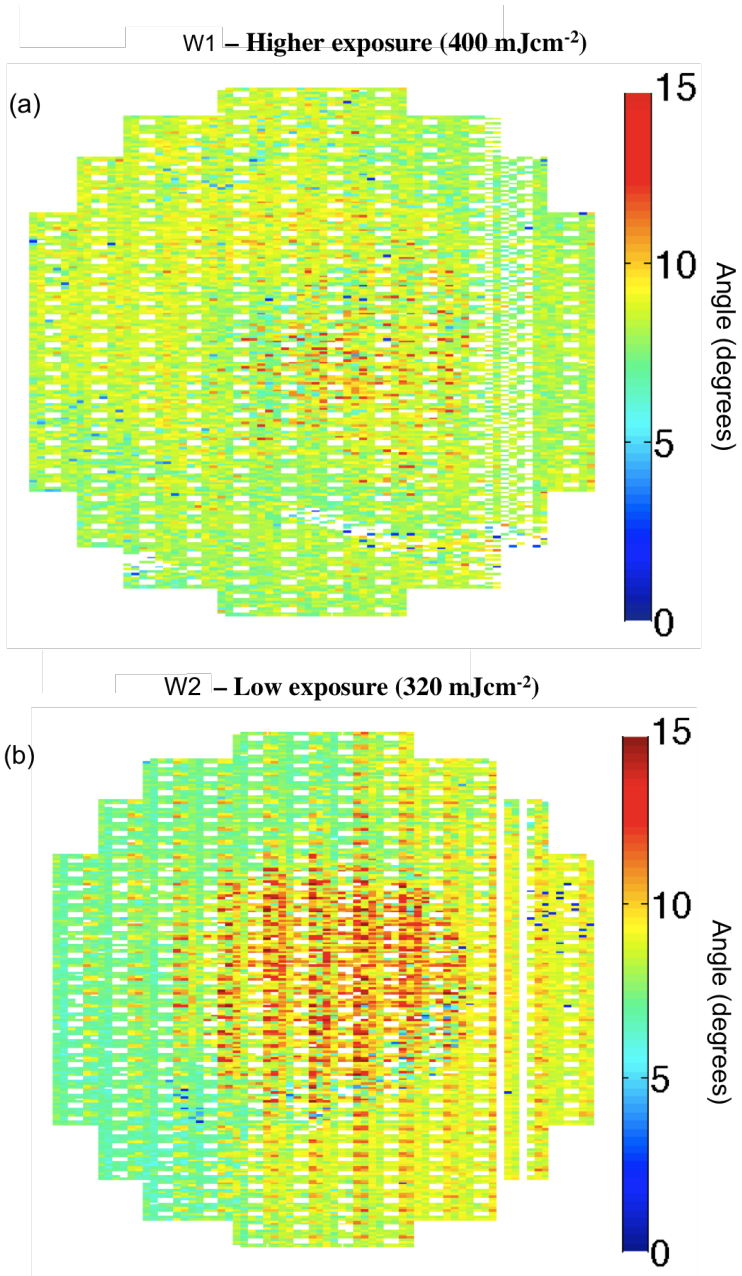

Figure 7.6: Wafer map of pointer rotation for a 200 mm wafer with SU-8 strain test structures UV exposed during lithography at (a) 400 mJcm^{-2} and (b) 320 mJcm^{-2}

In both figures, the areas without stress structures or where the structures have been damaged have been assigned a rotation value of 0° and appear white. This

also includes the area at the centre of each die where the electrical test structures are located.

7.4 Discussion

The results in Figure 7.6 show that there is much more variation in the pointer arm rotation on W2 than on W1, mainly between the centre and edge of the wafer but there is also a difference from left to right across the W2 wafer. This wafer also shows some clear variation within each die with larger rotations in the structures with the narrowed expansion arms. The average rotations for each value of ΔY/W have been calculated for a block of 6×18 dice in the center of the wafer and for the remaining dice around the edge. These are plotted against ΔY/W for both the standard structures and those with expansion arms that narrow where they connect to the pointer in Figure 7.7 (for W1) and Figure 7.8 (for W2). Each point on the graph represents the mean value while the error bars show the standard deviation (1σ). The number of structures that were measured to produce each point varies, but is at least 100 in every case.

SU-8 was found to have high tensile stress in all wafers. The results from wafer

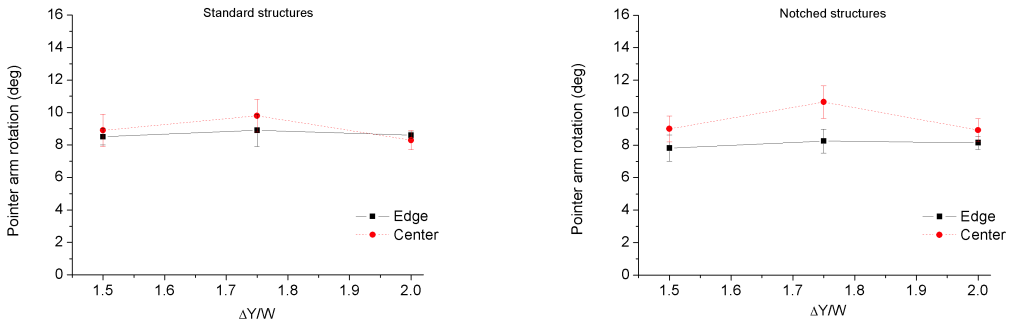

(a) Normal structures

(b) Narrow expansion arms

Figure 7.7: Average pointer arm rotations from W1 plotted against arm separation ratio for (a) standard structures and (b) structures with narrowed expansion arms.

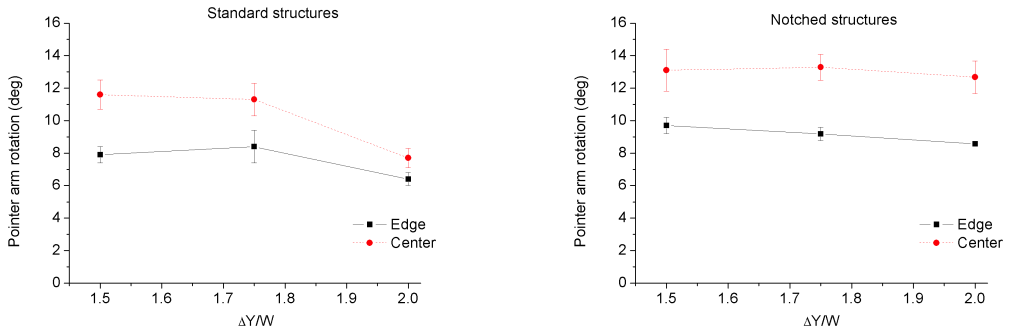

(a) Normal structures

(b) Narrow expansion arms

Figure 7.8: Average pointer arm rotations from W2 plotted against arm separation ratio for (a) standard structures and (b) structures with narrowed expansion arms.

W1 for standard test structures suggest that the level of rotation is largely independent of both the arm separation ratio and the position on the wafer. There does not appear to be a significant difference between the center and edge. The results from the structures on W1 with narrowed expansion arms, being more sensitive, show about 1° more rotation in the center. The results from W2 in Figure 7.8 show a much more significant difference between the centre and the edge. As the plots for both W1 and W2 do not show any significant dependence related to the pointer separation ratio, an average of all the structures in a die can be used to wafer map pointer rotation map which are presented in Figure 7.9.

These averaged results confirms that there is significantly more variation in stress across W2 than across W1. The pattern on W2 suggests an effect caused by the initial pour of the SU-8 resist. SU-8 3035 is extremely viscous and un-exposed wafers tend to show a pattern where the outline of the poured resist prior to spinning can be clearly seen (represented as a dotted circle). The original hypothesis was that the resist at the center is therefore slightly thicker than the resist across the rest of the wafer, which may be enough to alter the level of stress. Measurements of the resist thickness are impossible to perform by profilometry

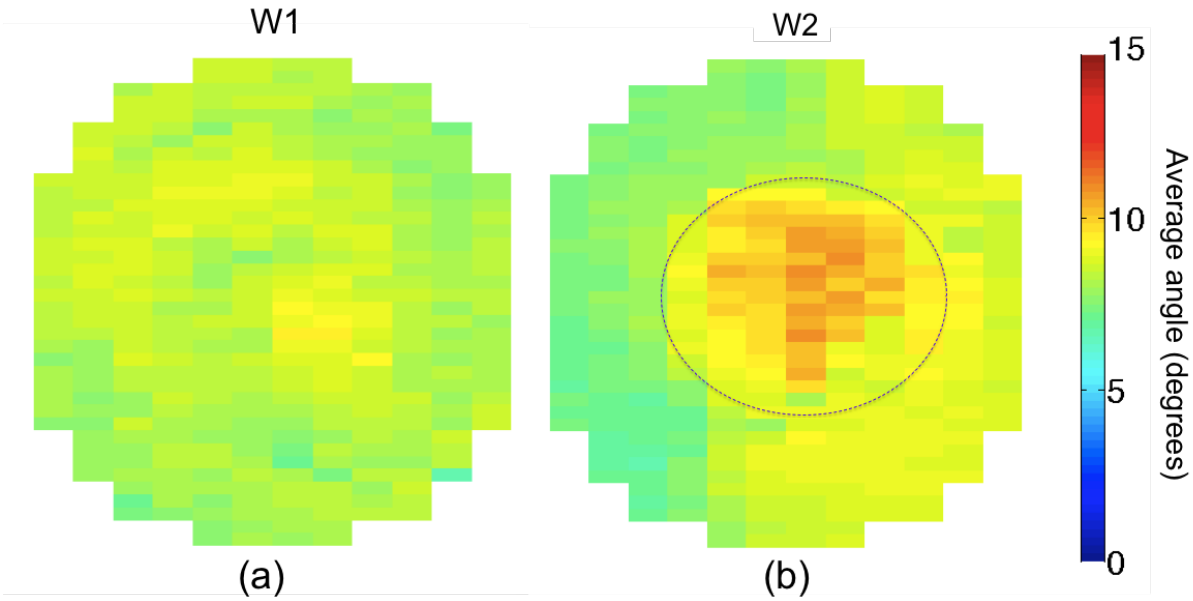

Figure 7.9: Wafer map of average strain structure pointer rotation for each die on a 200 mm wafer (a) W1 (b) W2

after the release of the test structures, and so there are no thickness data available for W1 or W2.

In order to investigate this further, an additional test structure wafer was fabricated using the same process with an exposure of 320 nm, but without the final release etch. Thickness measurements were made using a Dektak surface profiler in one column from top to bottom and one row from left to right. This gave a mean thickness of the cured SU-8 from 43 measurements of 33.42 µm with a variability (1σ) of 2 µm. Figure 7.8 shows that maximum values can be observed at the center of the apparent pour mark where the SU-8 is 2-3 µm thicker than the rest of the wafer. This suggests that there is an effect associated with the initial pour of the photoresist which is non-uniform UV penetration in the film of varying thickness across the wafer. With uneven thickness, the UV penetration can create non-homogeneous cross-linking chains in regions where the UV intensity was lower causing defects, which is a possible reason why more rotation was observed in the center of the wafer where the spin coated SU-8 film was thicker.

7.5 Conclusions

This chapter reports the first application of microrotating stress sensor test structures being used for the spatial characterization of SU-8 photoresist. The test structures were produced by patterning a ∼35-µm-thick layer of SU-8 3035 coated on a 200 mm silicon wafer and they were released from the silicon substrate using an XeF_2 vapour etch and subsequently observed to display clockwise rotation indicating significant tensile stress. Measurements of the pointer arm rotation were made on two wafers with different process parameters. The results from these wafers patterned with different exposures suggested that a larger exposure dose during lithography can reduce the level of tensile stress in the material.

The micromechanical test structures used in this work has demonstrated their usefulness in the measurement and wafer mapping of the stress in patterned SU-8. This included the identification of cross wafer variation, which may be introduced at the spin coating stage of processing. Stylus profilometry measurements confirmed that a variation of the SU-8 thickness did occur which can be attributed to the initial pour of the resist. There can also be other possible sources of variation, such as the uniformity of heating during the PEB process that can be explored in future.

Chapter 8

Conclusions

8.1 Introduction

The surging demand of high power applications has raised tremendous interest in the miniaturisation and integration of passive components such as microinductors with CMOS technology. A high Q-factor of these components is desirable to fully utilise the performance of the devices, which can be achieved by employing laminated electrochemically deposited ferromagnetic core such as permalloy with a highly conductive copper winding. These layers are required to be thick (tens of microns), however, having vertical thicknesses at this scale, can pose a series of integration challenges in IC technologies.

Residual stress is one of the important yield and reliability issue for MEMS, especially when employing NiFe alloys. Numerous journal articles have been published showcasing the reduction of stress using chemical additives such as saccharin. However, the exact mechanisms behind the origin of the stress is still under discussion. Besides this, the characterisation method employed for stress measurement for these NiFe films has also been problematic. Traditionally, it has been measured on wafers using the curvature method which can only provide the overall (average) stress value and also does not take account of the stress developed in the underlying layers during heat treatment steps. Therefore, a need for a measurement system able to spatial characterise stress in ECD films would be of significant benefit and would could be used to develop and control fabrication processes for microinductors.

8.2 Achievements and impact on knowledge

8.2.1 Spatial stress measurement system

In response to the issue above, the work presented in this thesis has demonstrated the first application of MEMS test structures to fully spatially map stress in thin films on silicon wafers of any size. Pointer arm rotating structures were employed to characterise strain in which the direction of rotation was successfully used to distinguish between compressive and tensile stress while the degree of rotation was used to quantify the values of localised strain. An automated high speed measurement system was created which was capable of extracting pointer arm rotations from over 12,000 structures, on a 200 mm wafer in less than 30 minutes. This made it feasible to comprehensively and routinely wafer map the strain (and ultimately stress using locally measured values of Young's modulus) over many wafers when developing new processes.

This complete strain measurement system was employed with the aim to characterise strain in electroplated materials used for the fabrication of microinductors. Nickel, NiFe alloy and Cu were electrochemically deposited to create a complete fabrication process of the test structure wafer. A full release of the test structure arms was a critical element associated with the performance of the device which was optimised for each material. It was observed that Ni and NiFe released easily compared to Cu which is less stiff and bends downwards after release causing stiction. This issue was overcome by depositing a thicker sacrificial layer and etching copper at much lower chamber pressures in a HF vapour release system. Another important contribution of this work has been the development of a unique chemical solution capable of selectively etching the copper seed layer when used alongside the NiFe test structures. With the modification any undesired effects of NiFe corrosion and Cu redeposition have been eliminated which significantly improved device yields. This new recipe has now been adopted widely in the fabrication facility (SMC) and currently being employed in the fabrication of all

microinductor and microswitches.

8.2.2 Process optimisation of ECD NiFe

To obtain an insight on the fundamental understanding of the origin of stress in ECD films, the effect of plating conditions and bath compositions were investigated. This would have required the disposal and change of the chemical compositions of plating tanks (typically 30 - 60 litres) which would be both expensive and environmentally challenging. However, taking the advantage of microfabrication, test structure chips were fabricated (1.3 $\times$ 1.7) cm, which provided quantitative strain measurements of ECD Ni and NiFe from a variety of experimental parameters with only 150 ml bath samples required for each beaker level setup. These yielded some useful information associated with the development of stress in Ni and NiFe films, which is summarised below:

- The plating efficiency of pure nickel was observed to be dictated by the amount of hydrogen evolving at the cathode surface which was decreased by plating at lower current densities in low concentrations of Ni(II).
- The presence of boric acid enhanced the under potential deposition of nickel by suppressing the hydrogen evolution reaction, producing films with low stress.
- Boric acid surprisingly had negligible effect on hydrogen evolution in the presence of iron(II) in a nickel bath as the overall reduction reaction was overwhelmed by the anomalous co-deposited of iron. Films produced in this case are unstable and delaminate due to high internal stress ($>$ 300 MPa).
- When the concentration of boric acid was increased, films were richer in Fe%, which suggested that boric may absorb on the electrode surface blocking the nickel ions whilst allowing the reduction of ferrous ions.
- No complex ions between Ni/Fe and boric acid existed.
- Saccharin ($>$ 1g/l) reduced the tensile stress of NiFe drastically down to $\sim$100 MPa whilst brightening the deposits.

From all these experiments it was concluded that the tensile stress developed in Ni and NiFe films has an inversely proportional relationship with the plating efficiency which is governed by the hydrogen evolution reaction occurring simultaneously with the nickel reduction. It was proposed that hydrogen would influence the film properties either by adhering to the film surface and inhibiting nickel reduction or by encapsulating into the plated film during deposition, in which case voids and cracks may form, inducing high levels of tensile stress in the plated films.

The approach of electroplating MEMS strain structures in a small beaker level setup has therefore, demonstrated great potential when optimising plating parameters to achieving high yielding processes. It can also be adopted in industry R&D facilities to accurately identify process windows and be able to predict the performance of the plated material prior to transferring the recipe on full scale production tools.

8.2.3 Spatial stress analysis in NiFe films

The optimum parameters obtained were further used to plate NiFe on 200 mm wafers, with the aim to characterise the spatial residual stress developed under non-uniform plating conditions. High resolution wafer-scale maps were obtained, for the first time, which provided measured values of the Young's modulus and residual stress ranging between 30 GPa to 180 GPa and 50 MPa to 220 MPa respectively on a single wafer. It was shown that non-uniformities in process conditions such as bath agitation influenced the properties of ECD films, where increasing the agitation produced film with more stress, while removing the agitation, at the chosen current density, produced a more uniform alloy film with less surface roughness and lower stress. This wafer-scale variation of stress and of the mechanical properties of electrodeposited NiFe has been a problem of important concern for the reliability of microfabricated devices which has been to date been unaddressed. However, the test structures coupled with an automated

measuring system developed in this work, has the ability to provide a deeper insight on the origin of stress and has huge potential towards further process optimisation.

This unique methodology has clearly demonstrated the attraction of measuring localised strain at high resolution within the layer of interest, compared to the wafer curvature technique where the contribution to stress of the underlying materials were not fully accounted for. Coupled with this fact and also the advantage of being CMOS compatible, this approach carries potential of becoming a standard quality assurance routine that can be applied for compliance check of equipment in semiconductor industry.

8.2.4 Spatial analysis of copper recrystallisation

Another impact of this study has been the use of the same test structures to characterise the self-annealing property of patterned ECD copper. High resolution spatial changes in film resistance were correlated with strain measurements by modifying the automated system so it could perform robust optical and electrical measurements simultaneously. It also enabled different time lapsed measurements over 4 days to be correlated and wafer mapped for the first time. Local resistance changes were observed to correlate with the strain measurements and it was shown that the rates of crystallisation varied spatially across the wafer due to variations in film thickness. Non-uniformities in plating influenced by proprietary Intervia 8540 additive and carrier concentrations and their effect on the self annealing were also analysed. With carrier and additive together the three phases of self annealing were more pronounced. This has been postulated as the impurity absorption-diffusion mechanism (of carrier) through finely packed grains (influenced by additive) could be responsible for the delay observed in the self annealing of ECD copper. The use of Greek cross test structures to measure the resistivity change over a small number of grains, suggests that the grain structure may vary in small areas or protrusion where current crowding effect is profound.

These irregularities in grain growth observed in patterned films using the test structure approach have not been reported, as historically four point probe and wafer curvature measurements were employed on blanket deposited films, in which case the bath additives and carriers would not act the same way and affect the results.

The presented methodologies have demonstrated the impact of process nonuniformities on electroplated films, and carry the potential for high resolution spatial analysis of parameters of interest which will enable the use of the ECD films for a number of applications though a better understanding of the plating process.

The third impact of this work has been the characterisation of spatial stress in SU-8, which is critical in the microinductor process where thick SU-8 moulds ($\sim$50 µm) are typically employed for the ECD of copper coils and also as an insulator for the magnetic core. The measurements made suggest that spatial nonuniformity in the coated film thickness over the wafer can cause variations in the UV exposure during photolithography that effects the cross linking of the polymer hence, inducing different levels of tensile stress in the material. Although, initially used for the characterisation of ECD films, the stress measurement technique has also shown to be capable of investigating process variations in polymer films which is equally important for the reliability of MEMS devices.

8.3 Final remarks and future work

As presented earlier the aim of this thesis has been the characterisation of the three main materials (NiFe, Cu and SU-8) used in the fabrication of a microinductor, with particular attention paid towards the minimisation of stress in NiFe. A novel fabrication and measurement system has been devised which can swiftly and robustly map spatial strain in potentially any material that can be successfully undercut to release the rotating arms of the test structures. The methodology has therefore opened up many possibilities and can be used for characterising newer materials employed in MEMS, fine-tuning the manufacturing processes to achieve

set goals in terms of material properties as well as uniformity and gaining a better understanding of the influence of processing conditions on the produced films. The mapping of parameters can also assist in the design and optimisation of process tools to achieve promising yields especially in this new era where MEMS and IC production volumes have reached high limits particularly with the emergence of smartphones in the consumer industry.

Based on the findings from this work, some improvements in the stress measurement methodology can be suggested. Firstly, the test chip was designed with strain test structures assuming constant Young's modulus however, this was proved wrong when non-uniformities in process conditions (e.g. agitation) was shown to have introduced variations in the nano-indentation results. The wafer had to be cleaved into quarters fo this, which is not ideal for obvious reasons. In future, a new test chip can be designed with a combination of both pointer arm rotating structures for strain and lateral resonant microactuators for local *in situ* Young's modulus measurements. An appropriate mechanical model can then be used based on the results to determine the residual stress in the film. Secondly, the strain sensors used in this work were designed to restrict rotations to 10°, which has not been optimum in some cases where the stress levels of NiFe exceeds 300 MPa. Therefore future designs would require the widening the side walls on either side of the pointer arms.

Apart from improvements in the test structure design, a few process related modification can also be suggested. Firstly, the replacement of boric acid has become essential as it has been recently flagged as a substance of very high concern by Europe's International Chemical Secretariat and included in the SIN list of hazardous chemicals. This provides another opportunity of investigating the use of other weak acids such as citric acid that can contribute towards suppressing hydrogen evolution during the ECD of Ni and NiFe. Another advantage of replacing boric acid is its low solubility in aqueous solution which can be as issue when attempting to dissolve large quantities for industrial plating tanks.

Pulse reverse plating technique has also generated a lot of interest recently where

understanding the effect of duty cycles on the structural and compositional properties of more complex magnetic materials such as NiFeCo and NiFeMo can also be explored by characterising stress and comparing with the standard DC plating technique.

Another structural material of interest is parylene which can be used as an alternative for SU-8 as it carries the advantage of providing completely conformal and pin hole free uniform films and can be patterned using standard plasma etching technique. Full stress characterisation can therefore be performed towards its use as a structural material and compared with SU-8.

In summary, the methodology presented in the work along with the modifications adopting the prescribed process parameters and procedures can be used for developing low stress materials, which can be directly transferred into the process flows of the mass production of MEMS microinductors.

Appendix A

Theory

This appendix summarises the techniques used within the research. The analysis of electrochemical reaction in laboratory takes place using a three electrode system which is described. Cyclic Voltammetry and chronoamperometry methods which use the three electrode system along with the plated film structural and electrical analysis using x-ray fluorescence, nano-indentation and sheet resistance measurement technique has been described. Magnetic properties extracted from the hysteresis loop using a B-H looper is also shown.

A.1 Electrochemical Study

Electrochemistry is the study of reactions taking place at the interface of an electric conductor which can be composed of an electrode made of either a metal or semiconductor material and a redox active solute species within an electrolyte. Electronic components are fabricated on silicon but plating directly on silicon may not be feasible due to its poor electrical conductivity therefore a thin layer of metal such as copper can be evaporated on it. Electrolytes can be either metal salts (metals dissolved in acids) or molten salts.

The study of electrochemical reactions taking place at a single electrode/electrolyte interface is essential for this study. However electrode reactions occur between two electrodes in an electrochemical cell. To ensure the reactions only taking place at a single electrode (the working electrode) are studied, the electrochemical cell set-up commonly used consists of three electrodes (working, counter

and reference) immersed in an electrolyte, shown schematically in Figure A.1. A

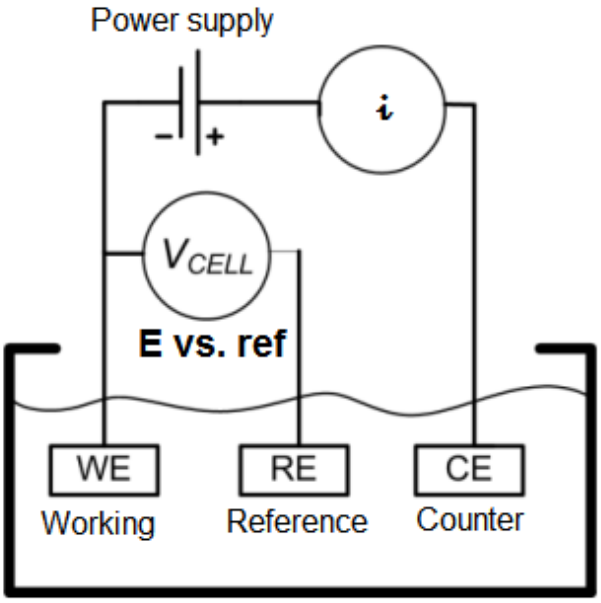

Figure A.1: Schematic of a three electrode electrochemical cell

potentiostat controls the operation of the electrochemical cell and has two modes. Firstly, the working electrode's potential is controlled relative to that of the reference electrode by applying a voltage between them and the current between the working and counter electrode is measured in response to this potential, in this case the system is said to be under potentiostatic control. Secondly, if the current is controlled between working and counter electrodes and the potential between the working and reference electrodes required for such current to flow is measured. The system in this case is said to be under galvanostatic control [217]. By controlling the electrode potential the electron transport reactions of interest can be observed at the working electrode. Generally this electrode is constructed from a non-reactive material and is considered inert. A common choice is platinum however the working conditions and requirements dictate the electrode material to be used. The surface area of the electrode has to be obtained which is an important factor to determine the magnitude of current within the electrochemical process. Larger the surface area, the larger the interface between the electrode

and electrolyte phases, therefore more current which can be passed.

To complete the electrochemical circuit a counter electrode is necessary. If a reduction reaction is performed at the working electrode then there is a net flow of electrons from the counter electrode, where an oxidation reaction occurs, to the working electrode. An example of nickel (II) species in aqueous solution is reduced at the copper working electrode and the oxidation of nickel concurrently occurs at the platinum counter electrode. A schematic is shown in Figure A.2. The oxidised

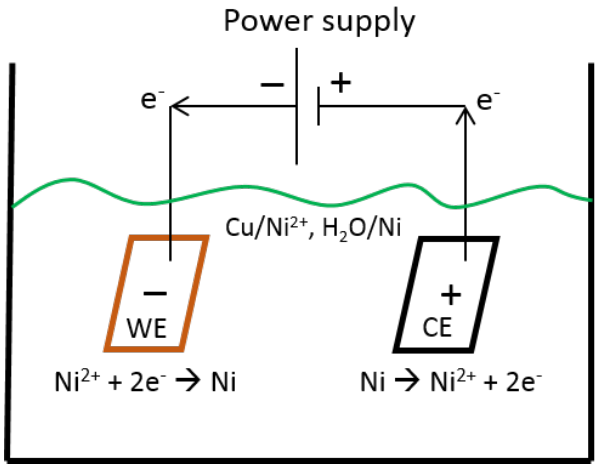

Figure A.2: Schematic of electron flow in a complete electrochemical circuit for a nickel electrodeposition experiment

and reduced species within the electrochemical system can be summarised in Equation A.1.

$$\mathrm{Ox} + \mathrm{ne}^{-} \rightleftharpoons \mathrm{Red} \tag{A.1}$$

'Red' is the reduced and *'Ox'* is the oxidised species, 'n' is the number of electrons involved in the redox reaction. To preserve the charge balance it can be seen that to every oxidation electron produced there must be an accompanying reduction electron consumed. For reduction to take place at the cathode current is required to provide the flow of electrons from the electrode to the electrolyte and conversely electrons are accepted from the electrolyte at the anode. All this is controlled by the potentiostat.The movement of charged species between the working electrode and counter electrode completes the electrochemical cell. Background electrolyte

ensures that the redox species do not have to move far from the electrode surface to do this, as the large numbers of ions in solution are available to carry the current.

The potential of the working electrode is measured with respect to the reference electrode which holds a stable electrochemical potential as long as no current flows through it. The reduction potential (or redox potential) of a chemical specie usually quoted, E^{ϕ}, is obtained using a standard hydrogen electrode (SHE) as a reference electrode. By definition its reduction potential is 0V and all other standard potentials are stated relative to the SHE. An SHE electrode consists of a piece of platinum immersed in an activity one solution ($\alpha = 1$) of a strong acid (sourcing $H^+(aq)$) with hydrogen gas bubbling at 1 atmosphere over it. The use of hydrogen gas experimentally is considered both dangerous and impractical other reference electrodes are used. The one used in this word is Standard Calomel Electrode (SCE), ($Hg/Hg_2Cl_2/KCl$(saturated in water)) which holds a constant potential 0.242V versus SHE because of the following equilibrium equation [218]:

$$Hg_2Cl_{2\,(s)} + 2\,e^- \longleftrightarrow 2\,Hg_{(l)} + 2\,Cl^-_{(aq)} \tag{A.2}$$

Since a large amounts of each reagent are present a small change in current does not change the equilibrium position, therefore resulting in a constant potential at the reference electrode. When a voltage is applied between the working and reference only the potential of the working electrode will change. For simplicity all potentials measured using a potentiostat in a three electrode system, in this work, will be stated with respect to SCE.

A.1.1 Cyclic Voltammetry

In electrochemistry cyclic voltammetry (CV) is the most commonly used technique as it provides a fast and simple method for initial characterisation of a redox active system. It can also provide an estimate of the redox potential and the rate of electron transfer between the electrode and the analyte. In this technique, the

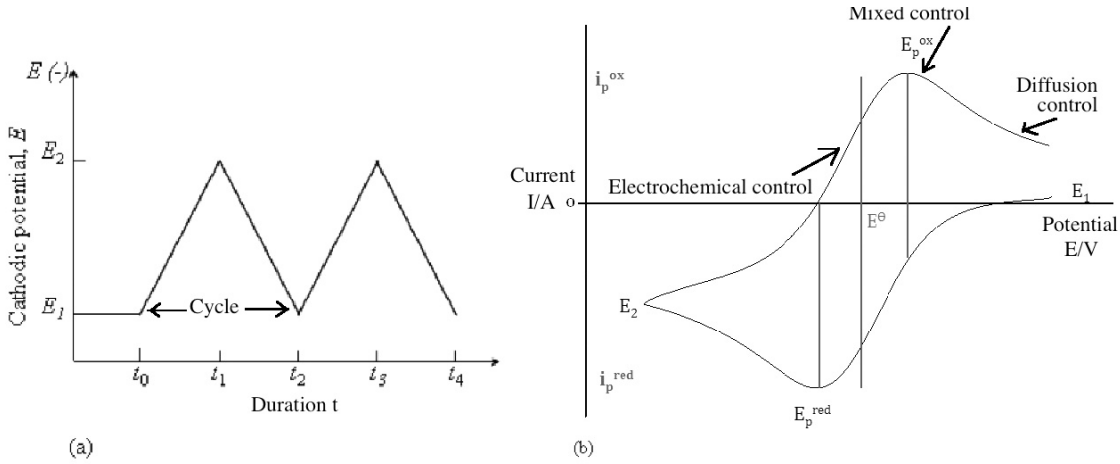

Figure A.3: (a) Typical cyclic voltammetry potential waveform, (b) Reversible cyclic voltammetry response for a reduced specie in solution

working electrode potential follows a linearly ramping potential versus time, as shown in Figure A.3(a), from a starting potential E_1, normally a potential with zero current flow, to an end potential E_2 at which point the potential sweep is revered and scans at the same rate back to the starting potential.

From Figure A.3(b) the waveform shows that the forward scan (E_1 to E_2) produces a current peak for any species that can be reduced through the potential range scan. The potential of this peak will increase in magnitude as the potential reaches the reduction potential of the species. The current will then decrease again as the concentration of the species is consumed within the depletion zone of the electrode surface, and the system is under diffusion (mass transport) control. In the reverse scan (E_2 to E_1) it reaches the potential at which the reduced species would be reoxidised, producing a peak of similar shape and size to the reduction peak but of reversed polarity. These data is then plotted as a change in current as a response to the potential sweep. The resulting plot is called a cyclic voltammogram. The peak currents i_p^{red} and i_p^{ox} are the cathodic and anodic peak currents respectively and the potentials at which these peaks occur are known as the peak potentials E_p^{red} and E_p^{ox} respectively.

Cyclic voltammetry experiments are performed in stagnant solutions to ensure that the transport of material to the electrode surface is limited by diffusion

(experimentally there will be some uncontrolled convection through density and thermal gradients along with vibration which should be minimised).

For a fully electrochemically reversible system the magnitudes of the forward and reverse peaks are the same, the peak positions are independent of sweep rate, v and the peak separation depends on the number of electrons, n involved in the transfer process. The peak separation can be written as:

$$\mathrm{E_p^{ox}} - \mathrm{E_p^{red}} = 2 \cdot 218 \, \frac{RT}{nF} \tag{A.3}$$

when:

$$\frac{i_p^{ox}}{i_p^{red}} = -1 \tag{A.4}$$

where T is the absolute temperature and R is the gas constant. Therefore a reversible electron transfer at 298K will have a peak separation of approximately 59/n mV, independent of scan rate [217]. Since the peak separation is independent of scan rate for fully reversible systems, the formal potential of the redox specie, E^θ can be found from the mid-point between the oxidation and reduction peak potentials at all scan rates, v.

$$\mathrm{E}^\theta = \frac{E_p^{ox} - E_p^{red}}{2} \tag{A.5}$$

and the relationship between E^θ and E the applied potential is written as:

$$\mathrm{E} = \mathrm{E}^\theta + \frac{RT}{nF} ln \frac{[Ox]}{[Red]} \tag{A.6}$$

Note: An equivalent representation using the reciprocal logarithm principal can be:

$$\mathrm{E} = \mathrm{E}^\theta - \frac{RT}{nF} ln \frac{[Red]}{[Ox]} \tag{A.7}$$

This equation is called the Nernst equation. Where E is the applied electrode potential (versus reference), E^θ the formal potential (when 'Ox' and 'Red' are

at equilibrium concentrations), R is the molar gas constant, T the absolute temperature, n is the number of electrons transferred, F the Faraday constant and $[Ox]$ and $[Red]$ the concentrations at the electrode surface of the oxidised and reduced species. When the activities of Ox and Red are equal then the measured electrode potential is that of the formal electrode potential, hence strictly the Nernst equation should be represented as:

$$\mathrm{E} = \mathrm{E}^{\theta'} + \frac{RT}{nF} ln \frac{[\alpha_{Ox}]}{[\alpha_{Red}]} \tag{A.8}$$

Where $E^{\theta'}$ is the standard reduction potential (versus the SHE) and α_{Ox} and α_{Red} are the activities of the oxidised and reduced species respectively. However, experimentally the activities of the redox species are rarely known. The activities of the oxidised and reduced species are related to the concentration of the oxidised and reduced species, shown through Equation A.9:

$$\frac{[\alpha_{Ox}]}{[\alpha_{Red}]} = \frac{\gamma_{Ox}[Ox]}{\gamma_{Red}[Red]} \approx \frac{[Ox]}{[Red]} \tag{A.9}$$

Care must be taken when interpreting CV's from experimental data without having compensated for resistance. Since the electrolyte within the electrochemical cell is resistive to the flow of current, the magnitude of the resistance will depend on the geometrical design of the cell, the concentration and nature of electrolyte used. When a cathodic current flows through the cell the true cell potential will be in reality less negative then that measured by an amount iRs, where Rs is the solution resistance between the working and reference electrode. The potential experienced at the surface of the electrode will be $E_s = E + iR_s$, where E_s is the surface potential and E is the applied potential. Clearly there is a current component within this relationship and hence, the difference between surface potential and applied potential is dependent on current. The consequence of this relationship in experimental terms is that the scan rate will no longer be a linear function and so E_p will be shifted from the true values.

Another important method which was mostly used to analyse electrochemical plating system is chronopotentiommetry, but it is essential to know the working of a galvanostat (controlled current supply).

A.1.2 Potentiostat/Galvanostat

A basic overview of the working principle of a potentiostat/galvanostat (PGSTAT) is presented. The connections of the instrument to the electrochemical cell can be (or must be) set up in different ways. Figure A.4 shows the three commonly used electrochemical cell setups.

In galvanostatic mode, the current flow between the WE and the CE is controlled.

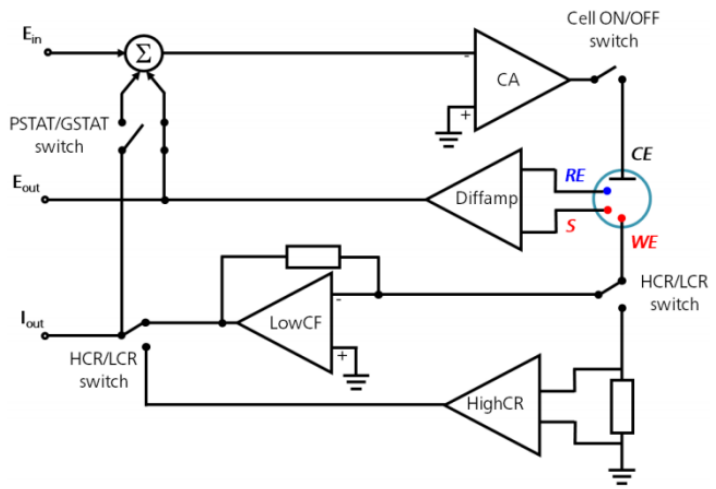

Figure A.4: Basic diagram of a potentiostat/galvanostat

The potential difference between the RE and WE and the current flowing between the CE and WE are continuously monitored. By using a PGSTAT, the value specified by the user (i.e. applied potential or current) is accurately controlled, anytime during the measurement by using a negative feedback mechanism.

As can be seen from the diagram, the CE is connected to the output of an electronic block which is called Control Amplifier (CA). The control amplifier forces current to flow through the cell. The value of the current is measured using a Current Follower (LowCF) or a Shunt (HighCR), for low and high currents,

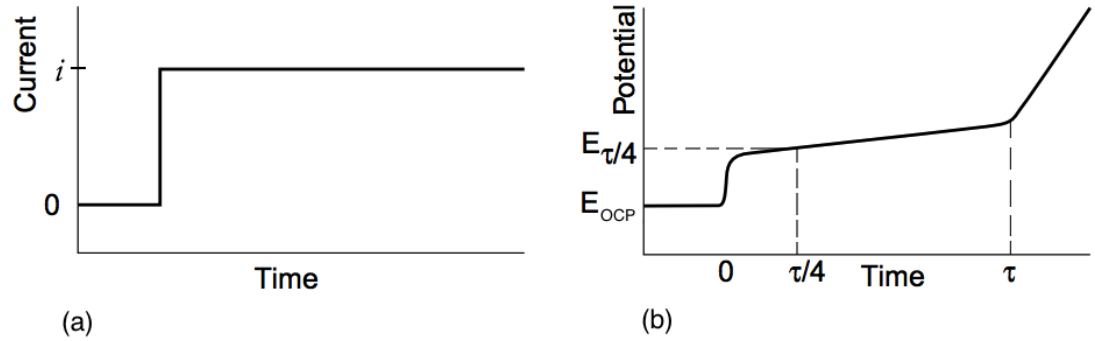

Figure A.5: (a) Current step supplied and (b) potential response measured for a chronopotentiommetry setup

respectively. The potential difference is measured always between the RE and S with a differential amplifier (Diffamp). The signal is then fed into the Summation Point (Σ) which, together with the waveform set by the digital-to-analog converter (Ein) will be used as an input for the control amplifier.

Chronopotentiomettry

This method is widely used in this study. In this technique the current flowing in the cell is instantaneously stepped from zero to some finite value.

$$M^{2+}(aq) + 2\,e^- \longrightarrow M(s) \tag{A.10}$$

A simple reaction can be considered for the reduction of metal (M) as shown in Equation A.10. The current step applied to the cathode for the reduction of the metal and the potential difference measured between the WE and RE is schematically shown in Figure A.5. The nature of the potential response can be rationalised by considered the concentration profiles of the redox species as a function of time as shown in Figure A.6. Firstly assuming zero current at the beginning. At this point the concentration of M^{2+} at the electrode surface is the same as in the bulk solution. The potential at this point is known as the rest potential or the open circuit potential (E_{OCP}). Once the current (i) is applied at the cathode, M^{2+} is reduced to M at the electrode surface in order to support the applied current and the concentration of M^{2+} at the electrode surface therefore

depletes. A concentration gradient of $[M^{2+}]$ appears between the bulk solution and the cathode surface. The potential is close to the redox potential for the reaction A.10 and its value given by the Nernst equation mentioned previously (Equation A.8). The concentration and thus potential would vary with time and an example output shown in Figure A.5(b). Once the concentration at the surface is zero the applied current can no longer support the electron transfer reaction. Another electron transfer reaction may proceed from this point and a large change in potential will be observed. The time (τ) taken for the concentration of M^{2+} at surface to reach zero depends on the current applied and is given by Sand equation:

$$\tau^{1/2} = \frac{nFAC(\pi D)^{1/2}}{2I} \tag{A.11}$$

where A is the electrode surface area, C is the bulk concentration of the analyte, and D is its diffusion coefficient . It is possible to apply more than one current step in a given experiment. Two-step experiments can be useful in characterizing electrode reactions in which the electron transfer reaction is followed by a chemical reaction.

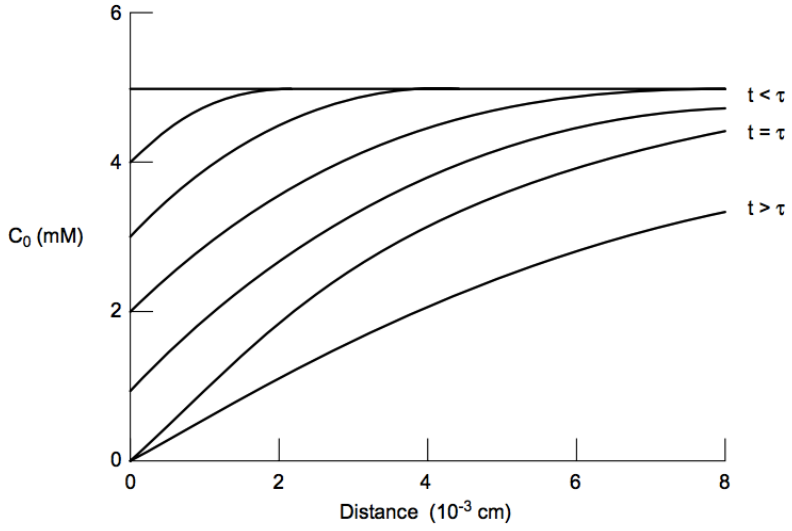

Figure A.6: Concentration-distance profiles during the reduction of M^{2+} to M by a current step

A.2 Material Characterisation

A.2.1 Plating Efficiency

When plating metals like nickel in the regime where the reduction potential of the metal coincide with the potential of other reactions like hydrogen evolution [154], the amount of metal plated will be less than expected as two reactions are occuring simultaneously. For example, during the deposition of Nickel in a chloride bath without additives, there could be the following cathodic reactions occurring: the deposition of nickel (Ni^{2+}) and reduction of acid (H_3O^+).

The simplest way for measuring the efficiency of plating is to weigh the amount of metal deposited following the ECD process. The substrate is weighed first and mass noted as m_0. After plating the mass 'm' was measured. The mass of the plated metals ($m_p = m - m_0$) can be used to calculate the plating efficiency (PE):

$$\mathrm{PE} = \frac{m_p}{m_{total}} \times 100\% \tag{A.12}$$

where m_{total} is calculated using A.13 and is the total mass of metal if all the current supplied was used up in depositing the metal (assuming 100% efficiency). The mass m(g) of a metal M plated from time(sec) = 0 to t can be calculated as:

$$\mathrm{m_{total}(g)} = \frac{A_r}{nF} \int_0^t I.dt \tag{A.13}$$

where I is the plating current in amperes, A_r is the atomic mass in grams per mole, n is the number of electrons required to plate the metal (e.g. n=2 for Ni^{2+} + $2e^- \rightarrow$ Ni) and F is the Faraday's constant F = 96,485 C/mol.

A.2.2 Deposit Thickness

The average plated film thickness 's' can be derived using the electroplated mass A.13, the density of metal and surface area of cathode. The thickness in microns can then be written as:

$$\text{s (cm)} = \frac{m_p}{A\rho} \tag{A.14}$$

where m is the mass of plated metal in grams, A is the surface area of the plated part in square centimetres[1] and ρ the density in grams per cubic centimetres. In MEMS semiconductor industry the electroplating rates are addressed in terms of the current density.

Therefore, substituting equation A.13 for m_{total} and current density (J) in mA/cm^2, the thickness can be written as:

$$\text{s (cm)} = \frac{JtA_r}{nF\rho} \tag{A.15}$$

The mean plating rate (R_p) in µm/min can then be expressed as:

$$\text{R}_\text{p}\ (\text{cm}/min) = \frac{JA_r}{nF\rho} \tag{A.16}$$

A.2.3 Young's Modulus (Nanoindentation)

Young's modulus, E is the ratio of stress to strain within the elastic region of the stress strain curve (prior to the yield point). It is a measure of the stiffness of a material.

Stress σ is the relationship between an applied force (load) L and a material's cross-sectional area (A) measured in Pascals (Pa $\equiv$ Nm^{-2}).

$$\sigma = \frac{L}{A} \tag{A.17}$$

1. Thicknesses can also be addressed in microns ($1cm = 10000\mu$m)

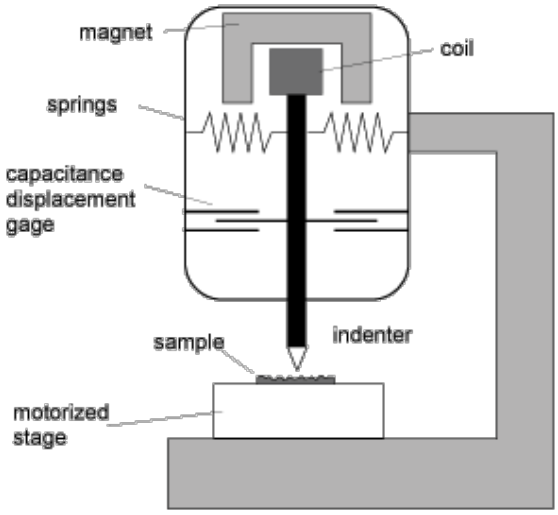

Figure A.7: Schematic of a nano-indenter

Strain is an engineering quantity that measures the change in length of a body relative to its original length when subjected to a load. Strain is a dimensionless quantity.

Robert Hooke was a 17th Century scientist principally remembered for his work on the elastic nature of materials. Hooke's Law describes the amount of elastic deformation that a material can sustain in tension or compression before it undergoes permanent plastic deformation.'Hooke's law states: 'stress is directly proportional to strain within the proportional limit.' From this, the mathematical relationship can be expressed as:

$$\text{Stress} = \text{E} \times \mathit{Strain} \tag{A.18}$$

Where E, is the constant of proportionality known as Young's modulus and has the same units as stress (Pa).

To quantify stress the value of Young's modulus for the material has to be obtained. Nanoindentation is one of the most commonly used methods to measure the hardness of small volumes of materials [219]. A schematic drawing is shown is A.7. The goal of the majority of nanoindentation tests is to extract Young's modulus and hardness of the specimen material from load-displacement measure-

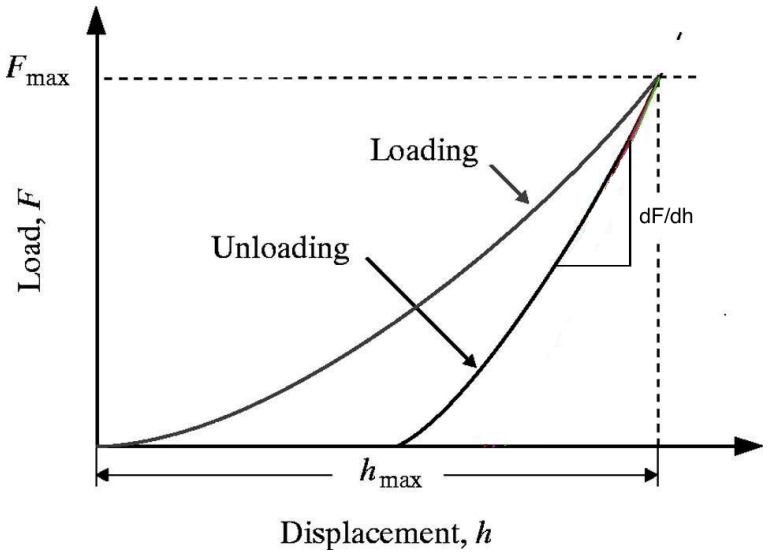

Figure A.8: Schematic of load-displacement curve for an instrumented nanoindentation test

ments, with the load created by an inductive force generator and the displacement continuously measured by a capacitance displacement gage. Conventional indentation hardness tests involve the measurement of the size of a residual plastic impression in the specimen as a function of the indenter load. This provides a measure of the area of contact for a given indenter load. In a nanoindentation test, the size of the residual impression is often only a few microns across and this makes it very difficult to obtain a direct measure using optical techniques. The depth of penetration beneath the specimen surface is measured as the load is applied to the indenter. The known geometry of the indenter then allows the size of the area of contact to be determined. The procedure also allows for the modulus of the specimen material to be obtained from a measurement of the 'stiffness' of the contact, that is, the rate of change of load and depth.

The indenter tip is conventionally made of diamond, formed into a sharp, symmetric shape such as the three-sided Berkovich pyramid. The pyramidal shape is chosen at least in part for its nominal geometric self-similarity, which makes for relatively simpler analysis using the methods of continuum mechanics. However, because of the very fine scale of nanoindentation testing, imperfections in the pyramidal tip shape are of paramount importance in such analysis, and much

effort has been focused upon methods of characterizing and cataloging tip shapes for more exact quantitative measurements [220][221][222][223]. A record of values of load vs. displacement can be plotted on a graph to create a curve shown in Figure A.8. Measurement of the Young's modulus follows from its relationship to contact area and the measured unloading stiffness through the relation:

$$\mathrm{S} = \frac{dF}{dh} = \beta \frac{2}{\sqrt{\pi}} E_{eff} \sqrt{A} \tag{A.19}$$

where E_{eff} is the effective elastic modulus defined by

$$\frac{1}{E_{eff}} = \frac{1 - v^2}{E} + \frac{1 - v_i^2}{E_i} \tag{A.20}$$

The effective elastic modulus takes into account the fact that elastic displacements occur in both the specimen, with Young's modulus E and Poisson's ratio v, and the indenter, with elastic constants $\mathrm{E}_i$and v_i. The dimensionless geometrical constant β is taken as unity and is used to account for deviations in stiffness caused by the lack of axial symmetry for pyramidal indenters [224].

A.2.4 X-Ray Fluorescence

X-Ray Fluorescence (XRF) spectroscopy is a powerful, versatile and non-destructive technique for the analysis and characterization of materials. It distinguishes different elements present in a sample according to their characteristic X-ray emission energies. A simple schematic representation is shown in Figure A.9. A stable

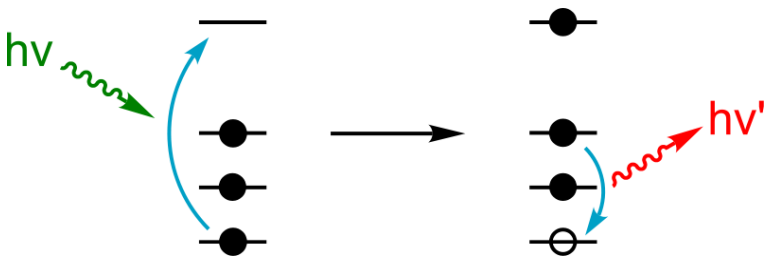

Figure A.9: Schematic representation of x-ray fluorescence

atom comprises a nucleus and a set of filled electrons orbiting it. Each filled

orbital is made up of two electrons electrons with the same energy and opposite spin. When a high energy incident (primary) X-ray collides with an atom, an electron is ejected from a filled orbital, creating a hole. As a result an electron from a higher energy level falls into this hole, emitting the energy as fluorescent or secondary X-ray and the amount of emission determines the proportion of the material, which are characteristic of the element.

XRF is widely used in analysing coating thickness of metals and metal alloys to quality control in the electronics and consumer goods industry [225]. Plated NiFe composition and film thickness were obtained using an XRF in this study.

A.2.5 Magnetic Properties

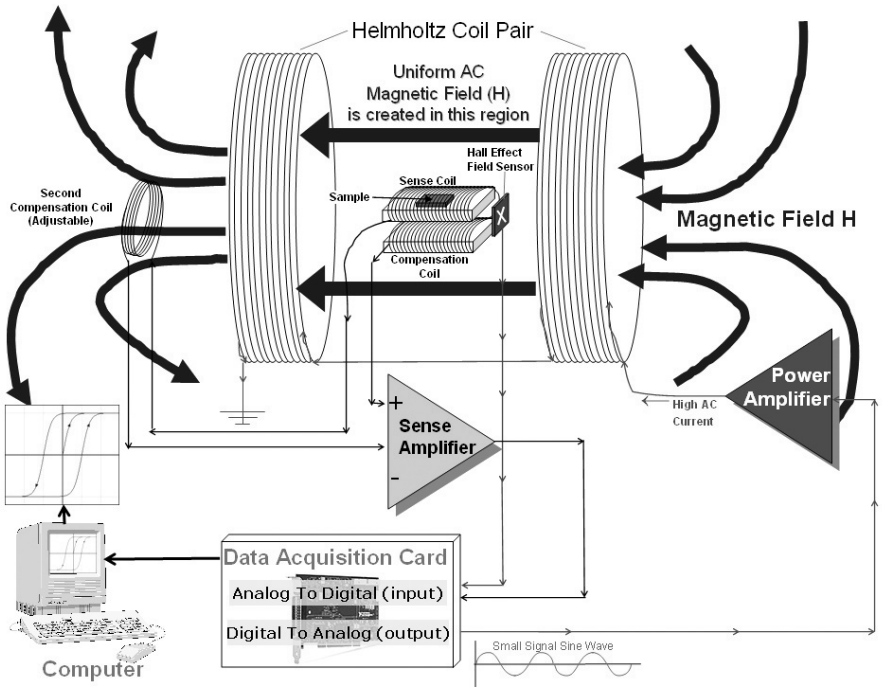

Figure A.10: B-H looper block diagram

A B-H looper (BHL) measures the hysteresis loop (Flux Density B versus Field Intensity H) of a thin magnetic film sample by applying a field to the sample and measuring the magnetic field produced by the sample's magnetization. A schematic of a simple B-H looper is shown in Figure A.10. Two Helmholtz coils create a constant magnetic field whose value is controlled by the amount of current

running in the coil wires. The sample is loaded and magnetised in the centre of the field. The magnetisation of the sample is picked up by the sense coil. The signals are acquired, amplified and filtered using the electronics and a hysteresis plot is obtained.

A schematic of a typical hysteresis loop for a ferromagnet is shown in Figure A.11. When initially deposited, the net magnetic moment for thin magnetic films is usually zero. On application of a field the magnetisation then increases until saturation, H_0, is reached following the dotted line to point 'a'. This initial part of the hysteresis loop can only be reproduced if the ferromagnet is demagnetised. On reducing the applied field to zero the magnetisation then reduces to a value M_r (point 'b'), known as the remanence. As the field is increased in the opposite direction the magnetisation goes to zero when $H = H_c$ (point 'f'), known as the coercivity. Hysteresis loops for ferromagnets (Iron, Nickel-Iron etc.) are typically symmetric and centred about zero. For ferromagnetic materials the coercivity is

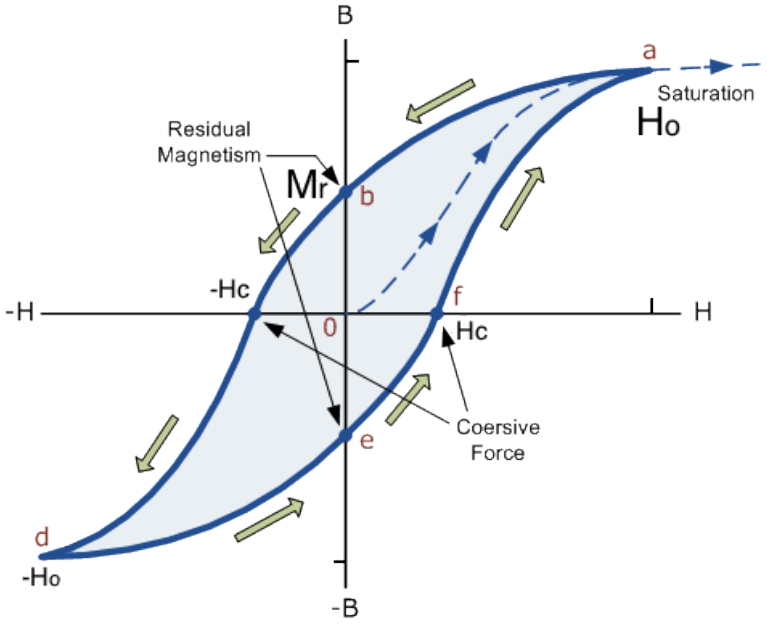

Figure A.11: Schematic of magnetic hysteresis loop [12]

the intensity of the applied magnetic field required to reduce the magnetization of that material to zero after the magnetization of the sample has been driven to saturation [226]. These properties govern the performance of magnetic devices like

micro-inductors and micro-switches and hysteresis loops were used extensively to study them.

A.2.6 UV-Vis Spectrometry

Ultraviolet-visible (UV-Vis) absorption spectrometry is the measurement of the attenuation of a beam of light on passing through a sample. Absorption measurements can be at a single wavelength or over an extended spectral range. Ultraviolet and visible light are energetic enough to promote outer electrons to higher energy levels, and UV-Vis spectroscopy is usually applied to molecules or inorganic complexes in solution. The UV-Vis spectra have broad features that are of limited use for sample identification but are very useful for quantitative measurement.

When electromagnetic radiation is absorbed by a solute molecule the intensities of the incident light I_0 and the transmitted light I are related by the Beer-Lambert law:

$$\mathrm{A} = \log_{10}\frac{I_0}{I} = \epsilon c x \tag{A.21}$$

where c is the concentration and x is the pathlength of radiation through the solution. The constant ϵ is the extinction coefficient. If c is measured in moldm^{-3} and x in cm, then ϵ is known as the molar absorption coefficient and is the value of the absorbance A for a 1 M solution when the light pathlength is 1 cm [227]. Since the absorbance is a dimensionless quantity it follows that the molar absorption coefficient has the units dm^{3}mol^{-1}cm^{-1}. The molar absorption coefficient varies with the wavelength of the light and is characteristic of the absorbing species. This law simply states that absorbance is directly proportional to the concentration of analyte in the sample.

This study will include the development of this method to produce a robust and quick method to monitor the depletion of nickel(II)chloride and iron(II)chloride in the electroplating bath. This replaces the laborious titrations done previously [228].

Appendix B

Process Equipment Parameters

B.1 PECVD Oxide

Deposition tool: Surface Technology Systems (STS) Multiplex PECVD

Recipe name: "HFSIO"

Target deposition rate: 500 Åmin^{-1}

A sequencer was used to run a batch of 2 wafers using the same parameters.

Table B.1: PECVD oxide (0.75 µm) deposition recipe using STS Multiplex tool

Parameters	Quantity
General	
Target thickness	0.75µm
Pump down time	0
Gas stabilisation time	10s
Process time	15 min
Pump out time	0
Pressure	
APC mode	automatic
Process pressure	550mTorr
Tolerance	25%
Pressure trip	1899mTorr
Temperature	
Platen temperature	300°C
Paten temperature tolerance	25°C
Showerhead temp/tolerance	250°C / 25°C
Gasses	
N_2O	1420 sccm
SiH_4	6 Sccm
RF	
Showerhead	380kHz
Power	60W
Tolerance	99%

Table B.2: Runcard for spin coating 50 µm thick SU-8

Step	Process	Equipment	Parameter	Date	Comments
A	**SU8 Wafer Preparation**				
A1	- Fuming Nitric Acid Rinse	Wet Bench	10mins		
A2	- DI Water Rinse	Dump Rinse			standard run
A3	- Wafer Drying	Maragoni Dryer			standard run
A4	- Anneal Wafers	Hotplate	20mins		200°C
A5	- Plasma Dry Wafers	Barrel Asher	10mins		
B	**SU8 Wafer Patterning**				
B1	- Coat SU-8 Resist	Manual Spinner Bay 10	50µm		500rpm/10s, 2000rpm/30s, dispense 3ml
B2	- SU8 Snap Spin	Manual Spinner Bay 10	Recipe 5		
B3	- Softbake 1	Hotplate	5mins		65°C
B4	- Softbake 2	Hotplate	15mins		95°C
B5	- Exposure	Karl Suss MA8			Vac-Cont/Spacer with i-line filter (al gap 100)
B6	- Postbake 1	Hotplate	3mins		65°C
B7	- Postbake 2	Hotplate	3mins		95°C
B8	- Develop Photoresist	Manual Spinner Bay 10	6mins		
B9	- Hardbake	Hotplate	10mins		150°C

B.2 Seed layers Ti-Cu-Ti sputter deposition

Sputter tool: Oxford Instruments Plasmalab System 400

Table B.3: Seed layer deposition

Process Steps and Parameters	
Argon Mill	
Process time	10min
Chamber pressure	7.5e-9 Torr
Ar Pressure	25 sccm
RF bottom electrode power	0.4 kW
Sputter Pre-clean	
Process time	1 min
Chamber pressure	7.5e-9 Torr
Ar Pressure	50 sccm
Magnetron power	1 kW
Target Magnetron ID	Ti
Titanium Deposition	
Target thickness	30 nm
Process time	10 min
Chamber pressure	7.5e-9 Torr
Ar Pressure	50 sccm
Magnetron power	1 kW
Target Magnetron ID	Ti
Sputter Pre-clean	
same as step 2	
Target Magnetron ID	Cu
Copper Deposition	
Target thickness	300 nm
Process time	30 min
Chamber pressure	7.5e-9 Torr
Ar Pressure	50 sccm
Magnetron power	1 kW
Target Magnetron ID	Cu
Titanium Deposition	
Target thickness	30 nm
Process time	10 min
Chamber pressure	7.5e-9 Torr
Ar Pressure	50 sccm
Magnetron power	1 kW
Target Magnetron ID	Ti

B.3 NiFe bath analysis

B.3.1 Ni^{2+} and Fe^{2+}

Rigorous chemical bath analysis is crucial in electrochemistry especially when the charge carriers are depleting with time, either due to reduction while plating or oxidation/corrosion within the solution. The most common substance to corrode in the acidic baths is Fe^{2+}.

The NiFe plating baths are usually termed as unusual or anomalous type [89]. According to Brenner's definition the iron group metals (Fe,Co,Ni) the less noble metal gets deposited preferentially and the percentage is higher and not proportional to its composition in the electrolyte [229].

It is rather essential to measure the composition of electrically active species in the electrolyte using a method which would give precise and quick results. Titration is one of the methods used to accurately calculate the concentrations of different species in an electrolytic bath [230]. It requires a lot of time and effort to setup and perform the tedious experiment. With the fact that nickel and iron forms different coloured complexes in water (Ni^{2+}:bluish-green, Fe^{2+}: yellow), meant a UV/Vis analysis could be performed.

The aim of this study was to propose a simple and rapid colorimetric method using UV/Vis (theory discussed in appendix A.2.6) to quantitatively determine the amounts of [Ni^{2+}] and [Fe^{2+}] in a standard electrochemical chloride bath of pH 3. The wavelength of maximum absorbance was calculated along with different volumes and ratios of both nickel and iron complexes. SSA (sulfosalicylic acid $C_7H_6O_3$) was used as an indicator (complexing agent) for the detection of Fe^{3+} (Fe-SSA complex) in acidic medium [231]. The iron(III)-SSA complexes are well known and their properties including thermodynamic stabilities and spectral properties have been exploited for a long time [232]. The complex forms a purple colour which will form as the basis for the colorimetric determination of oxidised Fe^{3+} species in the nickel-iron bath. The complexing reaction [230], [233] can be

represented as:

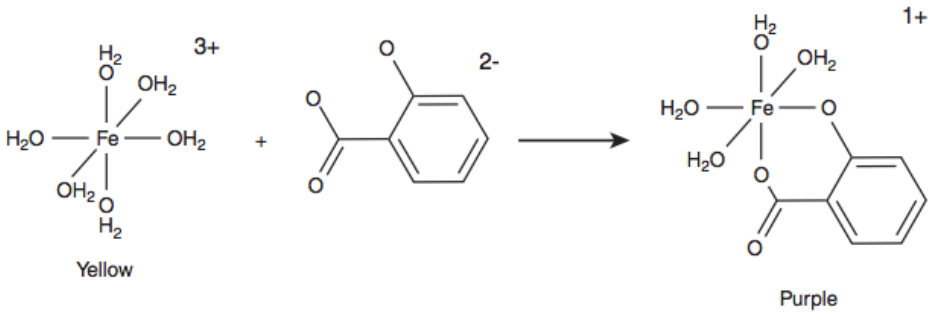

Figure B.1: Fe-SSA complex

B.3.2 UV-Vis of nickel(II)chloride

Table B.4: Bath samples prepared for Ni/Fe UV-Vis analysis (g/l)

Species	**A (buffer)**	**B (nickel)**	**C (nickel+iron)**
$NiCl_2.6H_2O$ (s)	-	0-250	50
$FeCl_2.4H_2O$ (s)	-	-	0-11
Boric Acid (s)	25	25	25
Na Saccharin (s)	1.0	1.0	1.0
Na dodecyl sulphate (s)	0.1	0.1	0.1
NaCl (s)	5.0	5.0	5.0
5-SSA (s)			1.0
H_2O_2 (aq)			2.0 M
Temperature (°C)	24 ± 1		
pH	2.6 ± 0.2		

As the bath contained both nickel and iron ions at different concentrations, it is essential to distinguish between the nickel and iron peaks. The UV-Vis

spectrometer is firstly calibrated by running a background scan of the aqueous buffer which contained the species, the standard concentrations of which are summarised in Table B.4.

The solutions were stirred at 25°C for 1 hour until all the solids were completely

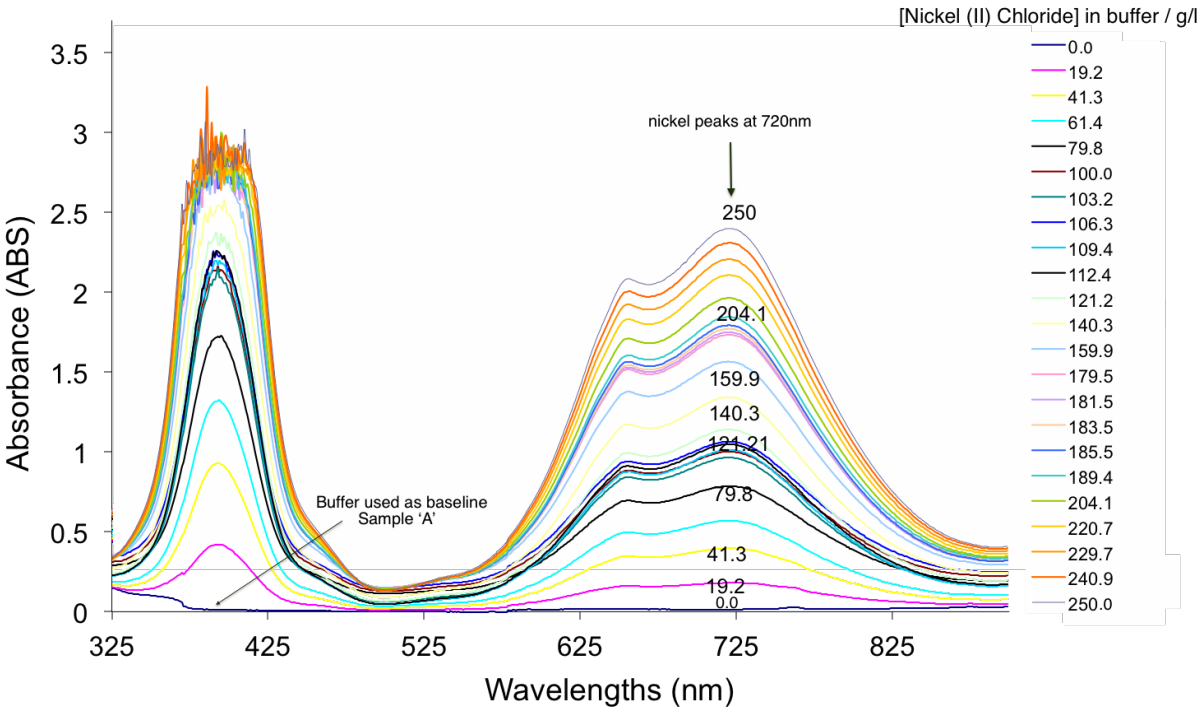

Figure B.2: Compiled UV-Vis spectrums of bath samples containing different concentrations of nickel(II)chloride in buffer (Sample set 'B')

dissolved. The pH of this buffer, sample 'A', was adjusted to 2.8 by adding a few drops of 1% HCl. The same buffer was used to make up 25 samples with varying $NiCl_2$ concentrations (0 - 250 g/l) - sample 'B'.

Each of these samples were scanned for 'absorbance' (ABS) in the wavelength range (300 - 850 nm), shown in Figure B.2. No peaks were observed for the buffer sample 'A' as expected while prominent charge transfer bands were obtained for sample 'B' at 375, 640 and 720 nm. The first peak seemed to saturate at concentrations of 220 g/l. Absorbance readings at 720nm increased with the nickel concentration and a linear regression here was applied to draw (ABS vs. Concentration) with data extracted from the peaks of the maximum sensitivity curve (720 nm), following the Beer Lambert equation explained in Chapter A.2.6.

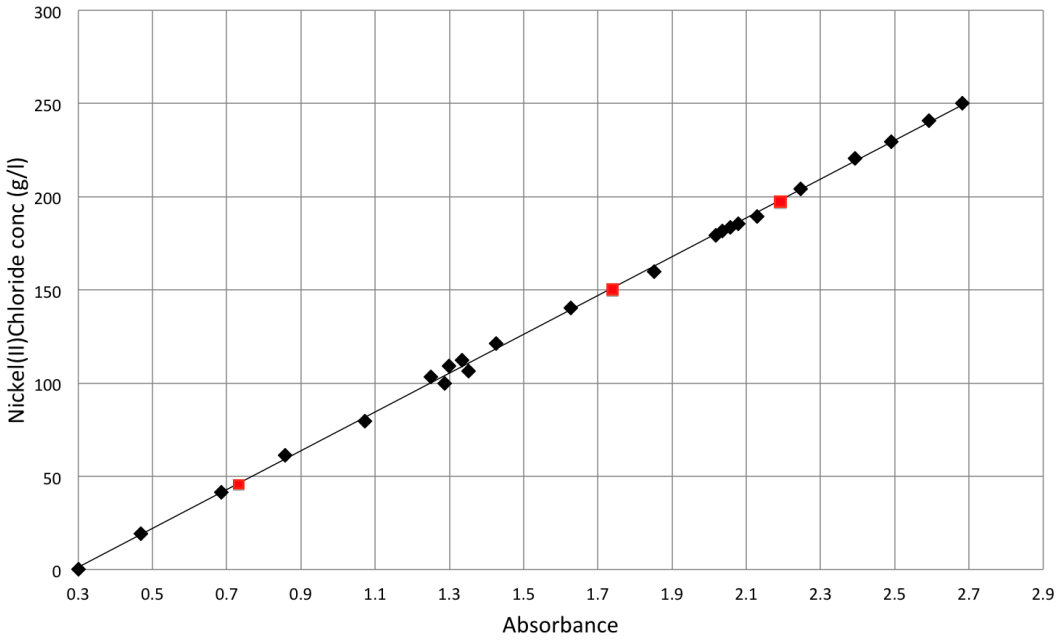

Figure B.3: Calibration curve extracted from different concentrations of nickel (II) chloride UV-Vis peak maximas at wavelength 720nm (Sample 'B')

The plot is shown in Figure B.3. This formulation was scrutinised against a known concentration (50, 150 and 200 g/l) of nickel chloride solution (marked in red) showing an accuracy of ±3%.

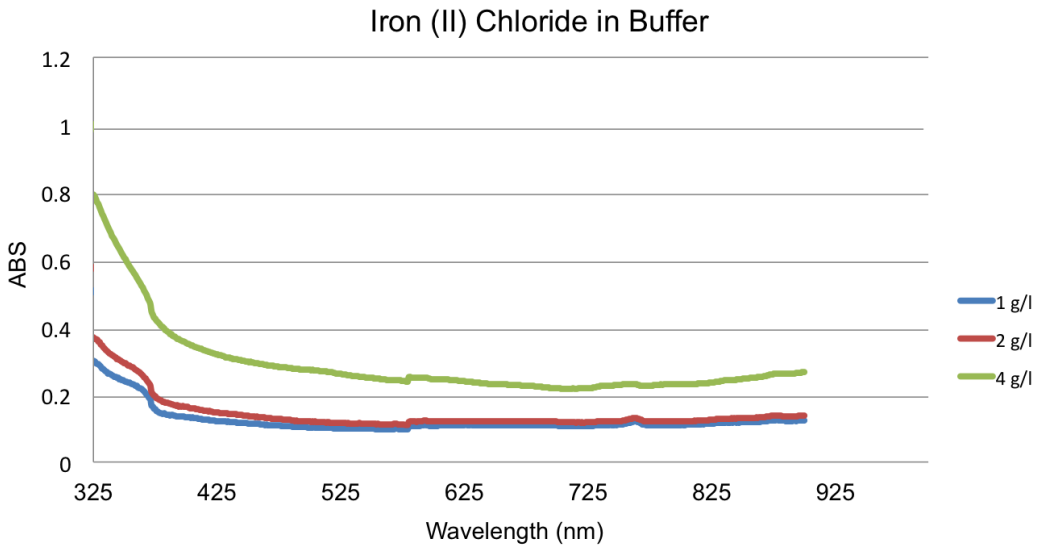

Figure B.4: UV-Vis spectrums of Iron(II)chloride in buffer

Buffer sample 'A' was used again to prepare solution samples with $FeCl_2.4H_2O$. The full spectrum's shifted upwards with the increment of iron in the solution, however no prominent peak were observed, as shown in Figure B.4. Nickel(II)chloride (50 g/l) was introduced and the iron composition varied from 0 to 5 g/l but no additional peaks appeared as the nickel complex with water dominated the colour of the solution.

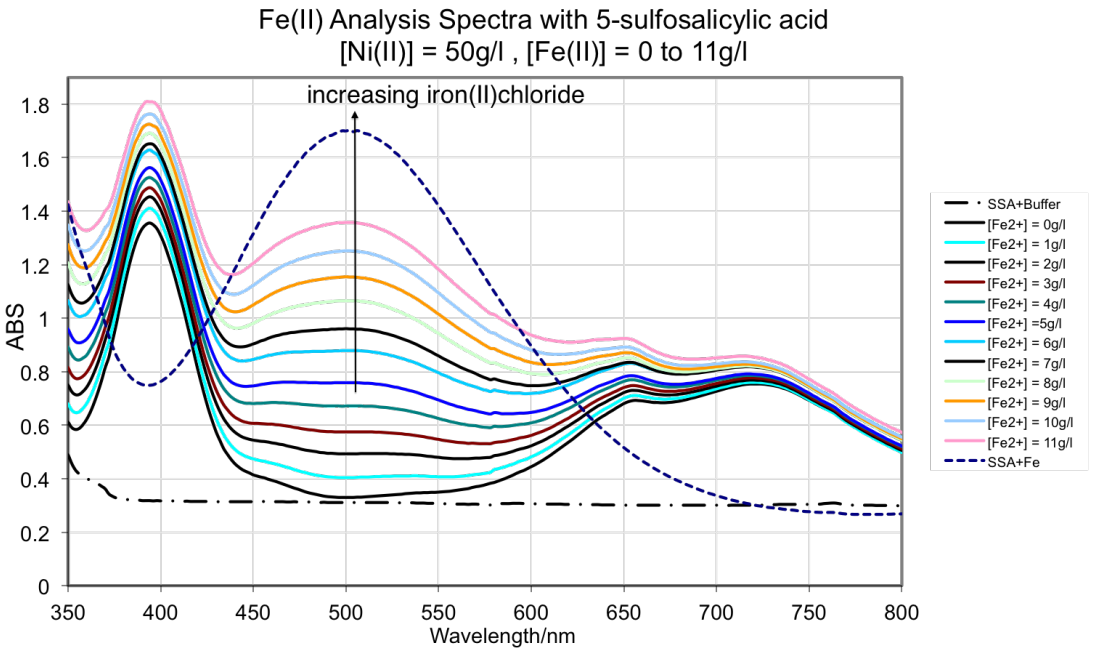

Figure B.5: UV-Vis spectrums of Sample 'C' containing nickel+iron+buffer+5-SSA. Peak height at 500nm changed with the iron composition

To measure the concentration of iron in the solution using 5-SSA all the Fe^{2+} had to be oxidised to Fe^{3+} which was achieved by adding hydrogen peroxide (2M). The addition of 5-SSA (reagent grade from Aldrich), formed a purple complex with Fe^{3+} in acidic media. Using this complexing agent for sample (C) showed clear charge transfer peaks at 500 nm increasing with the Fe-SSA complex concentration in the solution. A calibration curve was plotted which is shown below which was also tested to show the accuracy of $\pm$ 3% (Figure B.6). Nickel peaks for 50 g/l concentration was also observed in the same curve but a

broadening effect was visible which was eliminated by subtraction to determine Ni^{2+} from the same curve.

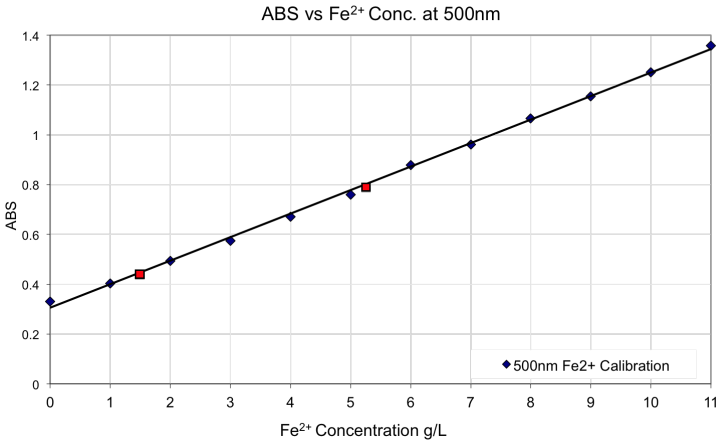

Figure B.6: Calibration curve extracted from different concentrations of Iron (II) chloride UV-Vis peak maximas at wavelength 500nm (Sample 'C')

This colorimetric method proved to be useful for periodic bath maintenance and quality checks which were carried out throughout the experiments.

B.4 Copper bath analysis

The copper baths used in this study contained the following species which were analysed using the methods described below:

1. $CuSO_4$ (aq)
2. H_2SO_4(aq)
3. Dow Intervia 8540 A (additive)
4. Dow Intervia 8540 C (carrier)

Here, 1 and 2 are measured using volumetric technique, while 3 and 4 using cyclic voltammetry.

B.4.1 Analysis of Cu^{2+}

Prerequisite:

Prepare starch solution by dissolve 10 ± 0.5 g of starch in boiling water and add 4 ± 0.5 mL of formalin. Top up with DI water to a total volume of 1 L.

- Pipette 10 mL sample of the Cu plating solution into 250 mL Erlen- meyer flask and add 100 ± 5 mL of DI water.
- Add 20 ± 2 mL of sulphuric acid (96%) and 5 ± 0.5 g of potassium iodide.
- Add 2 ± 0.5 mL of starch solution and titrate with 0.1M sodium thiosulphate.
- Titrate drop wise upon reaching end point. The solution changes to milky end point that persists for at least 30 s.
- Record the volume of 0.1M sodium thiosulphate solution used.

$[Cu^{2+}]$ / (gL^{-1}) = Titrate volume (mL) × 2.5

B.4.2 Analysis of H_2SO_4

- Pipette 2 mL sample of the Cu plating solution into 250 mL Erlenmeyer flask and add 100 ± 5 mL of DI water.
- Add 3-5 drops of methyl orange indicator and titrate with 1M sodium hydroxide solution.
- Titrate drop wise upon reaching end point. The solution changes to green end point that persists for at least 30 s.
- Record the volume of 1 M sodium hydroxide solution used.

$[H_2SO_4]$ / $(g\ L^{-1})$ = Titrate volume (mL) × 24.52.

B.4.3 Analysis of Intervia 8540A and 8540C

Equipment: TITRAPLATE®CP (CVS)

Potentiostat Software: Voltmaster

A special automated cyclic voltammetry system (TITRAPLATE) was used to monitor the levels of additive and carrier. This system was expressly developed by Micropulse Plating Concepts to allow routine maintenance operations on copper electroplating solutions. The tool uses a standard potentiostat with three electrodes (working, reference and auxiliary) immersed in the solution under test and runs cyclic voltage scans while measuring the conducted current. The system

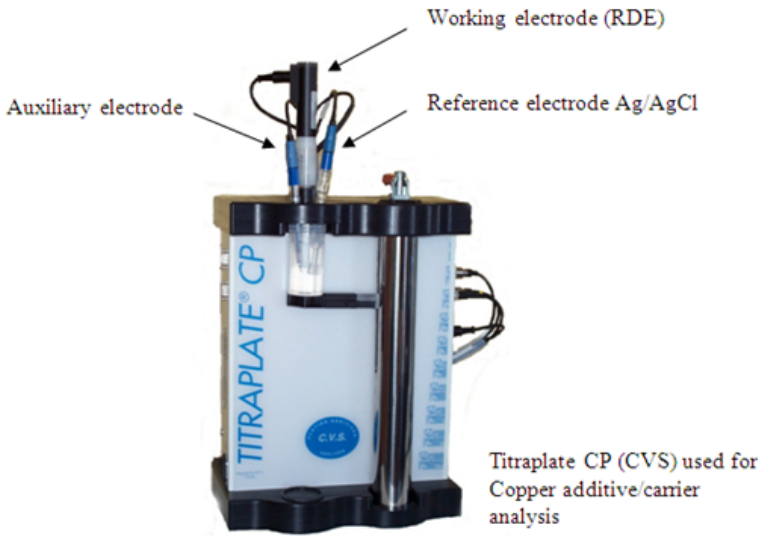

Figure B.7: Titraplate CP (CVS) used for Copper additive/carrier analysis

includes a Hamilton syringe module that allows precise volumes to be dispensed. The potentiostat and the syringe module are controlled via a single computer interface which allows to write automated running sequences. **Standard Solution: VMS** - Virgin Make-up Solution Prepare 5 L of VMS using the recipe below:

120 g/l $CuSO_4.5H_2O$

90 g/l H_2SO_4

50 mg/l Chloride

Standard Additive and Carrier Solution

5ml/l Intervia 8540 Carrier and 5 ml/l Intervia CU 8540 Additive in VMS (In 100 ml volumetric flask)

Electrode Conditioning

Fill plastic container with DI and run a conditioning recipe (50cycles at the beginning / end of the day, 20 cycles in between measurements).

B.4.3.1 Intervia 8540C (Carrier) analysis

1. Ensure the electrodes are conditioned (run 50 cycles or 20 cycles in DI, then a quick conditioning with VMS)
2. Prime the right tubes as described above with sample from the bath on the inlet.
3. Prepare a 100 ml pure VMS sample for the calibration.
4. Place the 100 ml pure VMS sample on holder and fit it with the column lever.
5. Once the syringe tubes are filled with calibration sample (after priming), remove the outlet from the syringe waste container, and place it in the hole above the burette, just above the 100 ml VMS sample.
6. Run a Carrier analysis recipe. Only push double arrow button when requested. No further manual input should be required.
7. As soon as the first cycle's results appear on screen, quickly click on the data tab and note down the ratio parameter. This is an indication of how well the measurement fits with the calibration curve stored. This value should fall in the 0.8 to 1.2 range, otherwise re-calibration is needed.
8. Note down the measured concentration as it appears in the software (Figure B.8).
9. Run 20 or 50 cycles conditioning in DI to clean the electrodes

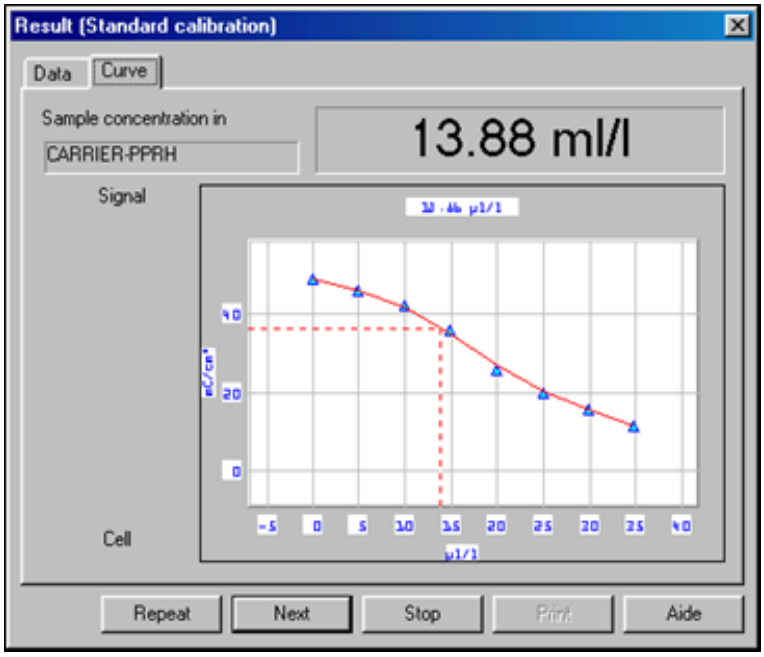

Figure B.8: Sample concentration curve showing the bath concentration of carrier

B.4.3.2 Intervia 8540A (Additive) analysis

1. Ensure the electrodes are conditioned (run 50 cycles or 20 cycles in DI, then a quick conditioning with VMS)

2. Prepare an 85 ml VMS + 5 ml GLEAM PPR CARRIER solution (90 ml in total).

3. Place the solution on holder and fit it with the column lever.

4. Run an Additive analysis recipe. Only push double arrow button when requested. The first cycle is done on the 90 ml sample. Then a 10 ml bath sample addition is required. Do that through hole on the top of the burette.

5. Remove the left outlet tube (Additive) from the syringe waste container and place it in the hole above the burette, just above the prepared sample.

6. No further input is requested.

7. Note down the measured concentration and fill the log spreadsheet.

8. Run 20 or 50 cycles conditioning in DI to clean the electrodes

Appendix C

Matlab and Labview VIs for Strain Measurements

C.1 Electrical Measurements

Agilent HP 4062UX Semiconductor Process Control System connected to the SUSS Semi-automatic prober, was configured with the following instruments (GPIB::PortAddress):

1. HP 4084B - Switching Matrix Controller (GPIB::22)
2. HP 4142B - Source / Monitor Unit (GPIB::23)
3. HP 3457A - Multimeter (used for precise voltage measurements) (GPIB::12)
4. SUSS PA200 Semi-automatic Prober (GPIB::01)

The GPIB addresses can be changed but are provided as references to these have been used in Labview code instead of the device name.

C.1.1 Device Initialisation

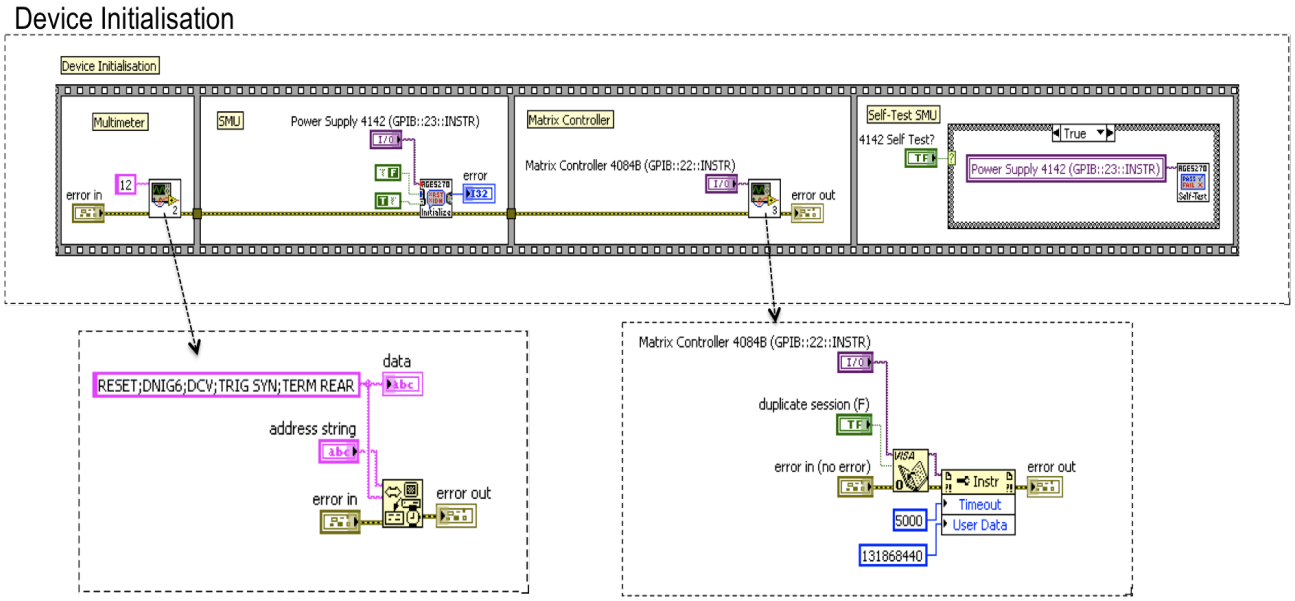

Figure C.1: Labview code: Device initialisation Vi of matrix controller and SMU for electrical measurements

C.1.2 Matrix Controller Pin Status

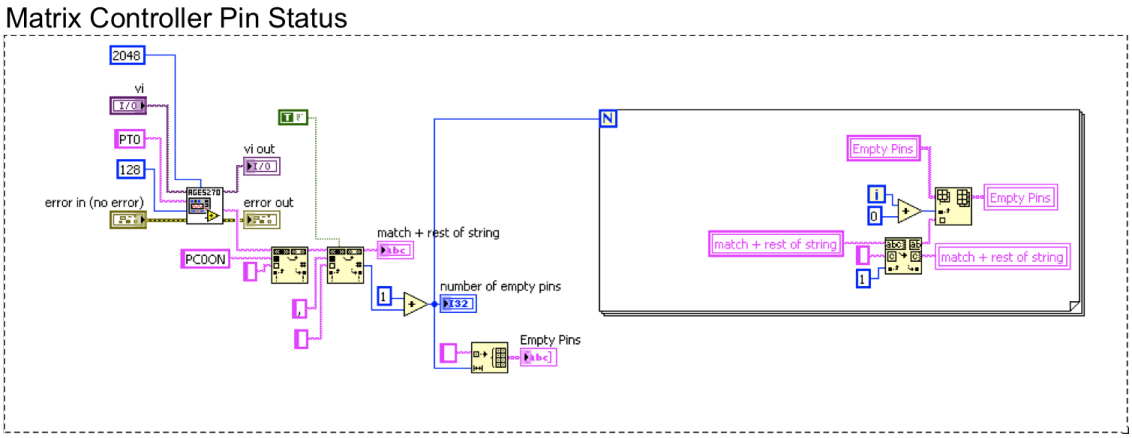

Figure C.2: Labview code: Matrix Controller Pin Status

C.1.3 Sheet Resistance

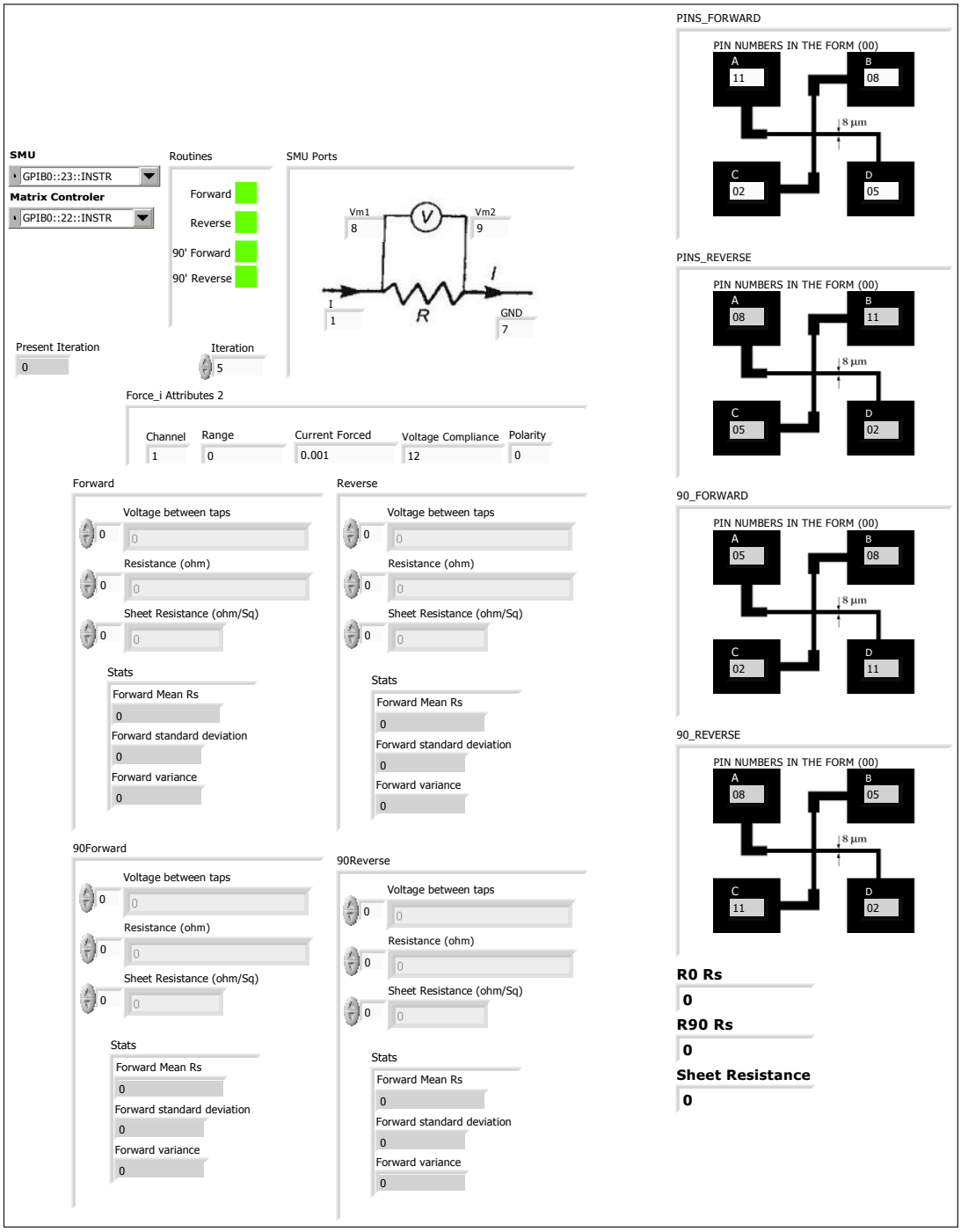

Figure C.3: Front end of vi used for stand-alone greek cross resistance measurements. Same vi is also used for full wafer measurement

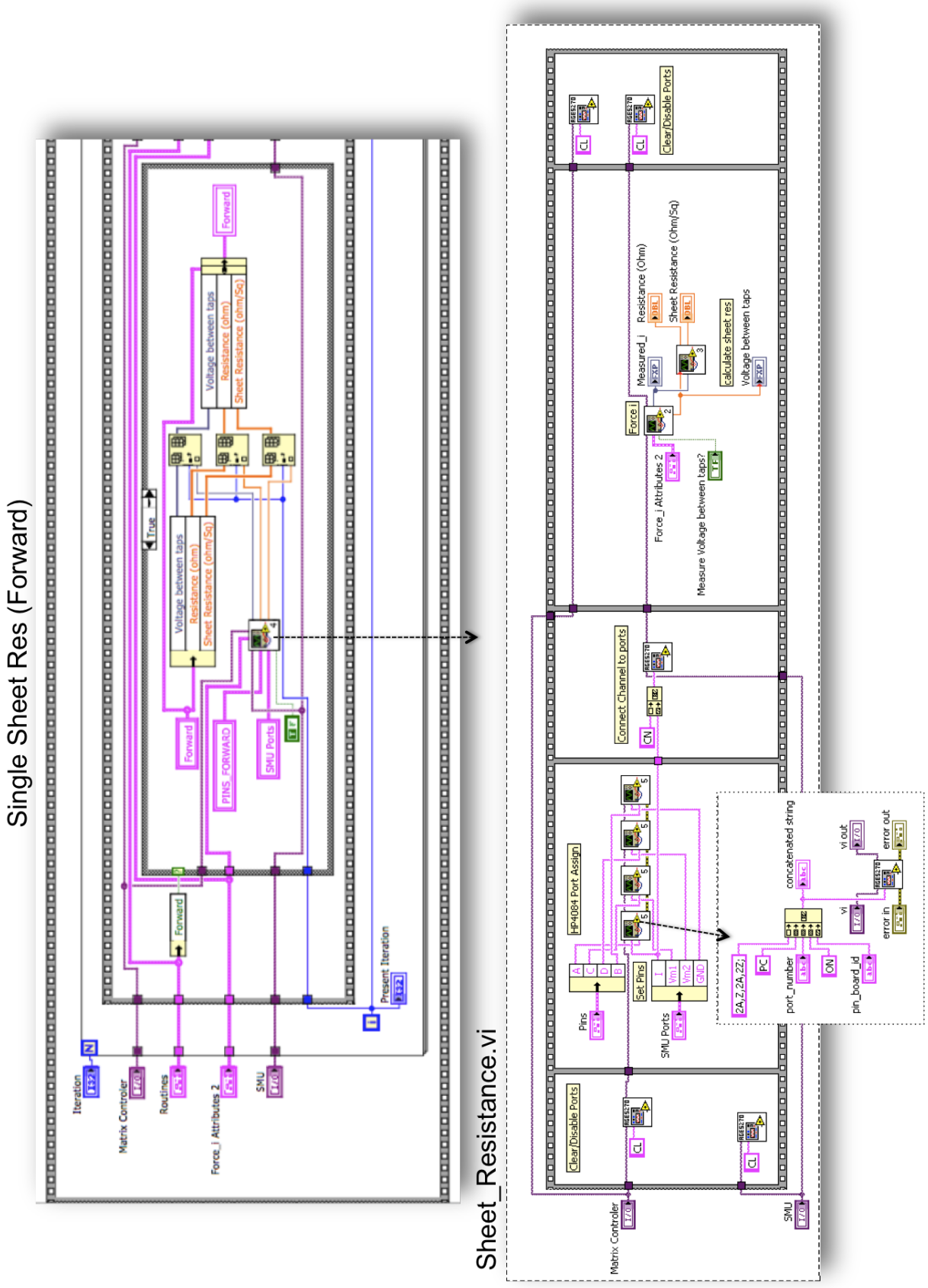

Figure C.4: Labview code: single sheet resistance routine

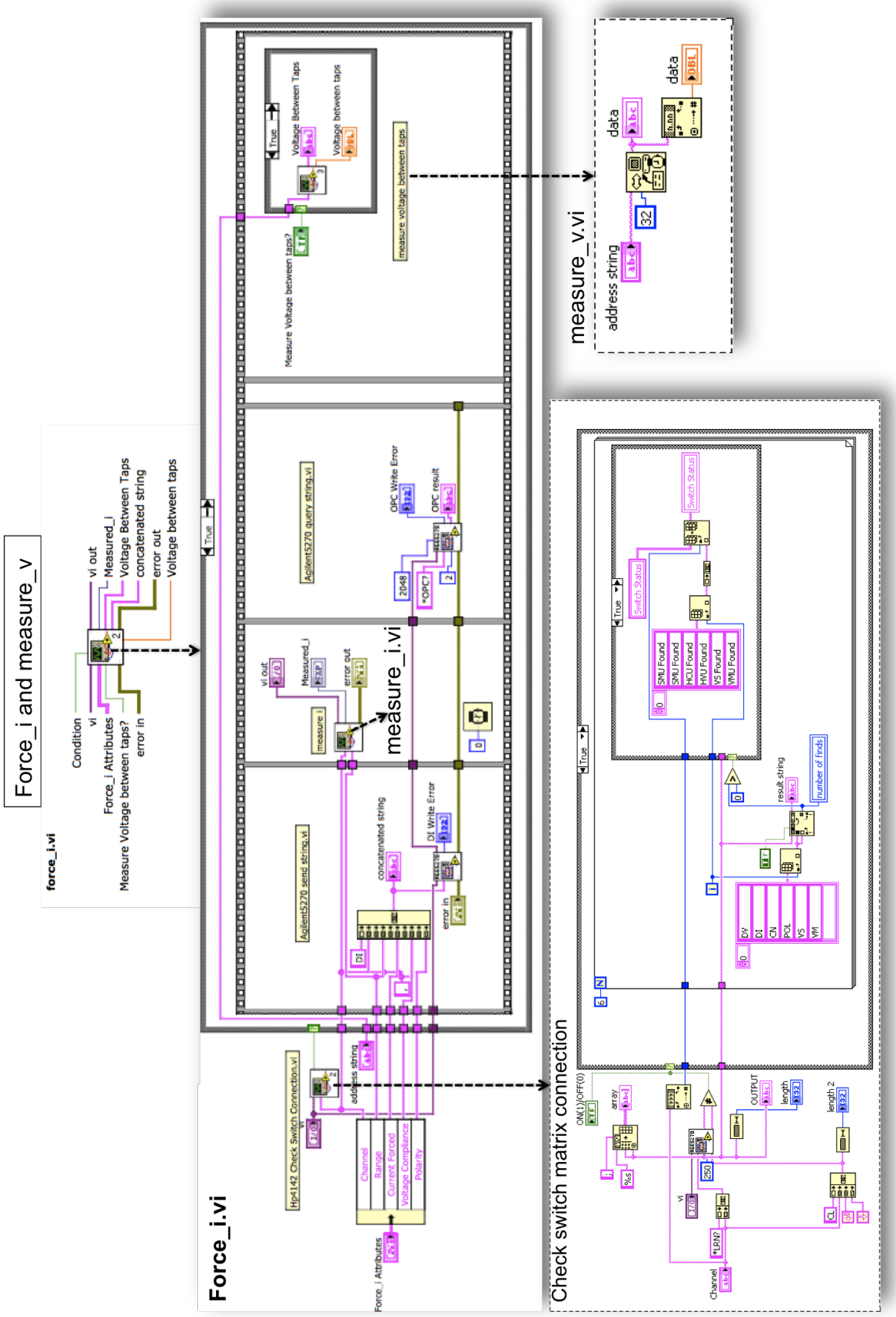

Figure C.5: Labview code: Complete sheet resistance routine

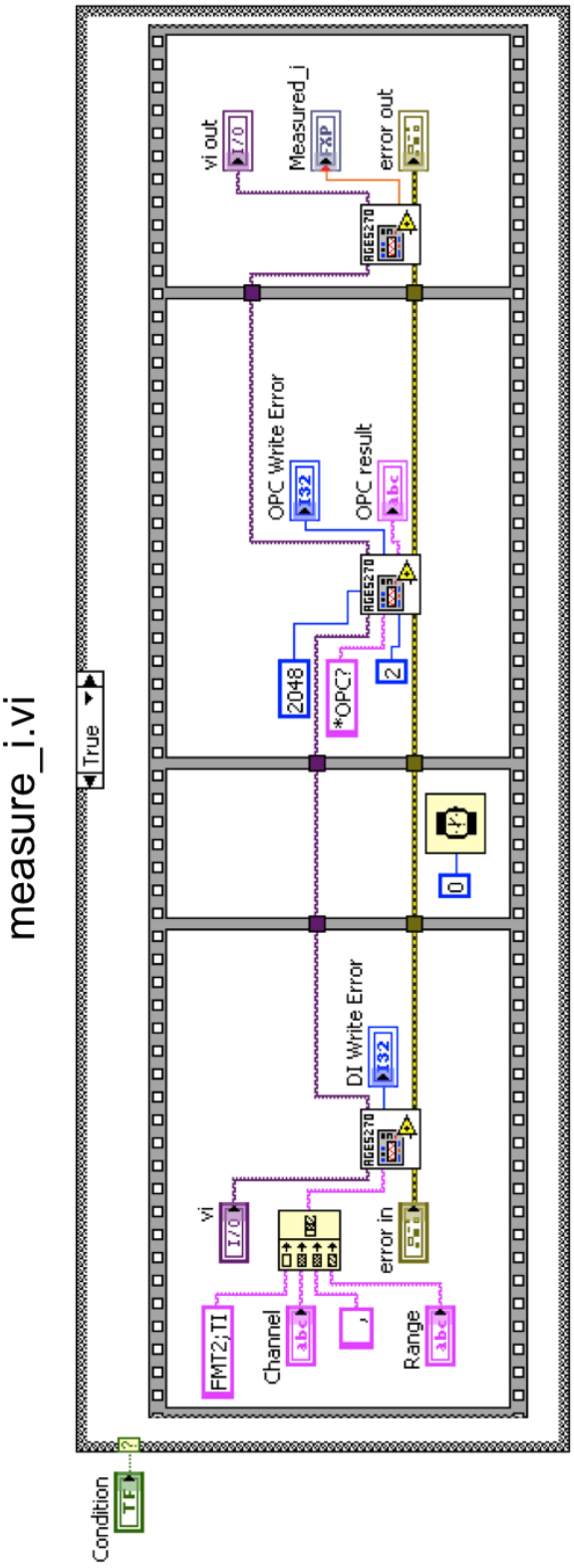

Figure C.6: Labview code: current measurement

C.2 Bridge Resistance Routines

C.3 Matlab Code for plotting Wafer Maps

C.3.1 Copper Self Annealing Calculate Transition Periods

```
close all;
clc;
%[filename, filepath]=uigetfile('*.*','Input xls or csv file');
%file = csvread(strcat(filepath,filename));
file=csvread('W10mAPlots.csv');
TStructs = 191;%191

%array=[117,105,110,98,106,118,109,97];%middle-right
%array=[115,127,124,136,116,104,111,123,81,93];%middle-left
%toop-middle-bottom
%TStructs=size(array,2);
array = 1:TStructs;
sizeArray=size(array,2);
module_no=0;%starts from 0
cycles=38; %36 cycles
moduleKelvin(cycles,6)=0;
Ravg=0;
LineW=0;
xOffset=1;
yOffset=5;
counter=1;

timec=17;
kelvinc=16;
greekc=7;


%moduleToPlot=1;
```

```
%moduleToPlot=input('Which module number? ');

for k=1:TStructs
    moduleToPlot=k;
    module_no=array(k);
    start_number=((module_no-1)*cycles+1);
    end_number=start_number+cycles-1;
    startEnd(1,1)=start_number;
    startEnd(1,2)=end_number;
    j=1; jj=1;
for i=start_number:end_number
    moduleKelvin(j,counter+2)=file(i,kelvinc);%Bridge
    moduleKelvin(j,counter+1)=file(i,greekc); %Greek sheet resistance
    moduleKelvin(j,counter)=(file(i,timec)-file(1,timec))/(3600000);
  if file(i,14)<1 && file(i,14)>0
    kelvin(j)=file(i,kelvinc);
    timek(j)=(file(i,timec)-file(1,timec))/(3600000);
    j=j+1;
  end
  if file(i,5)<0.1 && file(i,5)>0.001
    greek(jj)=file(i,greekc);
    timeg(jj)=(file(i,timec)-file(1,timec))/(3600000);
    jj=jj+1;
  end
    x=file(i,3);
    y=file(i,4);
    mod=file(i,2);
end
X1=timek(1,:);%Time for Kelvin Bridges
X2=timeg(1,:);%Time for Greeks
Y1=kelvin(1,:);%Bridge
Y2=greek(1,:);%Greek
modNumber=num2str(moduleToPlot);
filename=strcat('W2_ResPlotsForStruct_',num2str(moduleToPlot));

stepResponseB=stepinfo(kelvin,timek);
```

```
stepResponseG=stepinfo(greek,timeg);
transient(k,1)=stepResponseB.RiseTime;
transient(k,2)=stepResponseB.PeakTime;
transient(k,3)=stepResponseG.RiseTime;
transient(k,4)=stepResponseG.PeakTime;
transient(k,5)=x;
transient(k,6)=y;
transient(k,7)=mod;
moduleKelvin(1,counter+3)=transient(k,1);

scatterFig(X1,X2,Y1,Y2, 0.2,0.5,0.02,0.08,
 filename,modNumber,stepResponseB,stepResponseG); %Bridges
  kelvin(:)=0;
    greek(:)=0;
    timek(:)=0;
    timeg(:)=0;
counter=counter+4;
end

close all;
```

C.3.2 Kelvin/GreekCross Resistance Data Plotting

```
clear all;
clc;
[filename, filepath]=uigetfile('*.*','Input xls or csv file');
file = csvread(strcat(filepath,filename));
TStructs = 191;
KelvinRes(38,12)=0;
GreekRes(38,12)=0;
xOffset=1;
yOffset=5;
for(j=0:0) %82 total
    cycle_number=j;%starts from 0
    time=round(cycle_number*16/60);%from 0 hours
```

```
    start_number=(TStructs*cycle_number)+1;
    end_number=start_number+TStructs-1;
for i=start_number:end_number
KelvinRes(round(file(i,3)/9+xOffset),round(file(i,4)/18+yOffset))=file(i,11);
GreekRes(round(file(i,3)/9+xOffset),round(file(i,4)/18+yOffset))=file(i,7)*4.53;
end
%plottools; imagesc(Iron); figure(gcf)
timestr=num2str(time);
cyclestr=num2str(cycle_number);
titlename=strcat('J= 10mA/cm2 (Greek Cross Resistance of W2) at Time '''...
,timestr,''' hours');
filename=strcat('Greek',cyclestr,'_',timestr);
createfigureFrame(GreekRes,titlename,filename,4e-3*4.53,14e-3*4.53);
createfigureFrame(KelvinRes,titlename,filename,0.4,0.7);
end;
```

C.3.3 CreatefigureFrame function

```
function createfigureFrame(cdata1,titlename,filename,rangel,rangeh)
%CREATEFIGURE1(CDATA1)
%  CDATA1:  image cdata
%  Auto-generated by MATLAB on 06-Feb-2012 02:28:58
% Create figure
 figure1 = figure('XVisual','',...
     'Color',[1 1 1],...
     'Colormap',[1 1 1]);
% Create axes
axes1 = axes('Parent',figure1,'ZColor',[1 0.99 0.99],'YTick',zeros(0.99,0),...
    'YDir','reverse',...
    'YColor',[1 0.99 0.99],...
    'XTick',zeros(1,0),...
    'XColor',[1 0.99 0.99],...
    'Position',[0.13 0.108046875 0.701791652020735 0.815],...
    'Layer','top',...
    'CLim',[rangel rangeh]);
```

```
% Uncomment the following line to preserve the X-limits of the axes
% xlim(axes1,[0.5 12.5]);
% Uncomment the following line to preserve the Y-limits of the axes
% ylim(axes1,[0.5 38]);
hold(axes1,'all');

% Create image
image(cdata1,'Parent',axes1,'CDataMapping','scaled');

% Create title
title({titlename,''},...
    'FontWeight','bold',...
    'FontSize',12,...
    'FontName','Times New Roman');

% Create image
image(cdata1,'Parent',axes1,'CDataMapping','scaled');

% Create colorbar
colorbar('peer',axes1,'ZColor',[1 1 1],'XColor',[1 1 1],'FontSize',20);
% Resize the axes in order to prevent it from shrinking.
set(axes1,'Position',[0.13 0.108046875 0.701791652020735 0.815]);
saveas(figure1,filename,'jpg');
%close all;
```

C.3.4 XRF Data Extraction and Mapping

```
clear all;
clc;
[filename, filepath]=uigetfile('*.*','Input xls or csv file');
file = xlsread(strcat(filepath,filename),'Measurements');
TStructs = 384;
modules=2;
counter=1;
Ravg=0;
```

```
LineW=0;
xOffset=38;
yOffset=10;
for i=1:(TStructs)
   thickness(round(file(i,2)+xOffset),round(file(i,1)+yOffset))=file(i,3);
   Iron(round(file(i,2)+xOffset),round(file(i,1)+yOffset))=file(i,13);
end
plottools; imagesc(Iron); figure(gcf)
```

References

[1] Rob Forman. Advances in Wafer Plating and The Next Challenge: Through Silicon Via Plating. *Rohm and Haas Electronic Materials*.

[2] H. Guckel, T. Randazzo, and D. W. Burns. A simple technique for the determination of mechanical strain in thin films with applications to polysilicon. *Journal of Applied Physics*, 57(5):1671–1675, 1985.

[3] David Koester. Side-by-side comparison of passive mems strain test structures under residual compression. *Mechanical Properties of Structural Films*, 1413:168, 2001.

[4] B. P. van Drieënhuizen, J. F. L. Goosen, P. J. French, and R. F. Wolffenbuttel. Comparison of techniques for measuring both compressive and tensile stress in thin films. *Sensors and Actuators A: Physical*, 37–38(0):756–765, 1993.

[5] L Elbrecht, U Storm, R Catanescu, and J Binder. Comparison of stress measurement techniques in surface micromachining. *Journal of Micromechanics and Microengineering*, 7(3):151, 1997.

[6] H Guckel, D Burns, C Rutigliano, E Lovell, and B Choi. Diagnostic microstructures for the measurement of intrinsic strain in thin films. *Journal of Micromechanics and Microengineering*, 2(2):86, 1992.

[7] Mark G. Allen, Mehran Mehregany, Roger T. Howe, and Stephen D. Senturia. Microfabricated structures for the in situ measurement of residual stress, Young's modulus, and ultimate strain of thin films. *Applied Physics Letters*, 51(4):241–243, 1987.

[8] L Lin. Selective encapsulations of MEMS: Microchannels, needles, resonators, and electromechanical filters. Master's thesis, Thesis, Department of Mechanical Engineering,University of California, Berkeley, 1993.

[9] Xin Zhang, Tong-Yi Zhang, and Yitshak Zohar. Measurements of residual stresses in thin films using micro-rotating-structures. *Thin Solid Films*, 335(1–2):97 – 105, 1998.

[10] C. J. Wilson. Stress measurements in deep sub-micron damascene copper interconnects. *Ph.D. dissertation, Newcastle University*, 2009.

[11] S. Smith, N.L. Brockie, J. Murray, C.J. Wilson, A.B. Horsfall, J.G. Terry, J.T.M. Stevenson, A.R. Mount, and A.J. Walton. Analysis of the performance of a micromechanical test structure to measure stress in thick electroplated metal films. In *2010 IEEE International Conference on Microelectronic Test Structures (ICMTS)*, pages 80–85, march 2010.

[12] Wayne Storr. Magnetic hysteresis.

[13] Gordon E Moore et al. Cramming more components onto integrated circuits, 1965.

[14] Probir K Bondyopadhyay. Moore's law governs the silicon revolution. *Proceedings of the IEEE*, 86(1):78–81, 1998.

[15] Yale Patt. Requirements, bottlenecks, and good fortune: Agents for microprocessor evolution. *Proceedings of the IEEE*, 89(11):1553–1559, 2001.

[16] James Jeffers and James Reinders. *Intel Xeon Phi Coprocessor High Performance Programming*. Newnes, 2013.

[17] Robert N Noyce. Field effect transistor, November 21 1961. US Patent 3,010,033.

[18] Salvatore A Vittorio. Microelectromechanical systems (mems). *Cambridge Scientific Abstracts, October*, pages 1–11, 2001.

[19] Hiroyuki Fujita. A decade of MEMS and its future. In *Micro Electro Mechanical Systems, 1997. MEMS'97, Proceedings, IEEE., Tenth Annual International Workshop on*, pages 1–7. IEEE, 1997.

[20] M Mehregany and S Roy. Introduction to mems, 2000, microengineering aerospace systems, el segundo, 1999.

[21] Mohamed Gad-el Hak. *MEMS: introduction and fundamentals*. CRC press, 2010.

[22] W Rhett Davis, John Wilson, Stephen Mick, Jian Xu, Hao Hua, Christopher Mineo, Ambarish M Sule, Michael Steer, and Paul D Franzon. Demystifying 3D ICs: the pros and cons of going vertical. *Design & Test of Computers, IEEE*, 22(6):498–510, 2005.

[23] JH Smith, S Montague, JJ Sniegowski, JR Murray, and PJ McWhorter. Embedded micromechanical devices for the monolithic integration of mems with cmos. In *Electron Devices Meeting, 1995. IEDM'95., International*, pages 609–612. IEEE, 1995.

[24] Brice Jamieson, Jeffrey F Godsell, Ningning Wang, and Saibal Roy. Device geometry effects in an integrated power micro-inductor with a ni45fe55 enhancement layer. 2013.

[25] Ningning Wang, John Barry, Jason Hannon, Santosh Kulkarni, Ray Foley, Kevin McCarthy, Kenneth Rodgers, Finbarr Waldron, Mark Barry, Declan Casey, et al. High frequency DC-DC converter with co-packaged planar inductor and power ic. In *Electronic Components and Technology Conference (ECTC), 2013 IEEE 63rd*, pages 1946–1952. IEEE, 2013.

[26] Amrit Panda, Trifon Liakopoulos, Matthew Wilkowski, and Ashraf Lotfi. A unique magnetic alloy for integrated power systems on a chip. *ECS Transactions*, 50(10):107–118, 2013.

[27] Cian Ó Mathuna, Ningning Wang, Santosh Kulkarni, and Saibal Roy. Pwrsoc (integration of micro-magnetic inductors/transformers with active semiconductors) for more than moore technologies. *Eur. Phys. J. Appl. Phys*, 63:14408, 2013.

[28] Massimiliano Amato, Francesco Dalena, Cristina Coviello, Massimo De Vittorio, and Simona Petroni. Modeling, fabrication and characterization of micro-coils as magnetic inductors for wireless power transfer. *Microelectronic Engineering*, 2013.

[29] Frans Spaepen. Interfaces and stresses in thin films. *Acta Materialia*, 48(1):31–42, 2000.

[30] L Benjamin Freund and Subra Suresh. *Thin film materials: stress, defect formation and surface evolution*. Cambridge University Press, 2003.

[31] JJ Vlassak. Thin film mechanics. *Harvard University, Boston, MA*, 2004.

[32] Yu-Hin F Lau. *MEMS structures for stress measurements for thin films deposited using using CVD*. PhD thesis, Massachusetts Institute of Technology, 2001.

[33] HD Arnold and GW Elmen. Permalloy, a new magnetic material of very high permeability. *Bell System Technical Journal*, 2(3):101–111, 1923.

[34] Douglas C Giancoli. Physics for scientists and engineers with modern physics. *International Edition*, 4, 2000.

[35] Christine Whitman, Mehrdad M Moslehi, Ajit Paranjpe, Lino Velo, and Tom Omstead. Ultralarge scale integrated metallization and interconnects. *Journal of Vacuum Science & Technology A*, 17(4):1893–1897, 1999.

[36] Y Tsuru, M Nomura, and FR Foulkes. Effects of boric acid on hydrogen evolution and internal stress in films deposited from a nickel sulfamate bath. *Journal of Applied Electrochemistry*, 32(6):629–634, 2002.

[37] Fi.V. Tilak, A.S. Gendron, and M.A. Mosoiu. Borate buffer equilibrium in nickel electrorefining electrolytes. *J. Appl. Electrochem*, 7(6)(495-500), 1977.

[38] James P Hoare. Boric acid as a catalyst in nickel plating solutions. *Journal of the Electrochemical Society*, 134(12):3102–3103, 1987.

[39] K-M Yin and B-T Lin. Effects of boric acid on the electrodeposition of iron, nickel and iron-nickel. *Surface and Coatings Technology*, 78(1):205–210, 1996.

[40] CE Dávalos, JR López, H Ruiz, Alia Méndez, R Antaño-López, and G Trejo. Study of the role of boric acid during the electrochemical deposition of Ni in a sulfamate bath. *International Journal of Electrochemical Science*, 8(7), 2013.

[41] SE Hadian and DR Gabe. Residual stresses in electrodeposits of nickel and nickel–iron alloys. *Surface and Coatings Technology*, 122(2):118–135, 1999.

[42] Denish Gangasingh and Jan B Talbot. Anomalous electrodeposition of nickel-iron. *Journal of the Electrochemical Society*, 138(12):3605–3611, 1991.

[43] Robert C Weast, Melvin J Astle, and William H Beyer. *CRC handbook of chemistry and physics*, volume 69. CRC press Boca Raton, FL, 1988.

[44] S.I.Shah D.A.Glocker. Handbook of thin film process technology. *IOP Publishing*, 1995.

[45] L. W. Flott. *Metal Finishing, 64th Guidebook and Directory Issue, 94 (1A)*. 1996.

[46] Christopher L Chua, David K Fork, Koenraad Van Schuylenbergh, and Jeng-Ping Lu. Out-of-plane high-Q inductors on low-resistance silicon. *Microelectromechanical Systems, Journal of*, 12(6):989–995, 2003.

[47] Ningning Wang, Terence O'Donnell, Saibal Roy, Paul McCloskey, and Cian O'Mathuna. Micro-inductors integrated on silicon for power supply on chip. *Journal of Magnetism and Magnetic Materials*, 316(2):e233 – e237, 2007.

[48] Panos C Andricacos. Copper on-chip interconnections. *The Electrochemical Society Interface*, 8(1):6, 1999.

[49] A Kamto, Y Liu, L Schaper, and SL Burkett. Reliability study of through-silicon via (TSV) copper filled interconnects. *Thin solid films*, 518(5):1614–1619, 2009.

[50] James R Black. Electromigration failure modes in aluminum metallization for semiconductor devices. *Proceedings of the IEEE*, 57(9):1587–1594, 1969.

[51] Jack W Dini and Dexter D Snyder. Electrodeposition of copper. *Modern Electroplating, Fifth Edition*, pages 33–78, 2000.

[52] G Oskam, PM Vereecken, X Shao, and J Fransaer. Semiconductors, metal oxides, and composites: Metallization and electrodeposition of thin films and nanostructures. The Electrochemical Society, 2010.

[53] R. Taft and H. E. Messmore. *Phys. Chem.*, 35(2585), 1931.

[54] R. Taft and O. R. Bingham. *Phys. Chem.*, 36(2338), 1932.

[55] C. Struyk and A. E. Carlson. *Rev. Am. Electroplat. Soc.*, 33(923), 1946.

[56] H. M. Goodwin and W. H. Horsch. *Chem Metall Eng*, 21(181), 1919.

[57] E. F. Kern and M. Y. Chang. *Trans Am Electrochem Soc*, 41(181), 1922.

[58] GM Kimber, DH Napier, and DH Smith. Electrodeposition at rotating cathodes from acidified copper sulphate solution. *Journal of Applied Chemistry*, 17(2):29–35, 1967.

[59] Maria Nikolova and Jim Watkowski. Innovative high throw copper electroplating process for metallization of PCB.

[60] A. K. Graham and Trans. *Am Electrochem Soc*, 52(157), 1927.

[61] Y Fukunaka, H Doi, and Y Kondo. Structural variation of electrodeposited copper film with the addition of an excess amount of sulfuric acid. *Journal of The Electrochemical Society*, 137(1):88–93, 1990.

[62] W. A. Fairweather and Trans. *Inst Met. Finish.*, volume 62. 1984.

[63] A. Sato and R. Barauskas. *Metal Finishing, 64th Guidebook and Directory Issue, 94 (1A)*. 1996.

[64] E. F. Duffek and "Plating. *Printed Circuits Handbook*. McGraw-Hill, New York, 1996.

[65] YL Kao, KC Li, GC Tu, and CA Huang. Microstructural study of the effect of chloride ion on electroplating of copper in cupric sulfate-sulfuric acid bath. *Journal of The Electrochemical Society*, 152(9):C605–C611, 2005.

[66] RE Gana, MG Figueroa, and RJ Larraín. The effect of certain ions on the internal stress of bright copper electrodeposits. *Journal of Applied Electrochemistry*, 9(4):465–469, 1979.

[67] R Walker and SD Cook. High throw copper sulphate bath with chlorides. *Surface Technology*, 11(3):189–203, 1980.

[68] MRH Hill and GT Rogers. Polyethylene glycol in copper electrodeposition onto a rotating disk electrode. *Journal of Electroanalytical Chemistry and Interfacial Electrochemistry*, 86(1):179–188, 1978.

[69] M. Goodenough and K. J. Whitlaw. Transactions of the institute of metal finishing. 67(57), 1989.

[70] Mordechay Schlesinger and Milan Paunovic. *Modern electroplating*, volume 55. Wiley, 2011.

[71] G. Fuseya and K. Murata. *Trans American Electrochemistry Society*, 50(235), 1926.

[72] R. O. Hull and W. Blum. *J. Res. Natl. Bur. Stand.*, 5(767), 1930.

[73] DF Suarez and FA Olson. Nodulation of electrodeposited copper in the presence of thiourea. *Journal of Applied Electrochemistry*, 22(11):1002–1010, 1992.

[74] Jongsoo Kim and Heesan Kim. Effects of organic additives on preferred plane and residual stress of copper electroplated on polyimide. *Materials Chemistry and Physics*, 120(2–3):341 – 347, 2010.

[75] Masaki Kobayashi, Kouji Nakajima, Toshiaki Matubara, Masaharu Sugimoto, Hiroaki Kouzai, and Hideo Honma. Plating with copper sulfate bath using an end-modified peg compound. *Korea Institute of Surface Engineering Conference abstracts*, pages 260–260, 2008.

[76] H.I. Philip and M.J. Nicol. The kinetics and mechanism of the deposition of nickel from chloride solutions. *Chloride Hydrometallurgy (Proc. Cost), Benelux Metallurgie, Brussels*, pages 250–269, 1977.

[77] N.P. Finkelstein, RI. Philip, MJ. Nicol, and A.M.E. Balaes. The mechanism of the electrodeposition and dissolution of nickel from chloride media. *NIM Report No.I796, National Institute for Metallurgy, 1 Yale Rd., Milner Park, Johannesburg, South Africa*, page 31, April 21, 1976.

[78] M Fujimori, N. Ono, N Tamura, and T Kohga. Electrowinning from aqueous chlorides in SMM's nickel and cobalt refining process. *Chloride Electrometallurgy [Proc. Conn, ed. by P.D. Parker, The Metallurgical Society/AIME*, (155-166), 1982.

[79] Karl H. Gayer. The hydrolysis of cations baes. *Journal of Chemical Education*, 54(10):A429, 1977.

[80] Yu P Perelygin and D Yu Chistyakov. Boric acid. *Russian Journal of Applied Chemistry*, 79(12):2041–2042, 2006.

[81] W. J. Wruck. *Electrodeposition of Nickel from Chloride Solutions*. MS Thesis, University of Wisconsin, Madison, 1978.

[82] Wendy C Grande and Jan B Talbot. Electrodeposition of thin films of nickel-iron ii. modeling. *Journal of the Electrochemical Society*, 140(3):675–681, 1993.

[83] J. Ji, W. C. Cooper, D. B. Dreisinger, and E. Peters. Surface pH measurements during nickel electrodeposition. *Journal of Applied Electrochemistry*, 25:642–650, 1995. 10.1007/BF00241925.

[84] Howard G. Nelson. Hydrogen embrittlement. *Treatise on Materials Science and Technology*, 25:275–359, 1983. Cited By (since 1996):40.

[85] IM Bernstein and AW Thompson. Hydrogen effects in metals. *Warrendale, PA, Metallurgical Society of AIME, 1981, 1071 p*, 1981.

[86] John P Hirth. Effects of hydrogen on the properties of iron and steel. *Metallurgical Transactions A*, 11(6):861–890, 1980.

[87] D.R. Gabe. The role of hydrogen in metal electrodeposition processes. *Journal of Applied Electrochemistry*, 27(8):908–915, 1997.

[88] PC Andricacos, LT Romankiw, H Gerischer, and CW Tobias. Advances in electrochemical science and engineering, vol. 3. *New York*, page 227, 1994.

[89] Abner Brenner. Electrodeposition of alloys: principles and practices. 1963.

[90] Jean Horkans. On the role of buffers and anions in NiFe electrodeposition. *Journal of the Electrochemical Society*, 126(11):1861–1867, 1979.

[91] MJ Nicol and HI Philip. Underpotential deposition and its relation to the anomalous deposition of metals in alloys. *Journal of Electroanalytical Chemistry and Interfacial Electrochemistry*, 70(2):233–237, 1976.

[92] Michael Matlosz. Competitive adsorption effects in the electrodeposition of iron-nickel alloys. *Journal of the Electrochemical Society*, 140(8):2272–2279, 1993.

[93] Rodnei Bertazzoli and Derek Pletcher. Studies of the mechanism for the electrodeposition of FeCo alloys. *Electrochimica acta*, 38(5):671–676, 1993.

[94] Irving W Wolf. Composition and thickness effects on magnetic properties of electrodeposited nickel-iron thin films. *Journal of The Electrochemical Society*, 108(10):959–964, 1961.

[95] Yelena Sverdlov, Yuri Rosenberg, Yu.I. Rozenberg, Ron Zmood, Raviv Erlich, Sivan Natan, and Yosi Shacham-Diamand. The electrodeposition of cobalt–nickel–iron high aspect ratio thick film structures for magnetic MEMS applications. *Microelectronic Engineering*, 76(1–4):258 – 265, 2004.

[96] Frank Engel Rasmussen, Jan Tue Ravnkilde, Peter Torben Tang, Ole Hansen, and Siebe Bouwstra. Electroplating and characterization of cobalt–nickel–iron and nickel–iron for magnetic microsystems applications. *Sensors and Actuators A: Physical*, 92(1):242–248, 2001.

[97] S-H Kim, H-J Sohn, Y-C Joo, Y-W Kim, T-H Yim, H-Y Lee, and T Kang. Effect of saccharin addition on the microstructure of electrodeposited Fe36 wt Ni alloy. *Surface and Coatings Technology*, 199(1):43–48, 2005.

[98] Bonkeup Koo and Bongyoung Yoo. Electrodeposition of low-stress NiFe thin films from a highly acidic electrolyte. *Surface and Coatings Technology*, 205(3):740–744, 2010.

[99] D.-Y. Park, B.Y. Yoo, S. Kelcher, and N.V. Myung. Electrodeposition of low-stress high magnetic moment fe-rich feconi thin films. *Electrochimica Acta*, 51(12):2523 – 2530, 2006.

[100] Yong hua Zhang, Gui fu Ding, Yu li Cai, Hong Wang, and Bingchu Cai. Electroplating of low stress permalloy for MEMS. *Materials Characterization*, 57(2):121 – 126, 2006.

[101] Paul A Flinn. Principles and applications of wafer curvature techniques for stress measurements in thin films. In *MRS Proceedings*, volume 130. Cambridge Univ Press, 1988.

[102] Frontier Semiconductor 500TC. User manual. 1999.

[103] M S Benrakkad, M A Benitez, J Esteve, J M Lopez-Villegas, J Samitier, and J R Morante. Stress measurement by microraman spectroscopy of polycrystalline silicon structures. *Journal of Micromechanics and Microengineering*, 5(2):132, 1995.

[104] J. Samitier, S. Marco, O. Ruiz, J.R. Morante, J. Esteve-Tinto, and J. Bausells. Analysis by FT-IR spectroscopy of SiO2-polycrystalline structures used in micromechanics: Stress measurements. *Sensors and Actuators A: Physical*, 32:347 – 353, 1992.

[105] K. Kusaka, T. Hanabusa, M. Nishida, and F. Inoko. Residual stress and in-situ thermal stress measurement of aluminum film deposited on silicon wafer. *Thin Solid Films*, 290-291(0):248 – 253, 1996.

[106] Dehaven P and Goldsmith C. In *Mater. Res. Soc. Symp.*, pages 308 343–8, 1993.

[107] Yamamoto N and Sakata S. In *Extended Abstracts of the 1989 Int. Conf. on Solid State Devices and Materials (SSDM) (Tokyo, Japan)*, pages 221–4, 1989.

[108] S.G Malhotra, Z.U Rek, S.M Yalisove, and J.C Bilello. Analysis of thin film stress measurement techniques. *Thin Solid Films*, 301(1–2):45 – 54, 1997.

[109] Martin A Schmidt, Roger T Howe, Stephen D Senturia, and Joseph H Haritonidis. Design and calibration of a microfabricated floating-element shear-stress sensor. *Electron Devices, IEEE Transactions on*, 35(6):750–757, 1988.

[110] H. Guckel, D.W. Burns, C.C.G. Visser, H.A.C. Tilmans, and D. Deroo. Fine-grained polysilicon films with built-in tensile strain. *Electron Devices, IEEE Transactions on*, 35(6):800 –801, jun 1988.

[111] W Fang and J A Wickert. Post buckling of micromachined beams. *Journal of Micromechanics and Microengineering*, 4(3):116, 1994.

[112] Janake Schweitz and Fredric Ericson. Evaluation of mechanical materials properties by means of surface micromachined structures. *Sensors and Actuators A: Physical*, 74(1):126–133, 1999.

[113] M Boutry, A Bosseboeuf, JP Grandchamp, and G Coffignal. Finite-element method analysis of freestanding microrings for thin-film tensile strain measurements. *Journal of Micromechanics and Microengineering*, 7(4):280, 1997.

[114] Stephen D Senturia. Can we design microbotic devices without knowing the mechanical properties of materials? In *Proc. IEEE Micro Robots Teleop. Workshop*, page 3, 1987.

[115] Liwei Lin, A.P. Pisano, and R.T. Howe. A micro strain gauge with mechanical amplifier. *Microelectromechanical Systems, Journal of*, 6(4):313 –321, Dec 1997.

[116] French P J Goosen J F L, van Driee ÌÍLnhuizen B P and Wolffenbuttel R F. Stress measurement structures for micromachined sensors. *Tech. Dig. 7th Int. Conf. on Solid State Sensors and Actuators, Transducers '93 (Yokohama, Japan) June 7–10 1993 pp 783–6*, 1993.

[117] William C. Tang, Martin G. Lim, and Roger T. Howe. Electrostatic comb drive levitation and control method. *IEEE/ASME Journal of Microelectromechanical Systems*, 1:170–178, 1992.

[118] Y.B. Gianchandani and K. Najafi. Bent-beam strain sensors. *Microelectromechanical Systems, Journal of*, 5(1):52 –58, mar 1996.

[119] Fredric Ericson, Staffan Greek, Jan Soderkvist, and J Schweitz. High sensitive internal film stress measurement by an improved micromachined indicator structure. In *The 8th International Conference on Solid-State Sensors and Actuators, 1995 and Eurosensors IX.. Transducers' 95.*, volume 2, pages 84–87. IEEE, 1995.

[120] X. Zhang, Y. Zohar, and T.Y. Zhang. In *Mat. Res. Soc. Symp. Proc*, volume 444, page 111, 1997.

[121] J.M. David and M.G. Buehler. A numerical analysis of various cross sheet resistor test structures. *Solid-State Electronics*, 20(6):539 – 543, 1977.

[122] Martin G. Buehler and W. Robert Thurber. An experimental study of various cross sheet resistor test structures. *Journal of The Electrochemical Society*, 125(4):645–650, 1978.

[123] W. Versnel. Analysis of the greek cross, a van der pauw structure with finite contacts. *Solid-State Electronics*, 22(11):911 – 914, 1979.

[124] M.I. Newsam, A.J. Walton, and M. Fallon. Numerical analysis of the effect of geometry on the performance of the greek cross structure. In *Microelectronic Test Structures, 1996. ICMTS 1996. Proceedings. 1996 IEEE International Conference on*, pages 247 –252, Mar 1996.

[125] M.G. Buehler. Electrical sheet resistance and linewidth test structures. *ICMTS Tutorial Barcelona*, March 22nd 1993.

[126] Standard test method for determining the average electrical width of a straight thin-film metal line [metric]. *Tech. Rep. F1216M-96, American Society for Testing and Materials*, 1996.

[127] G. P. Carver, R. L. Mattis, and M. G. Buehler. Design considerations for the cross-bridge sheet resistor. *Tech. Rep. NBSIR 82-2548, National Bureau of Standards, Washington, DC*, 1982.

[128] H.A. Schafft, J.S. Suehle, and P.G.A. Mirel. Thermal conductivity measurements of thin-film silicon dioxide. In *Microelectronic Test Structures, 1989. ICMTS 1989. Proceedings of the 1989 International Conference on*, pages 121 – 125, march 1989.

[129] Precision measurement of metal line width in sub-quarter micron interconnect systems. *Tech. Rep. 4156-11, Agilent Technologies*, 2001.

[130] M.W. Cresswell, N.M.P. Guillaume, W.E. Lee, R.A. Allen, W.F. Guthrie, R.N. Ghoshtagore, Z.E. Osborne, N. Sullivan, and L.W. Linholm. Extraction of sheet resistance from four-terminal sheet resistors replicated in monocrystalline films with nonplanar geometries. *IEEE Transactions on Semiconductor Manufacturing*, 12(2):154 –165, May 1999.

[131] M. G. Buehler, S. D. Grant, and W. R. Thurber. Bridge and van der pauw sheet resistors for characterizing the line width of conducting layers. *Journal of The Electrochemical Society*, 125(4):650–654, 1978.

[132] D Yen and MG Buehler. A cross-bridge test structure for evaluating the linewidth uniformity of an integrated-circuit lithography system. *Journal of the Electrochemical Society*, 129(10):2313–2318, 1982.

[133] R.A. Allen, M.W. Cresswell, and L.M. Buck. A new test structure for the electrical measurement of the width of short features with arbitrarily wide voltage taps. *Electron Device Letters, IEEE*, 13(6):322 –324, june 1992.

[134] M.G. Buehler and C.W. Hershey. The split-cross-bridge resistor for measuring the sheet resistance, linewidth, and line spacing of conducting layers. *IEEE Transactions on Electron Devices*, 33(10):1572 – 1579, 1986.

[135] J.K. Luo, M. Pritschow, A.J. Flewitt, S.M. Spearing, N.A. Fleck, and W.I. Milne. Effects of process conditions on properties of electroplated Ni thin films for microsystem applications. *Journal of the Electrochemical Society*, 153(10):D155–D161, 2006.

[136] AB Horsfall, JMM dos Santos, SM Soare, NG Wright, AG O'neill, SJ Bull, AJ Walton, AM Gundlach, and JTM Stevenson. Direct measurement of residual stress in sub-micron interconnects. *Semiconductor Science and Technology*, 18(11):992, 2003.

[137] S. Smith, N.L. Brockie, J.G. Terry, N. Wang, A.B. Horsfall, and A.J. Walton. Application of a micromechanical test structure to the measurement of stress in an electroplated permalloy film. In *IEEE International Conference on Microelectronic Test Structures, 2009. ICMTS 2009.*, pages 75 –80, 30 2009-April 2009.

[138] Zhimin Zhou, Yong Zhou, Ying Cao, Wen Ding, and Haiping Mao. The evaluation of young's modulus and residual stress of Cu films by NiFe/Cu bilayer film microbridge tests. *Journal of Micromechanics and Microengineering*, 18(1):015027, 2008.

[139] ZM Zhou, Y Zhou, CS Yang, JA Chen, GF Ding, W Ding, MJ Wang, and YM Zhang. The evaluation of Young's modulus and residual stress of nickel films by microbridge testings. *Measurement Science and Technology*, 15(12):2389, 2004.

[140] Robert H Collins. Process for improving photoresist adhesion, December 22 1970. US Patent 3,549,368.

[141] MEGAPOSIT SPR220 series photoresists.

[142] RB Rebak, JR Dillman, P Crook, and CVV Shawber. Corrosion behavior of nickel alloys in wet hydrofluoric acid. *Materials and Corrosion*, 52(4):289–297, 2001.

[143] James R. Crum, Inco Alloys International Inc.; M.J. McNallan Gaylord D. Smith, and Sviatoslav Hirny. Characterization of corrosion resistant materials in low and high temperature HF environments. 1999.

[144] Nobuhiro Miki, H. Kikuyama, I. Kawanabe, Masayuki Miyashita, and T. Ohmi. Gas-phase selective etching of native oxide. *Electron Devices, IEEE Transactions on*, 37(1):107–115, 1990.

[145] Ann Witvrouw, Bert Du Bois, Piet De Moor, Agnes Verbist, Chris A Van Hoof, Hugo Bender, and Christiaan Baert. Comparison between wet HF etching and vapor HF etching for sacrificial oxide removal. In *Micromachining and Microfabrication*, pages 130–141. International Society for Optics and Photonics, 2000.

[146] Y Fukuta, H Fujita, and H Toshiyoshi. Vapor hydrofluoric acid sacrificial release technique for micro electro mechanical systems using labware. *Japanese Journal of Applied Physics Part 1-Regular Papers Short Notes & Review Papers*, 42:3690–3694, 2003.

[147] SEC 3000 toxic gas detector.

[148] Paul VC Hough. Method and means for recognizing complex patterns, 1962. US Patent 3,069,654.

[149] C.J. Wilson, A.B. Horsfall, A.G. O'Neill, N.G. Wright, S.J. Bull, J.G. Terry, J.T.M. Stevenson, and A.J. Walton. Direct measurement of electromigration-induced stress in interconnect structures. *Device and Materials Reliability, IEEE Transactions on*, 7(2):356 –362, June 2007.

[150] Nosang V Myung, D-Y Park, B-Y Yoo, and Paulo TA Sumodjo. Development of electroplated magnetic materials for mems. *Journal of Magnetism and Magnetic Materials*, 265(2):189–198, 2003.

[151] Jean Horkans. Effect of plating parameters on electrodeposited NiFe. *Journal of the Electrochemical Society*, 128(1):45–49, 1981.

[152] D. Flynn and M.P.Y. Desmulliez. Influence of pulse reverse plating on the properties of Ni-Fe thin films. *Magnetics, IEEE Transactions on*, 46(4):979 –985, april 2010.

[153] M Islam. Anomalous electrodeposition of Fe-Ni alloy coating from simple and complex baths and its magnetic property. *IIUM Engineering Journal*, 10(2), 2010.

[154] H Dahms and IM Croll. The anomalous codeposition of iron-nickel alloys. *Journal of The Electrochemical Society*, 112(8):771–775, 1965.

[155] Ki-Deok Song, Kwang Bum Kim, Seong Ho Han, and Hong Ke Lee. A study on effect of hydrogen reduction reaction on the initial stage of Ni electrodeposition using EQCM. *Electrochemistry communications*, 5(6):460–466, 2003.

[156] Allen J Bard, Roger Parsons, and Joseph Jordan. *Standard potentials in aqueous solution*, volume 6. CRC press, 1985.

[157] K.N. Njau and L.J.J. Janssen. Electrochemical reduction of nickel ions from dilute solutions. *J. Appl. Electrocehm*, 25:982, 1995.

[158] K.-M. Yin, J.-H. Wei, J.-R. Fu, B.N. Popov, S.N. Popova, and R.E. White. *J. Appl. Electrochem.*, 1994.

[159] A.H. DuRose. *Plat. Surf. Finish*, 64:52, 1977.

[160] W. L Jolly. Modern inorganic chemistry. *McGraw-Hill*, page 198, 1984.

[161] C.E. Housecroft and Sharpe A.G. Inorganic chemistry (2nd ed.). *Pearson Prentice-Hall*, pages 314–5, 2005.

[162] M.Y. Abyaneh and M. Hashemi-Pour. *Trans. IMF*, 72:23, 1993.

[163] S Armyanov and G Sotirova-Chakarova. Hydrogen desorption and internal stress in nickel coatings obtained by periodic electrodeposition. *Journal of The Electrochemical Society*, 139(12):3454–3457, 1992.

[164] C J Raub. Hydrogen in electrodeposits: of decisive importance, but much neglected. *Plating and Surface Finishing*, 80(9):30–38, 1993.

[165] T Boniszewski and GC Smith. The influence of hydrogen on the plastic deformation ductility, and fracture of nickel in tension. *Acta metallurgica*, 11(3):165–178, 1963.

[166] Milko Monev. Effect of the pH value of the hydrogenation solution upon the phase transformation of nickel into nickel hydride. *Electrochimica Acta*, 46(15):2373–2378, 2001.

[167] G. Di Giacomo, P. Brandani, V. Brandani, and G. Del Re. Solubility of boric acid in aqueous solutions of chloride salts. *Desalination*, 91(1):21 – 33, 1993.

[168] Sholeh Hessami and Charles W Tobias. A mathematical model for anomalous codeposition of nickel-iron on a rotating disk electrode. *Journal of The Electrochemical Society*, 136(12):3611–3616, 1989.

[169] JO Dukovic. Computation of current distribution in electrodeposition, a review. *IBM Journal of research and Development*, 34(5):693–705, 1990.

[170] Thomas M Harris and Jennifer Lyn St Clair. Electroplating bath for nickel-iron alloys and method, November 4 1997. US Patent 5,683,568.

[171] P. C. Andricacos, J. Locarnini, V. L. Oliver, and L. T. Romankiw. *Iron Autoanalyzer for Nickel-Iron Plating Bath*, volume 31(1). IBM Tech. Discl. Bull, 1988.

[172] MC Blakeslee, LT Romankiw, RE Acosta, S Krongelb, and B Stoeber. Electrodeposition process for fabrication of condutor 1st, SLM 2-MU Bubble Memory. In *Journal of the Electrochemical Society*, volume 125, pages C152–C152, 1978.

[173] A.B. Horsfall, Kai Wang, J.M.M. dos Santos, S.M. Soare, S.J. Bull, N.G. Wright, A.G. O'Neill, J.G. Terry, A.J. Walton, A.M. Gundlach, and J.T.M. Stevenson. Dependence of process parameters on stress generation

in aluminum thin films. *IEEE Transactions on Device and Materials Reliability*, 4(3):482 – 487, sept. 2004.

[174] G Schiavone, MPY Desmulliez, S Smith, J Murray, E Sirotkin, JG Terry, AR Mount, and AJ Walton. Quantitative wafer mapping of residual stress in electroplated NiFe films using independent strain and Young's modulus measurements. In *IEEE International Conference on Microelectronic Test Structures (ICMTS)*, pages 105–110. IEEE, 2012.

[175] William N Sharpe Jr. Mechanical properties of mems materials. *The MEMS handbook*, 3:1–33, 2002.

[176] PC Andricacos, C Arana, J Tabib, J Dukovic, and LT Romankiw. Electrodeposition of nickel-iron alloys i. effect of agitation. *Journal of the Electrochemical Society*, 136(5):1336–1340, 1989.

[177] R Vasudevan, R Devanathan, and KG Chidambaram. Effect of ultrasonic agitation during electroplating of nickel and copper at room temperature. *Metal finishing*, 90(10):23–26, 1992.

[178] R Walker and CT Walker. New explanation for the brightness of electrodeposits produced by ultrasound. *Ultrasonics*, 13(2):79–82, 1975.

[179] Frederick Herbert Wells. Electrodeposition of nickel, April 4 1967. US Patent 3,312,604.

[180] PBSNV Prasad, R Vasudevan, SK Seshadri, and S Ahila. The effect of ultrasonic vibration on nickel electrodeposition. *Materials letters*, 17(6):357–359, 1993.

[181] Arjan Hovestad and Leonard JJ Janssen. Electroplating of metal matrix composites by codeposition of suspended particles. In *Modern Aspects of Electrochemistry*, pages 475–532. Springer, 2005.

[182] CC Lee and CC Wan. A study of the composite electrodeposition of copper with alumina powder. *Journal of the Electrochemical Society*, 135(8):1930–1933, 1988.

[183] Yoshihiro Suzuki and Osamu Asai. Adsorption-codeposition process of Al2O3 particles onto Ag-Al2O3 dispersion films. *Journal of the Electrochemical Society*, 134(8):1905–1910, 1987.

[184] JA Di Bari. Electrodeposition of nickel. *Modern Electroplating*, pages 79–114.

[185] M Cook and TLL Richards. The self-annealing of copper. *Journal of the Institute of Metals*, 70:159–173, 1944.

[186] PC Andricacos, C Uzoh, JO Dukovic, J Horkans, and H Deligianni. Damascene copper electroplating for chip interconnections. *IBM Journal of Research and Development*, 42(5):567–574, 1998.

[187] Hongfang Sun, Zewen Liu, Jiahao Zhao, Li Wang, and Jing Zhu. The enhancement of Q-factor of planar spiral inductor with low-temperature annealing. *IEEE transactions on electron devices*, 55(3):931–936, 2008.

[188] *Comparative Cu Diffusion Studies in Advanced Metallizations of Cu and AI-Cu Based Thin Films*, volume 337. MRS Proceedings, 2011.

[189] IV Tomov, DS Stoychev, and IB Vitanova. Recovery and recrystallization of electrodeposited bright copper coatings at room temperature. ii. x-ray investigation of primary recrystallization. *Journal of Applied Electrochemistry*, 15(6):887–894, 1985.

[190] Rui Huang, Werner Robl, Hajdin Ceric, Thomas Detzel, and Gerhard Dehm. Stress, sheet resistance, and microstructure evolution of electroplated cu films during self-annealing. *Device and Materials Reliability, IEEE Transactions on*, 10(1):47–54, 2010.

[191] Stefan Enderling, Martin H Dicks, Stewart Smith, J Tom M Stevenson, and Anthony J Walton. Design rules to minimize the effect of joule heating in greek cross test structures. *IEEE Transactions on Semiconductor Manufacturing*, 17(2):84–90, 2004.

[192] Wikipedia. Nickel — wikipedia, the free encyclopedia, 2014. [Online; accessed 22-April-2014].

[193] Wikipedia. Copper — wikipedia, the free encyclopedia, 2014. [Online; accessed 22-April-2014].

[194] Alexander Milchev. *Electrocrystallization: fundamentals of nucleation and growth*. Springer, 2002.

[195] Keith Oldham and Jan Myland. *Fundamentals of electrochemical science*. Elsevier, 1993.

[196] Haebum Lee and Sergey D Lopatin. The influence of barrier types on the microstructure and electromigration characteristics of electroplated copper. *Thin Solid Films*, 492(1):279–284, 2005.

[197] Shih-Chieh Chang, Jia-Min Shieh, Bau-Tong Dai, Ming-Shiann Feng, and Ying-Hao Li. The effect of plating current densities on self-annealing behaviors of electroplated copper films. *Journal of The Electrochemical Society*, 149(9):G535–G538, 2002.

[198] Wen Dong, Jian Zhang, Jingwu Zheng, and Jiawei Sheng. Self-annealing of electrodeposited copper thin film during room temperature storage. *Materials Letters*, 62(10):1589–1591, 2008.

[199] Jie Gao. The influence of additives on microstructure evolution of electrochemically deposited copper films. 2003.

[200] M Stangl, J Acker, V Dittel, W Gruner, V Hoffmann, and K Wetzig. Characterization of electroplated copper self-annealing with investigations

focused on incorporated impurities. *Microelectronic engineering*, 82(2):189–195, 2005.

[201] Min-Seung Yoon, Young-Joon Park, and Young-Chang Joo. Impurity redistributions in electroplated cu films during self-annealing. *Thin Solid Films*, 408(1):230–235, 2002.

[202] Mark Lefebvre, editor. *Electrolytic Copper Bath Analysis for PCB Fabrication*. Dow Electronic Materials, 2010.

[203] VA Vas' ko, I Tabakovic, SC Riemer, and MT Kief. Effect of organic additives on structure, resistivity, and room-temperature recrystallization of electrodeposited copper. *Microelectronic engineering*, 75(1):71–77, 2004.

[204] Rozalia Beica, Charles Sharbono, and Tom Ritzdorf. Through silicon via copper electrodeposition for 3D integration integration. In *Electronic Components and Technology Conference, 2008. ECTC 2008. 58th*, pages 577–583. IEEE, 2008.

[205] Tohru Watanabe. *Nano plating-microstructure formation theory of plated films and a database of plated films*. Elsevier, 2004.

[206] Joseph R Davis. *Copper and copper alloys*. ASM international, 2001.

[207] Sébastien Lagrange, SH Brongersma, Moshe Judelewicz, Annelies Saerens, Iwan Vervoort, Emmanuel Richard, Roger Palmans, and Karen Maex. Self-annealing characterization of electroplated copper films. *Microelectronic Engineering*, 50(1):449–457, 2000.

[208] JME Harper, C Cabral Jr, PC Andricacos, L Gignac, IC Noyan, KP Rodbell, and CK Hu. Mechanisms for microstructure evolution in electroplated copper thin films near room temperature. *Journal of Applied Physics*, 86(5):2516–2525, 1999.

[209] Masayuki Yokoi, Saburo Konishi, and Tadao Hayashi. Adsorption behavior of polyoxyethyleneglycole on the copper surface in an acid copper sulfate bath. *Denki Kagaku oyobi Kogyo Butsuri Kagaku*, 52(4):218–223, 1984.

[210] E. Conradie and D. Moore. Su-8 thick photoresist processing as a functional material for mems applications,. *J. Micromech. Microeng*, 12(4):368–374, 2002.

[211] L. Yu, F. E. H. Tay, G. Xu, B. Chen, M. Avram, , and C. Iliescu. Adhesive bonding with SU-8 at wafer level for microfluidic devices. *J. Phys. Conf. Ser*, 34(1):776–781, 2006.

[212] C. Kourouklis, T. Kohlmeier, and H. H. Gatzen. The application of chemical–mechanical polishing for planarizing an SU-8/permalloy combination used in MEMS devices. *Sensors Actuators: A. Phys*, 106(263–266), 2003.

[213] R. Feng and R. J. Farris. Influence of processing conditions on the thermal and mechanical properties of SU8 negative photoresist coatings. *J. Micromech. Microeng*, 13(1):80–88, 2003.

[214] S. Bystrova, R. Luttge, , and A. van den Berg. Study of crack formation in high-aspect ratio SU-8 structures on silicon. *Microelectron. Eng*, 84(5-8):1113–1116,, 2007.

[215] W. Dai, K. Lian, and W. Wang. A quantitative study on the adhesion property of cured SU-8 on various metallic surfaces. *Microsyst. Tech- nol*, 11(7):526–534, 2005.

[216] Anthony J Walton and Stewart Smith. A review of test structures for characterising microelectronic and mems technology. *Advances in Science and Technology*, 54:356–365, 2009.

[217] Allen J Bard and Larry R Faulkner. Fundamentals and applications. *Electrochemical Methods*, 2, 1980.

[218] Vitaly V Pavlishchuk and Anthony W Addison. Conversion constants for redox potentials measured versus different reference electrodes in acetonitrile solutions at 25 °C. *Inorganica Chimica Acta*, 298(1):97 – 102, 2000.

[219] B. Poon, D. Rittel, and G. Ravichandran. An analysis of nanoindentation in linearly elastic solids. *International Journal of Solids and Structures*, 45(24):6018 – 6033, 2008.

[220] Jeremy Thurn and Robert F Cook. Simplified area function for sharp indenter tips in depth-sensing indentation. *Journal of Materials Research*, 17(5):1143–1146, 2002.

[221] Mark R VanLandingham, TF Juliano, and MJ Hagon. Measuring tip shape for instrumented indentation using atomic force microscopy. *Measurement Science and Technology*, 16(11):2173, 2005.

[222] KW McElhaney, JJ Vlassak, and WD Nix. Determination of indenter tip geometry and indentation contact area for depth-sensing indentation experiments. *Journal of Materials Research*, 13(5):1300–1306, 1998.

[223] Christopher A Schuh. Nanoindentation studies of materials. *Materials Today*, 9(5):32–40, 2006.

[224] W.C. Oliver and G.M. Pharr. Measurement of hardness and elastic modulus by instrumented indentation: Advances in understanding and refinements to methodology. *Journal of Materials Research*, 19:3–20, 1 2004.

[225] Masayuki Uda et al. Energy dispersion type X-ray diffraction/spectral device, April 1 2008. US Patent 7,352,845.

[226] Bernard Dennis Cullity and Chad D Graham. *Introduction to magnetic materials*. Wiley. com, 2011.

[227] Keiichiro Fuwa and BL Valle. The physical basis of analytical atomic absorption spectrometry. the pertinence of the beer-lambert law. *Analytical Chemistry*, 35(8):942–946, 1963.

[228] Hiroko Wada, Osamu Nakazawa, and Hajime Takada. Evaluation of PAC, TAC, 2-IAC as Metallochromic Indicators in the EDTA Titrations of Nickel. *Bulletin of the Chemical Society of Japan*, 50(8):2101–2103, 1977.

[229] Chi-Chang Hu. The inhibition of anomalous codeposition of iron-nickel deposits using pulse-reverse electroplating. In *Magnetic materials, processes, and devices VII and electrodeposition of alloys: proceedings of the international symposia*, volume 2002, page 398. Electrochemical Society, 2003.

[230] DG Karamanev, LN Nikolov, and V Mamatarkova. Rapid simultaneous quantitative determination of ferric and ferrous ions in drainage waters and similar solutions. *Minerals Engineering*, 15(5):341–346, 2002.

[231] DD Perrin. Stability of metal complexes with salicylic acid and related substances. *Nature*, 182:741–742, 1958.

[232] Rastislav Šípoš, Jozef Šima, Pavol Tarapčík, and Béla Gyurcsik. Solution properties of iron (iii) complexes with 5-fluorosalicylic acid—spectra, speciation, and redox stability. *Chemical Papers*, 62(5):496–503, 2008.

[233] RC DeGeiso, LG Donaruma, and EA Tomic. Polymeric ligands. I. some salicylic acid derivatives. *The Journal of Organic Chemistry*, 27(4):1424–1426, 1962.